Diss. ETH No. 20208

Optimising the fabrication of organic light-emitting diodes by laser-induced forward transfer

A dissertation submitted to

ETH ZURICH

for the degree of

Doctor of Sciences

presented by

JAMES ROBERT HOUSTON SHAW STEWART

Master of Natural Sciences,
University of Cambridge

born 04.04.1986

citizen of the United Kingdom of Great Britain

accepted on the recommendation of

Prof. Dr. Alexander Wokaun, examiner
Prof. Dr. Christophe Copéret, co-examiner
PD Dr. Thomas Lippert, co-examiner
Prof. Dr. Frank Nüesch, co-examiner

2012

O wad some Pow'r the giftie gie us
To see oursels as ithers see us!
It wad frae mony a blunder free us,
An' foolish notion.

Robert Burns

Contents

Abstract

Laser-induced forward transfer (LIFT) has been used to print different types of *organic light-emitting diode* (OLED) pixels: *Polymeric* OLEDs (PLEDs), *small molecule* OLEDs (SMOLEDs), and *phosphorescent* OLEDs (PhOLEDs). The LIFT process uses an intermediate *dynamic release layer* (DRL) to provide the propulsion force. The DRL material is a *triazene polymer* (TP), which decomposes, at least in part, photochemically meaning that thermal build-up is limited. The use of LIFT for all types of thin-film OLED materials has been enhanced by the reduction of the environmental pressure and the introduction of a well-defined donor-receiver substrate gap. In addition, theoretical insights into the LIFT process have been obtained through both experiments and numerical simulations, which look particularly at the flyer velocity, laser pulse length and thermal effects.

Fundamental analysis into TP ablation and the LIFT process has been investigated in a number of different ways. Two analytical modelling approaches have been outlined for UV TP ablation: a thermal model which has been used to evaluate the proportion of heat lost into the substrate for both frontside and backside ablation, and a flyer velocity model based on the explosive Gurney model. The model is compared to velocity results obtained at reduced pressure from shadowgraphy, and the large loss in energy from the laser to the flyer has been compared with the thermal energy in the substrate from the thermal model. TP ablation with different laser pulse lengths shows that shorter pulse lengths give a lower ablation depth per pulse, suggesting smaller thermal energy losses for shorter pulse lengths when analysed using the thermal model. Thermal ablation has been investigated experimentally by ablation of TP films using pulsed laser heating of a silicon substrate, and measuring the flyer by reflectometry.

Complementing the theoretical understanding of the LIFT process, pixel deposition of various types of OLED pixels (known as *LIFTed* pixels) has been optimised. LIFT of both Al / poly(2-methoxy-5-(2'-ethylhexyloxy)-1,4-phenylenevinylene) (MEH-PPV) and Ag / poly-(9,9-dioctylfluorene-2,7-diyl) (PFO) bilayer pixels, at atmospheric pressure, has been improved by modification of the receiver substrate to improve interfacial adhesion. Early successes with Al / MEH-PPV pixels at atmospheric pressure have been followed up by studies into the effects of a reduction in the environmental pressure and variation of the donor-receiver gap with a spacer. The reduction of atmospheric pressure, combined with a controlled donor-receiver gap of ~ 15 μm, has been used to deposit a number of different types of OLEDs: tri-colour PFO-based PLEDs and PhOLEDs; aluminium tri-8-hydroxyquinoline

(Alq_3) SMOLEDs; and alcohol-soluble polyfluorene (PFN) PLEDs. In addition to normal LIFTed PFN / Al bilayer pixels, sequential LIFT of single-layer PFN and Al films has also fabricated functional devices. All the OLEDs pixels fabricated using reduced pressure were LIFTed onto receiver substrates comprising of ITO / poly(3,4-ethylenedioxythiophene) blended with poly(sytrenesulfonate) (PEDOT:PSS) / poly(N-vinylcarbazole) (PVK).

The device performances of all the pixels mentioned above have been analysed, through current density - voltage - luminance (J-V-L) characteristics and electroluminescence (EL) spectra. Conventionally fabricated devices of all materials have been made for comparison with the LIFTed pixels: MEH-PPV, PFO (PLEDs and PhOLEDs), PFN, and Alq_3. In some cases the LIFTed pixels exhibited superior device characteristics to their conventional counterparts (MEH-PPV & PFO), and in some cases slightly less good device characteristics (green PFO PhOLEDs & Alq_3), but in all cases the performances were comparable. Even the sequentially transferred PFN pixels, despite high operating voltages, demonstrated reasonable efficiencies. Attempts were made to improve the devices with various electron-injecting materials at the cathode / light-emitting layer interface: poly(ethylene oxide) (PEO), Cs_2CO_3, and tetrabutylammonium hydroxide (TBA). The TBA was particularly successful with LIFTed PFO and Alq_3 pixels, improving the efficiencies by over 50 % (100 % for Alq_3).

The application of OLED pixels in flat-panel displays has been predicted for a long time, but is only now becoming a commercial reality. One of the main barriers to low-cost high-throughput OLED displays is the patterning of multi-colour pixels, with commercial approaches dominated by thermal evaporation of SMOLEDs, which wastes a large amount of expensive material. Ink-jet printing of soluble PLEDs is a good alternative, but requires significant optimisation of both the process and the polymeric materials to improve reliability. Laser-based deposition techniques are showing enormous potential, both for obtaining the sufficient high-definition of the pixels, and for low material wastage. The version of LIFT outlined in this study is unique amongst the laser-based techniques in that it transfers intact thin films across a μm-scale gap. The functionality of the PLED, SMOLED and PhOLED pixels presented here demonstrate the wide range of possibilities for OLED fabrication by LIFT.

Zusammenfassung

Laser-induced Forward Transfer (LIFT) wurde genutzt, um verschiedene Arten *organischer lichtemittierender Dioden* (OLEDs) herzustellen: *Polymer* OLEDs (PLEDs), *Small Molecule* OLEDs (SMOLEDs), und *phosphoreszente* OLEDs (PhOLEDs). Der LIFT Prozess verwendet eine *Dynamic Release Layer* (DRL) welche die benötigte Vorschubkraft erzeugt. Bei den DRL Materialien handelt es sich um *Triazen Polymere* (TP), welche zumindest teilweise photochemisch zersetzt werden, wodurch ein starker Temperaturanstieg limitiert wird. Der Nutzen von LIFT für alle Arten von OLED Dünnfilmmaterialien wurde durch eine Reduktion des Umgebungsdrucks und der Bestimmung eines optimalen Abstands zwischen Ausgangs- und Empfängersubstrat gesteigert. Außerdem wurden theoretische Erkenntnisse über den LIFT Prozess sowohl durch Experimente als auch numerische Simulationen gewonnen; insbesondere durch genauere Betrachtung der Geschwindigkeit der Transferschicht (Flyer), der Laserpulsdauer und thermischer Effekte.

Grundlegende Untersuchungen der TP-Ablation und des LIFT Prozesses wurden auf verschiedene Weisen untersucht. Zwei analytische Modellansätze wurden für die UV TP-Ablation behandelt: ein thermisches Modell, welches verwendet wurde, um den Wärmeverlust in das Substrat für vorder- und rückseitige Ablation zu bestimmen, sowie ein Modell zur Bestimmung der Geschwindigkeit des Flyers basierend auf dem Gurney Modell für Explosionen. Die Ergebnisse des zweiten Modells wurden verglichen mit Geschwindigkeiten, die aus Shadowgraphy Messungen bei reduziertem Druck gewonnen wurden. Daraufhin wurde der große Verlust an Energie zwischen Laserpuls und kinetischer Energie des Flyers verglichen mit der thermischen Energie im Substrat, welche mittels des ersten Modells berechnet wurde. TP-Ablation mit verschiedenen Laserpulsdauern zeigten, dass kürzere Pulse geringere Ablationstiefen pro Puls zur Folge haben, was nach dem thermischen Modell geringere thermische Verluste für kürzere Pulsdauern nahelegt. Rein thermische Ablation wurde experimentell untersucht über die Ablation eines TP Filmes auf einem mittels Laserpulsen geheiztem Siliziumsubstrat und Reflektometriemessungen des Flyers.

Ergänzend zum theoretischen Verständnis des LIFT Prozesses wurde die Abscheidung diverser OLED-Pixel optimiert. LIFT unter Atmosphärendruck von Al / Poly(2-methoxy-5-(2'-ethylhexyloxy)-1,4-phenylen vinylen) (MEH-PPV) and Ag / Poly(9,9-dioctylfluoren-2,7-diyl) (PFO) Doppelschichtpixeln wurde durch eine Modifikation des Empfängersubstrats verbessert, welche die Adhäsion vergrößerte. Auf frühe Erfolge mit Al / MEH-PPV Pixeln, hergestellt unter Atmosphärendruck, folgten Studien zu den Auswirkungen eines

verringerten Umgebungsdrucks und einer Variation des Abstandes zwischen Ausgangs- und Empfängersubstrat. Die Reduktion des Drucks kombiniert mit einem kontrollierten Abstand von ~ 15 μm zwischen Ausgangs- und Empfängersubstrat wurde verwendet um eine Reihe verschiedener OLED-Typen abzuscheiden: dreifarbige PFO-basierte PLEDs und PhOLEDs; Aluminium tri-8-hydroxyquinolin (Alq_3) SMOLEDs; und in Alkohol lösliche Polyfluoren (PFN) PLEDs. Neben mittels LIFT hergestellten PFN / Al Doppelschichtpixeln wurde auch sequentielles LIFT von einzelnen Schichten von PFN und Al durchgeführt um funktionsfähige Einheiten herzustellen. Sämtliche OLED-Pixel, welche bei reduziertem Druck hergestellt wurden, wurden durch LIFT auf Substrate übertragen, welche aus Indium dotierten Zinn-oxid (ITO) / Poly(3,4-ethylenedioxythiophen) gemischt mit Poly(sytrenesulfonat) (PEDOT:PSS) / Poly(N-vinylcarbazol) (PVK) bestanden.

Die Effizienz aller oben beschriebenen Pixel wurde mittels Stromdichte-Spannung-Lumineszenz (J-V-L) und Elektrolumineszenzspektroskopie (EL) untersucht. Einheiten aller Materialien wurden außerdem konventionell hergestellt zum Vergleich mit den LIFT-Pixeln: MEH-PPV, PFO (PLEDs und PhOLEDs), PFN, und Alq_3. In einigen Fällen zeigten die LIFT-Pixel bessere Eigenschaften als ihre konventionellen Gegenstücks (MEH-PPV und PFO), und in einigen Fällen geringfügig weniger gute Eigenschaften (grüne PFO PhOLEDs und Alq_3). In allen Fällen jedoch waren die Effizienzen vergleichbar. Sogar die sequentiell transferierten Pixel zeigten, abgesehen von hohen Betriebsspannungen, vergleichbare Effizienzen. Es wurden Versuche unternommen die Einheiten mit verschiedenen elektroneninjizierenden Materialien: Poly(ethylen oxide) (PEO), Cs_2CO_3, und tetrabutylammonium hydroxid (TBA) an der Grenzfläche zwischen Kathode und lichtemittierender Schicht zu verbessern. Insbesondere, die Nutzung von TBA war bei PFO und Alq_3LIFT-Pixeln mit gesteigerten Effizienzen von über 50 % (100 % bei Alq_3) erfolgreich.

Die Verwendung von OLED Pixeln in Flachbildschirmen wird seit langer Zeit vorhergesagt. Eine kommerzielle Nutzung ist allerdings gerade erst Realität geworden. Eine der Hauptbarrieren für günstige und lichtstarke OLED-Bildschirme ist das Design von Multifarbpixeln, welches kommerziell durch thermisches Verdampfen (von SMOLEDs) erzielt wird, was allerdings einen hohen und somit teuren Materialverbrauch mit sich bringt. Tintenstrahldruck löslicher PLEDs ist eine vielversprechende Alternative, erfordert jedoch noch entscheidende Optimierungen des Prozesses und der Polymere. Laserbasierte Abscheidetechniken zeigen ein hohes Potential um ausreichend gut definierte Pixel bei einem geringen Maß an Materialverschwendung zu erhalten. Die LIFT-Technik, welche in dieser Studie behandelt wurde, ist einzigartig unter den laserbasierten Techniken, da sie intakte Filme über eine Entfernung einiger Mikrometer übertragen kann. Die Funktionalität von PLED-, SMOLED- und PhOLED-Pixeln, die hier vorgestellt werden, demonstrieren die vielseitigen Möglichkeiten der OLED-Herstellung mittels LIFT.

Preface

Scientific motivation

Organic semiconductors are a relatively new class of electronic materials, and research on OLED devices only started in 1987 with Tang and VanSlyke's seminal work on Alq_3 diodes. Polymers quickly followed, from Heeger in California and Friend in Cambridge. In the following twenty years great advances were made, but organic devices were not a large-scale commercial reality when this PhD work was started in 2008. There are still many things to be improved, optimised, and even discovered. In this thesis OLEDs are being investigated, with the emphasis on fabrication method rather than the devices themselves (although this is important). OLEDs have great potential for display applications, but current deposition techniques are a significant limitation to this potential. At present, the only commercially viable technique is thermal evaporation which, besides wasting significant quantities of material, requires high vacuum and evaporable materials. The standard process for inorganic techniques is lithography, but this is not easy with organic materials which are overly sensitive to the chemicals used in the etching process.

Laser-induced forward transfer (LIFT) is the name for a process which has evolved over many years alongside the improvement in laser availability and the study of laser-material interactions. Other names for the same or similar processes include laser ablation transfer (LAT), laser decal transfer, laser direct write (LDW), as well as many others. The process which we are optimising here is applied to thin solid films, transferring them intact without any melting, evaporation or sublimation, across a defined gap on the order of 1-20 μm. The process was originally done in ambient conditions, but reduced air pressures were then applied successfully, and different inert gas environments have also been investigated. This technique is here applied to OLED pixels, but could be applied to any thin-film patterned deposition. It appears to be particularly useful for plastic materials such as polymers which require very short stresses in order to undergo brittle deformation, and also have strong interfacial interactions with the receiver substrate.

Personal motivation

Coming from a Natural Sciences BA and MSci, majoring in Geological Sciences, this topic of PhD research was something of a leap. I studied organic chemistry as part of my undergraduate degree and had a great interest in physics from the mineral physics courses, so felt a desire to explore these areas in greater detail and from a different perspective. In addition, I gained an interest in technology, and the semiconductor revolution in general, from my father who is a motion control engineer. He introduced me to computers, circuit boards, resistors, capacitors and many other things, interesting and bewildering alike. Whilst an undergraduate at Cambridge, when discussing with a lecturer in the Earth Sciences Department, Dr. Maren Daraktchiev, about my future in research, he advised me that trying a different field of research for my PhD was indeed possible. Dr. Daraktchiev provided the impetus to research abroad and investigate the field of organic electronics, and gave me the contact with Prof. Dr. Frank Nüesch that was pivotal in enabling me to start this PhD. The timing was impeccable, and a PhD opening was available straight away, to follow on from Dr. Romain Fardel's excellent postgraduate research on *laser-induced forward transfer using a triazene polymer DRL to fabricate OLEDs*. As a topic this surpassed all my expectations and I was immediately drawn in to the research, for both its scientific and engineering aspects.

The opportunity to undertake a PhD in a different research topic is not common, and for this reason I am indebted to Prof. Dr. Frank Nüesch, PD Dr. Thomas Lippert, and Prof. Dr. Alexander Wokaun for taking a risk in offering this PhD position to me. In the study of science and engineering, there are a lot of invisible barriers put up based on subject and application, which make different subjects appear more different than they really are. My experience of the PhD has taught me that there is more variability within the respective 'subjects' of earth science, materials science, and chemistry than there is between them. For this reason, anyone who is interested in experiencing other subjects should not hesitate in applying, although they will need open-minded supervisors willing enough to take a risk on them, as I had.

The support of my wife, Aimee, was integral to my whole application, and subsequent decision to come to Switzerland and do my PhD here. She has never let me lose sight of the potential of both the subject of my thesis and living abroad in Switzerland.

Part I

Background to the research

Chapter 1

Introduction

1.1 Organic electronics

1.1.1 Background

Organic electronics has been a field of technological interest for half a century, starting with studies into organic crystals as potential crystalline semiconductors in the 1950s and 60s [1–4]. Throughout this time, the perception of organic materials as purely electrical insulators changed as the potential for semiconducting and even conducting behaviour was observed. Electroluminescence was first observed in inorganic materials (silicon carbide) in 1907 [5], long before the observation of electroluminescence in an organic material [6]. In 1987 Tang and Van Slyke, at Kodak, made a breakthrough with low-voltage semiconducting light-emitting diodes based on thin films of $\sim$ 100 nm Alq_3 [7]. Shortly after, development on polymer light-emitting diodes commenced at Cambridge in Friend's group, and concurrently at Santa Barbara in Heeger's group [8, 9]. This early work on OLEDs has been continued in earnest by hundreds of research groups and many large electronics companies [10, 11]. The academic pioneers in this field have tended to move their focus from OLEDs to organic photovoltaics (OPVs) [12]. This field has much potential as a cheap and flexible alternative to more efficient inorganic PVs [13]. In addition, organic semiconductors have been used to make transistors, and the growth of flexible electronics has also pushed this research along [12, 14].

Organic electronic materials can be broadly divided into two categories based on their chemical structure: polymers and small molecules (monomers). In addition, oligomers are a grey area in-between, and organic bio-materials as active components are a very new area of interest [15]. Organic electroluminescence was first observed in thin-film crystalline anthracene in the 1960s [6]. Interest in the electronics of organic materials was stimulated by the discovery of conduction by doped polyacetylene (shown in figure 1.2) in the late 1970s [16]. These two materials, and most photo-relevant organic electronic materials, have one distinct thing in common: their conjugated π bonding systems.

All OLED materials are based on conjugated systems, lots of C=C double bonds, so an

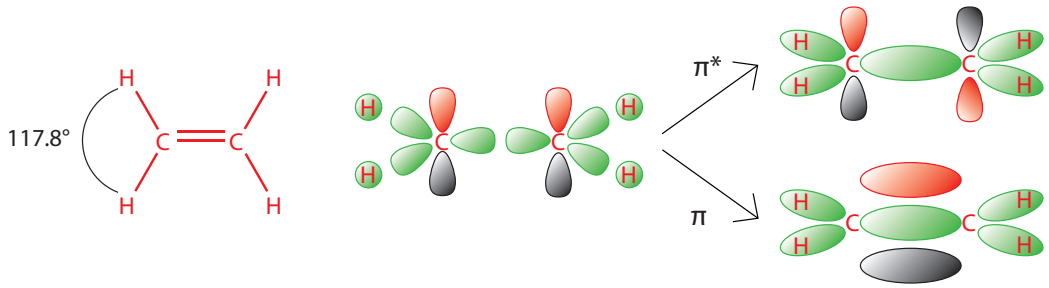

Figure 1.1 The molecular orbital (MO) make-up of ethene. The middle drawing shows all the valence shells of the hydrogens (just 1s), and the carbon (3 x sp^2, and 1 p_z). The two drawings on the right show the HOMO and LUMO of ethene. Both diagrams have the same σ bonding orbitals, both to the hydrogen, and within the C-C bond. The difference is with the bonding between the carbon p_z shells. In the stabler, lower energy HOMO (bottom), they form a delocalized π bond, and in the higher energy anti-bonding LUMO (top), they form localized atom-centred orbitals.

introduction to organic electronics requires an understanding of what a conjugated system is, and how it affects the electrical and optical properties of the material. The simplest molecule with a carbon double bond is shown in figure 1.1: ethene or ethylene. A double bond is based on the electron orbitals of carbon. A neutral carbon atom contains six electrons: two of these are in the 1s orbital (lowest energy), two in the 2s orbital, and two in the 2p orbitals (highest energy). The inner orbital (1s) is essentially a *core* electron shell, and the outer orbitals (2s and 2p) are the *valence* electron shells. p orbitals can hold six electrons in three pairs, orientated along each of the three physical axes (i.e. p_x, p_y, p_z). In a stable compound carbon fills up its valence shell by sharing electrons with other atoms, and carbon requires four electrons to fill up its outer shell. The middle drawing in figure 1.1 shows how carbon creates its bonding molecular orbitals (MOs) by hybridizing the s and p atomic orbitals. When carbon bonds to three different atoms it creates three sp^2 MOs and one p_z MO. The sp^2 MOs create σ bonds, lower in energy than the π bond created by overlap of adjacent p_z MOs. This means that, in terms of energy, the π bond is the 'highest occupied molecular orbital' (HOMO), and the anti-bonding π^* orbital is the 'lowest unoccupied molecular orbital' (LUMO). These two orbital states are shown to the right of figure 1.1.

Figure 1.1 shows the basic π bond, but figure 1.2 shows how this extends to adjacent C=C double bonds. Essentially, molecular orbital theory states that the total number of different π and π^* MOs is equal to the number of carbon atoms (n) available, and each MO has an additional node, starting from 0 in the lowest energy π MO, to $n-1$ at the highest energy π^* MO. This means that the neutral HOMO always has $n/2-1$ nodes, and the LUMO has $n/2$. A neutral molecule at equilibrium has all the bonding π MOs filled, and whilst there is a slight difference in energy between each MO, all the π orbitals have approximately the same energy compared to the energy gap with the π^* MOs. It was shown experimentally

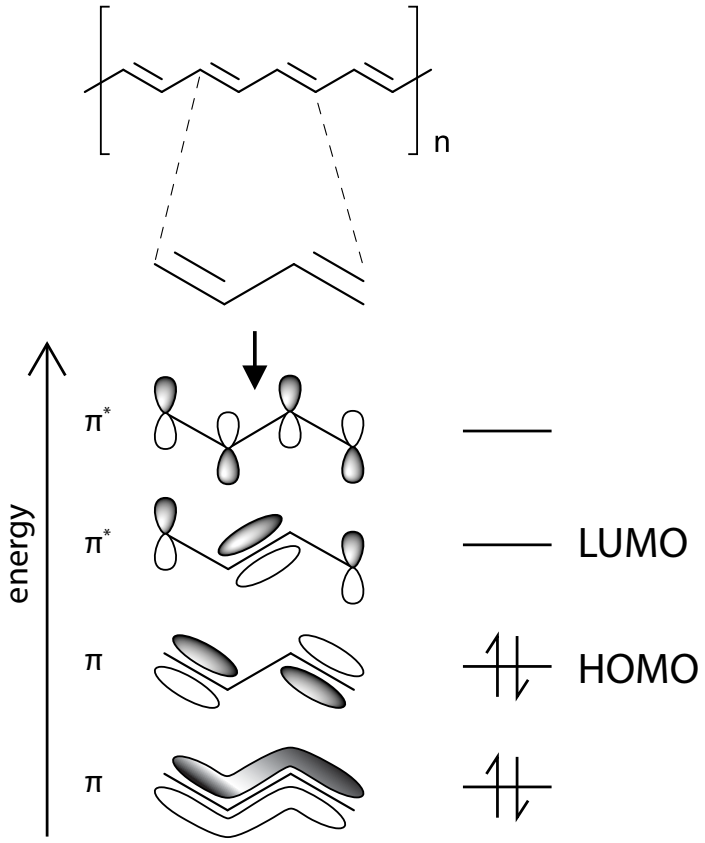

Figure 1.2 The conjugated polyacetylene is at the top. The conjugated π molecular orbital (MO) model is demonstrated for the case of but-1-ene shown below. The number of different π MOs in a conjugated system is always equal to the number of carbons. In a neutral molecule, half of the MOs are filled, all bonding π MOs (non-starred). The most important energy levels are the highest occupied MO (HOMO), and the lowest unoccupied MO (LUMO). In a doped system, such as the p-doped polyacetylene in reference [16], electrons are either removed from the HOMO to create positive *holes* or added to the LUMO to create *electrons*.

by Pope [17] that the extension of a conjugated π system quickly decreases the energy gap between the HOMO and LUMO energy levels creating small energy gaps, often within the visible frequency. The example of the first five polyacenes is shown in figure 1.3, and the energy gaps clearly converge as the conjugated system increases. [18] Conceptually, this can be visualised by an increased delocalization of the electrons from the atomic nuclei, meaning that the bonding is in effect stronger with greater conjugation.

Figure 1.3 shows a number of features of the polyacenes. Firstly, for each compound values are given for the gaseous phase (left, black bar) and the crystalline phase (right, band). In effect, the gaseous phase represents individual molecules, and the crystalline phase includes inter-molecular interactions, characterised by the polarization energy P. The quantities shown are given for the gas phase (g subscript) and the crystalline phase (c subscript). I is the ionization energy (energy required to remove an electron from the HOMO) and A is the electron affinity (binding energy released when an electron is added to the

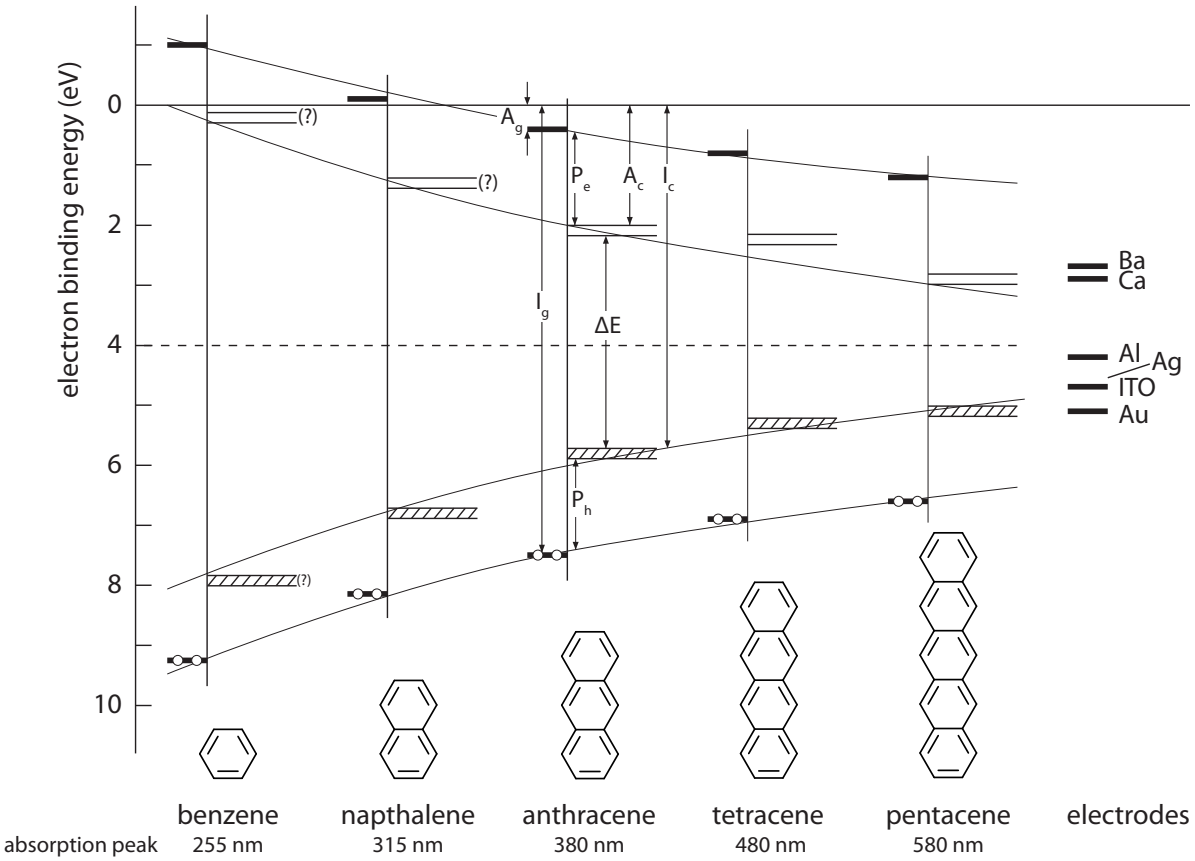

Figure 1.3 A graph showing a family of conjugated aromatic hydrocarbon molecules based on benzene, and their corresponding HOMO ionization levels and LUMO binding energies for gaseous phases (left) and crystals (right). In addition, the Fermi-levels of various relevant electrode materials are shown. A dashed line at around 4 eV is drawn in to illustrate the approximate Fermi level of all the molecules as the value upon which the HOMO and LUMO energies are converging. The values for the ionization and binding energies are from experimental data except for those marked with '(?)', and the diagram is based on a figure in reference [18], which also contains the experimental data.

LUMO). The polarization energies for electrons, P_e, and holes, P_h, are nearly symmetrical and constant at around 1.6 eV, and the consequence of the polarization energy is that ionization of a molecule in a crystal lattice requires less energy (ΔE) than in the gas phase. It also means that if an electron is excited to the π^* energy level and then radiatively recombines with the *hole* in the π ground state, the photon energy will be lower for a crystal than the gas. With increased conjugation, i.e. the number of rings in figure 1.3, ΔE decreases, meaning that the photon energy emitted from an electron-hole recombination will also decrease, bringing the photon from the UV into the visible.

In 1941, a letter by Szent-Györgyi stimulated interest in organic semiconductors by suggesting that intermolecular transfer of π orbital electrons may play a significant part in the fundamental physical processes of living organisms [19]. By bringing the HOMO and LUMO closer together, conjugated organic systems are reducing the 'band gap', analogous to the

band gap of inorganic semiconductors. This provided the extension of the concurrent interest in novel semiconducting crystals to organic compounds with research into polyacenes, azo-aromatics, pthalocyanines and various other compounds in the 1950s [2]. Experimental limitations, namely the difficulty of obtaining pure single crystals and the extraordinarily low conductivity of most organic semiconductors, as well as the enormous commercial success of inorganic semiconductors meant that organic semiconductor research lagged behind. Even the evidence of significant photocurrent [1] and electroluminescence [6] from organic crystals failed to significantly stimulate further research into organic semiconductors. Whilst the photovoltaic effect, particularly with regard to chlorophyll and photosynthesis [20], always remained of interest, the gulf in understanding between the synthetic organic semiconductors and natural compounds such as chlorophyll kept organic electronics a minor research topic. The three major recent breakthroughs in this field which have helped to make it the huge scientific topic it is today were the first observations of conductivity in doped polyacetylenes [16], the first thin-film OLED [7], and the first PLED [8]. In addition to OLEDs, organic light-emitting electrochemical cells (LECs) are an important class of ionic light-emitting devices [21].

1.1.2 Organic light-emitting diodes (OLEDs)

Figure 1.4 shows how a basic single-layer OLED works for the case of poly(2-methoxy-5-(2'-ethylhexyloxy)-1,4-phenylene vinylene) (MEH-PPV) sandwiched between ITO and Al. This device architecture has been used as an example because it is used in this thesis, and was one of the first PLED architectures [8, 9]. In figure 1.4a the vacuum level is constant because no electric field has been applied to the device. In figure 1.4b an electric bias is applied across the MEH-PPV layer, creating tilted HOMO and LUMO levels. Some charge can already overcome the Schottky barrier by thermionic emission at low electric field strengths, but the dominant process for charge injection is electron tunnelling, as outlined in equation 1.1. Figure 1.4c is similar to 1.4b, but with a larger bias applied. This changes the geometry of the barriers at both electrodes, aiding injection by changing the shape of the triangular geometry, outlined in equation 1.2.

$$J \propto E^2 \cdot \exp\left(\frac{-\kappa}{F}\right) \tag{1.1}$$

The basis for modelling charge injection across a potential barrier is often described by Fowler-Nordheim electron tunnelling theory, shown in equation 1.1 [22, 23]. J is the current density, E is the electric field strength, and κ represents a term dependent on the geometry of the barrier. Figure 1.4d shows the triangular geometry standardly used to model charge injection into organic semiconductors. In equation 1.2, κ is replaced by the term for a triangular geometry.

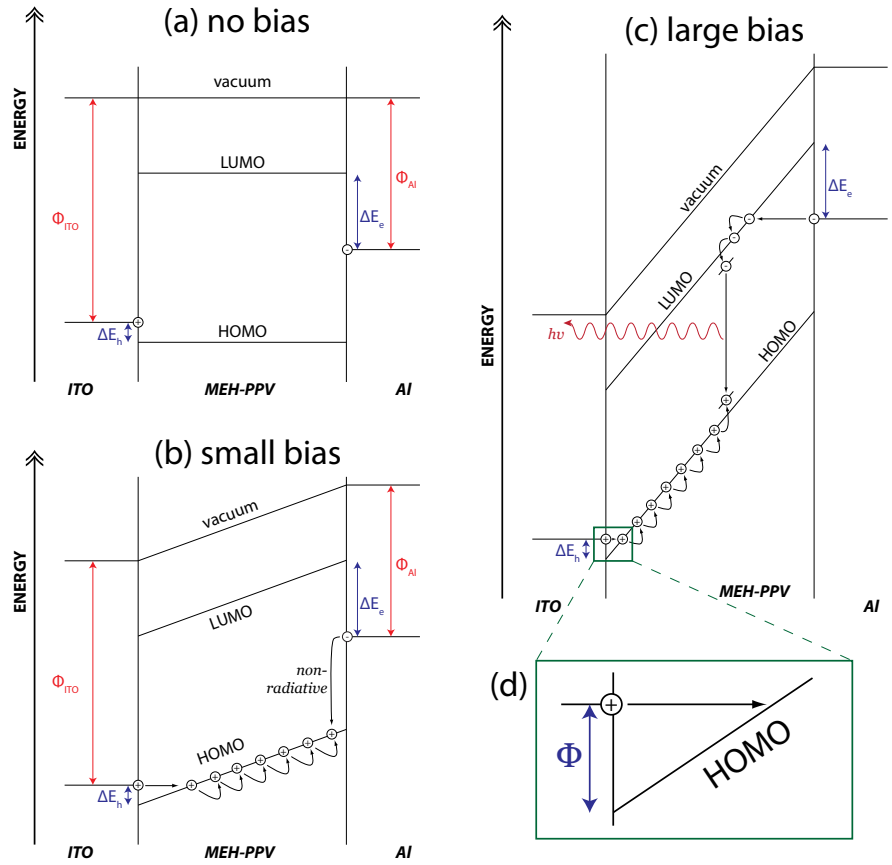

Figure 1.4 This diagram shows how the basic energy structure of a PLED is represented (a) under no bias, (b) when a small bias is applied, and (c) when a large bias is applied. (d) shows the triangular geometry of a simple Schottky barrier, and how charges tunnel across it according to Fowler-Nordheim theory [22], shown in equations 1.1 & 1.2.

$$J \propto E^2 \cdot \exp\left(-\frac{1}{E}\frac{8\pi\sqrt{2m^*}\Phi^{3/2}}{3qh}\right) \tag{1.2}$$

Whilst this is a useful simple model for charge injection, there are other mechanisms whereby charge injection may take place into organic semiconductors, and other effects which may dominate such as morphology [4]. In addition to charge injection, charge transport is a process which has been of great interest since the very beginning of organic electronic research [19]. Many models have been developed to explain electron transport in organic materials [4, 24]. Whilst the most basic of these started with band models based on electron-electron interactions similar to those of inorganic semiconductors, it has always been clear that organic semiconductor charge transport is more complicated [18]. In ordered organic crystals, electron-phonon interactions can be modelled to some extent, and detailed polaron models based on band-theory have been developed. If static disorder is

considered, then electronic bands are localised, meaning that intermolecular hopping, such as the Miller-Abrahams and Marcus models, need to be taken into account. In addition, a commonly used model is the field-limited Poole-Frenkel model of charge transport in dielectric materials. However this model does not take into account charge-carrier density which is an important factor in organic semiconductors [4, 24].

1.1.2.1 OLED materials

The two main structural categories into which OLED materials are split are small molecules (SMOLEDs) and polymers (PLEDs). A third class of dye-doped devices using phosphorescent dyes, known as PhOLEDs (phosphorescent OLEDs), is based on exciton transfer to small molecule emitters from a matrix which can be either polymeric or small molecule [25].

Polymers The first PLEDs were conjugated polymers, poly(phenylvinylene) (PPV), and due to the improved charge transport rates along the conjugated polymeric backbone compared to inter-molecular hopping rates, most subsequent PLED work has focused on conjugated polymers. [10] Polymers based on PPV remain of great interest with a structure known as super yellow commonly used as a model polymer [26]. Nevertheless, another class of polymers called polyfluorenes (PFs) have taken over as the dominant class of conjugated polymer in organic electronics [27–30].

One non-conjugated polymer widely used is poly(N-vinylcarbazole) (PVK), widely used as both a hole-injecting material and as a host for dyes [31,32]. Overall, polymers remain of great interest due to the low cost of manufacture and the potential of solution-processable deposition techniques, but one of the main barriers to commercialization is that they are generally far less pure than small molecules.

Small molecules As outlined above, the initial modern OLED breakthrough came with Alq_3, a SMOLED material [7]. Although an organo-metallic complex, it is considered an organic compound. SMOLEDs have been researched in great detail, and improvements in efficiency and stability have surpassed PLEDs [33, 34]. In this thesis, Alq_3 is the only small molecule investigated as whole layers, although small organo-metallic iridium complexes have also been used as dopants in polymeric matrix layers.

Full-scale commercial displays have been made using patterned thermal evaporation through a mask of small molecules, otherwise known as fine-metal masking (FMM) [35, 36]. However, the main limitation has not been surpassed: the cost of the material evaporation, where over 80 % of the material is wasted. PLEDs have more potential in this regard, being solution processable, but the technology is not as well-developed as evaporation.

Phosphorescent dyes Doping of a host material with an electroluminescent emitter was an early development in the history of OLEDs [37], and the idea was based on the well

known principles of Förster and Dexter energy transfer [38]. Förster energy transfer uses induced dipole coupling to transfer the energy via near-field coloumbic interactions. Although believed to be non-radiative, it has been shown to be analogous to radiative energy transfer by quantum electrodynamic calculations [39,40]. This means that effective energy transfer is only realised when the absorption of the acceptor overlaps with the emission of the donor. This mode of transfer is constrained by the spin-state of the acceptor which, when in the ground state, is always singlet. This can be overcome by a combination of energy transfer and actual physical exchange of the electrons via Dexter transfer at very close ranges [38]. As well as a strong inverse dependence on distance, good spectral overlap of the excitons is required due to the actual exchange of electrons [41]. These principles have been well demonstrated in practice [42].

Fluorescent emitters radiatively recombine only from the singlet state, with non-radiative triplet decomposition predominant due to the inability of a triplet exciton to recombine, which gives long lifetimes, which inevitably lead to a non-radiative energy dissipation process. Nevertheless, there are some materials which exhibit significant phosphorescent emission (radiative triplet recombination) by increased spin-orbit coupling [41]. These materials are normally organometallic complexes of second and third row transition metals such as platinum and iridium [25,41–43].

By combining a phosphorescent emitter with a host matrix with good spectral overlap, the limitations of standard electrodynamics are overcome and quantum efficiencies up to 100 % become possible in theory. This principle is also know as sensitizing - the absorption spectrum of the emitter is barely visible, but energy transfer is so efficient that emission from the host is barely visible, both in electroluminescence and photoluminescence. All of the record OLED efficiencies in section 1.1.3 are based on this combination of materials.

1.1.2.2 OLED fabrication methods

There are a huge range of methods which have been employed to deposit the thin-films required to make functioning OLEDs. These can be roughly divided into evaporative processes (‘dry’), and solvent-based processes (‘wet’).

‘Dry’ vacuum thermal evaporation (or sublimation of materials) is the most commercially advanced technology for both display applications and solid-state lighting [44], and was the technique used in the first modern OLED [7], and the first active matrix TFT OLED displays [45]. A basic scheme of this process is shown in figure 1.5a. However, whilst thermal evaporation may be suitable for smaller displays, it lacks resolution for larger-sized ‘mother’ glass substrates [46]. As a consequence, many laser-based patterning techniques have been developed which involve sublimation/evaporation of the materials, controlled by a patterned laser beam. These include laser induced local transfer (LILT) [47], radiation-induced sublimation transfer (RIST) from Kodak [46], and laser-induced pattern-wise sublimation (LIPS) from Sony [48].

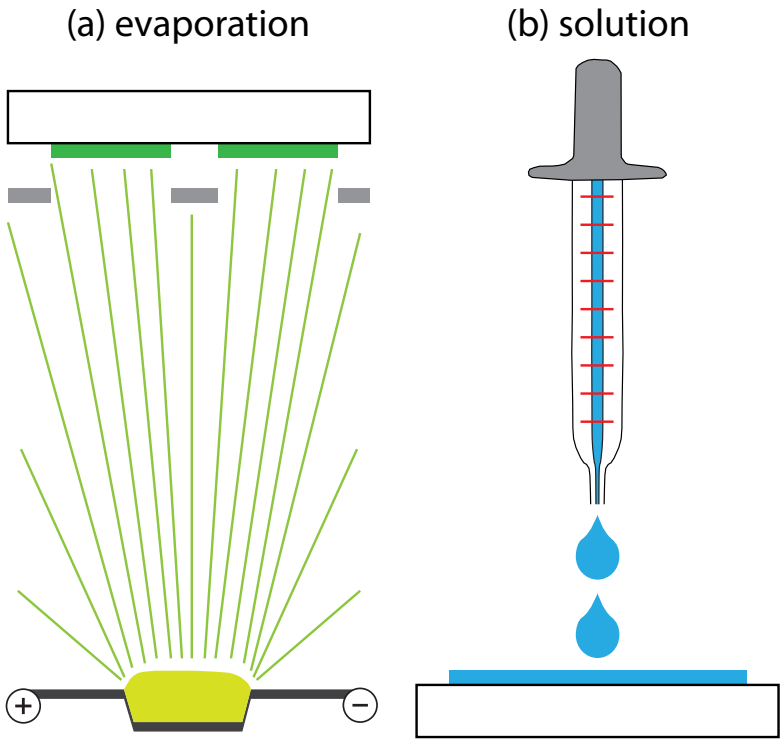

Figure 1.5 The principal, and original, OLED deposition techniques. (a) is thermal evaporation through a shadow mask, and (b) is spin-coating from solution.

'Wet' methods are all generally based on the principle of drop-casting, where a solvent is evaporated to create a controlled film thickness. The original technique for PLEDs was spin-coating [8,9], which is the main technique, along with thermal evaporation, used throughout this thesis for both conventional OLED devices[1] and donor and receiver substrate film deposition. A basic scheme of spin-coating is shown in figure 1.5b. Other solution based techniques include spray deposition [49] and doctor-blading [13], but most developments are printing related. Printing techniques such as ink-jet [50], screen-printing [51], and micro-contact printing [52] have all shown promise. For solution processable materials, there is always the consideration of unwanted interfacial mixing and/or erosion. This has led to large advances in water/alcohol-soluble polymers [53] and cross-linkable materials [54].

In addition to these mechanisms, there are numerous other innovative deposition and/or patterning techniques for OLEDs. Lithography, as the traditional patterning process for inorganic semiconductors, is worth mentioning, and large advances in the application of photo-lithographic techniques to organic thin films have recently been achieved, but require specific chemical modification of standard OLED materials [55]. There is a particularly large range of polymer deposition and patterning techniques, which are well outlined in a recent review by Xu et al. [56]. The final technique to mention is the one closest to

[1] *Conventional device* refers to 'conventional' fabrication methods for OLEDs i.e. standard ITO anode-up architecture with standard thin film deposition methods before patterned thermal evaporation of the cathode

LIFT itself, a well-developed technique through a corporate partnership between 3M in the USA and Samsung in South Korea called laser-induced thermal imaging (LITI) [11].

1.1.3 State of the art

The research and application of organic semiconductors are developing in many different directions, but some key properties of the materials used remain the same. To achieve good devices, purity and homogeneity are essential, and commercially available materials are often a long way behind the laboratory in this regard. For this doctoral work, all of the materials except for the triazene polymer were commercially acquired and so generally of poorer quality when compared to the state of the art. Nevertheless, it is worth evaluating what level has been reached in published work.

Starting with transistors and photovoltaics, there are many different figures of merit to consider, and numerous different subclasses within them. To summarise, uni-polar organic semiconductors have reached charge carrier mobilities of greater than 1 $cm^2V^{-1}s^{-1}$ for hole carriers, and up to 1 $cm^2V^{-1}s^{-1}$ for electron carriers. The best ambipolar semiconductors show similar peak mobilities, although rarely together.

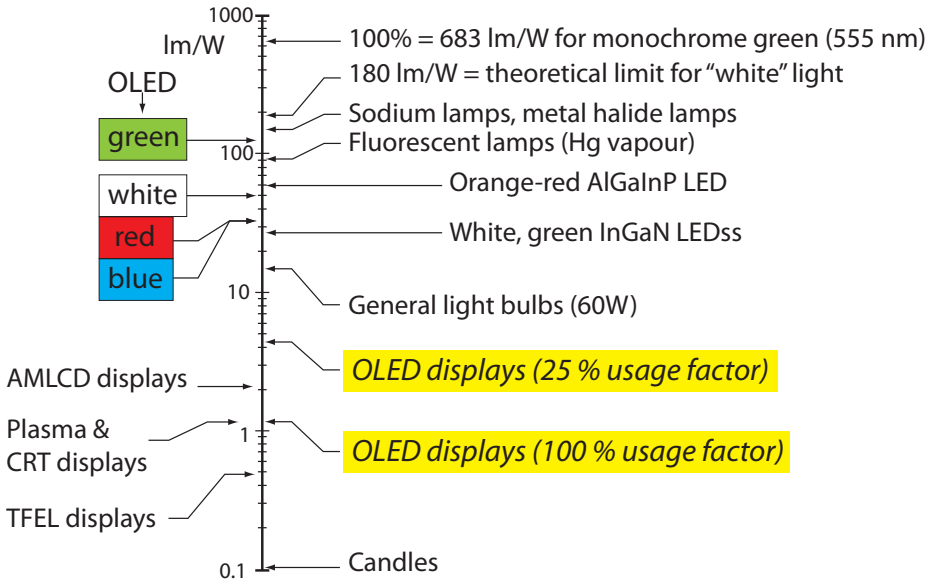

Figure 1.6 An overview of the state of the art of OLEDs relative to other lighting sources, based on a figure in reference [57]. The power efficiencies of various devices and displays are shown on a logarithmic scale.

OLEDs also have numerous subclasses and different figures of merit. The top PLEDs show operating voltages below 5 V, peak brightnesses of over 10^5 cd/m^2, and efficiencies over 30 cd/A. Lifetimes are in the region of thousands of hours with minimal performance decrease. However, these devices are currently not necessarily easily reproducible. Small molecule evaporable OLEDs show similar or better performance characteristics, but with

higher reliability due to better control over thermal evaporation compared to solution-based deposition methods.

Figure 1.6 shows the efficiency of various OLEDs compared to other lighting and display sources. In figure 1.6 the values for green and white on the right are both theoretical maxima at 100 % efficiency, and the values below are practical values for lamps, inorganic LEDs, and general halogen light bulbs. On the left are the maximum OLED results for red, green, blue, and white devices, which are all a little higher nowadays compared to 2003. The bottom efficiencies in figure 1.6 are comparisons of various displays, and OLEDs are shown with 25 % usage factor assuming only 25 % of OLEDs are lit at any time.

Current records for OLED efficiencies are all for evaporated PhOLEDs: green efficiency of 110 lm/W, or 50 % external quantum efficiency (EQE) [58], red efficiency of 32 lm/W, or 24 % EQE [59], and blue efficiencies of 35 lm/W, or 18 % EQE [34]. White devices report efficiencies of 50 lm/W reaching maximum of 90 lm/W, or 34 % EQE [33]. Phosphorescent dyes can also be incorporated into polymers to obtain similar efficiencies [25, 60]. PLEDs without dye doping are also quite efficient, with single-layer devices based on a green polyfluorene derivative, F8BT, reaching over 10 lm/W, or 7 % EQE [30].

Commercial OLEDs

OLEDs are now on the market in the two main sectors of interest: electronic displays [44], and large-area lighting application [61]. Lighting applications are not the main focus of this research, but ironically one of the leading lighting markets for OLEDs is backplane illumination in LCD flat screens (the so-called OLED TVs, as opposed to AMOLED), as well as markets where lightweight devices are required, such as in aircraft and space shuttles [61, 62]. On the electronic display side, whilst the first passive matrix (PMOLED) electronic displays were sold in the late 1990s by Pioneer for car radios, and other small display usage has grown, the large market for high-resolution computer and smartphone displays is just beginning to grow. For longer illumination, faster refresh times, and better control over the electroluminescence, more complicated 'active-matrix' transistor backplanes are required. These active-matrix OLED (AMOLED) displays allow for the illumination of one line at a time, rather than individual pixels as for passive matrix displays.

Samsung Mobile Display (SMD) leads the way in overall OLED display sales still (both PMOLED and AMOLED), as the pie-chart in figure 1.7a shows. Most of the other companies on the chart fabricate more basic displays such as monochrome radio displays, and until October 2011 there were only two companies with any presence in the AMOLED market, both Korean: Samsung and LG (and LG's presence is very minor at present). AUO, a multi-national display company based in Taiwan, has announced ambitions to create an AMOLED display fabrication unit, and has recently demonstrated functioning 32" display prototypes. However, Samsung have recently presented a prototype 70" ultra high definition (UHD) 3D display, and lead the market more convincingly than even the pie-chart, figure 1.7, sug-

gests: their share of all OLED display revenues was as high as 88.3 % in the first quarter of 2011 [44].

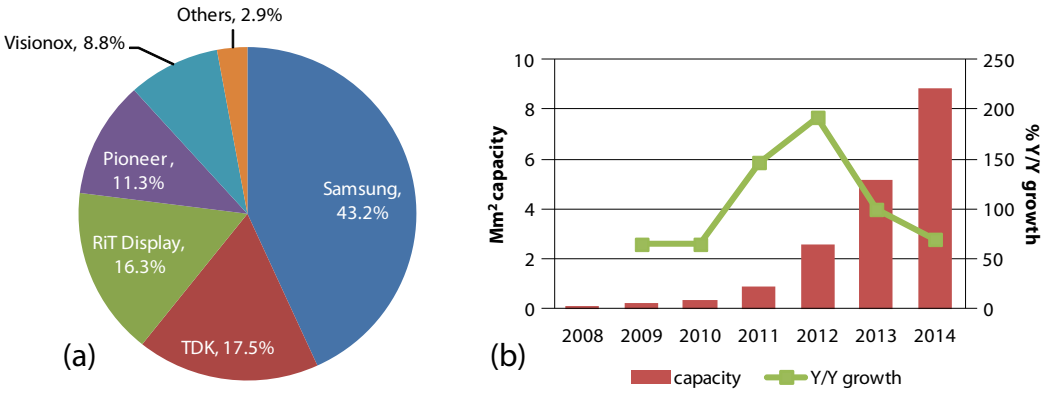

Figure 1.7 The market share of OLED displays in the second quarter of 2010 is shown in (a), taken from a CDT presentation, and the growth in Samsung's manufacturing capacity is shown in (b), based on data on *electronics.ca*. Capacity is given in Mm^2 of commercial AMOLED display area that can be made per year, and the values for 2012 onwards are forecasts by Samsung themselves.

Samsung is the only company to have produced substantial numbers of commercially-available AMOLED displays in the past year, and their development shows no signs of abating with their sights set on the potential for flexible, foldable AMOLED displays [63]. In fact, their overall market share in AMOLED display shipments in 2010 was 99.3 % (45.6 % of all OLED displays), and increased those high figures even higher in the first quarter of 2011 to 99.9 % of AMOLED displays and 51.5 % of all OLED displays [44]. However, Samsung's market dominance is not necessarily healthy for the OLED market, not because they are creating a monopoly in the field of AMOLED displays, but because they are so *vertically integrated*, i.e. have such a large share in the products that use electronic displays too, giving them significant control over the market. However, this has created a catch-22 situation where other potential suppliers are reluctant to invest in large-scale AMOLED displays fabrication due to the lack of competitive buyers, and where the companies that are potential purchasers of AMOLED displays cannot buy them because of the lack of competitive suppliers.

1.2 Laser-induced forward transfer

The use of laser-induced forward transfer (LIFT) is the fulcrum of this thesis. LIFT utilizes a laser beam to provide kinetic energy to a film by photo-induced ablation, in order to transfer the film from a donor substrate to a receiver substrate as shown in figure 1.8. Before looking at LIFT in detail, a bit of laser background is required, particularly the use

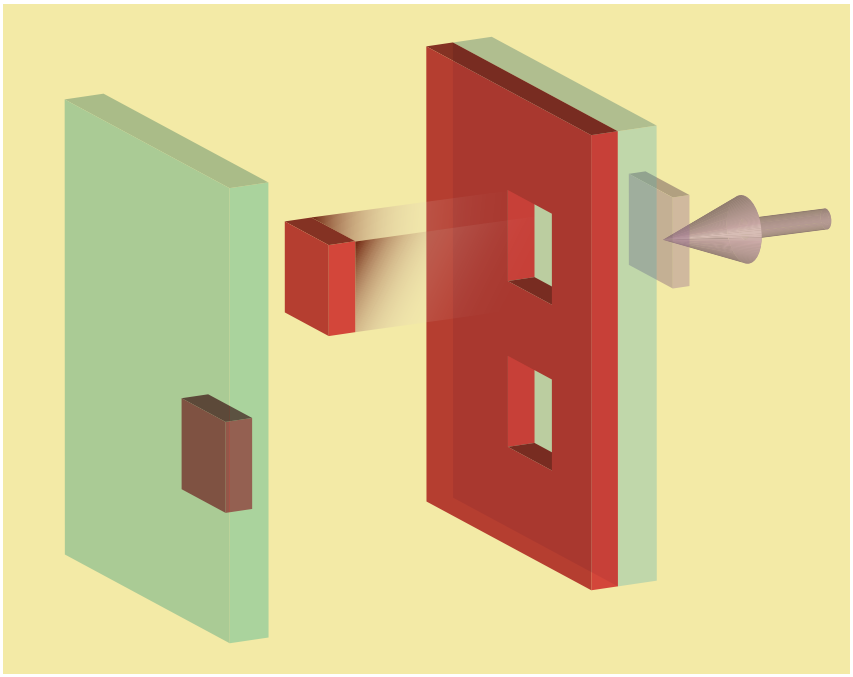

Figure 1.8 Basic 3D scheme of LIFT with a single-layer transfer.

of lasers for laser ablation. Laser ablation, the removal of material using a laser beam, is the means by which laser light is converted into useful mechanical work, transferring a pixel from a donor substrate to a receiver.

1.2.1 Laser ablation

The invention of the ruby laser in 1960 [64] sparked a flurry of potential applications, which have developed to the extent that the laser (*light amplification by stimulated emission of radiation*) is today ubiquitous. Lasers exhibit a large range of attractive properties, such as high spatial and temporal coherence, low wavelength bandwidth, and collimated beams. All of these properties depend on the laser used, but they enable a large range of applications, such as spectrometry, interferometry, and communications. However, lasers have also always demonstrated the potential for physical material removal and modification – such as cutting, welding, and cleaning – due to the high power outputs [65].

Present applications for laser ablation can be broadly divided into micro- and nano-structuring, material deposition, and micro-analysis. These three categories cover a huge range of sub-categories, such as micro-optics [66], direct-write ablation lithography [67], fuel-cell micropatterning [68], PLD (pulsed laser deposition) [69, 70], and laser-ablation ICP-MS [71]. There are of course other potential applications, such as laser propulsion, most of which are touched upon in a recent collection of work related to laser ablation [72]. LIFT falls in between the categories of microstructuring and material deposition, being an additive direct-write mechanism [73], and is explored in more detail in the following

sections.

Laser ablation is usually measured by a simple analysis of the depth removed per pulse [67]. This depth is used to calculate an effective absorption coefficient α_{eff}, according to Lambert-Beer's law of absorption, which is nearly always different from the linear absorption coefficient α_{lin} due to the nature of the way it is calculated. This means that a highly sensitive material, which ablates at relatively low thermal energies, will effectively absorb less (the light penetrates deeper), and for a material which does not ablate at all, α_{eff} will be higher than α_{lin}. The ablation depth d, is a function of fluence F and α_{eff} as shown in equation 1.3. F_{th} is the threshold fluence.

$$d = \frac{1}{\alpha_{\text{eff}}} \ln \frac{F}{F_{th}} \tag{1.3}$$

Using this equation, a phenomological characterisation of materials can be made, but it is a gross oversimplification, as the following section on laser ablation modelling will make clear.

Modelling of laser ablation

Modelling of laser ablation is vital to LIFT. While models for metallic and other inorganic material laser ablation are fairly accurate due to the thermal dominance of the excitation and decomposition process [74], there are two principal effects to consider in polymer laser ablation, namely photothermal and photochemical processes, as well as possible photophysical mechanisms [75].

Ab initio Monte Carlo molecular dynamical simulations have been done on PMMA (poly[methyl methacrylate]) in detail for ablation with various UV lasers [76]. These studies have shown how a rapid breakdown of the polymer matrix underpins all ablation, whether the photoexcitation is thermal, mechanical, or chemical. They point to a complex interplay between many different factors in polymer ablation, with no single mechanism completely dominant in any conditions. A more experimental approach to the laser ablation of various polymers, including triazene polymers, has demonstrated a fluence dependence of the ablation characteristics which also depend on the polymer structure [67]. Polymimide was used as a reference polymer, and the triazene-containing polymers were seen to have a greater photochemical effect than other polymers at lower fluences, as might be expected from the high photosensitivity of the triazene chromophore. A recent thermal modelling of triazene polymer ablation showed good fit to the experimental data for the threshold fluence as a function of TP film thickness [77]. The model stayed consistent when fitted to experimental data for three different substrates with different thermal diffusivities. This model shows the significance of the thermal build-up in the triazene for aiding the actual ablation process, even if the initial reaction may be photochemical.

Lambert-Beer's law of absorption, shown in equation 1.3 has been widely used by experimentalists [67, 78–80], but in fact explains very little about the physical mechanisms behind the ablation. It has been generally established that there are a number of fluence regimes of ablation with different α_{eff} [78]. For a start, absorption coefficients are often more accurately referred to as 'attenuation coefficients', as the whole process, even for α_{lin} is not necessarily absorption. Reflection is also significant. Nevertheless, with polymers absorption is often the main mechanism of attenuation, but with ablation the absorption process itself needs consideration. Firstly, there is the onset of ablation which is generally established to be sub-ns [75], meaning that during a ns laser pulse, ablation products will already be generated creating a dynamic solid-gas interface. In addition, there are the differences between photochemical and photothermal models of absorption and ablation to consider. These are additionally complicated by the range of electronic states in organic compounds that can be excited. A neat extension to the basic Lambert-Beer law was to consider three different absorption states for the chromophore: the linear one, an excited state, and a plume state (i.e. ablation products) [81]. This model showed that at higher fluences, the plume absorption became more significant, effectively taking into account the different solid-gas interface dynamics at different fluences.

In addition to studying the mechanism, some energy balances have been made based on time-resolved imaging of the shock wave created in air [82–84]. These measurements calculate the total energy released from the velocity of the shock wave. The results give a quantitative analysis to the qualitative results that can be gained by visualising the ablation plume and shock wave, and can be used to investigate the efficiency of energy transfer from the laser beam to the ablation products.

1.2.2 LIFT background

The use of lasers to directly print a structure was realised as early as 1969 [85, 86]. However, this early investigation was not widely followed up, and it was not until 1986 that the technique was applied to metals [87]. The research caught on, and a group at the University of Illinois pioneered the way, adding an intermediate layer to protect the transfer material. This intermediate layer they called a dynamic release layer (DRL) [88]. They referred to the technique as laser-ablation transfer (LAT) which became a very popular name for the technique in the 1990s. The original DRL was a thin aluminium film, and the mechanism for ablation was purely thermal which led to the layer also been known as a light to heat conversion (LTHC) layer [11]. Concurrently, research was developing in Japan on a new transfer method they termed laser molecular implantation (LMI) [89]. This process, as the name implies, involved specific molecular transfer, specifically aromatics. In a couple of years, LMI was used to successfully transfer fluorescent molecules using a new class of polymer called triazene polymer. The history of triazene polymer research is outlined in section 1.2.3. During this time, LAT had been developed commercially using a thermally ablated DRL (or LTHC) in contact with the receiver substrate, under the name of laser-

induced thermal imaging (LITI) [11]. Another similar transfer technique being pioneered at this time was matrix-assisted pulsed laser evaporation direct-write (MAPLE-DW) [90].

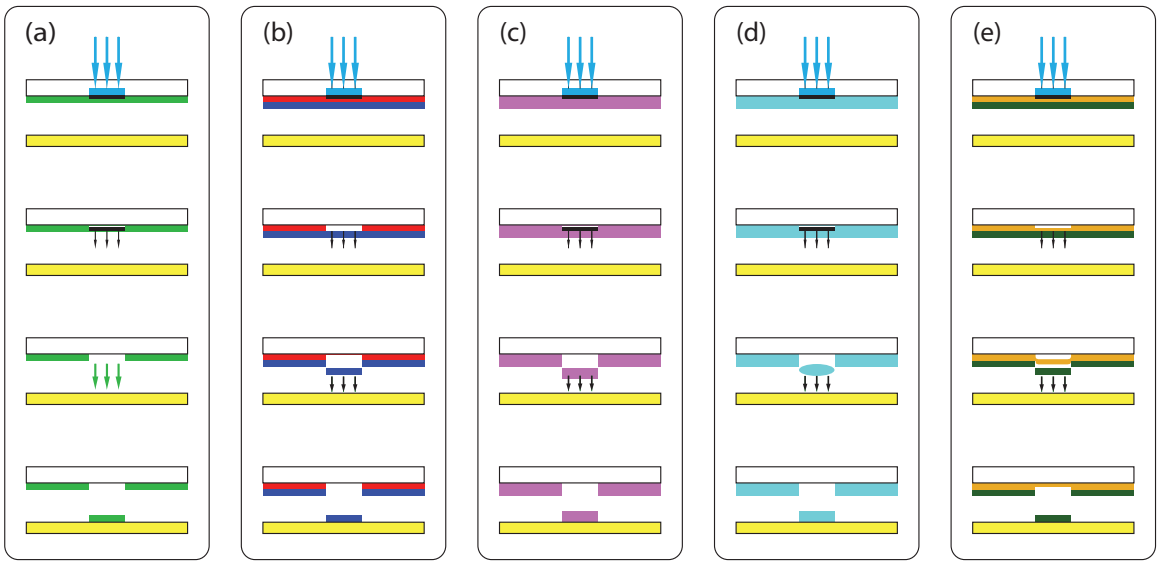

Figure 1.9 A schematic illustration of different categories of laser direct-write addition mechanisms, as outlined in Arnold's review [73]. The laser beam pulse is shown in blue, the donor substrate is transparent (white), and the receiver is yellow. The different schemes show: (a) traditional LIFT without a DRL, where the whole film is ablated and re-deposited; (b) LIFT with an intermediate DRL, as used in this thesis; (c) matrix-assisted pulsed laser evaporation direct-write (MAPLE-DW), where a sacrificial matrix is ablated; (d) LIFT of materials with special rheological properties which allow ablation of a thin layer to transfer the rest of the material; (e) a fifth class of LIFT in which the DRL is used to catapult the transfer material without ablating fully or even at all.

A more recent summary of laser-ablation was made in an MRS bulletin that summarised laser direct-write techniques, and categorised them into four distinct categories outlined in figure 1.9 (a-d) [73]. The first two LIFT categories in figure 1.9 (a & b) have been mentioned in the previous paragraph. The third category has been investigated further with regard to functional polymers for chemoresistor sensor applications and bio-molecules such as proteins and even living cells [91]. The fourth of these categories is a specific type of transfer for which not many functional materials have been investigated. In addition to these four categories, a fifth category has emerged, shown as figure 1.9e, which has been developed for use with both a metal DRL [92], and a polymer DRL [93]. The metal DRL technique was termed blister-based LIFT (BB-LIFT), and the polymer DRL technique termed blister-actuated LIFT (BA-LIFT), but both names mean the same thing. The technique has been applied successfully to solid powders and liquid films, but the transfer of intact solid films has not yet been demonstrated using this technique. A finite element analysis (FEA) model of BA-LIFT has been developed [94].

LIFT modelling

Modelling of the LIFT process is not widespread, but some work has been done related to it (see section 1.2.1 on laser ablation modelling). Recently, our group made an energy balance investigation into backside ablation observed by shadowgraphy [84]. This energy balance used a shock wave velocity energy model, designed for frontside laser ablation, for backside ablation as well [82,83]. As might be expected, the energy is nearly identical until low fluences, when most of the energy difference is probably attenuated by the overlying metal layer into phonons, or lost as thermal energy into the substrate [77].

A more process-driven model can be found in a different field from LIFT – the field of high-speed metal flyers driven by laser pulses. This is a different field, not because the process is different, but because the engineering application is for the generation of high-speed projectiles, rather than the printing-based application of LIFT. Nevertheless, the model of Lawrence and Trott for flyer velocity comprises a number of physically meaningful parameters [95]. The complex process of the ablation is simplified using the Gurney model for explosives where the source is simply considered as a reservoir of chemical potential energy [96, 97]. For laser ablation, that reservoir increases with fluence and ablation depth. Whilst this model is a very suitable model for single-layer metal flyers, it requires modification for use with a polymeric DRL LIFT process as used in this thesis, and an attempt is made in section 3.2 to do this. A simpler model of flyer velocity for LIFT has been developed, but this assumes that the kinetic energy is always proportional to the input laser energy [98], which is certainly not the case at low fluences, and also not at high fluences when the flyer fragments.

LIFT summary

The LIFT technique which is presented in this thesis is clearly the second category, figure 1.9b. To summarise, LIFT may be viewed as a natural modern development of the traditional press-printing with a laser acting as the press. The laser irradiates the sample from behind as if pushing the material towards the receiving substrate. Only the material that is irradiated will be transferred, which means that the laser defines the lateral shape of the deposition. Precisely defined deposition can be obtained by controlling the path of the laser beam using a beam steerer. The important factor here is the transfer material; with the traditional printing press the transfer material was an ink which was robust and transferred quite simply. In today's age, with hand-held high-resolution display devices, more factors need to be considered because we expect to transfer more things than a single ink, and in a more reliable way. So in order to be transferred efficiently it is desirable that the transfer material can absorb the laser wavelength, and that it can also transfer this photon energy into a mechanical energy fairly efficiently. For more detailed and precise printing - at finer resolutions - this may be hard to achieve. The addition of an intermediate, dynamic release layer (DRL) to carry out the energy transfer is beneficial in terms of both the quality of the

ablation, and also the reduction in degradation to the transfer material by light absorption, even managing to maintain the film morphology through the transfer. This is the role which triazene polymer plays as a DRL in laser-induced forward transfer.

1.2.3 Triazene polymer ablation

Background

Triazene polymers were developed in the early 1990s, specifically for laser ablation with a 308 nm XeCl excimer laser [99]. Triazene polymers contain aryl-triazene chromophores where a conjugated π system spreads over the three nitrogens and the benzene ring [100]. A fundamental aspect of the LIFT method is the clean laser-ablation of the triazene polymer. In the field of polymer ablation, triazene-based chemicals were originally used as dopants for the ablation of other polymers [101, 102] using 308 nm wavelength light from the common XeCl excimer laser, see the TP absorption spectrum in figure 1.10. Fairly soon, the group at Bayreuth incorporated the triazene chromophore into polymers themselves, firstly as a PMMA co-polymer with triazene side-chains [99], and then with the triazene chromophore along the polymer backbone [100] to improve the efficiency and quality of the polymer-ablation process. These novel polymers proved to be much more precise and clean in their ablation when compared to the doped PMMA [103]. In addition to the high photosensitivity, it was seen that triazene polymers also exhibit remarkably high thermostability, up to 230 °C [104].

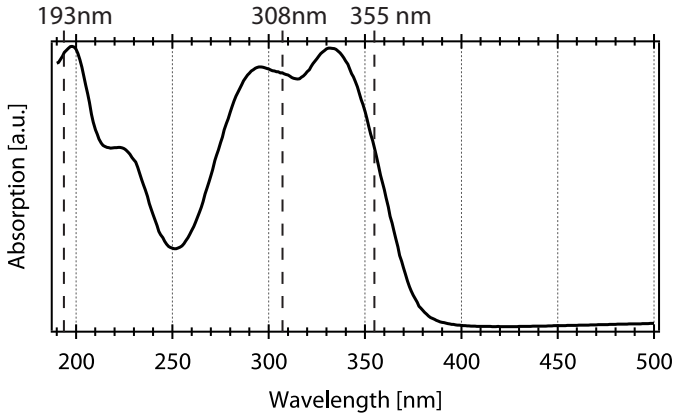

Figure 1.10 A UV-vis absorption spectrum of a typical triazene polymer thin film, spin-coated from chlorobenzene:cyclohexanone (1:1) solution. The dashed lines show the laser wavelengths used (308 nm and 355 nm), as well as 193 nm which has been used in previous studies [78, 105].

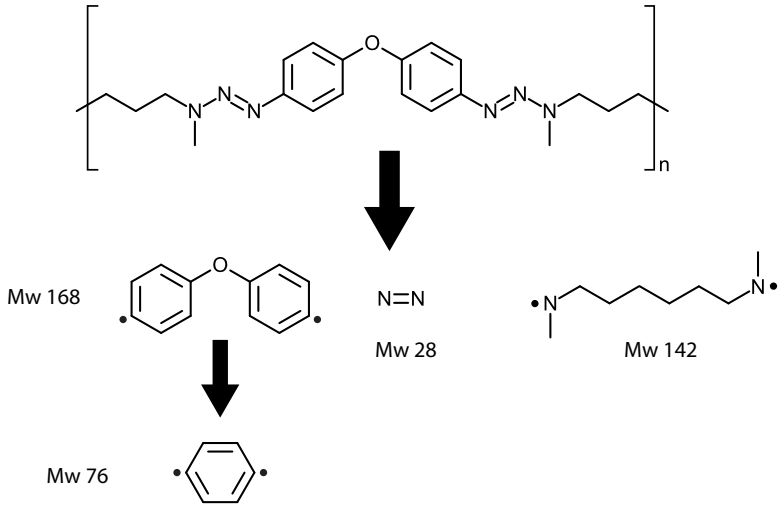

Figure 1.11 The primary radical ablation products from triazene ablation by a UV laser. Taken from reference [106] where the ablation products of 248 nm ablation were analysed using mass spectrometry.

Developments

The ablation of triazene polymers was initially seen as a promising photoresist technology [107]. However, the photosensitivity of the standard triazene polymers is matched by their sensitivity to acidic wet-etching processes [108]. This led to further structural alterations to triazene polymers, such as the insertion of ester groups into the backbone, enabling photo-cross-linking of the polymers without breaking up the polymers' backbones [67]. At the Paul Scherrer Institut other applications were explored, such as micro-optics formed by precise UV-ablation of the triazene, and laser-plasma thrusters for micro-satellites [109]. Also investigated was a form of laser transfer known as laser molecular implantation, where fluorescent molecules were contained within a triazene matrix and transferred via ablation [110]. Imaging techniques were used to analyse the ablation process of triazene, and the first attempts were made to understand the nature of the ablation process [83]. Further developments in these time-resolved methods enabled a greater understanding of the energy generated by this process [105, 111]. An improved triazene polymer synthesis procedure [112], developed at Empa, Dübendorf, has given more control to the structure of the triazene polymer, and therefore opened up the possibility of creating polymers with different structures [79], and possibly different physical and chemical properties, such as solubility or reactivity.

Triazene polymer LIFT

The use of triazene in the molecular implantation process [110] was eventually followed by the use of triazene as a DRL in the transfer of polymethyl methacrylate [113]. This

quickly led to the use of the triazene polymer as a DRL in the printing of other sensitive materials, such as living mammalian neuroblast cells in a polymer matrix [114], quantum dots [115], thin ceramic films [116], metals [79], polymers for sensors [117] and organic light-emitting diodes (OLEDs) [118].

1.3 LIFT of OLEDs

Laser-induced forward transfer of OLEDs is a relatively new topic. In the 1990s, work on laser-assisted printing of electronic and sensory thin films developed [90]. This technique was based on matrix-assisted pulsed laser evaporation (MAPLE) [119], and was labelled MAPLE direct-write (MAPLE-DW). Since then, various attempts have been made to transfer OLED materials in particular, but only a few have resulted in successful device fabrication.

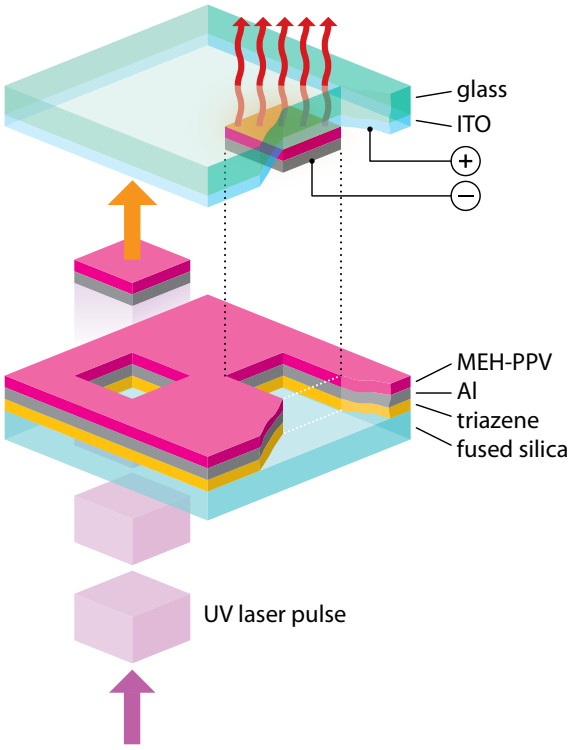

Figure 1.12 The outline of the system used for the original PLED transfer by LIFT [118]. The substrates were actually pressed together with no gap between, so that the process is similar to the LITI process in 1.13.

1.3.1 Laser transfer of OLED materials

Successful attempts were made to deposit MEH-PPV by resonant-infrared RIR-MAPLE and 248 nm UV-MAPLE by Haglund and co-workers [69]. The solvents used as matrices were chloroform for the RIR-MAPLE, and toluene and THF for the 248 nm UV-MAPLE. Attempts

to make MEH-PPV films using RIR-PLD were also attempted. PLD (pulsed laser deposition) is just MAPLE without a matrix. Smooth films were made, but functionality was lost in the ablation process.

The Princeton group of Arnold has tried various modifications of the LIFT process to transfer small molecule OLED materials, Alq_3 and 9-anthracenemethanol [120]. The three techniques they investigate are simple LIFT without any intermediate layer; LIFT with a thin TP DRL; and LIFT with a thick polymer layer which is not fully ablated (see BA-LIFT, or blister-actuated LIFT, in section 1.2.2). The way in which successful transfer was determined was NMR which only indicates whether the materials has maintained the chemical structure - important, but not the only requirement for functionality. Here the films transferred were viscous solutions of the organic semiconductor materials. This means that drying steps were required after transfer to create a completely dry solid film, as well as a complex deposition procedure for the liquid film. More recently, the same group demonstrated successful operation of devices fabricated by BA-LIFT, using a different small molecule OLED material [121], which they have also proceeded to model using finite element analysis [94]. However, as well as the subsequent drying step, thermal evaporation of the metal electrode added another step after the deposition.

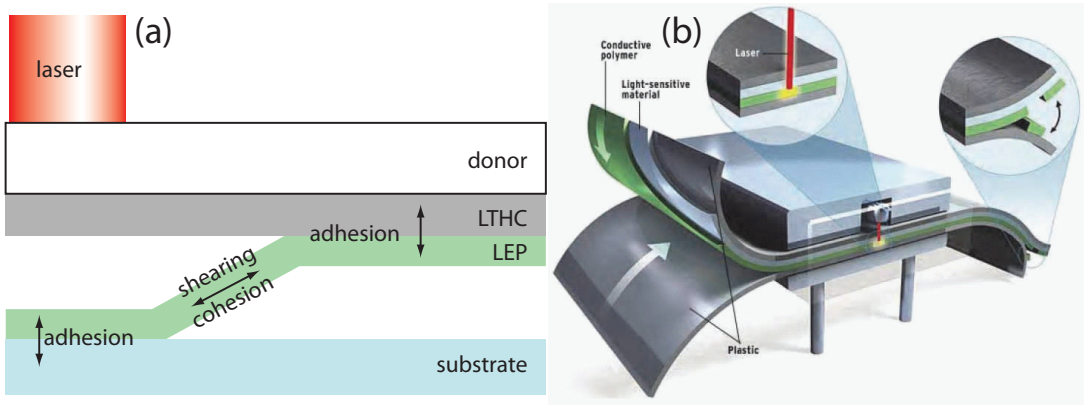

Figure 1.13 A basic force balance scheme (a) of the concept of LITI, taken from [11]. It must be remembered that the donor substrate is actually pressed in very tight contact with the receiver substrate, unlike the scheme suggests. LTHC stands for light-to-heat conversion layer, and LEP is the light-emitting polymer layer. A 3-D scheme of LITI in a roll-to-roll system is shown in (b).

LIFT includes a wide range of techniques based on a laser direct-write idea. In particular, the earliest work using a DRL by Dlott and coworkers formed the basis of the leading industrial laser-based OLED pixel deposition technology: laser-induced thermal imaging [88, 122]. Laser-induced thermal imaging, or LITI, has already been mentioned, and is worth looking at in more detail because of its similarity to LIFT. Figure 1.13 shows the basic concept, where a laser irradiates a light-to-heat conversion layer (analogous to the dynamic release layer outlined in section 1.2) and a target layer, in this case the LEP, is transferred to a receiver substrate. The films are in contact, and the basic process is a change of adhesion

from the donor to the receiver. As demonstrated in the diagram, the whole film is sill cohesive, even if it is stuck to the donor and the receiver at different points. It is not until substrate separation that the film breaks, and so the patterning is greatly dependent on the degree of adhesion to the receiver (and donor) substrates, as shown by an investigation into receiver surface polarity dependence of LITI [123]. The actual transfer process is a slow thermal process, and usually uses continuous wave (CW) lasers [11, 123]. One distinct advantage of the LITI process is is applicability to all types of film-formation techniques, including evaporated small molecule OLED materials [124].

1.3.2 LIFT of simple MEH-PPV OLED

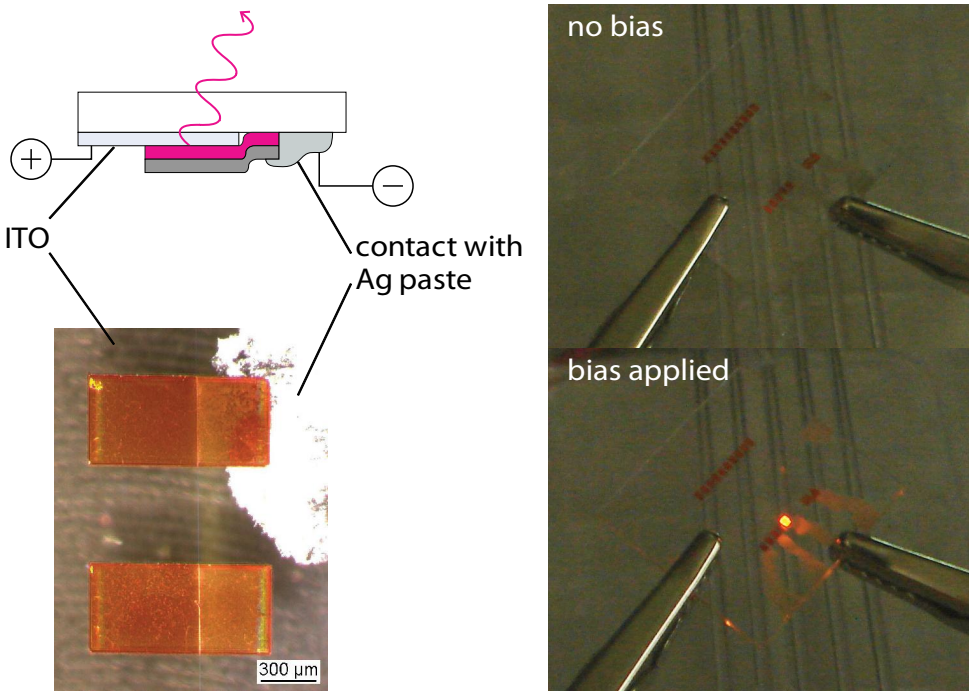

Figure 1.14 A summary of the results from the original OLED transfer with LIFT. The scheme on the left summarises the simple device architecture with two electrodes (ITO anode and Al cathode) and and the MEH-PPV light-emitting layer. The photos on the right show the successful operation of one of the transferred devices.

Preliminary work on the transfer of MEH-PPV OLEDs was undertaken by our group in 2007 [118]. This was one of the biggest recent breakthroughs in the field of LIFT, not just for OLEDs. Impressive functionality, and good pixel morphology was observed, shown in figure 1.14. The devices were made in the same manner as devices shown later, in sections 4.1, 5.1, with the method described in the experimental sections 2.1 and 2.2. A scheme of the process is shown in figure 1.12, where the materials used are shown, and the way in which the laser defines the shape of the transferred pixel. These transfers were made with the donor and receiver substrates in as close contact as possible.

Small cracks in the devices were a minor problem, but a larger problem was the reproducibility. On a single sample, about 8 pixels could be deposited on the two ITO edges. Even at the same fluence huge variations in pixel morphology could be observed on a single substrate, and from sample to sample the variation was even bigger. Improved cleaning procedures helped, but not conclusively. Results presented here in section 4.2.2 explain how the assumption that an uncontrolled gap gave poor transfer reliability helped to improve the reproducibility of the LIFT process.

This was the point at which this thesis started, and the following work all builds from this achievement of depositing an OLED pixel using LIFT.

Chapter 2

Experimental

2.1 Sample preparation

2.1.1 Substrates

Substrate properties

The donor substrates for LIFT are made of artificially fused silica, sometimes referred to as quartz substrates despite their amorphous properties. These are used as they are nearly 100 % transparent to the UV laser light used. For the frontside ablation investgations done in conjunction with the University of Konstanz in section 3.5, metallic silicon substrates were used, but the films formed by spin-coating the TP from the cycloheaxanone:chlorobenzene solution were the same thickness as those made on fused silica. In terms of the actual OLED device fabrication, figure 2.1 shows the main types of devices: 2.1a & c are conventionally fabricated devices; and 2.1b & d are LIFTed pixels.[1]

Substrate cleaning

All substrates followed the same basic cleaning procedure, particularly the ITO and fused silica substrates. Firstly, the substrates were washed in ultrasonic baths of acetone and ethanol, before an ultrasonic bath of the alkali glass cleaning agent (Hellmanex™, Hellma AG). The substrates are scrubbed with a toothbrush at this point. Several (at least three) ultrasonic baths of water purified by microfiltration were then used to rinse the substrates before they are dried using high-pressure filtered nitrogen and cleaned using UV-ozone surface treatment and a final rinse in purified water. Silicon substrates follow the same process without the Hellmanex and the UV-ozone treatment.

Old fused silica substrates were recycled by cleaning the substrates through leaving them in a nitric acid bath overnight before following the cleaning procedure above. The

[1] The terms *conventionally fabricated* and *LIFTed* refer to the fabrication method of the OLEDs, whether they are made in a normal way (conventional) or using the LIFT process (LIFTed). The noun 'device' is used in this thesis with the conventional fabrication method, generally, and 'pixel' is used to refer to OLEDs fabricated using the LIFT process. 'OLED' or 'PLED' are used as collective noun for both.

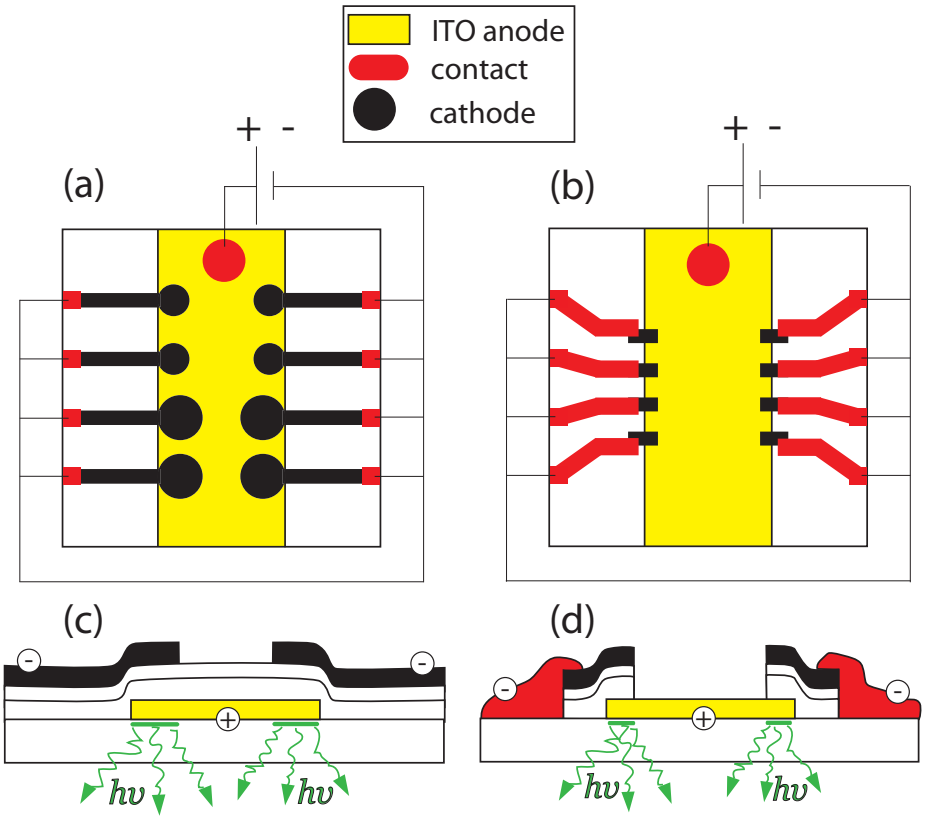

Figure 2.1 The two main device architectures used in this thesis, highlighting the conducting materials in the devices. The ITO is shown in yellow, the silver contacts, both paste and evaporated films, are shown in red, the metal cathodes are shown in black, and the substrate and organic layers are transparent. The conventionally fabricated device architectures are shown in (a) as a plan, and (c) as a vertically exaggerated cross-section. The LIFTed pixels are shown in (b) as a plan, and (d) as a vertically exaggerated cross-section.

thoroughness of the cleaning process is necessary for reproducibility, particularly when fabricating functioning organic electronic devices.

2.1.2 Film-forming methods

Any method for making thin films can in theory be used. However, triazene polymer films are very sensitive to aggressive deposition methods, and so the principle methods used in this research have been casting (particularly spin-casting or spin-coating) and thermal evaporation. Some other groups have found that thermal evaporation damages the triazene film, but we have not observed a significant reduction in the triazene film thickness from silver or aluminium evaporation. MAPLE has been used to deposit films on triazene [125] and doctor blading of solution-processable materials can also be used [13]. Other techniques such as sputtering and PLD would cause damage to the triazene.

Spin-coating

This is the main laboratory technique for thin-film deposition of solution-processable organic materials, particularly polymers. The triazene polymer can be simply drop-cast (essentially spin-coating without the spinning!), but spin-coating makes more homogeneous ultra-thin films. The polymer OLED materials, mentioned below in section 2.1.3, are all deposited using this technique. Tetrabutyl ammonium hydroxide was deposited from spin-coating, in theory adsorbing to form a monolayer on the cathode (aluminium) surface [126, 127]. The thickness of films made by spin-coating can be interpreted from an absorption curve calibrated from profilometry depth measurements.

Thermal evaporation

Thermal evaporation has been used to deposit the cathode metal layers, and also for some small molecule organics. In particular, Alq_3 has been deposited using this technique, which allows for online measurement of thickness using a calibrated quartz crystal microbalance. For the cathode evaporations, and the contact evaporations, proximal / contact masks were designed to control where the metal landed. For other connections, silver paste (Plano AG) was pasted onto the sample.

2.1.3 Materials

Triazene polymer

Triazene polymers (TPs) were synthesised at Empa by Matthias Nagel and his co-workers, particularly Ylenia Maniglio. The 'workhorse' TP is TP-6a in reference [112], with the chemical structure shown in figure 1.11. TP solutions were made by dissolving the TP in a mixture of chlorobenzene:cyclohexanone (1:1). The highest concentration that can be reliably dissolved is 5 wt%. Various concentrations were made, and the TP solution concentrations and spin-coating speeds (see section 2.1.2) were used to control the TP film thickness. The solubility of the TP seemed to vary slightly from batch to batch, and solutions were less soluble with age. Although only a few firm gel permeation chromatography (GPC) measurements were made [112], it can be inferred that some of the batches had different polymerization conditions which would lead to different molecular weights. In order to minimise disruption, the same batches were used as often as possible (mainly the lower molecular weight polymers), and each batch was individually characterised to work out the spin-coating parameters required for the different layer thicknesses.

Light-emitting OLED materials

Polymers Poly(2-methoxy, 5-(2-ethylhexyloxy)-1,4-phenylene vinylene) (MEH-PPV) was bought from American Dye Source, and the chemical structure is shown in figure 2.3b. The commercial polymer was characterised using GPC as: $\overline{M}_n = 144000$ g/mol; $\overline{M}_w = 776000$

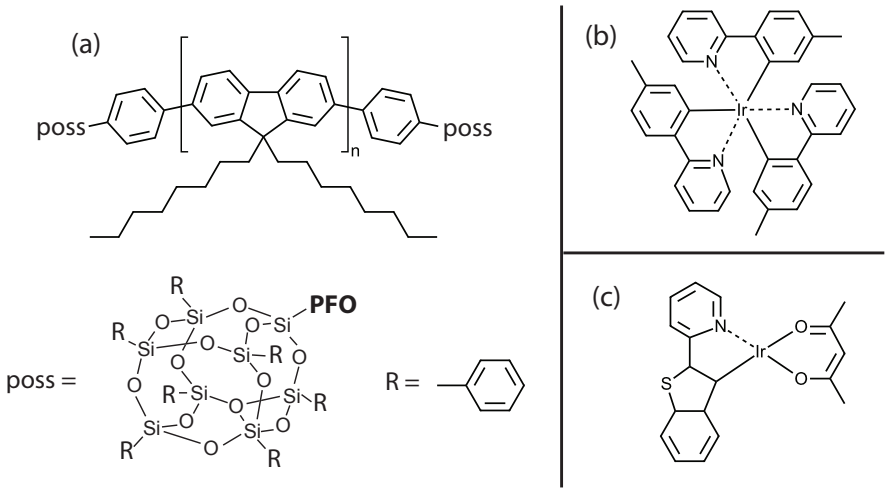

Figure 2.2 The chemical structures of PFO, one of the functional polymers used in this thesis. The main polymeric structure (a) is capped at the ends of the polymer chains by polyhedral oligomeric silsesquioxane (b) & (c).

g/mol; $D = 5.4$. The MEH-PPV was dissolved into chlorobenzene solutions to make 0.8 wt% solutions. It was also blended with PEO, again in chlorobenzene, to make an MEH-PPV:PEO (9:1) solution [128].

Poly(9,9-dioctylfluorenyl-2,7-diyl) capped with a silsesquioxanes (PFO) was also bought from American Dye Source. The silsesquioxane units are actually polyhedral oligomeric silsesquioxane (poss) units, and the chemical structure of the whole PFO polymer is shown in figure 2.2. The PFO was also characterised by in-house GPC measurements: $\overline{M}_n = 22000$ g/mol; $\overline{M}_w = 52000$ g/mol; $D = 2.4$. PFO is a blue emitter, and the electroluminescence spectrum is shown in figure 2.4. Because it is a short wavelength (and therefore high photon energy) emitter, it is also possibly to have energy transfer to dopants from a PFO matrix by Förster, and possibly Dexter, transfer (see the explanation on PhOLEDs in the introduction, section 1.1.2.1). For this reason, the PFO has been doped with concentrations of ≤ 10 wt% iridium dyes [32], outlined in the small molecule section below, giving the green and red electroluminescence spectra in figure 2.4. The PFO (or PFO:dye) was dissolved in toluene:*p*-xylene (1:1) to create solutions to spin-coat the PFO film from.

Finally, poly((9,9-di(3,3'-N,N'-trimethylammonium) propyl fluorenyl-2,7-diyl)-alt-(9,9-dioctylfluorenyl-2,7-diyl)) (PFN) was also bought from American Dye Source. This polyfluorene is actually an ionic species (see the chamical structure in figure 2.3c) which means that it is soluble in polar alcoholic solvents which won't dissolve the less polar polymers such as TP [53]. For this reason it can be safely spin-coated on top of the TP without any polymeric mixing. The PFN was dissolved in methanol:DMF (99:1) to create a 10 mg/ml solution.

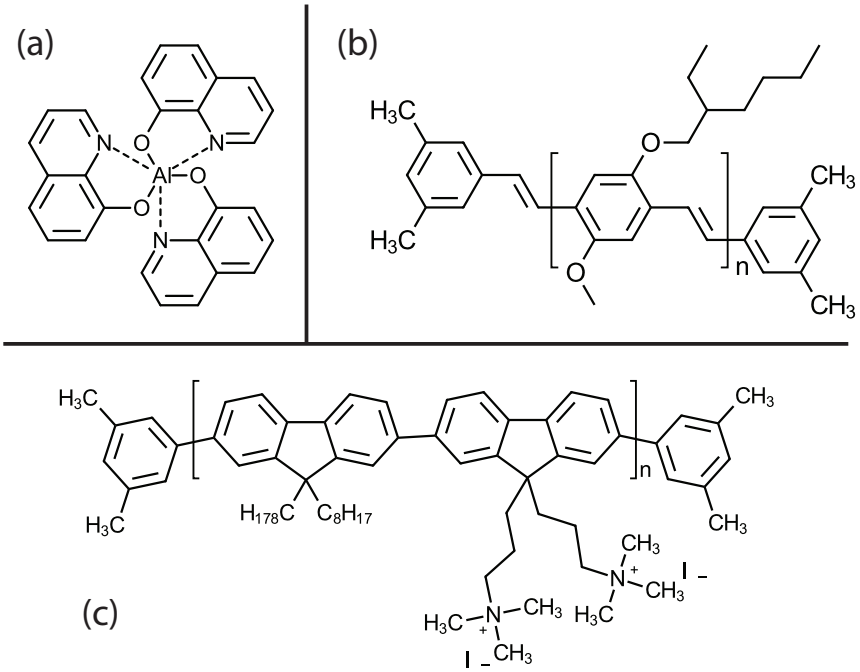

Figure 2.3 The chemical structures of some of the organic light-emitting materials. The small molecule organo-metallic complex is Alq_3 (a), and the polymers are MEH-PPV (b) and PFN (c).

Small molecules The main small molecule that has been investigated is the original OLED materials, aluminium tri-8-hydroxyquinoline (Alq_3) [7]. The chemical structure of this organo-metallic complex is given in figure 2.3a, and the material was bought from Sigma Aldrich (99.999 % sublimed grade). It is deposited by thermal evaporation in a vacuum chamber.

In addition, iridium organo-metallic complexes have been used as dopants in a PFO matrix. The green-emitter is *fac*-tris(2-(4'-methyl)-phenylpyridine) iridium ($Ir(Me\text{-}ppy)_3$) and the red emitter is bis(2-(2'-benzothienyl)-pyridinato-N,$C^{3'}$) iridium(acetylacetonate) ($btp_2Ir(acac)$)). The chemical structures of the dyes are shown in their respective emission colours in figure 2.4, along with PFO. The iridium complex family of molecules has been well studied, and the emission characteristics of both $Ir(Me\text{-}ppy)_3$and $btp_2Ir(acac)$ have been well characterised as part of their structural family [129].

Cathode materials

A number of different materials have been used for the OLED cathodes. For LIFT donor substrates, only aluminium and silver have been used as the cathodes, but they have also been coated in other materials to aid electron injection. Calcium has also been used for conventionally fabricated devices, but is too reactive to be used for LIFT samples. The metals were all evaporated in a high-vacuum ($< 5 \cdot 10^{-6}$ mbar), at rates < 2 Å/s (see

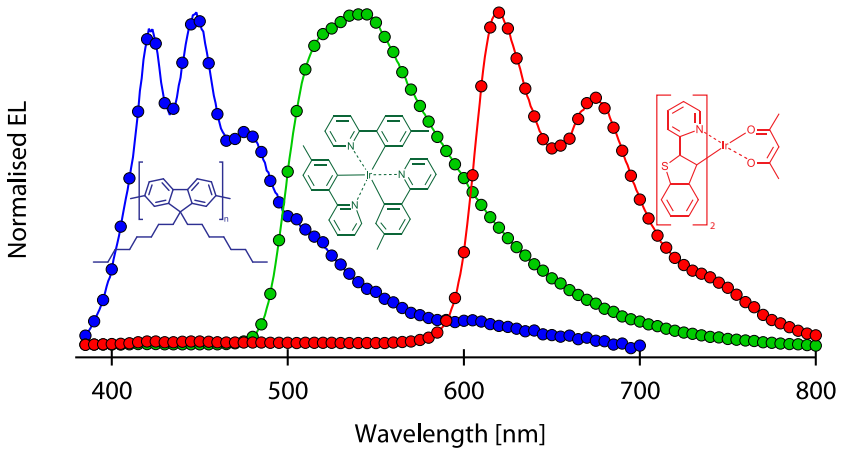

Figure 2.4 The electroluminescence (EL) spectra of three devices: the blue device uses pure PFO emission, and the red and green devices use iridium dye doping of the PFO by $btp_2Ir(acac)$ (red) and $Ir(Me\text{-}ppy)_3$ (green). The chemical structures of PFO, $Ir(Me\text{-}ppy)_3$, and $btp_2Ir(acac)$ are shown as insets on the graph.

section 2.1.2).

A number of different electron-transporting layers (ETLs) have been used to try and improve electron injection from the cathode. Firstly, poly(ethylene oxide) (PEO) has been used by spin-coating from acetonitrile solution. [130, 131] PEO was bought from Sigma-Aldrich, with a stated $\overline{M}_w = 400000$ g/mol. Gel permeation chromatography (GPC) was used in Empa, and gave the following results: $\overline{M}_n = 149000$, $\overline{M}_w = 274000$, $D = 1.85$.

The next material used was Cs_2CO_3, a material that has been much investigated recently [26, 30, 132–134]. It can be both evaporated or spin-coated, but thermal evaporation leaves questions as to what the final material really is, the pressure rise during evaporation indicating that a gas, probably CO_2, is given off during the evaporation process [26, 133, 134]. Whilst spin-coating films is possibly more reliable (although very thin films are hard to make), unexplained effects have been observed when the Cs_2CO_3 film is annealed to remove the solvent before depositing the polymer layer [30].

Finally, tetrabutyl ammonium hydroxide (TBA) was used to help shift the work function of the cathode. This material can only be deposited directly onto the cathode, in essentially a surface-modification via adsorption, and therefore was only done for LIFTed pixels. It is know that TBA will adsorb onto an oxygen-rich surface to create dipolar layers which shift the work function considerably ($\sim$ -0.7 eV) [126]. It has previously been used to inhibit hole injection from ITO, because it was not possible to fabricate good inverse devices when it was researched previously [127].

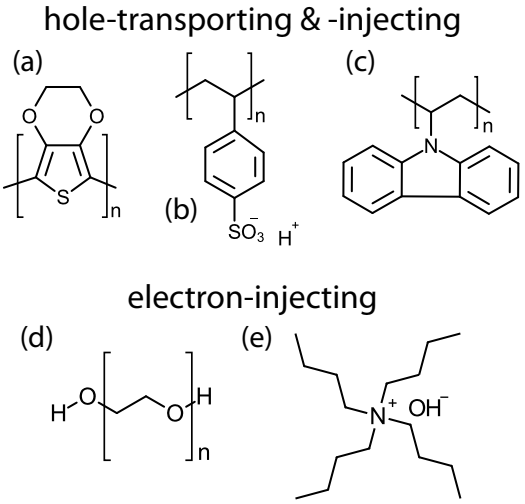

Figure 2.5 The chemical structures of charge-injecting materials. The hole-injecting materials are PEDOT (a), PSS (b), and PVK (c). The electron-injecting materials are PEO (d) and TBA (e).

Anode materials

Tin-doped indium oxide (ITO) is the most widely used transparent electrode commercially, and it was bought in pre-patterned on glass substrates. For all devices, conventionally made or LIFTed pixels, it was used in the research presented in this thesis. The ITO was measured as 140 nm thick (by Ambios XP-1 profilometer). The ITO pattern on the substrate is shown in figure 2.1a.

Poly(3,4-ethylenedioxythiophene) blended with poly(styrenesulfonate) (PEDOT:PSS) has been applied as an anode/hole-transporting layer (HTL) [135, 136]. It was bought from H.C. Stark, now Heraeus, and the particular product is Clevios™P VP Al 4083, which has a blend ratio of 1:6 (PEDOT:PSS) giving a work function of $\sim$ 5.2 eV [137].

Poly(N-vinylcarbazole) (PVK) is a widely used organic electronic material, both as hole transporter [31, 32, 138] and as a host for fluorescent/phosphorescent emitters [50, 139]. The chemical structure of PVK is shown in figure 2.5c, and it is not a conjugated polymer. Partly because it is non-conjugated it has relatively low charge mobilities even though it is a good hole transporter. The PVK was bought from Aldrich, and all the best devices used the high $\overline{M}_w$ variant ($\overline{M}_w$ = 1,100,000), but some of the earlier experiments mistakenly used the lower molecular weight variant ($\overline{M}_n$ = 40,000).

2.1.4 Sample holder

The sample holder for the LIFT experiments was developed in-house at Empa for square substrates of $\sim$ 25 × 25 mm. The design involved four screws with sprung ball bearings holding the substrate in the corners. Four sample holders are shown in the sample transporter in figure 2.6b. For the addition of a gap between the donor and receiver substrates,

spacers have been sandwiched between the edges of the two substrates, as outlined in figure 2.7.

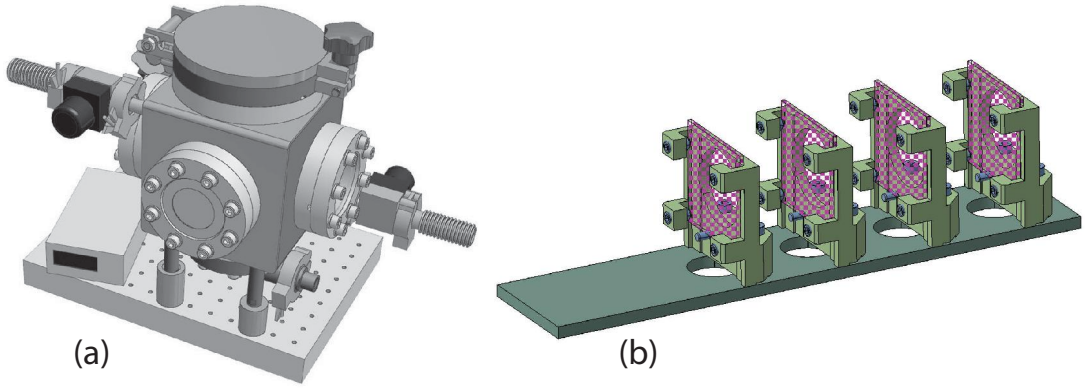

Figure 2.6 The gas chamber used to obtain the reduced pressures (a). The pressure monitor is shown to the left of the chamber, and the rough vacuum pump was connected to the chamber via the tube to the right of the chamber. Four sample holders, with purple substrates in them, are shown on the sample transporter (b). The final part of the transporter is the KF flange tube which is sealed to conserve vacuums and inert environments.

Sample transporter

In order to transport samples between Empa and PSI, a sample transporter was developed to hold substrates in boxes, and in the sample holder. For this purpose, 50 mm KF flange vacuum tubes were used to allow for both transfer in vacuum (from PSI to Empa) and in an inert gas (from the glove box at Empa to PSI). The largest KF flange standard, 50 mm, was necessary to fit both the boxes and the sample holders in.

Adding and measuring a gap between the substrates

The substrate-substrate gap distance was measured using a Vis-IR absorption spectrometer (Varian Cary 500). Using a technique derived from published literature, [140] the gap width can be found from the interference pattern in the absorption spectrum. An absorption spectrum in the range 800-2100 nm was acquired through both substrates, held together in a sample holder in the same way as for LIFT experiments. It is very simple to calculate the gap width from the interference in these spectra, assuming the refractive index of air to be 1. Using this method, the gap width for the samples 'in-contact' was calculated to be 2-3 μm, but was easily increased to > 10 μm with small amounts of dust contamination.

In order to control the gap, spacers were used. Thin metallic foils with known thicknesses were bought from Brütsch-Rüegger for this purpose. For the initial gap experiments in section 4.2, a variation in the gap across the sample was obtained by adding a spacer

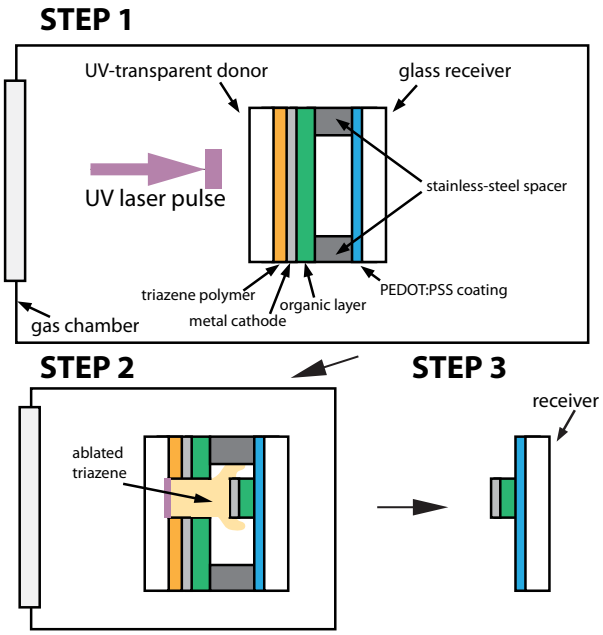

Figure 2.7 A schematic outlining the LIFT process, as detailed in the paper: **Step 1** shows the donor and receiver substrates, pressed together with a spacer between them, in the gas chamber with a laser pulse coming towards them; **Step 2** shows the sample during the transfer process; **Step 3** shows the removed receiver substrate after the transfer.

at one side of the substrate. The calculation of substrate-substrate gap width was done by assuming a linear gradation across the substrates from 'in contact' to the gap created by the spacer. The gap with the spacer on both sides of the sample was measured, and the gradation was then assumed to be from 2 μm ('in contact') to $\sim$ 40 μm. For further details see section 4.2.1. After the LIFT optimisation in section 4.2, transfers were always done with a 15 μmgap ($\pm$ 2 μm). This was the gap obtained using a spacer with a specified thickness of 0.01 mm, as calculated using the method shown in figure 2.8.

2.2 Laser setups

2.2.1 Laser choice

The main laser used was a 308 nm XeCl excimer laser at PSI, acquired from Lamda Physik. This laser was the laser originally used for triazene investigations [99, 102, 103, 141], and the triazene absorption is nearly maximum at 308 nm. Other UV lasers have been used for triazene polymer ablation including 193 nm [114, 115, 142, 143], 248 nm [99, 106, 144, 145], 266 nm [142], and 355 nm [80, 146].

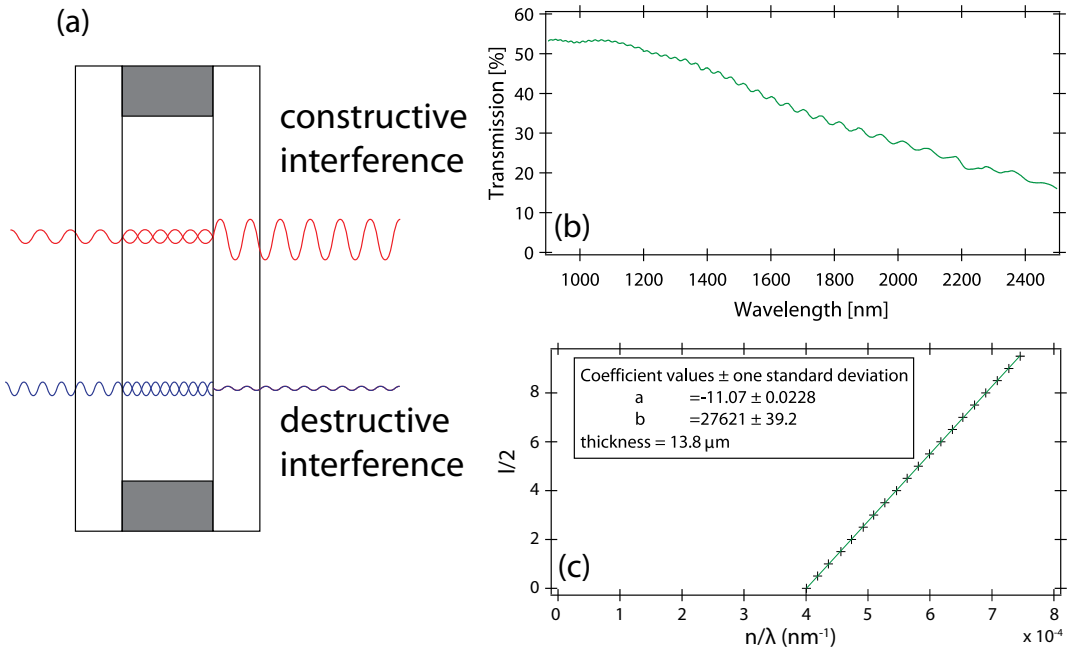

Figure 2.8 A summary of the technique used to measure the gap width. (a) shows a schematic summarising how interference from standing waves in a cavity depend on the wavelength of the light. The red wave exhibits constructive interference because the gap width is a multiple of half the red wavelength, whereas the blue wave is 90° out of phase when reflected meaning that the interference is destructive. (b) shows a typical IR-absorption spectrum for a fused silica / 10 μm spacer / glass sandwich, and (c) is the interpretation of this spectrum.

Properties of different lasers

The obvious differences between the lasers are the wavelengths (308 nm, 355 nm, 532 nm) and the pulse lengths (ps vs ns). There are also beam profile homogeneity differences, and various other technical differences between the lasers. The principle technical difference between the lasers is the lasing medium; the 308 nm is a XeCl excimer laser, i.e. with a gaseous lasing medium, and the 355/532 nm lasers are solid state lasers with a crystalline (Nd:YAG) lasing medium. They are also pumped differently; the excimer is electronically pumped, and the Nd:YAG laser is Xe-flashlamp pumped. The geometry of the excimer electrodes means that a rectangular beam profile is created with a clear Gaussian energy profile across the short axis, and a flatter profile along the long axis. The ns Nd:YAG laser has a beam diameter of $\sim$ 8 mm, and the excimer has a profile approximately 10×40 mm. Both beams are fairly divergent, but the excimer is worse, particularly along the long axis.

Beam characterisation

The principle measurement undertaken with the LIFT experiments is an average energy measurement for 50 or 100 pulses, also measuring the fluctuation with the standard devia-

tion. This was done using a Gentec QE12 pyroelectric energy detector with a Solo monitor, although the earlier experiments were done using a Gentec pyrometer for the higher energies, and a Moltech pyrometer for the lower fluences.

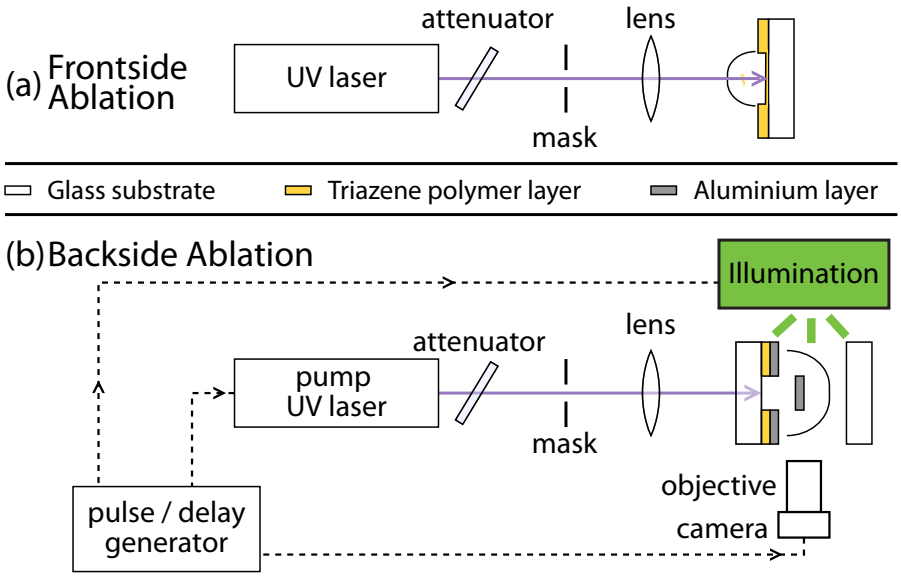

Figure 2.9 Schemes of the basic laser layouts for (a) frontside ablation, and (b) backside ablation, with a shadowgraphy setup included.

2.2.2 Frontside ablation

Frontside ablation refers to experiments where the material (TP) was ablated directly, not through a substrate. The laser beam irradiates the film perpendicular to the film surface, and is directly absorbed at that point. The ablation depth per pulse (known as the ablation rate) is the main quantity obtained from these experiments. The threshold fluence can then be evaluated by measuring the ablation depth at various fluences. These experiments were only carried out in section 3.3 in this study, but references to previously published work on TP ablation are made throughout the thesis [79, 147].

The geometry is shown in figure 2.9a, and is quite simple. The laser beam intensity is controlled by a variable attenuating plate, passes through a proximity mask which is then imaged onto the sample using a standard achromatic lens, with the ablation starting from the air-TP interface.

2.2.3 Standard backside ablation / LIFT

Backside ablation is where the laser beam comes from the *back side* of the sample, that is to say, through the carrying substrate. In this thesis, this means the laser beam travels

through the fused silica substrate before being absorbed by the TP layer. The incidence of the laser beam upon the sample is kept as close to 90° as possible. This 'backside' geometry causes the ablation to be constrained between the remaining film and the substrate, and is the basis for LIFT. The geometry is shown in figure 2.9b as the pump laser, and uses the same basic laser setup as frontside ablation, but the sample is orientated 180° round.

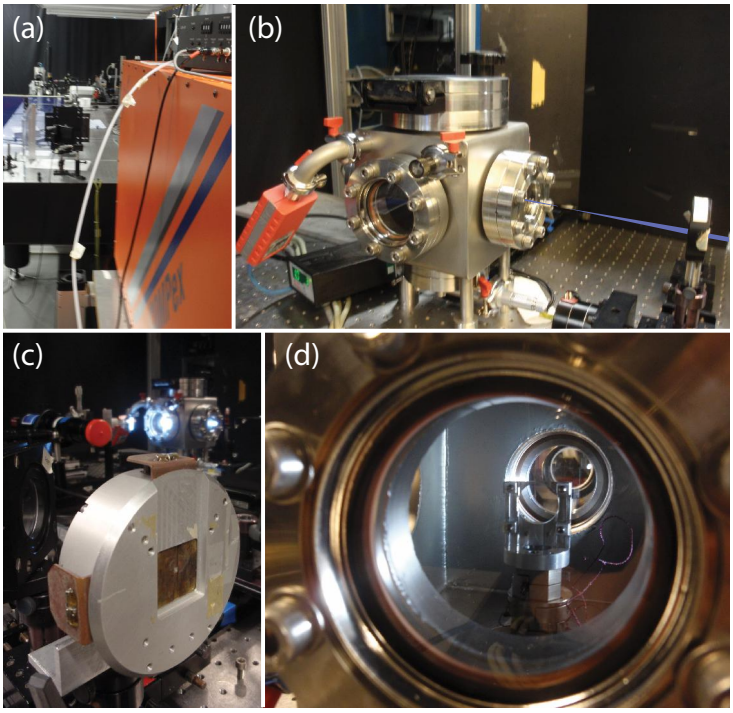

Figure 2.10 Photographs of the experimental setup at PSI. They show the view from the 308 nm XeCl laser (in orange) down the laser lab (a), the gas chamber with the lens and a laser beam drawn (in blue) focussed down by the lens (b), the adjustable rectangular laser proximity mask with the chamber in the background (c), and the view from behind the lens, in the distance, and the sample holder, in the gas chamber (d).

2.2.4 Lateral time-resolved imaging

The main technique used was a form of shadowgraphy (also known as focussed shadowgraphy due to the use of an objective lens unlike normal shadowgraphy). In addition to shadowgraphy, the setup was improved with the aim of producing Schlieren images, although optimal results were not obtained during this study. In addition, time-resolved surface interferometry using a tradition Michelson interferometer was utilised, but not used to produce results for this thesis.

Shadowgraphy

The technique is well established at PSI, and the optical setup is shown in figure 2.9b. The backside ablations setup acts as the 'pump', and a second light source acts as a stroboscopic

'probe' for a camera with a long shutter time relative to the laser pulse length for most experiments. For the experiments in Marseille (the ps exeriments in section 3.3), a gated ICCD camera was used with a cw laser (Nd:YAG, $\lambda = 532$ nm).

Different strobe sources

The standard strobe source at PSI was laser-illumination of a dye solution, but this was changed to a ns spark flashlamp by the end of the thesis ($\tau = 20$ ns). A Nd:YAG laser ($\tau = 5$ ns) was used to illuminate a solution of Rhodamine 6G.

2.2.5 Gas chamber

The gas chamber was specially designed in-house for LIFT at reduced pressures. The chamber has a rough vacuum pump attached, and also a standard pressure gauge, which shows that a maximum vacuum of $2 \cdot 10^{-2}$ mbar can be achieved. A 3D image of the chamber is shown in figure 2.6a, and photos of the chamber are in figure 2.10.

2.2.6 Reflectometry

The setup for detecting the laser ablation of triazene layers consists of a fast reflectometer (cw laser diode, $\lambda = 660$ nm) with a fast photodiode (below 1 ns) and a high spatial resolution in the vertical direction (< 10 nm) [148]. A second cw laser diode was used with a lower-speed photodiode to use reflectometry to measure the thickness of the film before ablation. The ablation is initiated by a focused Nd:YAG laser pulse ($\lambda = 532$ nm, FWHM $= 10$ ns) with nearly orthogonal incidence ($\approx 80°$). The pulse energy was monitored with a thermal energy detector. All the experimental details are well outlined in the literature [148, 149].

2.3 Device characterisation

2.3.1 I-V curves and luminescence

I-V (current-voltage) curves were measured using a Keithley 2400 Sourcemeter controlled with a LabVIEW programme outlined in appendix A. The luminescence (L) was measured with a Minolta LS-110 luminance meter, and was integrated into the LabVIEW programme to allow concurrent I-V and L measurements.

Sample holder

A specially-designed sample holder is used at Empa for all electrical characterisation of organic electronic devices. The sample holder is designed to hold a $\sim 25\times \sim 25 \times 1$ mm glass slide with an ITO stripe along the middle, and four other electrodes coming off to

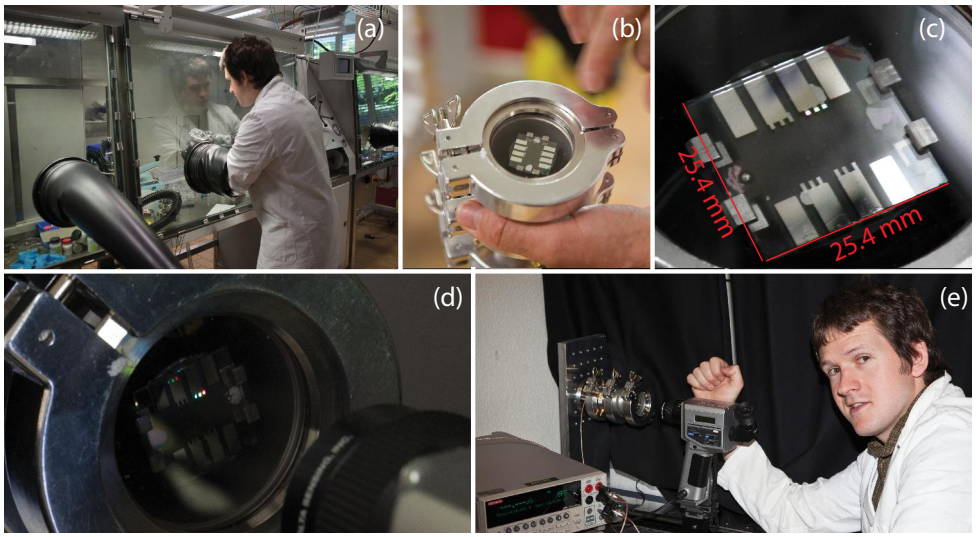

Figure 2.11 (a) shows the author using the glove-box to fabricate devices in an inert nitrogen environment. The next photographs show PFO tri-colour OLED pixels in the device characterisation holder (b), a close-up with a bias applied (c), the sample holder in the IV characterisation setup with luminance meter (d), and the author with the whole device characterisations setup including the sourcemeter (left) and the luminance meter (e).

either side, making eight devices. The holder itself consists of four pins down two opposite sides for connection to the evaporated electrodes (shown as the eight small red circles in figure 2.1a), and a single pin in the middle of the other two for connection to the pre-patterned ITO electrode.

Integration of luminescence-meter and sourcemeter

A LabVIEW programme, shown in appendix A, was developed for the OLED characterisation. The interface was based on an existing IPCE programme for the testing of OPVs, but the drivers came from the Keithley website and an American government website for the sourcemeter and the luminance-meter respectively.

2.3.2 Fluorescence

All fluorescence measurements were done using a Jobin Yvon Horiba FL311 Fluorolog.

Standard fluorescence

Standard fluorescence refers to normal photoluminescent experiments done with the apparatus. Both solutions and thin-films can be measured easily. For thin-films the preferred orientation of the sensor was front-face (FF), where the luminescence emission is measured back, around $\sim 170^\circ$ from the incidence of the excitation beam. The sensor could also be positioned in the right-angle (RA) position, 90° from the excitation beam.

Photoluminescence (PL) is the excitation of a material using light to stimulate the emission of light from the material. The light has lower photon energies (higher wavelengths) than the excitation beam. There are two principal modes of fluorescence measurements: emission and excitation scans. All the experiments outlined here are emission scans, where the excitation wavelength is kept constant and a scan of the emission (PL) is made, giving a PL spectrum.

Electroluminescence

Electroluminescent (EL) experiments were all done externally using an add-on which also allowed for external photoluminescence. This used mirrors in the sample cavity; the first mirror reflects the excitation beam into a fibre optic cable, which has the other end outside the machine, and can be directed to the sample within the sample-holder. There is then a second output parallel to the excitation beam input, which is directed to a mirror reflecting the beam in the direction of the right-angle emission sensor.

The devices, outlined in chapter 5, are operated within the characterisation sample holder using the Keithley sourcemeter, and the end of the fibre-optic cable is clamped in place, positioned towards the OLED.

Integrating sphere fluorescence

An integrating sphere was bought to fit the Fluorolog from Jobin Horiba. The experiments were carried out according to a basic procedure proposed by de Mello et. al [150].

2.3.3 Microscopy

Light microscopy

Three different microscopes were used for the images shown here, all based at Empa: a Leica DM2000 (highest resolution), a Zeiss Axioplan, and a Zeiss Stemmi SV11 (lowest resolution). The sample holder could be used with the Stemmi microscope only.

Scanning electron microscopy

Two different SEMs were used: a Hitachi S-4800, and an FEI ESEM XL30, both based at Empa. Secondary electron (SE) mode in high vacuum was used for the data presented in this thesis. In addition, back-scattered electron (BSE) mode and chemical sensitive energy-dispersive X-ray spectroscopy (EDX) were also used, but the data not used in this thesis.

Part II

Results and Discussion

Chapter 3

Fundamentals of triazene polymer dynamic release layer ablation

3.1 Thermal modelling of triazene polymer ablation[1]

3.1.1 Model outline

The thermal model presented here is not a steady-state model but is still a significant simplification of laser ablation. The model itself is quite complicated, but by analysing it step-by-step it can be more easily understood. The basic heat equation is fairly simple, and a 1-D version is shown in equation 3.1:

$$\frac{1}{\chi}\frac{\partial T}{\partial t} = \frac{\partial^2 T}{\partial z^2} + Q(z,t) \tag{3.1}$$

χ is the thermal diffusivity, T is the temperature, t is the time, z is 1-D depth, and $Q(z,t)$ is the distribution of thermal energy from the laser which is shown in equation 3.2:

$$Q(z,t) = \frac{F}{t_l}\, g(t)\, F(z) \tag{3.2}$$

F is the average laser fluence, t_l is related to the laser pulse length at full width half maximum ($t_l = 0.409 \cdot \tau$), g(t) is the pulse shape in equation 3.3, and $F(z)$ is the 1-D distribution of the laser fluence shown in equation 3.4.

[1] The model used in this section stems from previous work by our group in conjunction with Professor Boris Luk'yanchuk [77]. The basics have been outlined straight from the previous publication, but modifications have been made subsequently to apply the model to different situations, both for frontside and backside ablation of the triazene polymer.

$$g(t) = \frac{t}{t_l} \exp\left(-\frac{t}{t_l}\right) \tag{3.3}$$

$$F(z) = \frac{\alpha_{\text{lin}}}{\kappa}(1-r)\, q(z) \tag{3.4}$$

α_{lin} is the absorption coefficient, κ is the thermal conductivity, r are the reflective losses, and $q(z)$ is the normalised 1-D distribution of the laser intensity. The reflective losses can be calculated accurately using equations dependent on the refractive index and extinction coefficient differences at the relevant interfaces [77]. When applying equation 3.4 to the system of a laser-transparent substrate and a DRL film, a couple of assumptions are made:

1. The absorption coefficient (α_{lin}) of the substrate is assumed to be zero as it is considerably lower than the absorption coefficient of the DRL (see table 3.1), meaning that $F_s(z) = 0$.

2. The laser energy deposition in the DRL is defined by the Lambert-Beer law of absorption (see equation 3.31), meaning that $q_f(z) = \mathrm{e}^{-\alpha_{\text{lin}} z}$.

On top of these assumptions, the following equations are based on a frontside ablation geometry, shown in figure 3.1a. For frontside ablation, z increases from $z = 0$ at the TP / air interface to $z = h$ at the substrate / TP interface (h = TP film thickness), then $z > h$ within the substrate. The simplifications create the following heat equations for the DRL film (3.5) and the substrate (3.6):

$$\frac{1}{\chi_f}\frac{\partial T_f}{\partial t} = \frac{\partial^2 T_f}{\partial z^2} + (1-r)\frac{\alpha_{\text{lin}}}{\kappa_f}\frac{F}{t_l}\frac{t}{t_l}\exp\left(-\frac{t}{t_l}\right)\mathrm{e}^{-\alpha_{\text{lin}} z} \tag{3.5}$$

$$\frac{1}{\chi_s}\frac{\partial T_s}{\partial t} = \frac{\partial^2 T_s}{\partial z^2} \tag{3.6}$$

The subscripts f and s refer to the DRL (film) and the substrate respectively. These equations need to be solved within certain boundary conditions. In particular we consider thermal insulation at the edges where the air / substrate interface does not allow any heat flux and the substrate is a perfect heat reservoir, meaning that the temperature is zero[2] infinitely deep into the substrate:

$$\kappa_f \left.\frac{\partial T_f}{\partial z}\right|_{z=0} = 0, \qquad T_s(z)\big|_{z\to\infty} = 0 \tag{3.7}$$

[2] $T = 0$ in this model is actually room temperature. For this reason, the temperature calculated by the simulation is actually ΔT.

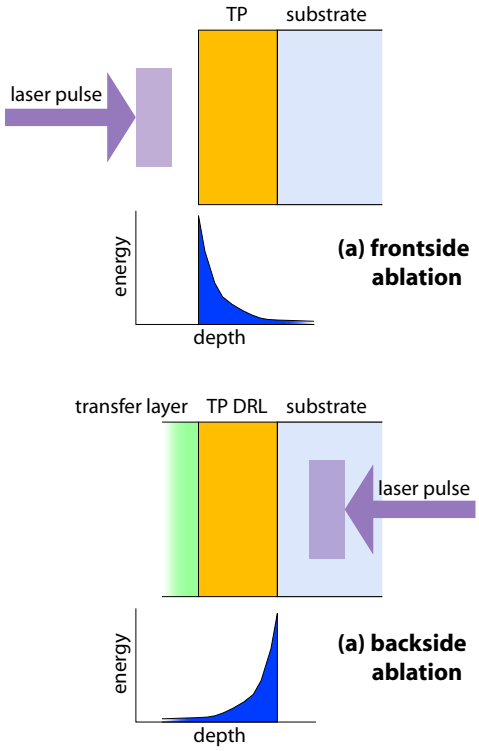

Figure 3.1 The two different geometries of ablation investigated in this thesis. Frontside ablation (a) is the normal ablation orientation for the basic study of light-material interactions. Backside ablation (b) is the orientation used to generate the force to drive the transfer in LIFT. The layers shown are the substrate, the triazene polymer (TP) dynamic release layer (DRL), and the transfer layer. The energy profiles shown are based on simple exponential Lambert-Beer's absorption without any thermal diffusion.

Two further conditions come from the continuity of the temperature and thermal flux between the substrate and the TP film:

$$T_f\Big|_{z=h} = T_s\Big|_{z=h}, \qquad \kappa_f \left.\frac{\partial T_f}{\partial z}\right|_{z=h} = \kappa_s \left.\frac{\partial T_s}{\partial z}\right|_{z=h} \tag{3.8}$$

and the initial temperatures are zero:

$$T_f(z)\Big|_{t=o} = T_s(z)\Big|_{t=o} = 0 \tag{3.9}$$

The differential equations 3.5 and 3.6 can be solved using the Laplace transform. This is a process whereby the solving of the differential equation is helped by transforming the dimensionality of the variable of interest from a function of time t, to a function of a transform variable p. The Laplace transform is governed by equation 3.10:

$$\tilde{T}(z,p) = \int_0^\infty \mathrm{e}^{-pt}\, T(z,t)\, \mathrm{d}t \tag{3.10}$$

This transform can generate the following DRL film (3.11) and substrate (3.12) differential equations:

$$\frac{\mathrm{d}^2\tilde{T}_f}{\mathrm{d}z^2} - \frac{p}{\chi_f}\tilde{T}_f + \frac{(1-r)F}{(1+pt_l)^2}\,\mathrm{e}^{-\alpha_{\mathrm{lin}}z} = 0 \tag{3.11}$$

$$\frac{\mathrm{d}^2\tilde{T}_s}{\mathrm{d}z^2} - \frac{p}{\chi_s}\tilde{T}_s = 0 \tag{3.12}$$

So the Laplacian boundary equations for the transformed functions in equations 3.11 and 3.12 are then:

$$\left.\frac{\partial\tilde{T}_f}{\partial z}\right|_{z=0} = 0, \quad \tilde{T}_s(z)\big|_{z\to\infty} = 0, \quad \tilde{T}_f\big|_{z=h} = \tilde{T}_s\big|_{z=h}, \quad \kappa_f \left.\frac{\partial\tilde{T}_f}{\partial z}\right|_{z=h} = \kappa_s \left.\frac{\partial\tilde{T}_s}{\partial z}\right|_{z=h} \tag{3.13}$$

The solutions of equations 3.11 and 3.12 are:

$$\tilde{T}_f = a\exp\left(-z\sqrt{\frac{p}{\chi_f}}\right) + b\exp\left(z\sqrt{\frac{p}{\chi_f}}\right) - \frac{\alpha_{\mathrm{lin}}\chi_f}{\kappa_f(\alpha_{\mathrm{lin}}^2\chi_f - p)}\frac{(1-r)F}{(1+pt_l)^2}\mathrm{e}^{-\alpha_{\mathrm{lin}}z} \tag{3.14}$$

and

$$\tilde{T}_s = c\exp\left(-z\sqrt{\frac{p}{\chi_s}}\right) \tag{3.15}$$

The unknown constants a, b, and c in equation 3.14 can be obtained from the boundary conditions (equations 3.13). These differential equations can be numerically solved by doing an inverse Laplacian transform, according to equation 3.16:

$$T(z,p) = \int_{\gamma-\mathrm{i}\infty}^{\gamma+\mathrm{i}\infty} \mathrm{e}^{pt}\,\tilde{T}(z,p)\,\mathrm{d}p \quad . \tag{3.16}$$

γ is a real constant selected to be larger than the real part of all the singularities of $\tilde{T}(z,p)$ meaning that the integral converges. This integration is done using Mathematica® script.

Table 3.1 Input constants for the thermal model taken from reference [77].

	308 nm α_{lin} [cm^{-1}]	n [-]	κ [W cm^{-1} K^{-1}]	χ [cm^2 s^{-1}]
fused silica	$8.8 \cdot 10^{-1}$	1.49	$1.4 \cdot 10^{-2}$	$8.1 \cdot 10^{-3}$
triazene polymer	$2.3 \cdot 10^{5}$	1.64	$1.3 \cdot 10^{-3}$	$1.0 \cdot 10^{-3}$

For backside ablation, similar assumptions are made. $z = 0$ is the top of the DRL (i.e DRL / transfer layer interface), and $z = h$ is the DRL / substrate interface. The laser energy distribution in the film is then $q_f(z) = \mathrm{e}^{-\alpha_{\text{lin}} h - z}$. The same assumptions as for frontside ablation are made for the boundary conditions, meaning that the top of the DRL is insulating. The difference between the frontside differential equations 3.5 and 3.11 and the backside equivalents is solely due to the laser energy deposition. In the end, this means that equation 3.14 is now:

$$\tilde{T}_f = a \exp\left(-z\sqrt{\frac{p}{\chi_f}}\right) + b \exp\left(z\sqrt{\frac{p}{\chi_f}}\right) - \frac{\alpha_{\text{lin}}\chi_f}{\kappa_f(\alpha_{\text{lin}}^2\chi_f - p)} \frac{(1-r)F}{(1+pt_l)^2} \mathrm{e}^{\alpha_{\text{lin}} z - h} \tag{3.17}$$

and equation 3.15 remains the same:

$$\tilde{T}_s = c \exp\left(-z\sqrt{\frac{p}{\chi_s}}\right) \tag{3.18}$$

These equations are relatively simple and modifications have not been made to the equations, but they have been used to look at how the temperature might be expected to vary as a function of time and depth. Standard input parameters for triazene polymer and fused silica are shown in table 3.1.

3.1.2 Thermal depth profiles of frontside and backside ablation

As well as the surface time-temperature profiles published before [77], this model can generate depth-temperature profiles at fixed points in time. These are interesting for conceptual understanding of the temperature build-up, and for quantifying the heat loss into the substrate. In particular, the order of magnitude of the heat loss as a proportion of input laser fluence is a useful parameter. Figure 3.2 shows the first depth profiles for two different fluences with a 350 nm TP film and the input parameters from table 3.1.

Fluence dependence

As the main energy input to the model, it can be expected that varying the laser beam energy will have a significant effect on the temperature. The basic effect is shown in figure 3.2, and the graph makes the nature of the fluence dependence of the temperature profile clear: the temperature at any particular depth, and at any time is directly proportional to

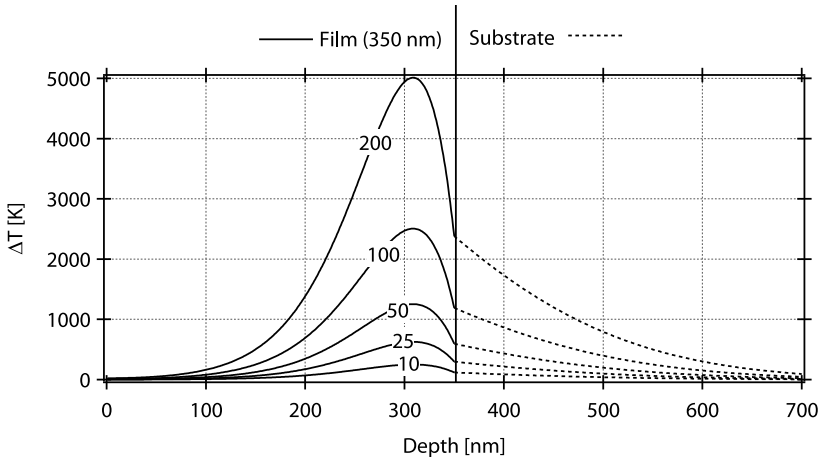

Figure 3.2 Temperature depth profiles at 30 ns using the thermal model for backside ablation at different fluences. The fluences are marked on the curves and are given in mJ/cm^2. A 350 nm TP film is used, with the temperature in the TP film shown on the left, and in the fused silica substrate shown on the right with an interface in the middle.

the fluence. This is logical, because the shape of the laser pulse stays the same for different fluences, meaning that the relative spatial distribution of the energy via the absorption coefficient also stays the same. The only difference is the total amount of energy being deposited (i.e. the integral under the spatial energy distribution). This means that for comparing temporal effects, it is only necessary to look at single fluences.

This is another over-simplification. A dynamic ablation process means that the effective absorption coefficient should vary with fluence [67,81]. This is because higher fluences will mean ablation starts during the laser pulse. There is then a trade-off between absorption of the laser beam by the ablation products (which would increase the effective absorption), and moving of the gas-TP interface (which would decrease the effective absorption). It would be useful to build these processes into the model.

Time dependence

The temperature depth profile is very dependent on time, and by running simulations at different times, 3-D graphs can be made showing the temperature as a function of depth and time. Figure 3.3 shows such graphs for both backside (a) and frontside (b) geometries. 150 nm TP films are used for both samples, with a fluence of 100 mJ/cm^2, and yet there is an enormous discrepancy in the temperature. Conceptually, this is a very important figure for helping to understand why frontside ablation parameters should not be used to fit backside ablation data if thermal loss into the substrate is an important factor for frontside 30 ns ablation. It has already been shown in reference [77] that thermal loss into the substrate is important for frontside 30 ns ablation, and is again shown in section 3.3.4 where differences in threshold fluence for different pulse lengths have been modelled by thermal loss into the fused silica substrate.

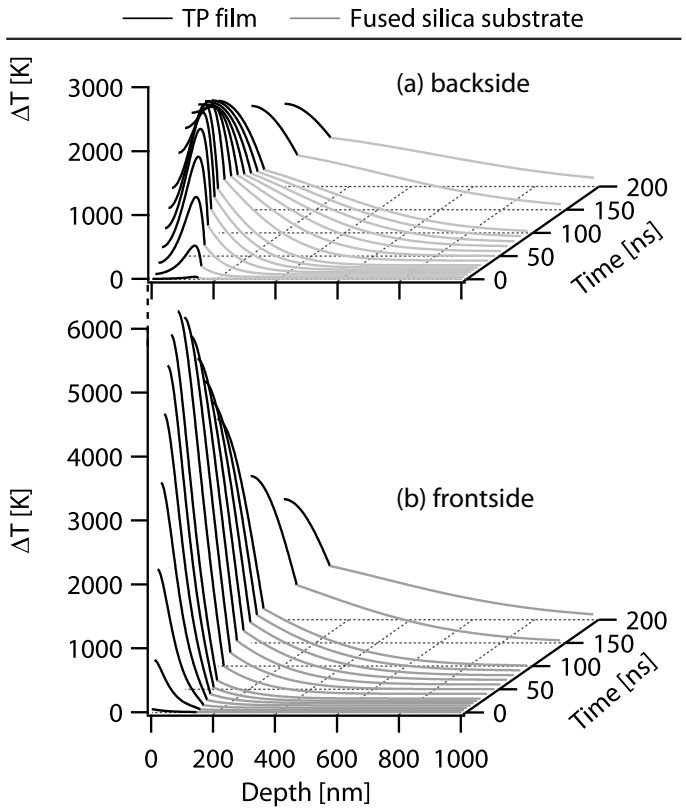

Figure 3.3 Temperature-time-depth profiles through 150 nm TP / fused silica substrate. 100 mJ/cm^2 from a 308 nm / 30 ns laser is being irradiated in backside (a) and frontside (b) geometries.

As well as helping conceptual understanding, these graphs can be analysed quantitatively by integrating under the curves and multiplying the integral with the heat capacity and the density to give the heat energy. Whilst absolute values for the heat energy may be unrealistic, the proportion of heat loss into the substrate may be calculated. This has been carried out for the pulse length comparison in section 3.3.4, and has provided a useful 'ball-park' figure for the heat loss to add to the model in the following section 3.2.

3.2 Modelling the flyer velocity at reduced pressures[3]

This section presents an adaption of a model developed for pulsed laser ablation of single-layer metal films [95] for use with bilayer (DRL / transfer layer) samples. The model is based on pioneering work by Gurney into the velocities of fragments from bombs, shells and grenades during the Second World War [96]. Despite the importance of mechanical shock waves of transferring energy from explosives to surrounding munitions cases, Gurney's

[3]Work from this section is in press (in the proceedings of EMRS 2011, Symposium J Laser Processing of Materials) as reference [151].

assumptions were not based on shock mechanics at all. Gurney assumed that: 1) a given explosive will release a fixed amount of energy per unit mass which will all end up as kinetic energy driving the inert material (metal) and the explosive gaseous products; and 2) the gaseous products have a uniform density and a linear one-dimensional velocity profile. The first assumption means that the efficiency of energy transfer to the metal fragments is consistent regardless of the system geometry, which works as long as there are no significant 'end losses' of the gaseous products. The second assumption is for situations where there are opportunities for multiple shock reverberations in the gaseous product space while the confinement is still intact [97].

3.2.1 Model outline

The basis for this LIFT flyer model is work by Lawrence and Trott [95]. The geometry is standard backside ablation, as used in LIFT [152, 153]. This means the laser light goes through a transparent substrate and hits the DRL perpendicular to the plane of the substrate and films, which are assumed to be perfectly parallel to one another. Along with the original Gurney model assumptions stated above, a number of further assumptions are made. The substrate is assumed to be mechanically rigid with respect to the ablation products, which is reasonable for the 1 mm thick fused silica substrates, relative to the DRL and transfer layer thicknesses of < 1 μm. The deposition of the laser energy is assumed to be an approximation of a standard exponential profile controlled by an effective optical absorption coefficient α_{eff} of the DRL, according to Lambert's law. This effective absorption coefficient is either an empirical value, derived from frontside ablation data [147], or it is calculated from the true optical absorption coefficient α_{lin} of the DRL, the DRL thermal diffusivity χ_d, and the laser pulse length τ (equation 3.23). The total absorbed energy is assumed to equilibrate over the ablation depth during the pulse length. The model is 1-D, as stated in Gurney's second assumption above, which is reasonable for our samples which usually have lateral dimensions ~ 500 μm, and thicknesses < 500 nm.

The bilayer (DRL / transfer layer) structure assumes that the overlying transfer layer ablates at much higher energies than the DRL, and is therefore not ablated at all. This is a reasonable assumption, as long as the fluence is not high enough for a large amount of laser energy to impinge on the transfer layer. As soon as all the DRL is ablated we may say that the model stops being valid because of this assumption.

The Gurney model is applied to laser ablation by assuming that the geometry of the ablation represents one half of a 'symmetric sandwich' [97, 154]. The ablated portion of the DRL replaces the explosive material in the original model, and the substrate interface replaces the symmetry plane. The Gurney energy, on the left-hand side of equation 3.19, is equated to the kinetic energy of the flyer and the kinetic energy of the ablation products, on the right-hand side of equation 3.19:

$$\rho_d x_d E = \frac{\rho_t x_t + \rho_d (x_0 - x_d)}{2} v_0^2 + \frac{\rho_d}{2} \int_0^{x_d} \left(\frac{x}{x_d} \right)^2 v_0^2 \, \mathrm{d}x \tag{3.19}$$

ρ_d is the DRL density, ρ_t is transfer layer density, x_0 is the initial DRL thickness, x_d is the ablated layer thickness, x_t is the transfer layer thickness, v_0 is the initial velocity of the flyer, and E is the Gurney energy (calculated in equation 3.29). From the second of Gurney's original assumptions outlined in the introduction, the velocity of the ablation products is assumed to follow a linear Lagrangian profile:

$$v(x) = \left(\frac{v_0}{x_d} \right) x \tag{3.20}$$

Using equation 3.20 the solution to equation 3.19 for the velocity v_0 is:

$$v_0 = \sqrt{\frac{6E\rho_d x_d}{3\rho_t x_t + \rho_d (3x_0 - 2x_d)}} \tag{3.21}$$

The Gurney energy E is the total energy transformed into kinetic energy of gaseous products and flyer. This means that it is all the energy inputs minus any loss mechanisms other than kinetic energy, as shown in equation 3.22.

$$E = total\ input\ energy - total\ energy\ lost \tag{3.22}$$

The input energy comes from two sources: the laser fluence F and the energy from the decomposition reaction of triazene ΔH_{dec}. There are four output energies defined by the model: the energy in the flyer's kinetic energy, the energy lost in the kinetic energy of the decomposition products, the proportion of input laser energy lost due to reflection r (incorporated in E), and the energy lost below the minimum energy required for ablation ε_0 (incorporated in E). There may be other energy losses in the process, but here we assume that they are all included in r, and are therefore uniform with respect to the fluence. In order to calculate the laser energy deposition, the effective absorption coefficient α_{eff} must be determined. Following Lawrence and Trott [95], we can also calculate an effective absorption coefficient by adjusting the true optical absorption coefficient α_{lin} to take into account thermal diffusion χ_d in the film during the laser pulse length τ:

$$\alpha_{\text{eff}} = \frac{\alpha_{\text{lin}}}{1 + k\alpha_{\text{lin}} \sqrt{\chi_d \tau}} \tag{3.23}$$

k is included as a correction factor for the thermal diffusivity and absorption coefficients, but here it is always assumed to be 1. The energy per unit mass deposited by the laser $\varepsilon(x)$

can be calculated as a function of depth using α_{eff}:

$$\varepsilon(x) = \frac{\alpha_{\text{eff}} F(1-r)}{\rho_d} \exp\left(-\alpha_{\text{eff}} x\right) \tag{3.24}$$

At the substrate / DRL interface ($x = 0$), the energy density is maximum:

$$\varepsilon_0 = \frac{\alpha_{\text{eff}} F(1-r)}{\rho_d} \tag{3.25}$$

The laser energy density is a function of depth, shown in equation 3.24. A minimum energy density parameter ε_d is now created, representing the threshold energy required for ablation. ε_d is also the laser energy at the ablation depth x_d. ε_d was the decomposition energy required to vaporise the metal in the original model of Lawrence and Trott [95]. However, the triazene decomposition is an exothermic reaction, with a decomposition enthalpy created by the release of the 'potential energy' in the chemical bonds ΔH_{dec}. ε_d may be partly dependent on the activation energy of the DRL decomposition, but it is more complicated than just the activation energy. It is simpler to think of ε_d as an irreversible ablation activation energy.

If the ablation depth is already known, for example from frontside ablation experiments [80, 147], ε_d can be calculated from the ablation depth x_d using equation 3.24:

$$\varepsilon_d = \varepsilon(d) = \frac{\alpha_{\text{eff}} F(1-r)}{\rho_d} \exp\left(-\alpha_{\text{eff}} x_d\right) \tag{3.26}$$

If the x_d is not known, ε_d can be calculated using the threshold fluence F_{th}. F_{th} can be either estimated or empirically derived. Equation 3.27 is an adaptation of equation 3.25, where $\varepsilon_0 = \varepsilon_d$ because $x_d = 0$:

$$\varepsilon_d = \frac{\alpha_{\text{eff}} F_{th}(1-r)}{\rho_d} \tag{3.27}$$

Using ε_d, the ablation depth can be calculated by rearranging equation 3.26:

$$x_d = \frac{1}{\alpha_{\text{eff}}} \ln\left(\frac{\alpha_{\text{eff}} F(1-r)}{\rho_d \varepsilon_d}\right) \tag{3.28}$$

We now have all the parameters required for this simple Gurney energy model:

$$E = \frac{F(1-r)}{\rho_d x_d} + \Delta H_{dec} - \varepsilon_d \left\{1 + \frac{1}{\alpha_{\text{eff}} x_d}\right\} \tag{3.29}$$

On the right-hand side, the first term is the total available deposited laser energy (*input*), the second the enthalpy of decomposition of the triazene (*input*), the third is the threshold (and therefore unused) energy (*output*), and the fourth is the energy lost beyond the ablation depth (*output*). The Gurney energy can now be simply inserted back into

Table 3.2 Input constants for the model.

name	symbol	value	unit
TP density[a]	ρ_d	1100	kg/m^3
TP decomposition enthalpy[b]	ΔH_{dec}	$6.24 \cdot 10^5$	J/kg
TP thermal diffusion[a]	χ_d	$1 \cdot 10^{-7}$	m^2/s
TP 308 nm absorption coefficient[a]	α_{lin}	$2.3 \cdot 10^7$	m^{-1}
aluminium density	ρ_t	2700	kg/m^3
aluminium film thickness	x_t	$8 \cdot 10^{-8}$	m
laser pulse length	τ	$3 \cdot 10^{-8}$	s

[a] From [77]
[b] From [83]

equation 3.21 to calculate the flyer velocity.

3.2.2 Using the model

To use the model a number of input parameters were taken from the literature, which are summarised in table 3.2. The film thicknesses were measured using a profilometer, and the laser pulse length has been observed using a high-speed photodiode [80]. The aluminium transfer layer thickness was 80 nm, shown in table 3.2, and the applied TP DRL layers were 150 and 350 nm, to match the experimental data from section 3.4.

The model was operated in four different ways, varying two aspects of the model: 1) the method of calculating the effective absorption coefficient α_{eff}, and 2) the incorporation of the DRL decomposition enthalpy ΔH_{dec}.

α_{eff} can either be found empirically by fitting the single-pulse ablation depth from frontside ablation [81], or they can be calculated from more fundamental parameters according to equation 3.23: the true optical absorption coefficient of the TP α_{lin}, the thermal diffusivity α_d of the TP, and the laser pulse length τ. For the latter method, an estimate for F_{th} must be made to calculate ε_d from α_{eff} using equation 3.27. For our fit we have assumed a threshold fluence of 25 mJ/cm^2, a value based on previous observations [147, 152], as well as the experimental data points presented here. Equation 3.27 is a valid model for metals, but for polymer ablation it is less applicable due to the photochemical nature of the ablation indicating that the ablation time-scale is below the laser pulse length [155]. Nevertheless, it is interesting to compare how the calculated effective absorption coefficient differs to the frontside experimental data.

For both types of absorption coefficients, once the laser fluence rises above the fluence required to ablate the whole DRL, the model remains partially valid until the laser fluence starts to ablate the transfer layer, which is not taken into account by this model. Furthermore, additional absorption from reflection off a reflective transfer layer is not taken into account, although this will only be a tiny proportion of the absorbed energy due to the exponential decrease in absorbed energy.

Finally, the velocity was calculated from the Gurney energy according to equation 3.21. Additional analytical parameters can then be calculated from the velocity such as the energy-coupling efficiency f, the kinetic energy of the flyer divided by the fluence:

$$f = \frac{\left(\rho_d(x_0 - x_d) + \rho_t x_t\right) v_0^2}{2F} \tag{3.30}$$

This is an interesting parameter because it outlines the proportion of energy going into the flyer's kinetic energy from the input laser energy. f is plotted as a function of the fluence F (shown in figure 3.5).

3.2.3 Comparison with experimental results

The experimental results are taken from shadowgrams shown in section 3.4, and were published in part by our group previously [156]. These shadowgrams were taken at reduced pressure, meaning that deceleration due to air drag is negligible, and the velocity is effectively the initial velocity, v_0. The velocity is measured by taking shadowgrams at defined delays after the laser pulse, and plotting the position of the flyer against this delay time. From this a linear fit can be made to give the velocity.

Figure 3.4 shows the fit of the model flyer velocities to the experimental data, for four different input parameters outlined above. The best model fit is either model fit (2) or model fit (3). Model fit (2) uses the experimentally-derived α_{eff} without ΔH_{dec}, whereas (3) is the calculated α_{eff} with ΔH_{dec} included. Unfortunately, all of the model fits enormously over-estimate the available energy. Reflection loss at both of the fused silica substrate interfaces r should only be around 0.1-0.15 [77, 84] which would give velocities more than double what we observe. When ΔH_{dec} is included, r is higher, as expected when an extra input is added. For 350 nm TP DRL with fits (2) and (3), the model can be made to fit the data fairly well just by increasing r. However, for 150 nm TP this is not the case for high fluences. The explanation for this is based on the difference in triazene polymer DRL thickness. The whole 150 nm DRL is ablated by 200mJ/cm^2, whichever α_{eff} is used, whereas the 350 nm DRL is not fully ablated until higher fluences. The actual fluence where a 350 nm TP DRL is completely ablated varies slightly more depending on the model parameters. A consequence of this can be seen in figure 3.5 where the four different curves in figure 3.5a intersect at a wider range of fluences than figure 3.5b. As mentioned above, this does not mean that the model is automatically invalid at fluences above the complete DRL ablation, but the model does not take into account ablation of the transfer layer if the fluence is high enough to ablate it. For 150 nm TP DRL this appears to happen between 300 and 550 mJ/cm^2, from the shadowgraphy in section 3.4, but the flyer does not even ablate at 550 mJ/cm^2 for a TP DRL thickness of 350 nm. This suggests that the model should be able to fit all the experimental data points for a TP DRL of 350 nm, but not the 550 mJ/cm^2 data point for a TP DRL of 150 nm. This is indeed the case for the best model fits in figure 3.4.

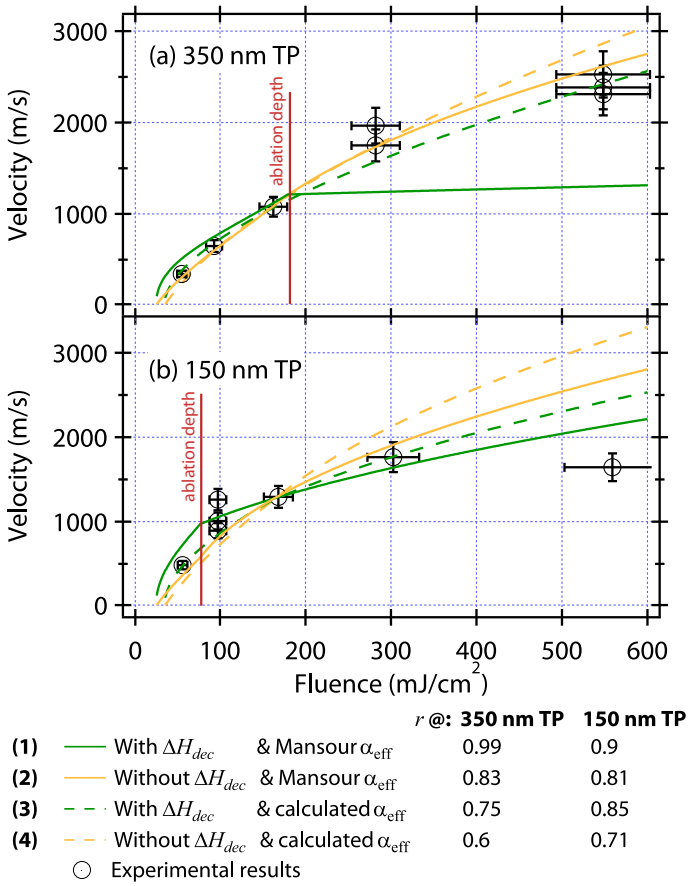

Figure 3.4 Flyer velocity as a function of fluence, comparing the model results with experimental data points for (a) 350 nm TP / 80 nm Al and (b) 150 nm TP / 80 nm Al. All the model operations were fitted by only altering r so that they matched the experimental point at $\sim 170\text{mJ/cm}^2$. Mansour α_{eff} indicates that the effective absorption coefficient was calculated according to a fit to experimental frontside ablation data. Calculated α_{eff} means that the effective absorption coefficient was calculated according to equation 3.23. The red line shows the fluence required for frontside ablation of the thickness of TP obtained from previous experiments [79]. This is the same depth as the Mansour α_{eff} uses, but is not the same as that obtained from the calculated α_{eff}.

In figure 3.4, the match of model fit (2) to the experimental data is in support of the common assumption that frontside ablation depths can be correlated to backside ablation depths [80, 147]. The fit of model (3) is harder to understand, but perhaps suggests that when the decomposition enthalpy is taken into account, the simple model for α_{eff} is valid at least in terms of energy generated. Nevertheless, the ablation depths per fluence are considerably smaller than the frontside experiment observations when a calculated α_{eff} is used. This will need to be investigated further once additional loss mechanisms are incorporated into the model.

The energy coupling efficiencies f for the model have also been calculated, according to equation 3.30. The results for the fitted velocities are shown in figure 3.5. These show very different shapes between the different applications of the model. All of them appear

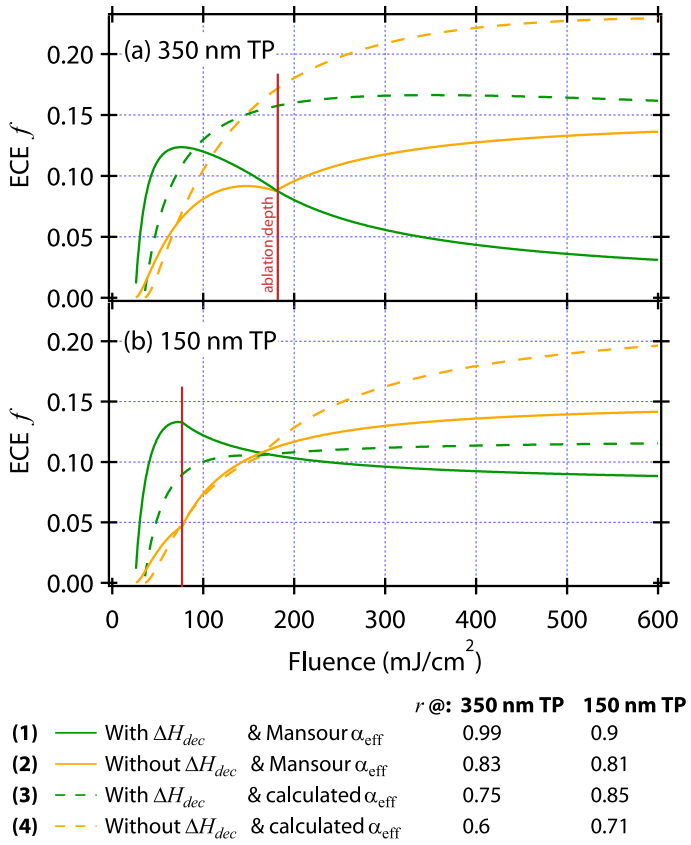

Figure 3.5 The energy coupling efficiences f of the model, as normalised in figure 3.4, for (a) 350 nm TP / 80 nm Al and (b) 150 nm TP / 80 nm Al. The fluences required for frontside ablation of the triazene thickness is again shown with a red line [79].

to move towards a horizontal asymptote at high fluences, but the inclusion of ΔH_{dec} (green curves) shows a faster increase in f (particularly when the higher r values are taken into account). This is presumably because more energy is produced for less TP ablation, meaning that the flyer is thicker, and greater kinetic energy is required to make the flyer reach the velocity experimentally observed for a lighter flyer. This is also the reason why the 150 nm DRL shows an intersection in f at $\sim$ 180mJ/cm^2, whereas the 350 nm DRL does not; 150 nm TP is completely ablated by $\sim$ 180mJ/cm^2 for all four different model fits, whereas the different model inputs ablate different thicknesses of the 350 nm DRL at $\sim$ 180mJ/cm^2 creating different masses of flyer. The empirically derived frontside ablation fits (labelled Mansour in the graph: (1) and (2)) show an interesting initial peak in f, because the Mansour α_{eff} has a lower effective absorption coefficient than the calculated α_{eff}. These curves show that altering the model slightly can have a large effect on the overall flyer velocity as a function of fluence.

Besides the shapes of the curves in figure 3.5, the absolute values of f are interesting. Because of the quality of the match of the model with the experimental data they give us an idea of what the experimental energy coupling efficiency is. About 10 % of the input

laser energy is converted into useful flyer kinetic energy. When gaseous kinetic energies are considered this increases to 15-20 %. The problem with this model is that the main loss mechanism is assumed to be uniform with fluence (reflectivity). The proportion of energy loss via ε_d *decreases* proportionally with fluence, whilst our observations indicate that proportion of loss should *increase*. Mechanical loss mechanisms are unlikely to increase with fluence, but thermal loss mechanisms are probably the most promising explanation. A good starting point will be to investigate thermal loss into the substrate, as has already been done for frontside ablation [77]. These loss mechanisms should be further investigated in detail in the future.

3.2.4 Flyer velocity model conclusions

The Gurney model provides a good base from which to model the LIFT process by giving a good physical description of the flyer velocities. It is only a starting point, and there are a number of areas for improvement, but the fit was very adequate both when 1) the effective absorption coefficient α_{eff} was fitted from frontside ablation data for the DRL, without the DRL decomposition enthalpy ΔH_{dec}, and 2) the effective absorption coefficient was calculated from more fundamental material properties, with an estimate for threshold fluence, and when the decomposition enthalpy of the TP was included.

A large proportion of energy is not accounted for in the model, and processes for energy loss other than reflection need to be investigated in closer detail. Thermal and mechanical losses are the main areas which should be looked at, with a particular emphasis on thermal heat loss into the substrate.

3.3 Pulse length effects[4]

3.3.1 Specific experimentals

The samples were composed of fused silica substrates spin-coated with a layer of TP. For backside ablation shadowgraphy only, 80nm Al was evaporated on top of the TP layer, and the triazene was ablated from the 'backside' through the fused silica substrate. Three different TP thicknesses were investigated for backside investigations: 350 nm, 150 nm, and 50 nm. For frontside ablation, the laser beam ablated the triazene from the 'frontside', directly at the air / TP interface. Various different TP thicknesses were used from 7 nm up to $\sim$ 450 nm for the frontside ablation studies.

For all the experiments in this section, a 500 μm square laser beam shape was used. The shadowgraphy took place as outlined in the experimental section 2.2.3. Frontside ablation was measured using a profilometer to give the ablation depth per pulse, otherwise known as the *ablation rate*.

[4]The experimental results within this section were published (in the proceedings to EMRS 2009, symposium Q) as reference [80].

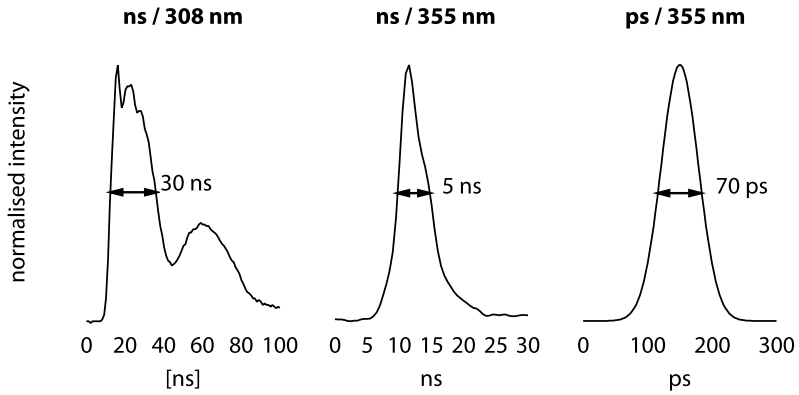

Figure 3.6 The temporal laser beam profiles of the three different lasers used for comparison of effect of different laser pulse lengths upon triazene polymer ablation.

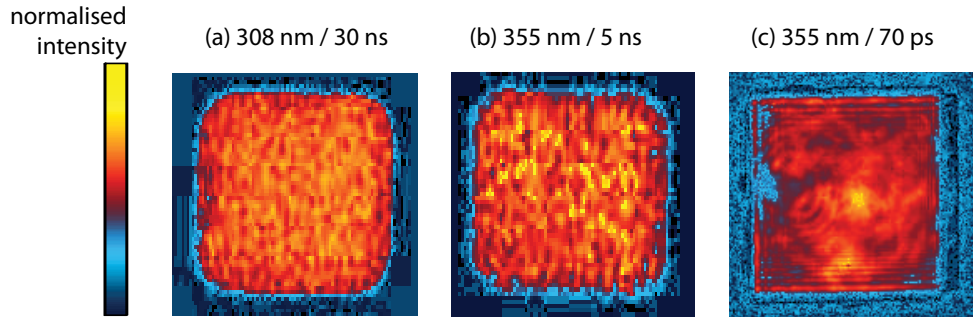

Figure 3.7 The laser beam energy profiles for mask-imaged beams of: (a) 308 nm / 30 ns XeCl excimer laser, (b) 355 nm / 5 ns Nd:YAG laser, and (c) 355 nm / 70 ps Nd:YAG laser. The masks have all been demagnified to give beam profiles $\sim 0.5 \times 0.5$ mm^2, but only (c) was taken in the image plane - (a) and (b) were obtained directly after the laser beam was masked, meaning that the profile is $\sim 2 \times 2$ mm^2. The energy profiles have been normalised.

Laser differences

Three different lasers were used in this study, all with different pulse lengths, as shown in figure 3.6. However, the lasers are not just different in terms of pulse length. They are also slightly different types of lasers and wavelengths. The normal laser used in the LIFT-based research of our group is the 308 nm XeCl laser with the 30 ns pulse length with two peaks in figure 3.6. The other two lasers used were both solid-state Nd:YAG lasers, using the 3rd harmonic which gives a wavelength of 355 nm. The whole beam is also spatially smaller, with more pronounced spatial beam energy homogeneity variation due to a Gaussian profile, than the 308 nm excimer laser. In addition, both the Nd:YAG lasers exhibit some hot and cold spots of beam energy, particularly the 70 ps laser as shown in figure 3.7c. The pulse length may be the main difference between the lasers, but these other differences need to be kept in mind.

3.3.2 Frontside ablation studies

Two outcomes of the frontside ablation studies are graphically depicted in figures 3.8 and 3.9: the ablation depth for a single pulse (known as the ablation rate) as a function of laser beam fluence (3.8), and the threshold fluence as a function of film thickness (3.9). In both graphs there are clear differences between all three lasers.

Figure 3.8 shows the ablation rate as a function of fluence, using ~ 420 nm TP films. The threshold fluence for 308 nm (~ 21 mJ/cm^2) irradiation appears lower than for both of the 355 nm lasers (~ 25-30 mJ/cm^2), but figure 3.9 shows that there is too much experimental scatter to conclude that the 308 nm ablation always has a lower threshold fluence. The 308 nm laser appears to ablate deeper craters than both of the 355 nm lasers for the fluence range of the graph. However, differences in the shapes of the curves suggest that the ns / 355 nm curve will intersect the ns / 308 nm curve long before the whole film is ablated. The ps / 355 nm curve appears to be asymptotically approaching an ablation depth far below the curves of the two nanosecond lasers. The shapes of the curves give the effective absorption coefficients by fitting them to a classical ablation equation modified for ablation from Lambert-Beer's law of absorption [157]:

$$d = \frac{1}{\alpha_{\text{eff}}} \ln\left(\frac{F}{F_{th}}\right) \tag{3.31}$$

where d is the ablation depth, F is the fluence, F_{th} is the threshold fluence, and α_{eff} is the effective absorption coefficient. The fits give a higher α_{eff} for the ps / 355 nm (~ $8.6 \cdot 10^4$ cm^{-1}) than the nanosecond / 355 nm (~ $6 \cdot 10^4$ cm^{-1}) laser. The ns / 308 nm laser has an effective absorption coefficient in between (~ $7 \cdot 10^4$ cm^{-1}). There is a possibility that these α_{eff} values for the nanosecond pulses are due to the difference between α_{lin} at the different wavelengths. However, a study into the ablation characteristics of different types of triazene polymer structures with different chromophore densities showed that the different TPs exhibited the same ablation rates despite having different α_{lin} [79].

The ps / 355 nm ablation rate is noticeably lower than both of the nanosecond lasers in figure 3.8. The increase in the effective absorption need only be linked to the shorter pulse length; a reduction in thermal diffusion may be one reason for this, but there are other explanations. The ps pulse time means that any movement of the solid-gas interface during the pulse length will be kept to a minimum by the kinetics of the ablation (which are generally sub-ns [75,76]) and this means that there will not be any extension of the optical penetration depth by the movement of this interface during the picosecond pulse. Another effect, which can occur at picosecond timescales, is two-photon and multiple-photon absorption, which would increase the effective absorption of the TP [158].

Figure 3.9 shows the increase in the threshold fluence F_{th} at low TP film thicknesses, and it is particularly in this that the lasers show significant differences. There may also be some variation in the thickness at which the onset of threshold fluence increase occurs. The

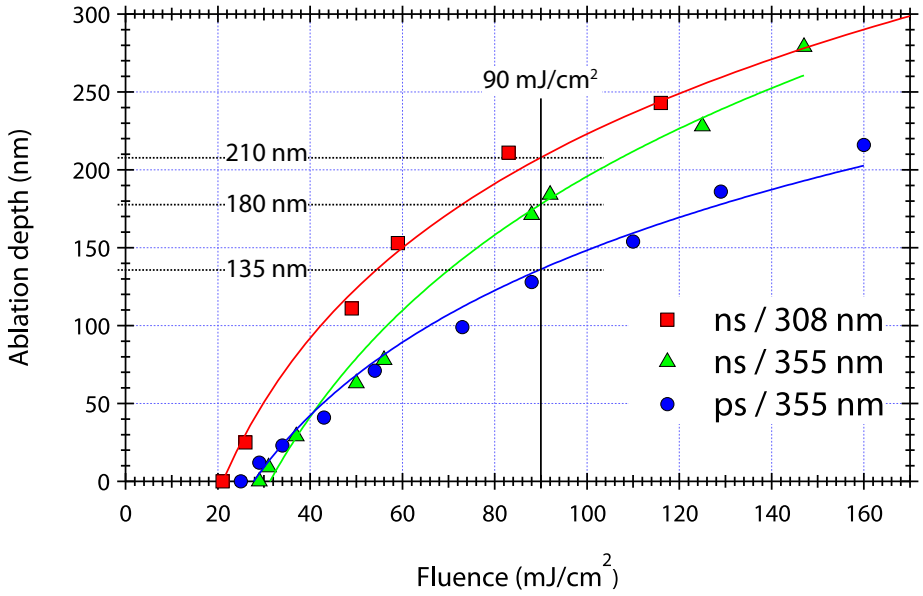

Figure 3.8 Ablation depth versus fluence for frontside ablation of 420 nm TP films. The error in measured ablation depth is about ± 5 nm, and the standard deviation in the measured fluence is between 3 and 5 %. The curves are fitted according to the empirical relation given in equation 3.31. The guidelines at 90 mJ/cm^2 are reference values for the ablation rates in 3.10

threshold fluences do not show much variation for films thicker than ∼ 100 nm, other than experimental scatter. While the instrumental error of the fluence is a maximum of ± 5 %, the error for the threshold fluence is likely to be larger, as that depends on additional factors such as the number of experimental data points used to calculate the threhold fluence, the range of the data, the reliability of all those fluences being accurate, and the quality of the equation used to fit the data points. Figure 3.8 gives an example as to how the threshold fluence is calculated by fitting the experimental points using equation 3.31. This uncertainty increases the threshold fluence error by ∼ 10 %. The spread in the film thickness measurements is up to 5 nm, so negligible at large thicknesses but more significant for the films below 100 nm.

Figure 3.9 shows that the threshold fluence of frontside ablation by the ps / 355 nm laser does not increase significantly for thinner TP films. However, F_{th} does increase significantly for frontside ablation by both nanosecond lasers. The 30 ns laser shows much larger F_{th} increase than the 5 ns laser for thin TP films. This gives a clear pulse length trend of increasing pulse length giving larger F_{th} when the TP film thickness is $< \sim 50$ nm.

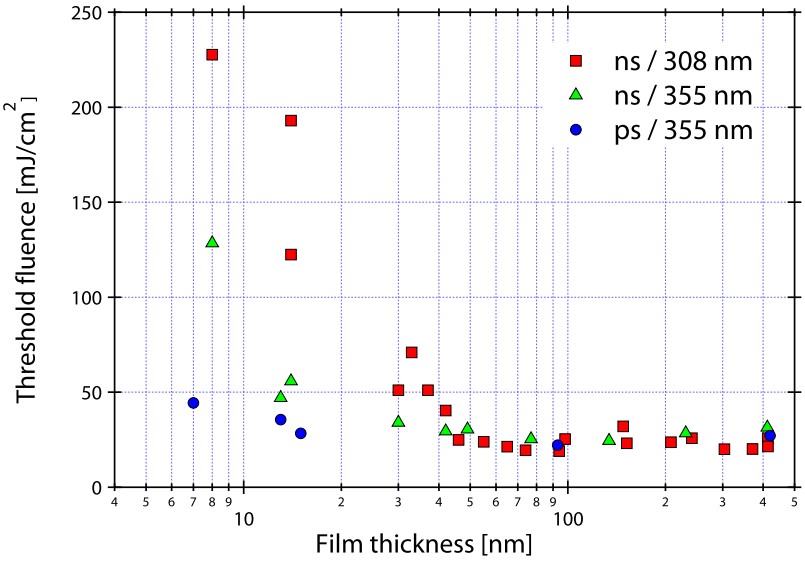

Figure 3.9 Threshold fluence for a single pulse as a function of TP film thickness. The error in the threshold fluence is that of the fluence ($\sim$ 5 %) plus the error from fitting a range of them (8-10 %), giving a total of $\sim$ 15 %. The film thickness variation is $\pm$ 5 nm.

3.3.3 Backside ablation and shadowgraphy

The flyers shown in figure 3.10 were produced by backside ablation of 350 nm TP / 80 nm Al at 90 mJ/cm^2 using the three different lasers. The clearest observation is that ps / 355 nm ablation generates faster flyers and shock waves than ablation by either of the two nanosecond lasers. The two nanosecond lasers have the same flyer and shock wave velocities as each other within experimental error. In addition, the flyer quality (i.e. its morphology, or state of consolidation) appears to worsen significantly as the pulse length decreases. However, this may be due to another factor: the laser beam spatial energy profiles in figure 3.7.

It is usually assumed that ablation rates measured by frontside ablation will be the same for backside ablation [159]. This means that the shock wave speed should be directly associated to the volume of TP ablated by frontside ablation. The ablation depth at 90 mJ/cm^2, for each laser, is marked on figure 3.8; this clearly shows that the picosecond pulse has a lower ablation rate, yet still propels the projectile at much greater velocity than the nanosecond pulses. A smaller volume of TP being ablated, yet with a greater build-up in gas pressure, means that the ablation products are smaller and have more kinetic energy. In addition to this, the increased pressure build up could be the result of a reduction in post-ablation energy losses in the ps / 355 nm ablation, such as gas leaks due to the speed of gas build up, or pre-ablation energy losses, such as thermal diffusion. These reductions in energy losses could be explained by the shorter pulse length shortening the timescale over which all energy losses can occur.

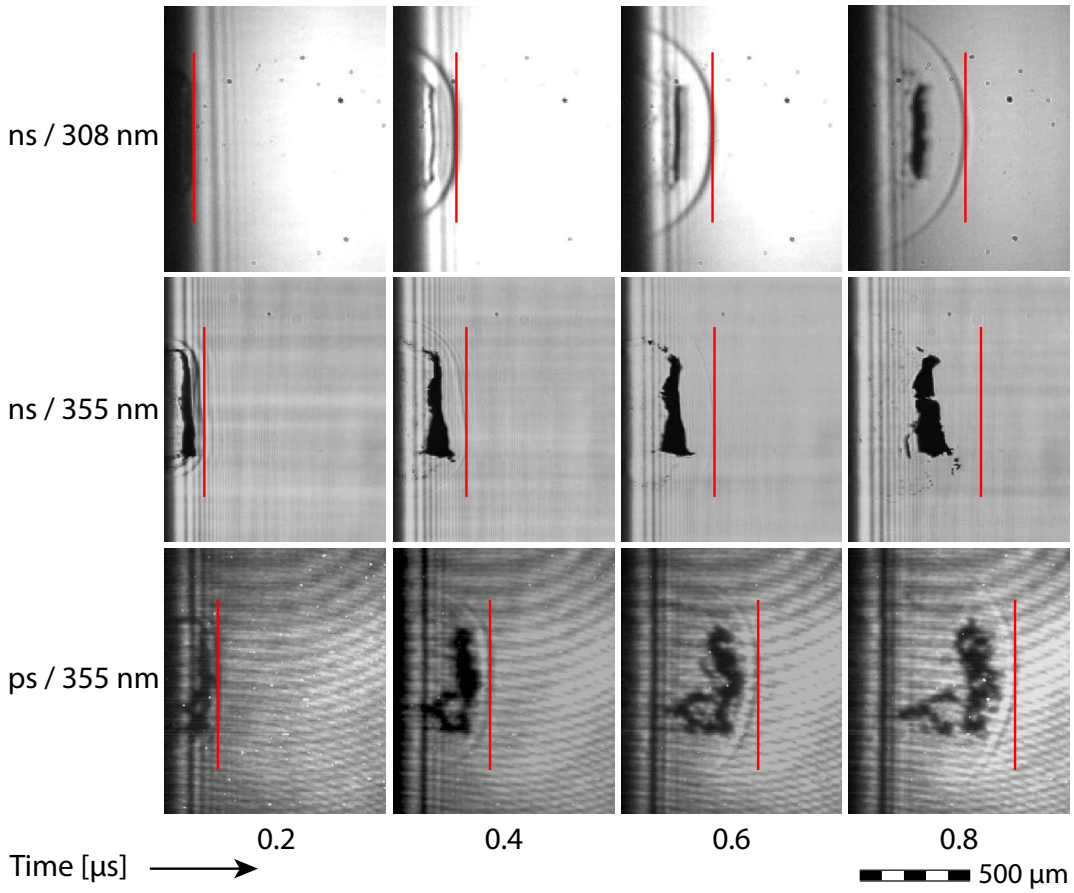

Figure 3.10 Time-resolved shadowgraphy images of backside ablation using samples comprising 350 nm TP coated with 80 nm Al, irradiated at 90mJ/cm^2. The line on each image highlights the shock wave position.

The velocity of the ps / 355 nm shock wave (above Mach 2), in figure 3.10, has been calculated to be about 30 % faster than the shock waves of the ns pulses, giving an increase in the shock wave kinetic energy of 70 %. So assuming all the energy derived from the laser at a fluence of 90 mJ/cm^2, this means that the proportion of total input energy in the shock wave increased from about $^1/_3$ for the 308 nm irradiation [84] to $^1/_2$ for picosecond 355 nm irradiation. This equates to a reduction in energy losses of at least 20 % of the input energy at 90 mJ/cm^2 for the 70 ps pulse when compared to the ns pulses.

The flyer quality decrease is likely to be the result of a combination of the poorer beam energy homogeneity of the Nd:YAG lasers compared with the excimer, and more explosive ablation at the picosecond pulse lengths. In addition to lacking any hot spots, unlike both of the Nd:YAG lasers, the flat-top nature of the excimer beam enables a more homogenous energy profile to be obtained than the Gaussian Nd:YAG beams. Due to the nature of the beam energy profiles the beam energy homogeneity can be seen as a major reason why the flyers are more fragmented with the Nd:YAG lasers, particularly with the picosecond laser, which was the least homogeneous.

The main hypothesis for the observed behaviour is based on heat loss. A previous study

by our group looked at how using substrates with different thermal conductivities affects the TP ablation characteristics. The higher the thermal conductivity, the more the heat loss for thin TP films, and the greater the threshold fluence. This was backed up by the thermal model in section 3.1, and the model is used here in section 3.3.4 to look at thermal diffusion as a function of pulse length.

3.3.4 Thermal modelling of different pulse lengths

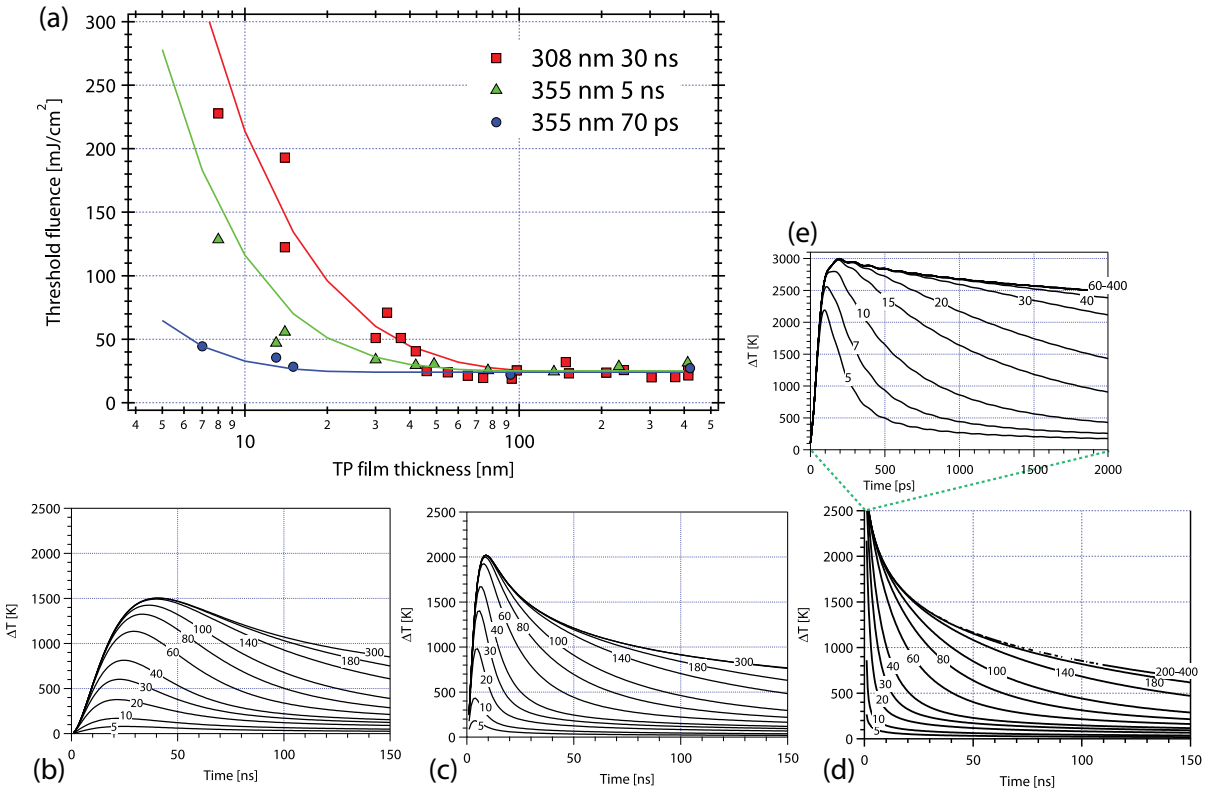

Figure 3.11 (a) shows fitting of the experimental points in figure 3.9 with the thermal model from section 3.1. The graphs in (b)-(e) show surface temperature profiles as a function of time for different TP film thicknesses, all for a fluence of 25 mJ/cm^2, assumed to be the threshold fluence for all of the lasers at larger TP film thicknesses. (b)-(d) show the profiles with the same axes for direct comparison, and (e) is a zoomed-in spectrum (over 2 ns rather than 150 ns) for the 70 ps laser.

Theoretical fits for the threshold fluence data, in figure 3.9, have been made using the model from section 3.1. Some of the input constants for the model have been taken from table 3.1 in section 3.1. In addition to those parameters and the FWHM pulse lengths in figure 3.6, the TP absorption coefficient α_{lin} at 355 nm is assumed to be 80 % of that at 308 nm (see the TP absorption spectrum in figure 1.10). This makes the 355 nm $\alpha_{\text{lin}} = 1.8 \cdot 10^5$ cm^{-1}.

The theoretical threshold fluence is obtained by finding the maximum temperature (T_{max}) at the threshold fluence (F_{th}) for a thick triazene DRL where there is no variation in threshold fluence due to the substrate, e.g. 300 nm. For all of the lasers this fluence is ~ 25 mJ/cm^2 (± 5 mJ/cm^2). From figures 3.11b-e, taken at the large thickness F_{th}, the effect of using thinner TP films can be seen. The threshold fluence is calculated by finding the time, t_{max}, where the temperature reached the maximum (equation 3.32), then solving the integration of the inverse Laplacian transform (equation 3.16) for the fluence, F.

$$T(F)|_{t=t_{max},z=0} = T_{max} \tag{3.32}$$

The solution of equation 3.32 gives the threshold temperature T_{max}, and this is solved for a variety of TP film thicknesses from 5 to 400 nm. The results are the fits to the experimental points in figure 3.11a. For the 30 ns / 308 nm laser system and the 70 ps / 355 nm the fit is as good as it could be, and only for the 5 ns / 355 nm is the fit slightly off. Even then, the curve shows the right qualitative path, and the result is possibly within the experimental error for these thin films.

These results again reaffirm that the thermal loss is a mechanism worth investigating further. Quantitatively, the model also provides good threshold results, but the actual temperature measurements show how the 'threshold' temperature T_{max} increases with shorter pulse lengths. However, as has been shown before with detailed ab-initio modelling, polymer ablation is ultimately a complicated thermo-mechanical process that ejects material, also dependent on the time that the high temperatures are maintained for [76].

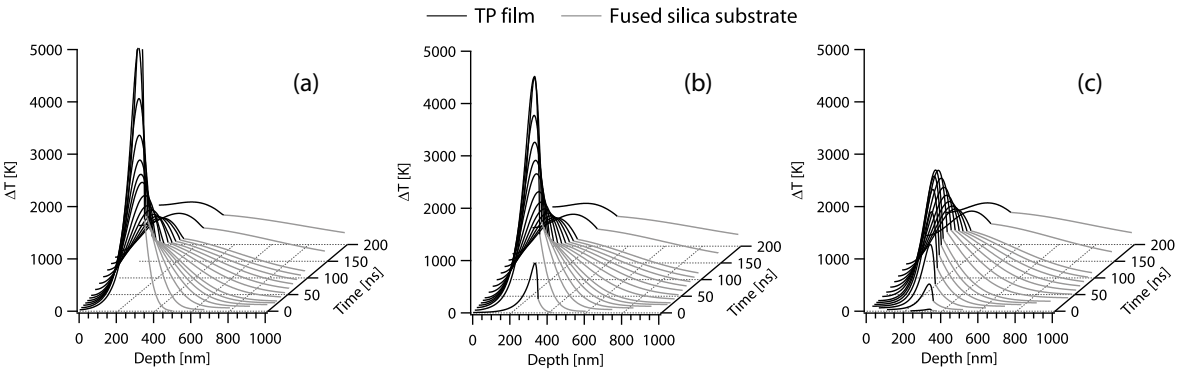

Figure 3.12 Thermal depth profiles through a 350 nm TP film and 650 nm of the fused silica substrate, for different times (up to 200 ns), using a 355 nm / 70 ps laser (a), a 355 nm / 5 ns laser, and a 308 nm / 30 ns laser.

In addition to modelling the frontside ablation, thermal profiles have been modelled of backside ablation by the different lasers. Figure 3.12 shows temperature profiles for 350 nm TP plotted on three axes: temperature (z), depth (x), and time (y). These graphs cannot be directly linked to experimental data, but they provide visualisation of how the

thermal energy theoretically varies with depth and time. The three plots are all done for the same laser fluence, so the obvious conclusion is that shorter pulse lengths create higher temperatures. However, other than the initial peak height the plots are remarkably similar for the three different lasers.

Figure 3.12 may not be validated on its own, but some further calculations give some interesting results. By integrating under the temperature profile curves, the proportion of thermal energy in the TP film and in the fused silica substrate can be calculated. Heat capacities and densities of 1100 J $Kg^{-1}K^{-1}$ and 1100 Kg/m^3 (*sic*) for the TP [77]; and 800 J $Kg^{-1}K^{-1}$ and 2200 $Kg/m^3$for the fused silica [160] were used for the conversion from the integrals under the profiles in figure 3.12 to 1-D J/m^2. The results are shown for both 350 nm TP and 150 nm TP in figure 3.13.

The proportion of heat loss into the fused silica substrate in figure 3.13 are very significant, but entirely time dependent. The first point is that there is no great variation in thermal loss between different pulse lengths, as a function of time. However, there is clearly greater heat loss for the 150 nm TP film than the 350 nm TP. This increased loss is due to the smaller volume of TP meaning that the total heat in the 150 nm film will always be smaller than the 350 nm film in equilibrium. This suggests that the time at which the 150 nm TP heat loss goes significantly above the 350 nm TP is already too long time-scale for ablation. Because photochemical ablation is a sub-ns process [75, 76], and shadowgraphic observations of backside ablation show ablation onset less than 100 ns after the laser pulse starts, only the heat loss during the laser pulse lengths is relevant for the nanosecond lasers, and the smallest time-step calculated for the 70 ps laser is the most relevant: 1 ns.

1 ns after the start of the laser pulse, the heat loss into the substrate for the 70 ps laser is 16 % (150 nm TP) and 15 % (350 nm TP). 5 ns after the start of the laser pulse, the heat loss into the substrate for the 5 ns laser is 21.5 % (150 nm TP) and 20 % (350 nm TP). 30 ns after the start of the laser pulse, the heat loss into the substrate for the 30 ns laser is 43.5 % (150 nm TP) and 42 % (350 nm TP). All of these values are high, but the 30 ns laser's thermal loss is particularly significant. The 30 ns values are good ball-park figures to account for the energy loss in the flyer velocity model, in section 3.2. In fact, the time required to account for all the flyer velocity model's un-accounted loss using this thermal model has been calculated in section's conclusion 3.2.4.

3.3.5 Pulse length conclusions

Laser pulse length has been shown to play a significant role in both the frontside ablation rates and the conversion of laser beam energy into kinetic energy of the flyer's from backside ablation. Shorter pulse lengths exhibit shallower ablation depths as a function of fluence. The threshold fluence for frontside ablation of TP films has been observed to increase dramatically for thinner films. With shorter pulse lengths this effect decreases.

There are two good explanations for this difference in ablation rate with pulse length. Firstly, the longer pulses have a higher ablation rate from thermal processes because there

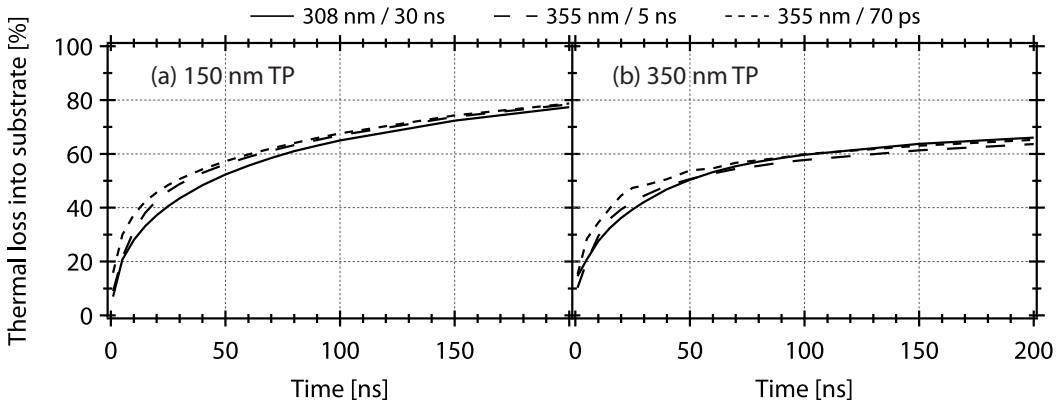

Figure 3.13 Backside ablation thermal loss into the substrate as a percentage of the total thermal energy in the film and substrate from the thermal model in section 3.1. The thermal loss percentage is shown up to 200 ns after the start of the laser pulse for the three different lasers, and for two different TP thicknesses, 150 nm (a) and 350 nm (b).

is larger 'thermal build up', i.e. the length of time that the TP experiences high temperatures, meaning that more decomposition reaction will happen due to Arrhenius kinetics. In addition, the thermal ablation will penetrate further into the film due to thermal diffusion. Secondly, the longer pulse lengths will mean that ablation will start during the pulse, making the gas (air or decomposition products) / TP interface move into the film, meaning that the laser beam will penetrate deeper into the TP later on during the laser pulse..

For shadowgrams of the three different lasers at the same fluence, in figure 3.10, the 70 ps laser showed a significantly faster flyer, but the two nanosecond laser pulses resulted in roughly the same velocity. Additionally, the 355 nm Nd:YAG lasers looked significantly less homogeneous, and more broken-up. This could be explained by the shorter laser pulses making the ablation more explosive, and less regular, but is better explained by the beam energy profiles, in figure 3.7. The Nd:YAG lasers, particularly the 70 ps /355 nm laser system, show large heterogeneity with pronounced hot- and cold-spots.

Finally, a thermal model of ablation has been applied to the frontside ablation to compare the experimental threshold fluences, as a function of TP film thickness, to a model for heat loss into the substrate. Good correlation between the model and experimental data has been obtained for threshold fluences, suggesting that heat loss into the substrate plays a significant part in the increase in the threshold fluence for thinner TP films.

In addition to the modelling of threshold fluences, temperature-depth profiles through TP films and the fused silica substrate have been obtained from the thermal model for various times after the laser pulse. From these profiles, the proportion of heat loss into the fused silica as a proportion of the total heat energy (the model assumes that there is no conversion of energy from heat). These plots show that the proportion of heat loss at any time after the beginning of the laser pulse is approximately the same for all three laser

pulse lengths.

3.4 Reduced pressure effects[5]

3.4.1 Specific experimentals

Backside ablation of TP / 80 nm Al films has been investigated. The TP was spin-coated onto the fused silica substrates to give three different thicknesses: 50 nm, 150 nm, and 350 nm. The aluminium was then evaporated on top of the TP. A gas chamber has been used to reach reduced pressures of $3 \cdot 10^{-2}$ mbar, and the shadowgraphy has been set up as outlined in the experimental section 2.2.

3.4.2 Time-resolved imaging

In figure 3.14 shadowgrams are shown from backside ablation at atmospheric pressure (top) and at reduced pressure (bottom). These pictures summarise the difference in flyer velocity at atmospheric pressure and reduced pressure well. Although the reduced pressure flyer is only slightly ahead of the atmospheric pressure flyer at 200 ns, it is over 3 times further away at 800 ns. This shows how much both the air resistance and energy loss into the acoustic shock wave slow down the flyer. For experimental flyer velocity data, the position of the flyer (relative to the substrate) is plotted as a function of time after the laser pulse. At reduced pressures there is no deceleration and so the points can be fitted linearly to give the velocity.

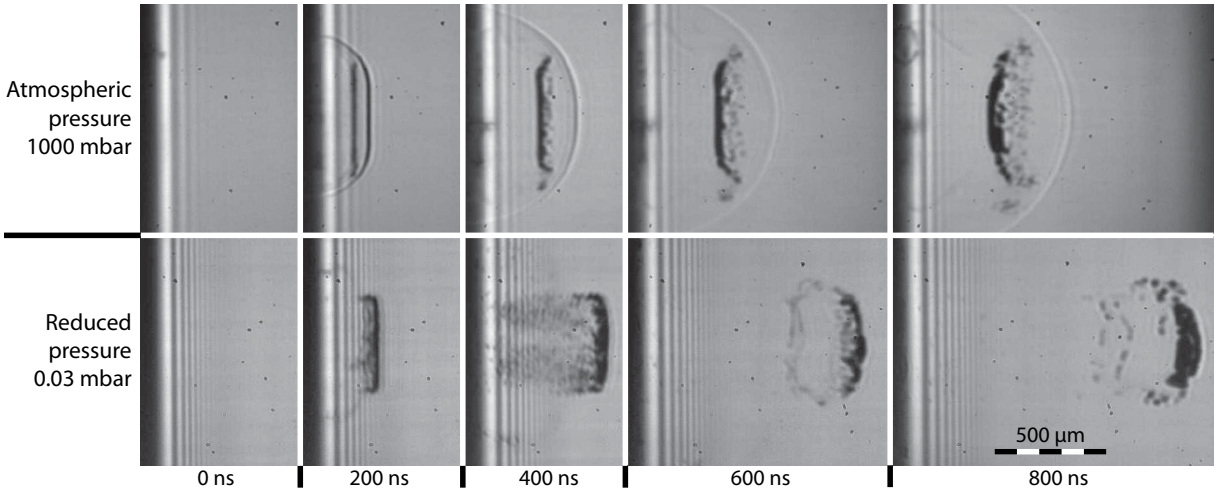

Figure 3.14 Shadowgrams of the backside ablation of 350 nm TP / 80 nm Al with a laser fluence of ~ 280 mJ/cm^2, at two different environmental pressures: 1000 mbar (top) and 0.03 mbar (bottom). The time after the laser pulse is given below in ns.

[5]Some shadowgraphy of flyers at reduced pressure results were published by Dr. Fardel in reference [152], but not the results present here.

The results of fitting many different shadowgram sequences are shown in figure 3.15 where the flyer velocity is plotted as a function of fluence. Data points for three different TP thicknesses shown: 50 nm, 150 nm, and 350 nm. These points obviously have a relatively large amount of error in them, roughly 10 % along the fluence (5 % jitter, plus another 5 % drift), and probably a maximum of 10 % in the velocity too. This obviously depends on the regression of each fit, and they could be calculated independently too. In section 3.2, the flyer velocity model has been fitted to the velocities in figure 3.15, with error bars included.

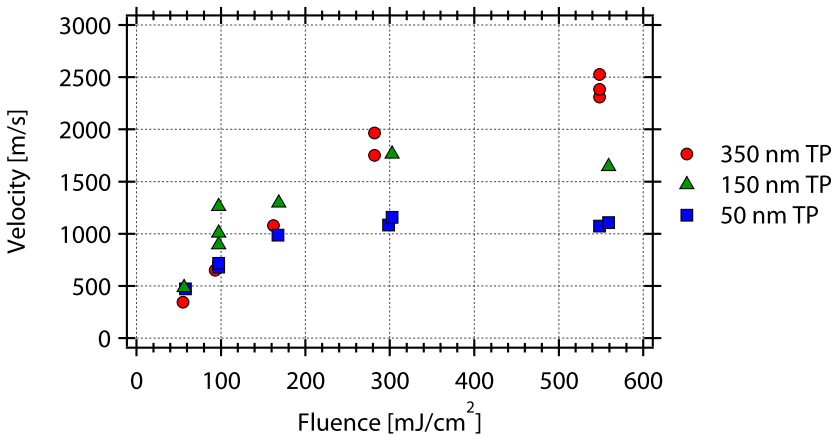

Figure 3.15 Velocities of the flyers for different laser fluences, at reduced pressure (0.03 mbar). The speeds are for flyers from backside ablation of TP / 80 nm Al, where the TP layer was 350 nm (red), 150 nm (green), and 50 nm (blue).

Previous work in our group has investigated the possibility of transferring metals across large gaps with LIFT, and to this purpose shadowgraphy experiments were carried out imaging the LIFT of aluminium and Al / MEH-PPV bilayers onto glass substrates across gaps of 0.5 and 1 mm [152]. The shock wave was observed to reflect off the receiver substrate and collide with the oncoming flyer. This caused the fragmentation of the flyer, as well as (in some cases) changing the flyer's momentum so it returned to the donor substrate instead of landing on the receiver. For this reason, reduced pressure experiments were carried out to observe the effect of removing the possibility for a strong gas acoustic shock wave. The results obtained in this section come from the same experiments.

The earlier investigation observed that the reduction of the atmospheric pressure removed the destructive effect of the shock wave, but raised new problems of high-speed impact collisions between the flyer and the receiver substrate. However, these transfer experiments were not optimised, as the results in section 4.2 highlight. Nevertheless, the large gaps used probably mean that any transfers in good fluence window highlighted in chapter 4 of this thesis ($\sim$ 60-140 mJ/cm^2) will create folded pixels with large gaps of 0.5-1 mm.

3.5 Silicon-substrate thermal ablation[6]

The ablation of the triazene polymer was studied using visible, 532 nm laser light (2nd harmonic of Nd:YAG laser), $\tau = 5$ ns. This work was motivated by the fundamental processes of material ejection by laser-induced thermal ablation from the University of Konstanz [148, 149]. This topic was complimentary to this thesis because it investigates a purely thermal ablation process, as well as investigating much slower material ejection than normal LIFT. The experimental apparatus used in these experiments is explained in the experimental section 2.2.6

3.5.1 Reflectometry

The ejection and dynamics of triazene polymer layers in the thickness range of 40 nm to 600 nm upon nanosecond laser ablation at a wavelength of 532 nm were investigated. The ablation is due to laser-induced thermal degradation of a small part of the polymer in contact with the silicon substrate. The subsequent dynamics of the flying polymer layer are measured with sub-nanosecond time resolution. The evaluation of the initial velocity for different film thicknesses gives insight into the energy transfer process during the acceleration of the films.

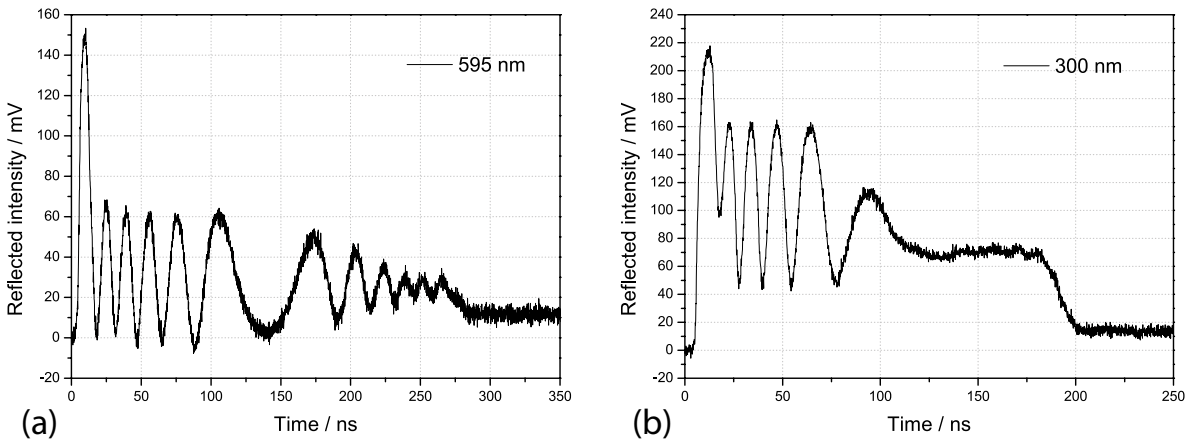

Figure 3.16 Reflected intensity of 300 nm (a), and 595 nm (b) thick triazene layer flying from a silicon substrate after laser ablation.

Typical signals of the fast reflectometer for the ablation of the triazene polymer with two different layer thicknesses are shown in figure 3.16. The incident energy density is about 30 % above the melting threshold of silicon. The first dominant peak is therefore due to the enhanced reflectivity of molten silicon [162]. The re-solidification takes place on the order of ten nanoseconds. The signal of the triazene flyer in this time period is not substantially

[6]The reflectometry studies were undertaken with Pascal Frank in Professor Paul Leiderer's group at Konstanz. The results presented here were published in [161].

disturbed. The signal of a 595 nm thick TP film, in figure 3.16a, shows oscillations in the reflected intensity which slow down at about 150 ns. The oscillations then speed up again and after 290 ns the signal drops back to a constant value. The signal for the thinner film (300 nm, figure 3.16b) starts qualitatively similar, but lacks pronounced features past 100 ns. It drops back to a near initial value after 200 ns. The descent is smeared out over 20 ns.

The signals in figure 3.16 are from the flight of the TP layer after ablation both away from and back to the silicon substrate. The laser pulse heats the silicon substrate well above the thermal degradation temperature of the TP, which starts at 500 K for quasi-static heating [99]. The threshold fluence for TP ablation at the used laser parameters is around 70 % of the melting threshold of silicon. In comparison with the melting temperature of silicon (1685 K), the actual ablation temperature is in the order of reported values with comparable laser pulse length (see figure 3.11 in section 3.3.4 where the threshold temperature for the 5 ns laser was $\sim$ 2000 K). The heat then diffuses into the first few nanometers of the polymer, which then degrade and form a layer of the degradation products of the polymer. Since most of these products are gaseous, this layer is at elevated pressure [145]. The overlying polymer layer is therefore accelerated from the substrate. The reaction kinetics of the degradation process taking place at the very beginning of the flight is too fast to be resolved with the experimental setup. In addition, it is obscured by the prominent signal of the melting silicon. The interference of the reflections of the detecting laser beam from the moving TP layer and the silicon substrate is used to detect the distance between the layer and the substrate. Figure 3.17 shows the calculated reflectivity of a multilayer system consisting of a TP layer of given thickness, a gaseous layer of variable thickness and the silicon substrate. By comparing the calculated values to the experimental signals it is feasible to get access to the full information on the trajectory of the flight of the layer.

Thus the varying oscillation frequency of the signals in figure 3.16a can be explained. As the period decreases, the flyer slows down with increasing distance to the silicon substrates. It stops at 150 ns, which corresponds to a distance of 2.1 μm, and the flyer returns to the substrate afterwards. This could be due to gravity, or the elastic restoration forces at the edge of the spot. In addition, because the experiments are done under ambient conditions, the kinetic energy of the flyer is at its maximum after leaving the substrate, which is then transformed into potential energy because of a pressure difference, as the pressure underneath the films drops below the ambient value. This accelerates the film back towards the substrate. The return is only possible, if the pressure difference can build up and is not diminished by gas flow through holes or from the surrounding. It would not be observable if the film broke up into small fragments. The minimal lateral dimension of such fragments is determined by the speed of the gas, flowing around the edges of the fragments. Assuming this will not be faster than the speed of sound, the minimal value is a few 100 micron.

However, different fragment sizes within the focal spot of the detecting laser (about

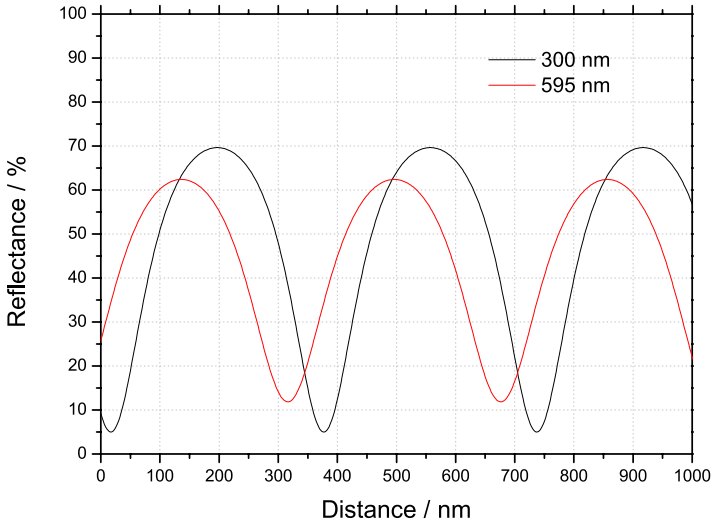

Figure 3.17 Calculated reflectance of the system consisting of a TP layer of given thickness, a gaseous layer of variable thickness and the silicon substrate.

200 micron) will lead to velocity differences. These result in a distance inaccuracy which smears out the distinct interference of the reflected beams. This could be the reason for the fading of the signal intensity on both signals, which is however very prominent at the data of the 300 nm thick TP layer in figure 3.16b. A lateral displacement of around 150 nm leads to almost completely different signal information, so only weak interference is observable. The return of the different fragments to the silicon substrate is therefore not simultaneous, but staggered.

The considerations about the flight trajectory due to the pressure differences are analogous to a detailed model in [148], which describes the flight of *fluid* films. The model is based on the assumption that the potential energy, which is kept in the gas cushion with elevated pressure after the degradation, is transformed into kinetic energy of the film. After a certain distance (a couple of 100 nm, depending on the generated pressure and the amount of transformed material) the pressure equals ambient pressure. At this point, 30 to 50 ns after the lift-off of the layer, all energy is transferred into kinetic energy. Subsequently the pressure underneath the film drops below values of the pressure above it, which is nearly constant at ambient pressure since the velocity of the flyer is distinctly below the velocity of sound in air. The initial velocities are extracted for TP layers in the thickness range between 40 nm and 600 nm, and are shown in figure 3.18. Figure 3.18a shows the data as function of the incident laser energy.

The velocity increases by less than 15 % when the incident energy is doubled. A close consideration of the energy dependence would have to be based on the dissipated energy, which is depending on the temperature of the substrate and the actual ablation time after the onset of the laser pulse. This demands an accurate temperature simulation and measurement of the ablation time in the sub-nanosecond regime, as the heating rate during the

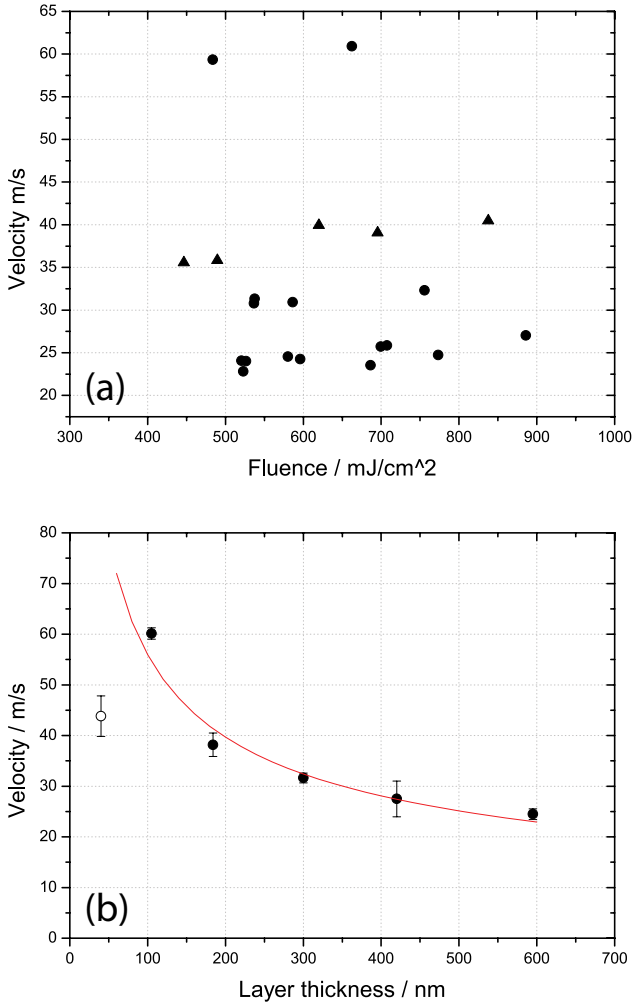

Figure 3.18 (a) shows the maximal velocity of TP layers with thicknesses between 105 nm and 595 nm depending on the incident laser fluence. The triangles mark the velocities of 184 nm thick films. The velocity of 40 nm to 595 nm thick TP films are shown in (b). The red line indicates a power law fit to the filled data points with exponent $m = -0.5$.

laser pulse is very high. As most of the measurements are done above the silicon melting threshold, the determination of the ablation time is not feasible. It is nevertheless obvious that the dependence of the velocity on the TP layer thickness is significant (see figure 3.18b). The velocity is about 60 m/s for thin (105 nm) layers and decreases to 25 m/s for thicker (595 nm) layers. The value for the thinnest examined films (40 nm) contradicts this trend, but the signals of these films do not display well-defined characteristics. The ablation of these thin films is most probably not homogeneous and a rupture of these films is likely to occur. Thus the pressure is not completely transferred into kinetic energy.

The kinetic energy E depends on the velocity v, on the layer thickness d and the density ρ. Per unit area it is: $E = \frac{1}{2}\rho d v^2$. Hence constant kinetic energy leads to $v \propto d^{-0.5}$. This dependence is indicated in figure 3.18b by the red line which fits the data for films thicker

than 100 nm. The kinetic energy of the different films is almost equal. The assumption of a thickness-independent transfer process of energy is therefore justified. Assuming that the kinetic energy is uniform, the thickness of ablated triazene can be calculated by plotting $1/v^2$ vs d and looking at the x-intercept. The x-intercept is 39 nm, but there is far too much uncertainty due to the lack of data points, with a linear regression showing that the standard deviation is 36 nm.

3.5.2 Thermal ablation conclusions

The flight of thin layers of triazene polymers has been investigated after laser-induced ablation from a silicon substrate. Under sufficiently homogeneous conditions, the layers return to the substrate after some hundred nanoseconds. The maximum distance of the flyers to the substrate is in the range of a few microns. The initial velocity of the films, extracted from the trajectories, determines their maximum kinetic energy. In comparison to previous studies on different materials, namely liquid isopropanol and solid microporous CO_2 layers [149], the TP shows a thickness-independent kinetic energy as seen for fluid films. The CO_2 films reveal an additional dissipation mechanism, which is due to its porosity, but not understood in detail yet. The TP films are solid, too, but have a porosity which is at least one order of magnitude less than the CO_2 films. Hence their behaviour is directly comparable to that of the intact liquid isopropanol films. The considerations of the flight of thin polymer films therefore contribute substantially to the general understanding of the flight of thin films after laser ablation.

Chapter 4

Optimisation of the laser-induced forward transfer conditions

4.1 Fabrication of MEH-PPV pixels at atmospheric pressure[1]

4.1.1 Specific experimentals

Most of the sample details are outlined in section 5.1.1. The donor substrate were 150 nm TP / 80 nm Al / light-emitting polymer (LEP) ($\sim$ 70 nm). The LEP was either plain MEH-PPV, MEH-PPV:PEO blend, or MEH-PPV / PEO bilayer. The receiver substrates were either plain 140 nm ITO, ITO / 20 nm PEDOT:PSS, or ITO / 50 nm PEDOT:PSS.

The LIFT process is summarised in figure 4.1. The LIFT donor and receiver substrates were pressed together without a gap using spring-loaded ball-bearing screws with even pressures, applied to the four corners of the donor substrate (in a $\sim$ 23 mm square). This meant the transfer was done 'in contact', and in ambient conditions (i.e. atmospheric pressure as opposed to the reduced pressures used in the following sections). Because the samples were 'in contact' there are a couple of difficulties: firstly, the gap between the substrates is not known and therefore hard to control, and separation of the substrates can be difficult if the pixel is partly adhered to both substrates (see previous work in references [118, 152]).

4.1.2 Effect of receiver substrate

LIFT was carried out to fabricate three different types of PLED pixels, both with and without a PEDOT:PSS HTL coated on top of an ITO receiver substrate. As a function of fluence, microscopy images of the transferred blend pixels are shown in figure 4.2 for a plain ITO receiver substrate, ITO coated with a 50 nm film of PEDOT:PSS and ITO coated with 20

[1] The data from this section was published as part of [153].

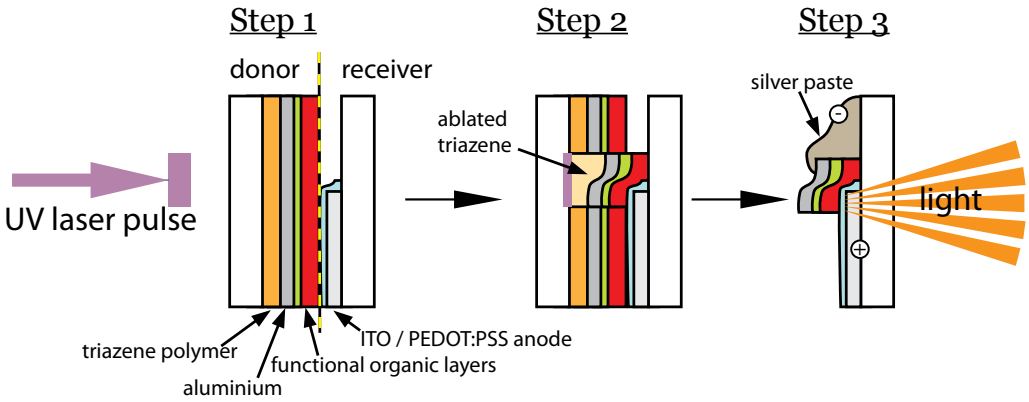

Figure 4.1 A schematic diagram of the LIFT process used for the MEH-PPV transfers in three steps: Step 1 shows the prepared substrate architectures – the dashed line separates the donor substrate from the receiver substrate; Step 2 shows the transfer process as the pressure build up from the gaseous products of triazene ablation push the overlying layers onto the receiver substrate; Step 3 shows the receiver substrate after the donor substrate has been taken away and a bias is applied across the pixel for light emission.

nm of PEDOT:PSS. The pattern observed for this blend PLED transfer stack was the same for single-layer and the bilayer pixels. The difference between plain ITO and ITO with a PEDOT:PSS coating is quite stark; the addition of PEDOT:PSS clearly reduces the fluence required for a successful transfer. Transfer onto a plain ITO receiver substrate was optimal at 200-300 mJ/cm^2 whereas transfer onto a bilayer ITO / PEDOT:PSS receiver substrate is achieved at only 70-100 mJ/cm^2. This is a distinct advantage for transfer quality because a lower fluence means less energy entering the system, and therefore a lower chance of damaging the sensitive transfer materials, in other words, a *softer* transfer. This was observed for all pixel PLED architectures. From figure 4.2 it can also be seen that at the fluence for the best transfer onto plain ITO (200-300 mJ/cm^2) there is also a slight improvement in transfer onto ITO / PEDOT:PSS. This looks like a second applicable fluence regime for transfer, and pixels LIFTed[2] at this fluence onto a plain ITO receiver substrate have been analysed in section 5.1, in figure 5.4 in particular.

Successful transfer onto PEDOT:PSS in the low fluence regime occurs at the lowest fluences at which complete delamination is achieved, giving a very soft transfer. For transfer onto ITO, the lack of success at low fluences is best explained by a lack of interfacial adhesion between the ITO and the MEH-PPV. Pixels were occasionally transferred onto plain ITO at low fluences, but they appeared to be very poorly stuck to the ITO surface. Successful

[2] *LIFTed* is used here as a verb, as in 'transferred by LIFT'. Throughout this work, *LIFTed* is used extensively as an adjective to describe the fabrication method of an OLED pixel, i.e. that it is fabricated by LIFT as opposed to the *conventional devices* fabricated using conventional methods, see the beginning of chapter 5 for more information.

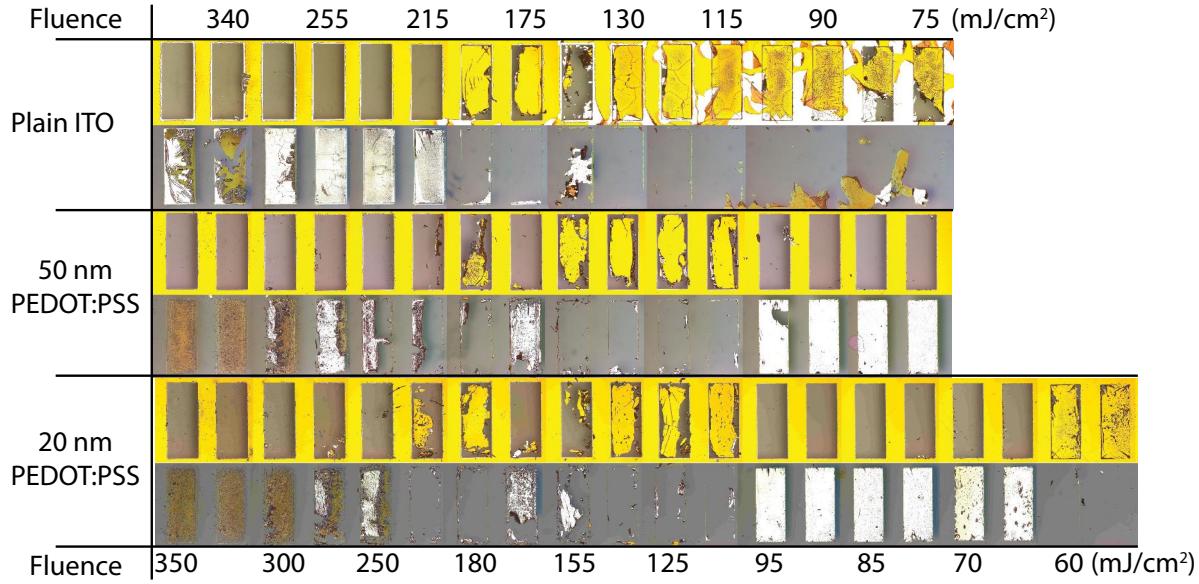

Figure 4.2 Matrix of transferred MEH-PPV:PEO / Al with 150 nm triazene polymer for decreasing fluence (from left to right). The top line for each different sample is the LIFT donor substrate, and the bottom line is the receiver substrate, viewed from above (so the aluminium is on top).

LIFT onto plain ITO in the high fluence regime appears to have an upper limit at the fluence where the flyer begins to break up, either due to the thermal load from the laser or because of the impact with the receiver substrate.

At fluences between 100 and 200 mJ/cm^2 for all three types of receiver substrates, there is poor or no transfer of the pixel, and the flyer is often returned to the donor substrate, see the donor substrates in figure 4.2. The flyer appears to have delaminated from the rest of the donor substrate, but is somehow still where it began. Whether this feature is due to the shock wave accompanying the laser ablation is under investigation [84, 152]. The fact that there is almost no difference in transfer quality as a function of fluence between the thick (50 nm) and thin (20 nm) PEDOT:PSS receiver substrates, suggests that the main benefit of PEDOT:PSS in comparison with plain ITO, is the stronger attractive surface force interactions with the transferred flyer that make the PEDOT:PSS 'stickier' than plain ITO. The main barrier to transfer must be some sort of force opposing motion. At present we are investigating whether this is mainly due to the collision with the receiver substrate, or the reflected shock wave generated ahead of the flyer (which may pass through the air or, as they are in contact, through the receiver material).

4.1.3 Reproducibility

It was mentioned in the introduction section 1.3.2 that previous successful studies into LIFT had also exhibited unreliability in terms of successful transfer. These led our group

to implement more rigorous cleaning procedures outlined in the experimental section 2.1, but there are still many possibilities for contamination of the sample, particularly with the transfer between Empa in Dübendorf, and PSI, near Villigen. A new sample transporter was developed along with a number of sample holders to try to counter this, as outlined in experimental section 2.1.4. However, an improvement in reliability was not obvious and, if anything, poorer reproducibility was observed.

4.1.4 Conclusions from MEH-PPV pixel fabrication

The main conclusion from these LIFT experiments with MEH-PPV are that the transfer quality can depend significantly on the receiver material. The effect of the receiver substrate has again been looked at with a variable gap between the substrates in section 4.2.3, where the addition of PFO onto the receiver substrate has improved transfer onto plain PEDOT:PSS. These results suggests that the interfacial forces are vital, highlighting the similarity between LIFT and LITI as it was outlined in figure 1.13 in the introduction section 1.3. Work on LITI has investigated altering the polarity of the receiver substrate surface, a PEDOT film, by doping the PEDOT with an organic material to change the water wetting angle [123]. Detailed investigations into the polarity of the ITO and PEDOT:PSS surfaces have not been made here, particularly since the next step involved an optimisation which took the focus away from the interfacial adhesion between the flyer and the receiver (except for the PFO gap results). Nevertheless, this should be investigated as these results suggest that the interfacial adhesion is important, but this must be separated from other possible explanations such as damping of the shock wave or the flyer upon impact by the addition of the polymeric PEDOT:PSS layer.

4.2 LIFT gap and pressure optimisation[3]

4.2.1 Specific experimentals

These experiments summarise the optimisation of the LIFT process by adding in a controlled gap and reducing the environmental pressure. Various thin-film architectures have been used for the donor substrate, but the receiver substrate has been kept constant as glass / 60 nm PEDOT:PSS, following the conclusions from the previous section 4.1. After the success with MEH-PPV, LIFT attempts were made using the same basic donor substrate architecture, 150 nm TP / 80 nm Al / $\sim$ 70 nm light-emitting layer. However with a PFO or an Alq_3 light-emitting layer the attempts were fruitless. For this reason it was concluded that the process needed to be optimised. As well as the gap and pressure, the cathode was considered and due to it's favourable evaporation properties (allowing the deposition of thicker layer) silver was chosen over aluminium.

[3]The results from this section has been published in reference [163].

The donor substrate used in this section had differing thicknesses of TP (depending on the experiment), although the most common thickness was ∼ 190 nm TP. The next layer is invariably silver, although the thickness is either 200 nm (for the earliest experiments), 150 nm or 80 nm. In each section it is explained what thickness is used. The organic layer is either small molecule Alq_3 or polymeric PFO. Alq_3 and PFO were used because both were thought to represent a step up from MEH-PPV, although transfer at the same conditions as MEH-PPV in the previous section proved impossible.

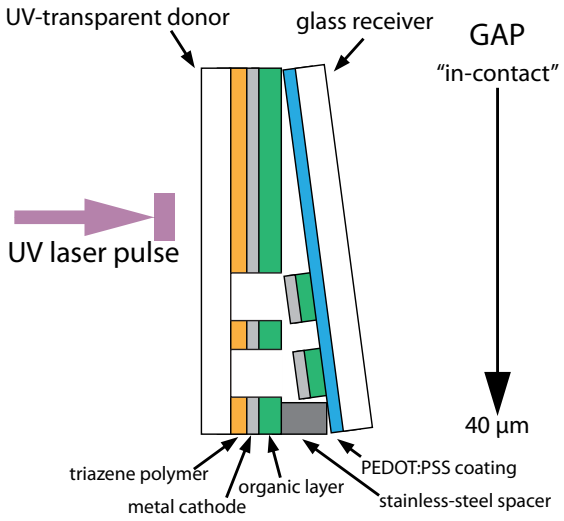

Figure 4.3 A schematic showing how the substrate-substrate gap width was varied linearly across the sample. The idea was based on a paper by Banks et al. [164].

LIFT was undertaken in much the same way as the previous section 4.1, but a controlled gap was inserted along with a reduction in pressure from section 4.2.4 onwards. A variation in gap width across the sample was achieved by adding the spacer at one side, as shown in figure 2.7. However, because of the limitations of the size of the light beam for the absorption spectrometer, measurements of the gap width along the gradient could not be made. The gap width can only be measured for a constant gap width. To measure the variation in gap width in figure 4.3 the gap was measured with the spacer in and then an assumption of a linear gap gradient is made between the spacer and the 'in contact' edge. In atmospheric pressure, the spacer used was 40 μm, and measurements were taken across the whole sample. Because of the travel-distance limitations of the piezoelectric stage in the gas chamber (∼ 7 mm maximum), a 100 μm spacer was used, and the measurements started $3/5^{\text{th}}$ of the way across the sample from the spacer.

4.2.2 Effect of adding a gap

As mentioned in the experimental section, there is a dual leap in materials used from the MEH-PPV transfers in section 4.1 in terms of both the organic layer and the metal cathode

layer. At first, only the organic material was changed in an attempt to make Alq_3 and PFO OLEDs in the same way as the MEH-PPV pixels. However, we were met with no success and so a process of optimisation was embarked upon, as outlined in this section. As well as the gap and pressure, the cathode thickness was investigated. And for this reason, silver has replaced the aluminium because of its superior evaporation qualities, as well as its similarity with MEH-PPV in terms of general physical and electrical properties. The initial transfers in atmospheric pressures were done using donor substrates with a thick (200 nm) Ag layer. The main advantage of using a thicker layer was to prevent the flyer from fragmenting, which it does fairly easily at atmospheric pressure. The triazene DRL thickness was constant at 190 nm ± 10 nm for these experiments. The setup yielded a matrix of attempted transfers with decreasing gap, from left to right, and increasing fluence, down the sample.

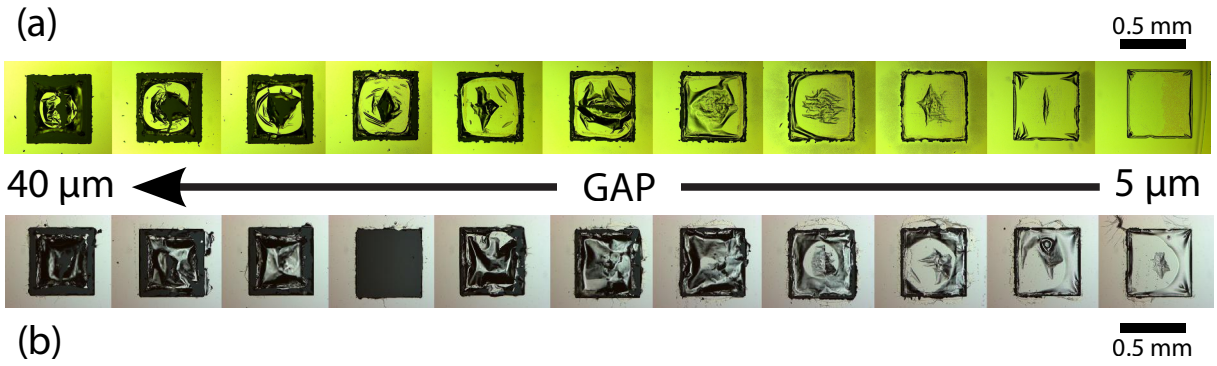

Figure 4.4 Light micrographs of the donor substrates consisting of fused silica / 190 nm TP / 200 nm Ag / (a) 80 nm Alq_3, or (b) 80 nm PFO. The flyers are in the middle of the ablation spot after backside ablation with a fluence of 70 mJ/cm^2, with a linearly varying gap to the receiver substrate (glass / 30 nm PEDOT:PSS).

The transfer material will be referred to as a flyer when it is still on the donor substrate, and a pixel when it is deposited on the receiver substrate. It must be emphasised that for both Alq_3- and PFO-coated donor substrates the threshold fluence for ejection without a receiver substrate is around 50 mJ/cm^2. Attempted transfers of Alq_3 onto a receiver substrate resulted in almost no pixel deposition. The donor substrate for Alq_3 is shown in figure 4.4a, for ablation at a fluence of 70 mJ/cm^2, with the gap increasing from right to left. As the gap increases, the size of the flyer starts to shrink, and a hole also appears in the middle. The hole only really starts at a minimum gap distance of $\sim$ 20 μm, at about the same time as the flyer starts to get noticeably smaller. It appears that the flyer is smaller at larger gap distances because the edges fold up, particularly in the corners.

Except for the organic layer material, figure 4.4b (PFO) shows the same donor substrate as figure 4.4a (Alq_3). PFO shows a similar trend to that observed for Alq_3, but there is less clearly defined flyer contact with the donor substrate. For the flyers between 5 and 20 μm gap the trend looks very similar, but above 20 μm the flyers appear more distorted.

Overall, the area in contact with the donor substrate is less clear for PFO than for Alq_3, and the edges are not folded in the same uniform fashion as for Alq_3. For the fourth ablation crater from the left, at a gap width of 25-30 μm, the flyer is not present, indicating that a pixel has been deposited on the receiver substrate, which has indeed been observed (see figure 4.5, pixel circled in red).

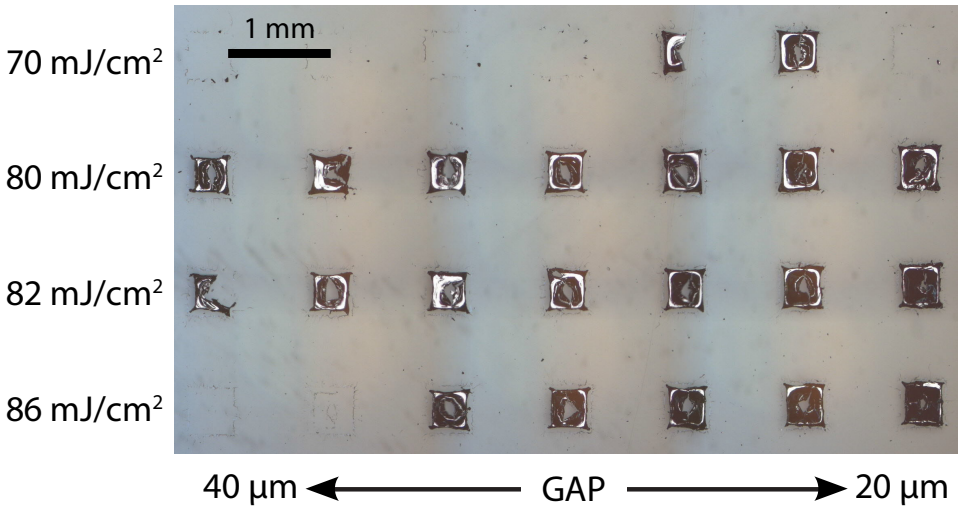

Figure 4.5 Micrographs of the receiver substrate for the 190 nm TP / 200 nm Ag / 80 nm PFO donor substrate where transfer was achieved, but of non-functional pixels. A distinctive *doughnut* shape to the transferred pixels can be observed. The edges of the pixel, and the hole in the middle, are in contact with the substrate.

Figure 4.5 shows the receiver substrate with pixels transferred from the 200 nm Ag / 80 nm PFO donor substrate from figure 4.4b. The corresponding Ag / Alq_3 pixels were not transferred as successfully. The transferred Ag / PFO pixels clearly have a hole in the middle of them, and have a shape akin to a holed *doughnut*. At fluences greater than 86 mJ/cm^2, no pixel transfer was observed. The optimal fluence is around 80 mJ/cm^2.

4.2.3 Effect of putting an organic layer on the receiver substrate

In section 4.1, it was observed that the receiver substrate can play a significant role in the transfer. This particular observation suggests that the interfacial adhesion between the flyer and the receiver substrate is particularly important, although other interpretations such. Following on from these observations, in this study the receiver substrate has been modified by adding the organic material that's being transferred from the donor substrate (PFO in figure 4.6), onto the receiver substrate. For Alq_3, this proved to make very little difference, but the observations for PFO were interesting.

Figures 4.6a & b show two different receiver substrates for the same PFO donor substrate. Figure 4.6a is an ordinary glass / PEDOT:PSS receiver substrate with the red rectangle corresponding approximately to the same fluence and gap window as figure 4.5. Figure

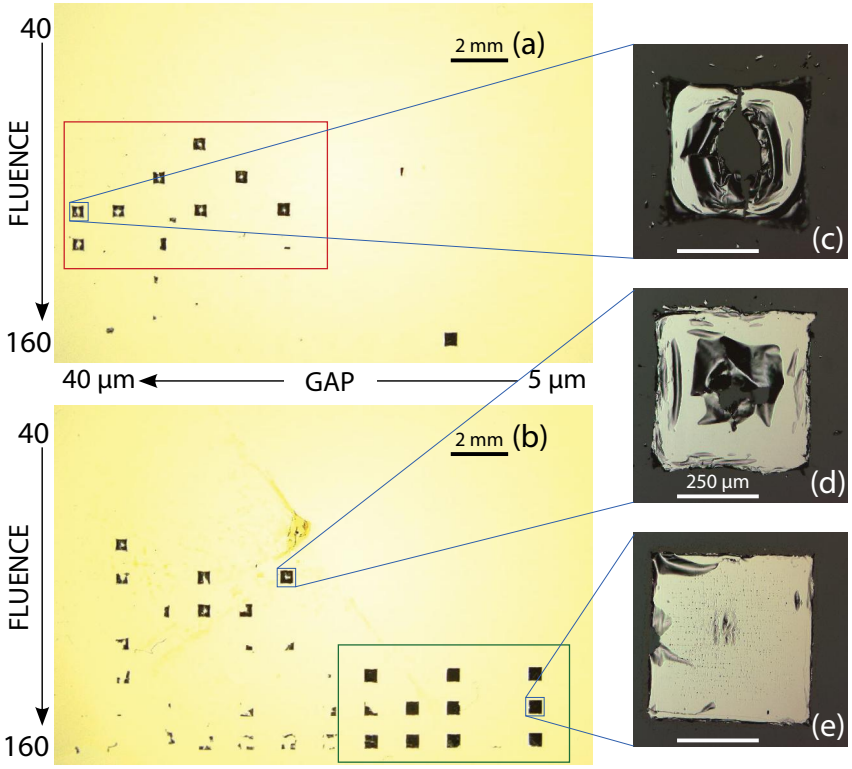

Figure 4.6 Micrographs of receiver substrates of PFO transfers, back-illuminated. The donor substrate for both was: 190 nm TP / 150 nm Ag / 80 nm PFO. (a) is an ordinary receiver substrate, glass coated with 30 nm PEDOT:PSS, and (b) is the same as (a), but with 80 nm PFO spin-coated onto the PEDOT:PSS. Fluences are in mJ/cm^2. Close-up micrographs of some representative pixels are also shown (c-e).

4.6b is the same receiver substrate, but coated with an additional 80 nm PFO layer. The addition of PFO to the receiver substrate clearly improves the likelihood of the transfer at smaller gaps and higher fluences (green rectangle). In addition, the pixels have a better shape at smaller gaps, < 20 μm, without the hole in the middle, and a sharper square frame.

Close-up images of some pixels are shown in figures 4.6c-e. Figure 4.6c shows a pixel transferred at large gap widths (~ 40 μm), onto a plain PEDOT:PSS receiver substrate. It has the distinct *doughnut* shape, mentioned in the previous section, associated with the larger gaps. The pixel in figure 4.6d still has a hole in the middle, but was transferred across a smaller gap and this is reflected in the more square shape of the pixel. Both figures 4.6d & e are of pixels on a PEDOT:PSS / PFO receiver substrate, and the best overall pixel morphology is quite clearly in figure 4.6e, where the gap was smallest (and the fluence a bit higher). This demonstrates the benefit of receiver substrate modification, particularly at atmospheric pressure with a gap between 2 and 20 μm.

4.2.4 Transfer of PFO stacks at reduced pressures

Despite some successes with the PFO transfer across a gap in ambient conditions, it is clear that most of the deposited pixels would not be functional. The difficulty of LIFT at atmospheric pressure has been investigated before using larger gaps (0.5 & 1 mm) [152]. In that earlier study, shadowgraphy was used to investigate the flyer formation and transfer success (the gaps are large enough to image), and an acoustic shock wave was observed to reflect off the receiver substrate and fragment the oncoming flyer, often pushing it back to the donor substrate. In that study, reduced pressures were attempted, but not with great success as the flyers appeared to disintegrate upon impact with the receiver, apparently because the flyer had too high velocity [152]. The difference between showdowgrams obtained at reduced pressure and atmospheric pressure, with a slower flyer and stronger shock wave, are shown in section 3.4. For the experiments outlined in this section, the environmental pressure in the gas chamber was reduced from 1 bar (atmospheric pressure) down to $3 \cdot 10^{-2}$ mbar. The samples for these experiments were the same as those used before, except that only 80 nm Ag was used. Thinner silver films were used to highlight the improvement in transfer quality because thinner metal films show noticeably poorer transfer at atmospheric pressure: see red box in figure 4.7a compared to figure 4.5 and the red box in figure 4.6a. In addition, the experimental steps take between the successful MEH-PPV results in section 4.1, outlined in the appendix C.1, led to the use of thicker metal layers which is easier to obtain with silver than with aluminium.

4.2.4.1 Pressure improvement

Figure 4.7 shows the large improvement of pixel transfer at reduced pressures. At 100 mbar (figure 4.7b) the transfer is already greatly improved, and below 10 mbar (figures 4.7c-f) the transfer is even better, but does not obviously improve with further pressure reduction. There is a degree of variation from sample to sample, but this is negligible, and probably dependent on the long-term variation in laser energy ($\sim$ 5 %). In addition, the standard deviation of the fluence varied by $\pm$ 5 % from pulse-to-pulse instability. Nevertheless the pressure trend is fairly clear, and the transfer consistency below 10 mbar is obvious: rows 3-6 (from top) are all completely transferred for all the figures 4.7c-f, 10-0.3 mbar. The close-up SEM images, figures 4.7g-i, show three main observations. Firstly, there is folding just inside the edges. The folding is more pronounced at lower fluences, e.g the single lines parallel to the pixel edges for pixels transferred at 55 mJ/cm^2 in figures 4.7c-f. They are particularly prominent within the pixel at low fluences and gap distance (an example is circled with a green ellipse in figure 4.7h). Secondly, irregular ripping of the metal along the edges can be clearly seen. Figure 4.8 suggests that the metal ripping is partly fluence dependent. An additional rip/fold is circled in a red elipse in figure 4.7i to show a characteristic feature that appears after a subsequent transfer close enough to damage the pixel which has already been deposited, i.e. it isn't a consequence of the original transfer.

In figure 4.7i the chronology of the transfers went from top to bottom, hence the transfer in line 5 of figure 4.7d, at 90 mJ/cm^2, would affect the line above where the pixel in figure 4.7i came from. The precise mechanism for this post-depositional effect is not clear, but is possibly the acoustic shock wave or from the gaseous TP decomposition products. Lastly, a striped pattern can be observed parallel to the edges, particularly the right and left edges. This pattern has been highlighted in figure 4.7g with blue lines. Supplementary to this last observation are circles which appear to be embedded in the same way, as a topographical variation, indicated with blue arrows in figure 4.7g.

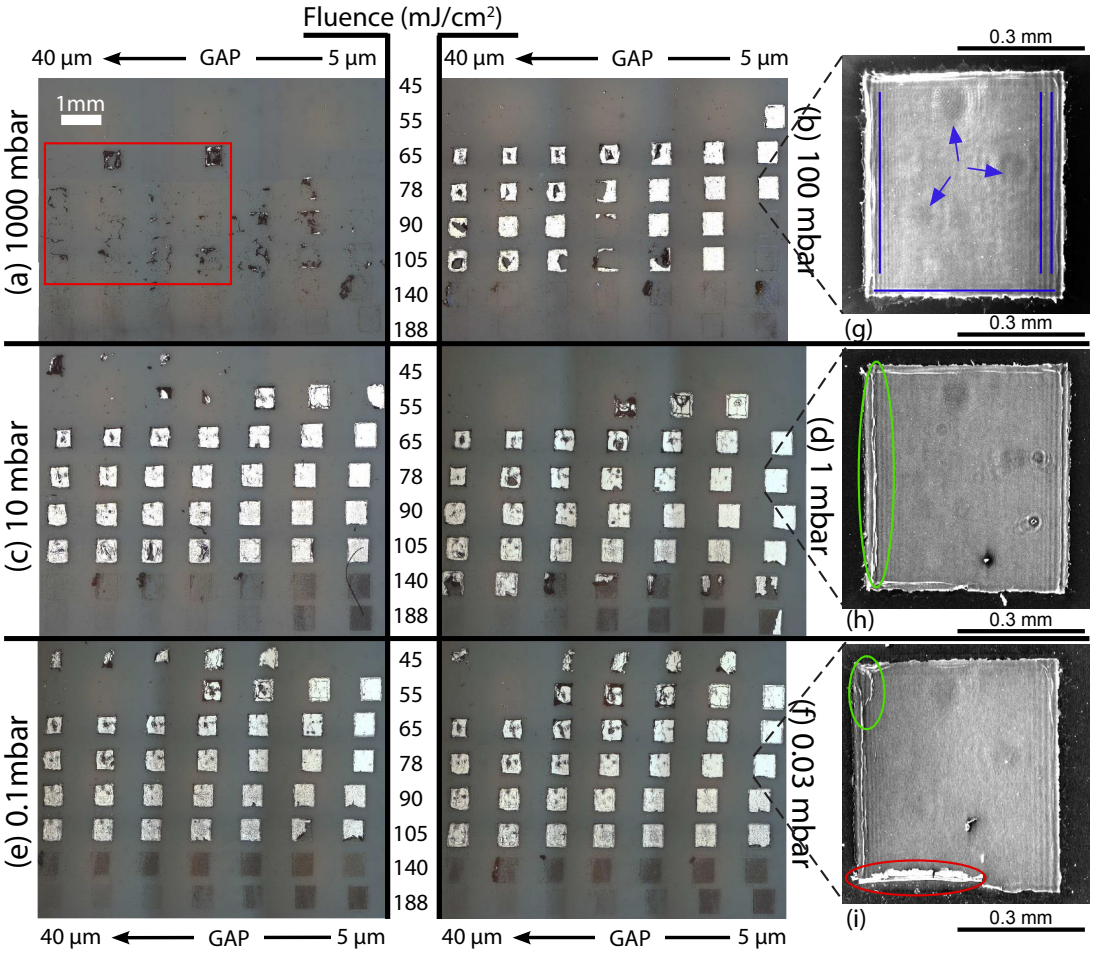

Figure 4.7 Light and SEM micrographs of the PEDOT:PSS-coated glass receiver substrates for 190 nm TP / 80 nm Ag / 80 nm PFO donor substrates with different environmental pressures. (a) is atmospheric pressure (1000 mbar), and each subsequent picture from (b) to (f) is one order of magnitude lower. The fluence goes down from top to bottom, and the gap increases, from 5 to 40 μm, from right to left. Figures (g) to (i) are SEM images of the pixel at $\sim$ 5 μm gap distance and 78 mJ/cm^2, for: (g) 100 mbar, (h) 1 mbar, and (i) 0.03 mbar.

Figure 4.8 shows some SEM images of pixels transferred at 1 mbar. The pixels in the first row were transferred at a laser fluence of 65 mJ/cm^2, and those in the second row were transferred at a laser fluence of 90 mJ/cm^2. The gap distances for the pixels are

shown below the images. As well as the folding within the pixel in figure 4.8c (green ellipses), the folding up of the edges is far more pronounced in pixels transferred over a larger gap (figures 4.8a & b). The overall effect of the folding is to shrink the pixel, similar to the observation for the Alq_3 flyers in ambient pressure in figure 4.4a. The pixels transferred at higher fluence, 90 mJ/cm^2, do not show such pronounced folding. However, some curling-up of the pixel edges is clear in figure 4.8d. The folding circled in a red ellipse is post-depositional damage caused by subsequent transfers, as explained in the previous paragraph for the pixel in figure 4.7i. The folding/curling-up observations from figure 4.8 match the shape of the flyers observed in shadowgraphic investigations at reduced pressure [152]. The shadowgrams in that paper showed that the flyer edges curled towards the donor substrate, the same direction as the folding in these SEM observations of pixels transferred at reduced pressure.

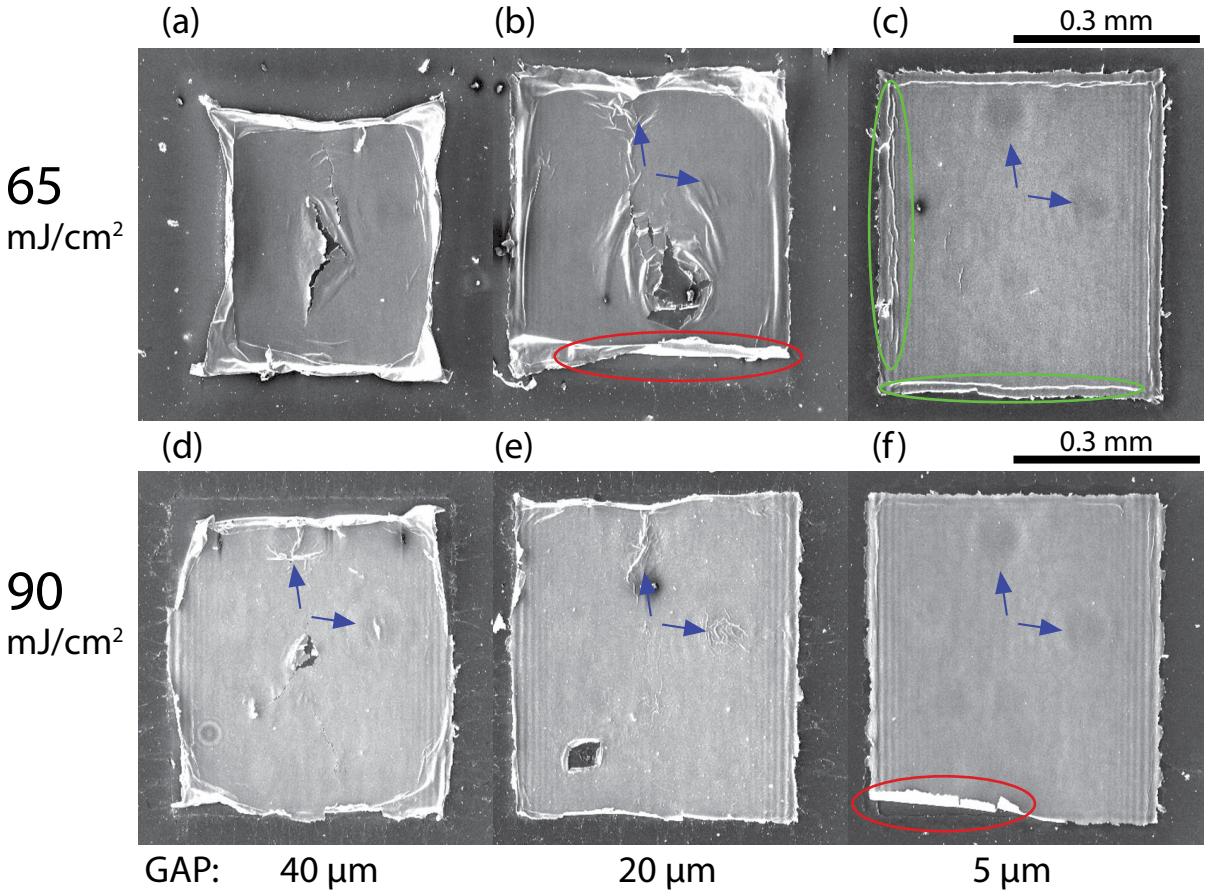

Figure 4.8 SEM images of individual pixels transferred at two different fluences, and three different gap distances at a pressure of 1 mbar (see figure 4.7d). (a) to (c) are at 65 mJ/cm^2, and (d) to (f) are at 90 mJ/cm^2.

An additional observation from the SEM images is the regularity of the topological patterns, other than the folding. These patterns are hard to interpret and it is not clear what they are exactly. The stripes along the edges highlighted by blue lines in figure 4.7g are

clearly present in some of the pixels in figure 4.8. The circular patterns indicated with blue arrows in figure 4.7g are also clearly present in some of the pixels in figure 4.8. The circular patterns appear to be located in the same places of the pixel, irrespective of the sample and pressure. Without additional research it is hard to interpret these patterns, but similar oscillatory patterns have been observed in frontside ablation of triazene before [77, 147]. One question may be that the gap gradient is relatively significant even across the width of one pixel. In the following section 4.3, figure 4.12 shows OLED pixels with a silver cathode fabricated across a constant 15 μm gap, however. The alignment of the morphological features is not as strong in the light micrographs, although there is a linear feature along the vertical edges of the pixels. The SEM image in figure 4.12 shows how different features are picked up by light and electron microscopy. There are similar features in the SEM micrographs in figure 4.12 to those observed in figures 4.7g-i.

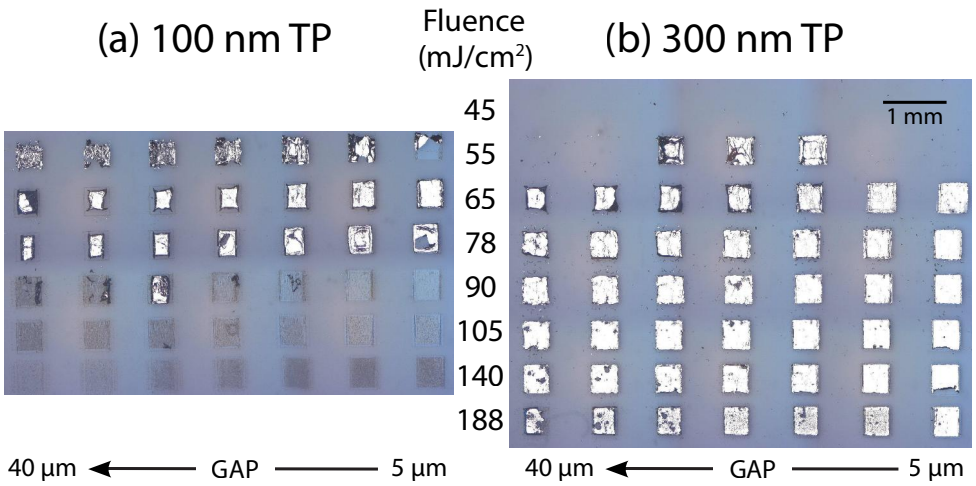

Figure 4.9 Light-microscopy images of the PEDOT:PSS-coated receiver substrates for TP / 80 nm Ag / 80 nm PFO donor substrate transfers at a range of fluences and gap distances. The pressure is 1 mbar. (a) is for a donor substrate TP DRL thickness of 100 nm, and (b) is for a donor substrate TP DRL thickness of 300 nm.

4.2.4.2 Triazene DRL thickness comparison

In addition to the pressure and substrate-substrate gap dependence, the effect of changing the triazene DRL thickness was also investigated. The two extremes for successful transfer of 300 nm and 100 nm are shown in figure 4.9. The only TP film thinner than 100 nm that we investigated, 40 nm, did not appear to give any successful transfers, and we did not investigate thicknesses above 300 nm. Figure 4.9 shows the big difference in transfer success for 100 nm and 300 nm TP at 1 mbar, with varying gap distance, as a function of fluence. Successful transfer is obtained above 140 mJ/cm^2 for 300 nm TP DRL, in figure 4.9b, whereas the flyer has been completely disintegrated by 90 mJ/cm^2 for 100 nm TP DRL. From frontside ablation depth measurements of TP, a single 308 nm pulse of 60 mJ/cm^2 is

enough to ablate 100 nm TP. More than 150 mJ/cm^2 is required to ablate 300 nm TP [79]. This explains the general trend of successful transfer at higher fluences for a greater TP DRL thickness.

4.2.5 Effect of metal layer thickness

In section 4.2.3, the transfer at 20-40 μm gap in figure 4.6a, shown in the red rectangle, is not quite as successful as that observed in figure 4.5 (in that not all the pixels were transferred), the pattern is the same, with most of the successful transfers at gaps of 20-40 μm. These results for 150 and 200 nm Ag can also be compared with a comparable receiver substrate for 80 nm Ag, in figure 4.7a, with the relevant fluence and gap range again in a red rectangle. These images show a distinct trend in terms of the influence of the metal layer thickness on the success rate of transferring these PFO pixels. In figure 4.5 the Ag layer of the donor substrate was 200 nm thick, in figure 4.6a it was 150 nm thick, and in figure 4.7a it was 80 nm thick. This shows that the thicker the Ag layer is, the better the chance of successful pixel deposition at gaps of 20-40 μm. However, it cannot be said that the transfer is altogether successful, even in figure 4.4, given the *doughnut* shape of the pixels which would almost certainly make non-functional OLEDs. The pixels at low gaps and high fluence in figure 4.6b may make functional OLEDs, but the use of PFO onto both the receiver and donor substrate is not the goal in terms of PLED device architecture.

In addition to the pressure and gap effects, a trend in the influence of the metal layer thickness can be observed with figures 4.5, 4.6a, and 4.7a. The thicker the Ag metal layer, the better the likelihood of transfer at gaps $>$ 20 μm, at atmospheric pressure. At reduced pressure the trend is not relevant as the 80 nm Ag films all deposited successfully within a given fluence window. Thickening the silver layer may widen the fluence window for successful transfer slightly, but thicker silver films have not been investigated at reduced pressure. Figure 4.5 uses a Ag layer of 200 nm, figure 4.6a a Ag layer of 150 nm, and figure 4.7a uses a Ag layer of 80 nm. Two possible (but by no means exclusive) reasons for this trend are, firstly, that a thicker layer is mechanically stronger, and secondly, that a thicker layer gives the flyer more momentum to overcome air resistance and the reflected shock wave energy.

4.2.6 Conclusions from the gap and pressure optimisation

Following section 4.1 the shock wave has been proposed as the source of flyer destruction [153]. In an earlier paper, reduced pressure environments were also investigated to try and remove the effect of the shock wave [152]. That investigation used time-resolved shadowgraphy to observe the flyer velocity and morphology, and to observe transfers over gaps of 0.5 and 1 mm. Although air resistance was clearly reduced, folding at low fluences and high-impact at high fluences meant that transfer was unsuccessful over these big gap

widths. It was actually concluded that transfer was better at atmospheric pressure with gaps of 0.5 and 1 mm [152].

In this study, figure 4.4 shows some of the best evidence for the power of the shock wave pushing back the flyer onto the donor substrate. For the Alq_3 donor substrates (figure 4.4a) the flyers at the larger gap distances (> 20 μm) show a very interesting morphology. The edges of the flyer curl up, but an almost circular area of the flyer shows flat, uniform contact with the donor substrate. In the middle, a small hole appears like a hole punched through the flyer, resulting in a *doughnut* shape. The area of the flyer in contact with the donor substrate appears pressed down by the shock wave, and the edges which curl up are where the shock wave/air resistance force has dissipated enough to be too weak to push the flyer back onto the donor substrate. This effect should increase dramatically with gap distance, and indeed figure 4.4a shows this. Although not shown, a deposit is left on the receiver substrate which indicates that the flyer comes in contact, or at least close to contact, with the receiver substrate before being pushed back onto the donor substrate. Figure 4.4b does not show the same uniform contact with the donor substrate as figure 4.4a, presumably because of the different material properties of the organic PFO layer vs. the Alq_3 layer. The polymeric PFO should have better film cohesion than the small-molecule Alq_3, and may well be more adhesive as well, particularly to another polymeric material (PEDOT:PSS). Due to the better PFO adhesion, transfer is expected to be better in atmosphere compared with Alq_3 films (figure 4.5). It may also explain why the PFO flyers are more folded and dishevelled in figure 4.4b than the Alq_3 flyers in figure 4.4a, because the adhesive force between the flyer and the PEDOT:PSS receiver is closer to the force exerted by the shock wave pushing the flyer back towards the donor substrate for PFO than Alq_3.

The improvement in transfer from the addition of the PFO layer onto the receiver substrate, shown in figure 4.6, backs up the hypothesis that the adhesive force between the PFO and the PEDOT:PSS is only just below that of the force preventing transfer. The PFO was added onto the receiver substrate with the expectation that it will have a higher adhesion to the PFO flyers than PEDOT:PSS. A significant increase in transfer success is achieved at smaller gaps with the PFO on the receiver substrate. Previously, we observed that the addition of PEDOT:PSS greatly improved transfer of MEH-PPV 'in contact', at low fluences [153]. This result further increases the evidence for the effect of the receiver substrate upon the quality of transfer. However, it is important to note that the improvement may not be entirely due to adhesion, despite the hypothesis. The mechanical properties of the films may play a big role in dissipating energy in either the shock waves in the gas, or from the impact of the flyer. This could also affect the quality of transfer.

Our understanding of the transfer process has been aided by the control of the gap width on the μm scale. Onto plain PEDOT:PSS coated substrates, the PFO transferred much better across gaps > 20 μm at atmospheric pressure, shown in figure 4.5. In contrast, MEH-PPV (not shown, but used in previous investigations [118, 153]) was observed to transfer onto PEDOT:PSS well with a gap < 10 μm. This explains why some degree of inconsistency

was observed with MEH-PPV OLEDs 'in contact' as light contamination of dust particles increases the gap from 'in contact' to > 10 μm. At reduced pressure good transfer appears more consistent, covering a larger range of fluences and gaps (figures 4.7 & 4.8). The morphology of the transferred pixel is greatly dependent on gap width, with significant folding observed even above 20 μm at lower fluences in figure 4.7. The reason that the transferred pixel shrinks as the gap width increases is probably because of the gaseous products of the triazene decomposition pushing their way around the edges of the pixel, as observed in earlier shadowgraphy studies [152]. The larger the gap is, the more this process is allowed to develop, and the more folded the flyer will be. However, this process is also fluence dependent, as shown in figure 4.8. Increasing the fluence will decrease the amount of folding, but at the cost of ablating more of the transfer material.

The transfer improvement by reducing the pressure is significant, as shown in figure 4.7. At atmospheric pressure, figure 4.7a, transfer of these thin films was very variable and difficult. At reduced pressures, the transfer is far more reliable and creates higher quality pixels, demonstrating the benefit of removing the air resistance and the shock wave, which are both proportional to pressure. In a previous study the energy in the shock wave was calculated as a function of fluence. [84] In that article, the shock wave energy was calculated to be 30-40 % of the input laser energy. The flyer kinetic energy was calculated to be $\sim$ 3-4 %, one order of magnitude lower. As the pressure is reduced, the shock wave energy is reduced. The shock wave energy is directly proportional to the gas density, i.e. pressure. Therefore, a single order of magnitude reduction in pressure brings the energy of the shock wave energy to the same order of magnitude as the flyer. As has been observed, reducing the shock wave energy increases the flyer energy [152]. This means that at $\sim$ 100 mbar, the flyer energy will start to be above the shock wave energy, and transfer can be relied upon. Following this hypothesis, it would be expected that below 10 mbar no improvement in the transfer quality would be observed because the energy of the shock wave should already be at least one order of magnitude less than the flyer kinetic energy. The hypothesis is thus backed up by our observations, demonstrating the importance of efficient energy transfer from the laser energy into flyer kinetic energy .

A feature common to quite a lot of the data presented here is the hole in the middle of the pixels creating the *doughnut* pixels. This is primarily evident in the atmospheric pressure transfers with gaps above 20 μm, in figures 4.4 and 4.5. A minor hole is also seen in lower-fluence pixels with large gap widths at reduced pressures, in figure 4.8. The origin of the hole is probably the stress from TP decomposition gas pressing on the back of the flyer. However, at least two mechanisms must be in play because higher pressure and greater gap width, as well as the less significant effect of lower fluence, all contribute to increase the likelihood and size of holes in the centre of the pixels. It must be considered that larger gaps mean that the flyer is in flight for a longer time allowing heterogeneities to be accentuated. Higher air pressures also slow down the pixel, but additionally have air resistance and an acoustic shock wave affecting the flyer morphology.

From frontside ablation studies, it is known that around 80 mJ/cm^2 is required to fully ablate 190 nm TP (section 3.3 and references [79, 147]). This means that the triazene may not be completely decomposed until a fluence of up to 80 mJ/cm^2, and possibly even above it. However, for this method of making OLEDs, with the relatively inert cathode already attached, this problem is irrelevant. What is clear, though, is that transfer can be achieved above the fluence where all the triazene is expected to be ablated (see figure 4.9a). All of the samples in this study used Ag as the metal, but when aluminium is used, the flyer can be transferred at even higher fluences [153]. Figure 4.9 also shows a minimum range of TP DRL thicknesses that can be chosen, from 100 nm to 300 nm.

Despite the vast improvement in transfer quality at reduced pressures and small gap widths, the SEM images show new smaller-scale problems: ripples, irregular tearing at the edge of the flyers, and folding at lower fluences. Additionally, as mentioned before, a non-decomposed TP film may be left on the back of flyer, particularly at lower fluences. This study was done using silver as the metal transfer layer, but in the next section 4.3 a direct comparison of pixels printed with aluminium and silver is undertaken.

4.3 Fabrication of PFO pixels at reduced pressures

4.3.1 Specific experimentals

For all these LIFTed pixels,[4] a donor substrate consisting of fused silica / 190 nm TP / 80 nm cathode / PFO(:< 10 wt% dye) has been used. For the earlier experiments thicker PFO films were used ($\sim$ 80 nm), and for the optimised pixels, thinner PFO films were used ($\sim$ 50 nm). The receiver substrates are all coated with 60 nm PEDOT:PSS and 40 nm PVK.

The laser scheme is summarised in figure 4.10, where the transfer of a pixel from a blue donor substrate is shown onto a receiver substrate with two green and red pixels already deposited. Single pulses from the 308 nm XeCl excimer laser were shaped into a rectangle with a width of 500 μm, and a length of at least 1.2 μm on the substrate, using a projection mask demagnified four times onto the substrate. For all of these experiments, a $\sim$ 15 μm ($\pm$ 3 μm) donor-receiver substrate gap has been used with a reduced environmental pressure of 1 mbar. The gap was measured using the interference technique in the experimental section 2.1.4.

4.3.2 Preliminary attempts to fabricate PFO pixels

Using the results from the previous section 4.2, attempts were made to print functional OLED pixels side-by-side with a controlled gap and at reduced environmental pressure.

[4] *LIFTed* is used here as a verb, as in 'transferred by LIFT'. Throughout this work, *LIFTed* is used extensively as an adjective to describe the fabrication method of an OLED pixel, i.e. that it is fabricated by LIFT as opposed to the *conventional devices* fabricated using conventional methods, see the beginning of chapter 5 for more information.

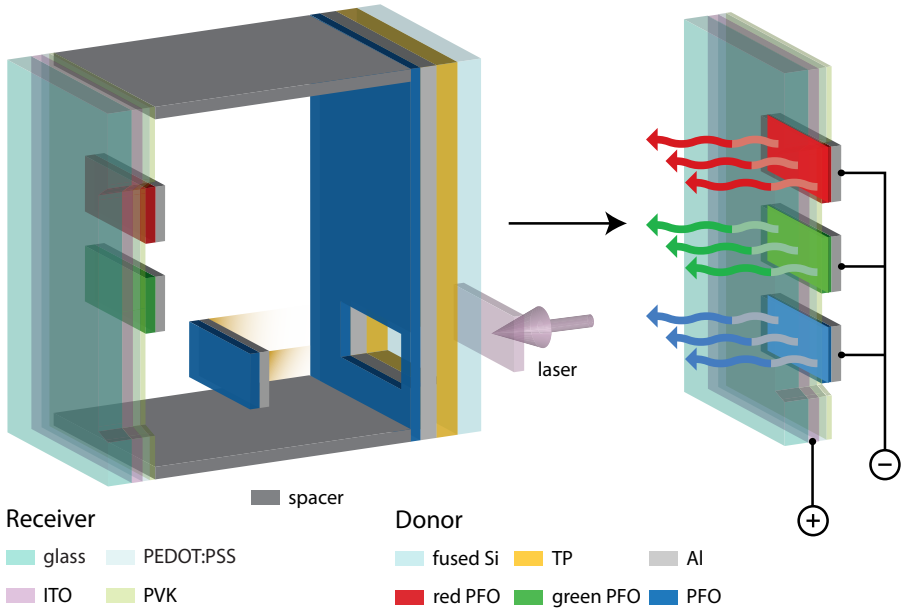

Figure 4.10 A scheme of the red-green-blue PFO pixel transfer. The left image shows the transfer of the third, blue, pixel after the other two colours have already been transferred. The right image shows the receiver substrate alone with a bias across the three pixels creating electroluminescence. The scheme is not proportional with a large positive exaggeration in the axis perpendicular to the films. The real gap is $\sim 12\ \mu$m, the film thicknesses are all 50-200 nm thick, and the glass and fused silica substrates are both 1 mm thick. In addition, the lateral dimensions are not proportional; the real pixels are $\sim 0.5 \times 1$ mm, and the substrates $\sim 25 \times 25$ mm.

This section summarises the preliminary investigations, and the next section outlines the optimised three-colour pixels in a little more detail. The aim of these studies is summarised in 4.10, and the resulting OLEDs at various stages in the optimisation are shown in figure 4.12.

Figure 4.11 shows micrographs of the blue OLEDs made with three different cathode layers: Al, Ag, and Ag / Cs_2CO_3 (the Cs_2CO_3 layer was < 5 nm). The main conclusion to take from the images is that aluminium cathodes create smoother pixels than silver cathodes when deposited by LIFT, both when imaged by the reflection of the light microscopy, and by back-scattered electrons in SEM. A good explanation for these morphology differences is the heat conductivities; silver is double as conductive than aluminium at nearly all temperatures [165]. However, this must not be assumed to be the reason, particularly because green emission in the EL spectra is far more prevalent in the Al pixels than the Ag pixels in figure 5.10. This is a feature often assumed with oxidation of the PFO, increased by elevated temperatures. Another explanation for the morphological differences is the respective mechanical properties of the metals, particularly because silver is far more malleable than aluminium, giving it a Brinell hardness one order of magnitude lower than aluminium [165].

The pixel morphologies in figures 4.11 and 4.12 are the main reason why aluminium

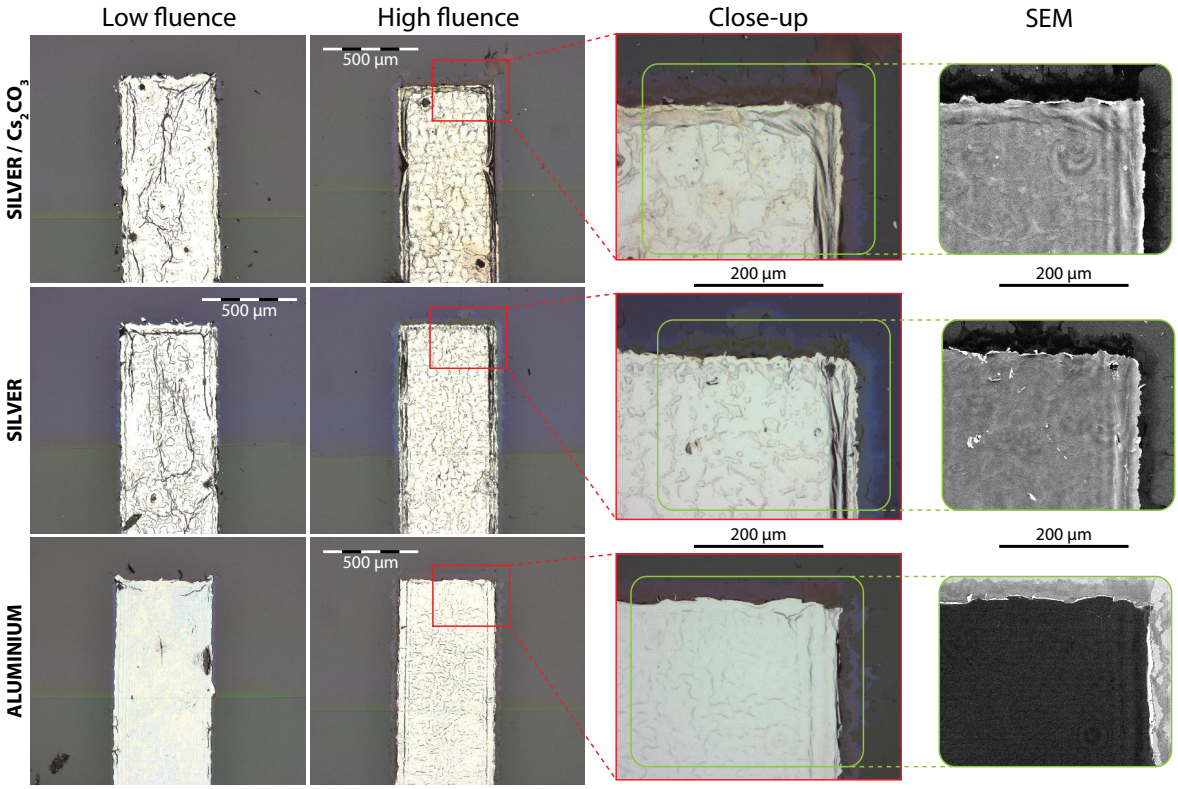

Figure 4.11 Light micrographs of the preliminary PFO pixels. All the pixels have plain PFO as they're emitting layer, and the only difference between the high and low fluence pixels is the laser fluence used for the LIFTed transfer. A closeup of the high fluence pixel is shown on the right, with the relevant area ringed in a red box. The fluence for the low fluence transfer was 60 mJ/cm^2, and the high fluence was 90 mJ/cm^2.

was chosen for the optimised devices in the following subsection. The respective device performances in table 5.2 also played a part, but this advantage was somewhat negated by the extra green EL emission in figure 5.10. Supporting the morphological evidence, the top row in figure 4.13 also shows preliminary PFO PLED pixels with silver cathodes transferred at different fluences. They are compared directly with optimised PFO PLED pixels with aluminium cathodes transferred at the same fluences. The comparison between these two types of devices is the same as comparing between figure 4.12b and figures 4.12d & e.

4.3.3 Optimised three colour PFO pixels side-by-side

The best evidence for the morphology improvement is shown in figure 4.13 where the optimised Al pixels (bottom) are directly compared with the preliminary pixels (top) for transfers at the fluence. The optimised Al pixels show almost perfectly smooth morphology across the whole range of fluences, with only slight folding around the edges. At high fluences there is some rippling in the middle of the pixel, but it is minor (and of a different nature) to that observed in the Ag pixels. The rippling in the Ag pixels is very coarsening from fairly course lines at 105 mJ/cm^2 to large bubble-like structures at 62 mJ/cm^2. At 52

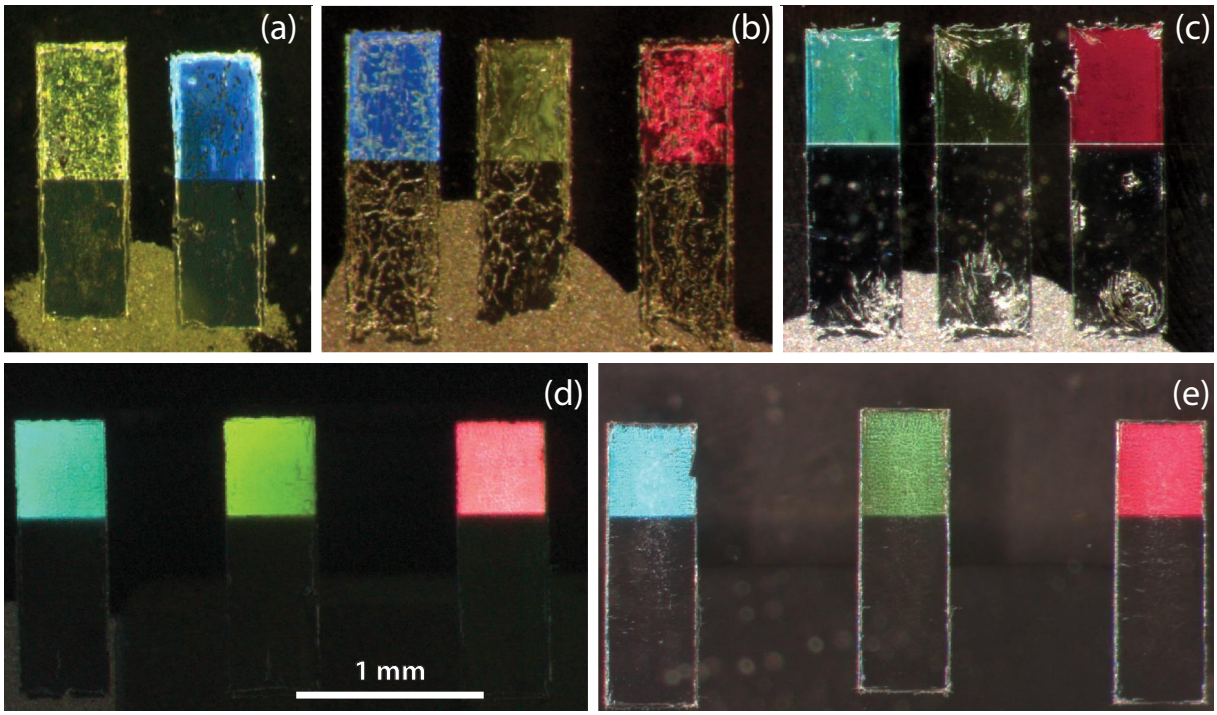

Figure 4.12 Progress in the transfer of multiple PFO PLED pixels by LIFT. The first transfers of plain blue and green transfers with Ag / Cs_2CO_3 cathode are shown (a), then the first three colour pixels with a silver cathode (b), then the preliminary pixels with an aluminium cathode (c), before the optimised pixels with an Al cathode (d) and an Al / TBA cathode (e). All the pixels were transferred at approximately the same fluence, a fluence of $\sim$ 70 mJ/cm^2.

mJ/cm^2, the Ag pixel is remarkably folded. Whilst the energy measurement may be out by 10 %, it is also possible that the result represents a real difference between the pixel depositions. If the rough Ag pixel morphology is indeed created by mechanical effects, it is possible that more energy is lost in the ductile deformation of the Ag than the more brittle deformation of the Al, particularly at the edges where the extreme folding at 52 mJ/cm^2 could be the result.

The source of the morphological differences is probably mechanical or thermal, or partially both. However, the actual mechanism is very hard to speculate about given all the steps of the LIFT process. The complexity of the pixel morphologies points to the need to understand these processes further, particularly the ejection and impact of the flyer.

Figure 4.14 show close-up microscopy images highlighting the morphology at different fluences. Of the pixels shown, those deposited at fluences between 60 and 100 mJ/cm^2 generated functioning OLED pixels with very similar device characteristics. There are small variations in the performance, and these have been investigated in detail for preliminary PFO pixel deposition in section 5.2. Pixels deposited above 100 mJ/cm^2 have not been tested, but the morphologies are usually not very good, like the pixel transferred at a fluence of 135 mJ/cm^2 in figure 4.14b. As well as the orthogonal ridges (highlighted by red lines in

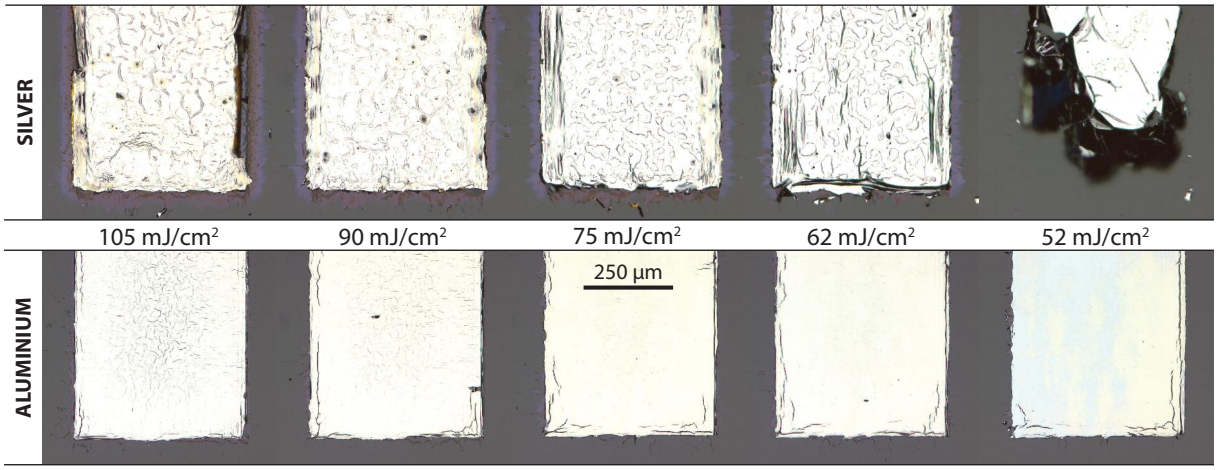

Figure 4.13 Light micrographs of PFO PLED pixels transferred at different fluences for the first PFO pixels with a silver cathode (top) and the optimised PFO PLED pixels with an aluminium cathode (bottom). The preliminary pixels have a ∼ 80 nm PFO layer whereas the optimised pixels have a ∼ 50 nm PFO layer.

figures 4.14b & c, and also present to a lesser degree in d), there are also rips in the metal, some of which are highlighted by red arrows. It is likely that although it may be possible to generate light at fluences above 100 mJ/cm^2, the output will be heterogeneous, like it already is from transfers at a laser fluence of around 100 mJ/cm^2. Also, the irregular pixel morphology may lead to short circuits which would disable the electroluminescence.

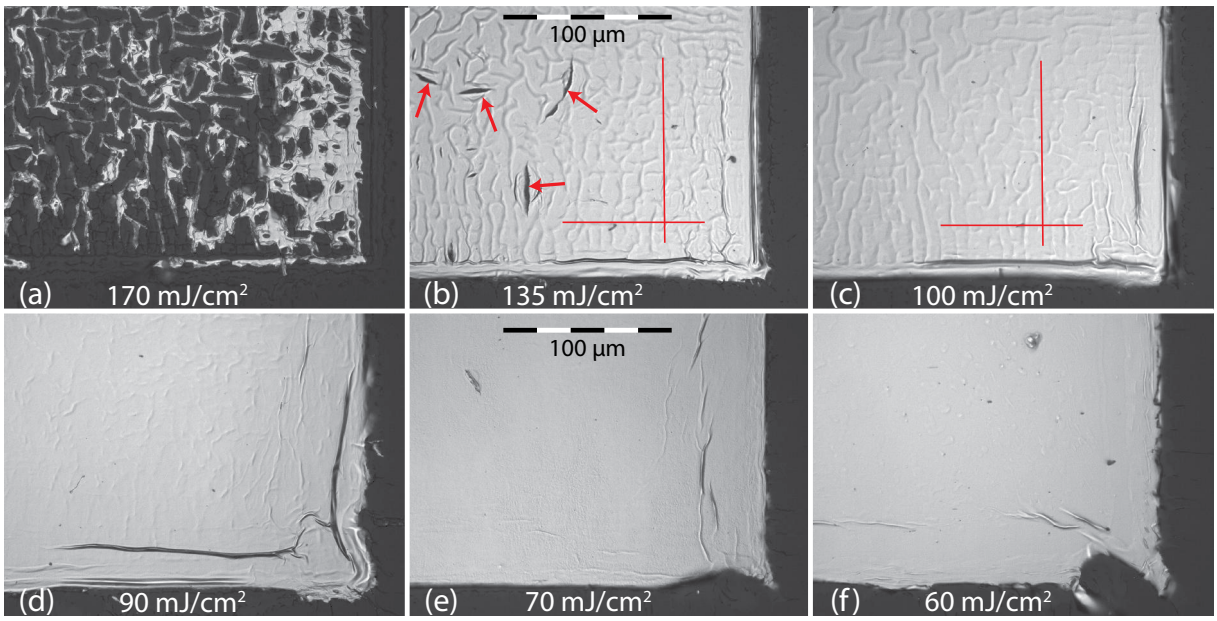

Figure 4.14 Close-ups of LIFTed pixels (made with an Al / TBA cathode) transferred at different fluences.

The ridges are a significant morphological feature at higher fluences, but at the lower

fluences (60 and 70 mJ/cm^2, figures 4.14e & f) they are not observable with the micrographs. Another area of great morphological importance is the edge of the pixels. There are two main reasons why it is hard to conclude a lot from these images, both because of the laser beam energy. The exact laser beam energy is not known at the sample, even though it is inferred from the projection of the mask, and the resultant ablation crater. If the sample is just out of the depth of field, then the area where the energy variation will be most pronounced is at the edges. As it is impossible to image a projection of a mask perfectly, this will certainly be the case to some degree. In addition, the natural heterogeneity of the laser beam is likely to be at its most pronounced at the edges (i.e. lowest at the edges), particularly when the gaussian profile of the full (un-masked) beam is taken into account.

4.3.4 Shaped deposition with high resolution

The shapes used in this section are exclusively letters making up the acronyms, 'ETH' and 'PSI'. Projection laser masks were fabricated with the desired shapes, and applied in the optical setup where the laser mask usually goes. The mask was imaged onto the sample, in the same way as the rectangular mask has been in all the other cases. The TP DRL then ablates with the desired shape to create a patterned deposition on the receiver substrate. These transfers test the lower size limits of patterned depositions by the LIFT process *with our existing experimental setup*, i.e. they do not represent the best possible resolution, but are a good indicator of what is achievable with a basic system.

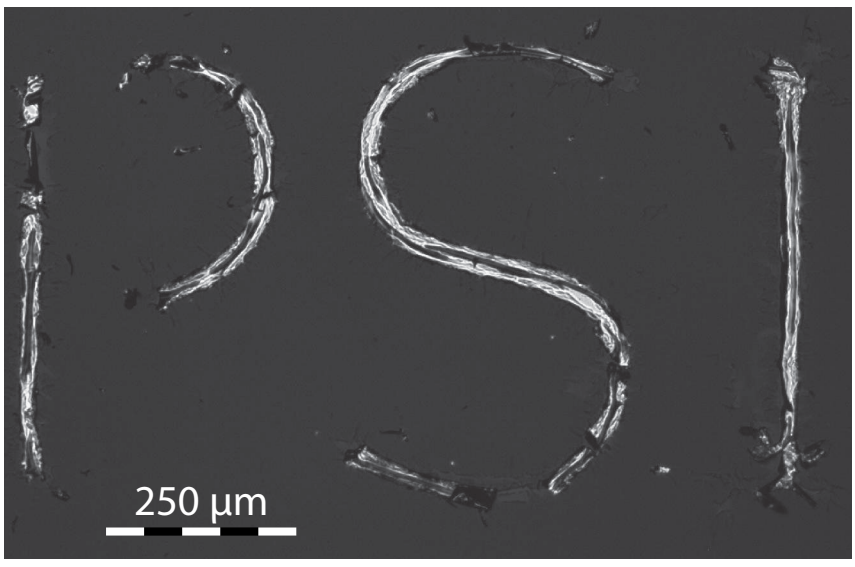

Figure 4.15 A transferred pixel with the shape, 'PSI'. This transfer was across a 15 μm gap controlled by a spacer at a fluence of $\sim$ 80 mJ/cm^2.

Figure 4.15 shows a deposition made using the optimised parameters from section 4.2; the LIFT was done at a reduced pressure of 1 mbar and with a gap of $\sim$ 15 μm. This pixel

was made from a 190 nm TP / 80 nm Al / 50 nm PFO donor substrate, and deposited onto a PEDOT:PSS / glass receiver substrate. Whilst the mask shape has not been perfectly preserved in the deposition, the image shows the PSI shape nicely. The line width of the digits is less than 50 μm, and whilst there is folding prevalant in many places, it does not seem to overly dominate.

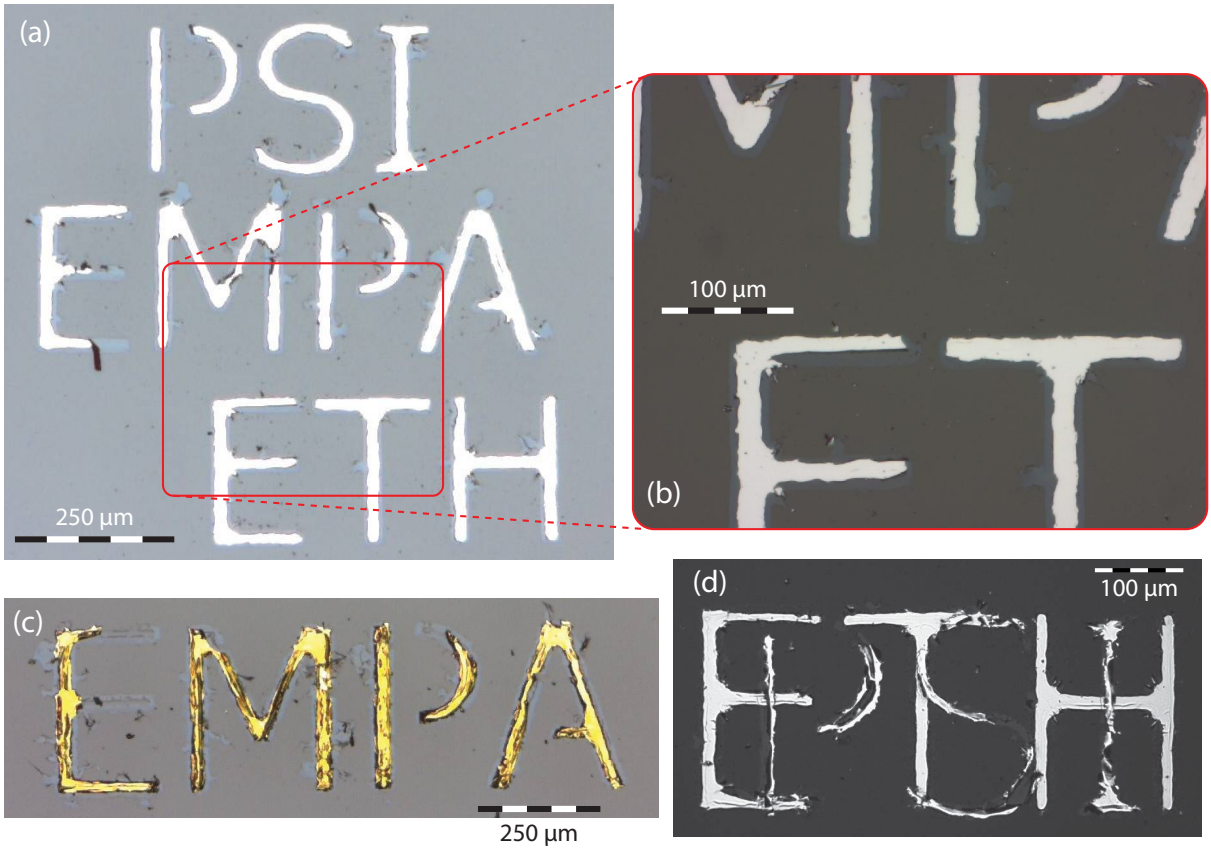

Figure 4.16 These transfers were done in contact, with fluences of $\sim$ 120 mJ/cm^2 (a) & (b) and $\sim$ 80 mJ/cm^2 (c) & (d). (a), (b) and 'ETH' in (d) were done with aluminium, (c) is gold, and 'PSI' in (d) is silver.

Figure 4.16 shows four sets of transfers done 'in contact'. From the gap widths measured by interferometry in the experimental section 2.1.4, it is known that the minimum gap obtained 'in contact' is around 2 μm, and if there is any debris on either substrate the gap can be over 10 μm. The pixels in figure 4.16a, b & d (ETH) were done with the same donor substrate as used for the transfer in figure 4.15; 190 nm TP / 80 nm Al / 50 nm PFO. Figure 4.16c uses a 190 nm TP / 60 nm Au / 50 nm PFO donor substrate, and the second transfer (PSI) in figure 4.16d is from a 190 nm TP / 150 nm Ag / 80 nm PFO donor substrate. There is a marked difference in transfer quality for different metals, echoing the optimisation process in section 4.3.2. The poorer quality of the gold pixel in figure 4.16 relative to the Al pixels backs up the explanation that the poor silver pixel morphology may have been due to the high malleability of the metal.

From figure 4.16a, b & c, it is clear that line widths of less than 20 μm are achievable with the setup at PSI. The edges are not perfect, but the closeup in figure 4.16b shows that while the smoothness of the line may not be perfect, they are not particularly folded. The main restriction on the resolution of good transfers (such as the 'E' in 'EMPA' in figure 4.16a) appears to be the focus of the setup, which is a parameter which can certainly be optimized further.

4.3.5 Conclusions from PFO pixel fabrication

The previous section 4.2 on the optimisation of the transfer through the reduction of the environmental pressure and the addition of a spacer to give a defined gap marked the breakthrough in this work, but this section represents the first consolidation of that breakthrough. Optimised pixels were made with both silver and aluminium metal layers in the preliminary transfers in section 4.3.2, and the device characteristics have been reported in section 5.3.

Aluminium was chosen as the cathode material for optimised pixels, and three-colour pixels were fabricated who's optical-electrical characteristics are analysed in section 5.2. The fluence dependence of the morphologies has been studied in section 4.3.3. These showed that the optimal fluence for Al / PFO pixel deposition is around 70-80 mJ/cm^2, but fluences from 50 mJ/cm^{2}to above 120 mJ/cm^2 may be used.

The deposition of shaped pixels using aluminium and other metals has highlighted the advantage of aluminium over more ductile metals, and allowed an investigation into the maximum resolution of pixels fabricated by LIFT. Using the LIFT setup at PSI (with proximity masks), pixels with line-widths of around 20 μm or less can be obtained. However, small variations in laser energy and laser beam focus can have a major effect on the pixel quality and further optimization is needed to find out the minimum pixel size.

4.4 Fabrication of Alq_3 pixels at reduced pressures

4.4.1 Specific experimentals

These results follow on almost directly from the optimised PFO pixels in section 4.3.3, because tetrabutyl ammonium hydroxide (TBA) was also used, like the PFO pixels. The TP thickness (190 nm), environmental pressure (1 mbar), or gap width (15 μm) have not been optimised, and are the same as the PFO. However, the fluence for these parameters has been optimised, in figure 4.17.

Donor substrates of 90 nm Al and 80 nm Alq_3 have been used on 190 nm TP. TBA has also been spin-coated from a 10^{-4} M methanol solution onto the aluminium before the Alq_3 evaporation. The receiver substrate is ITO / 60 nm PEDOT:PSS / 40 nm PVK.

4.4.2 Optimised Alq_3 pixels

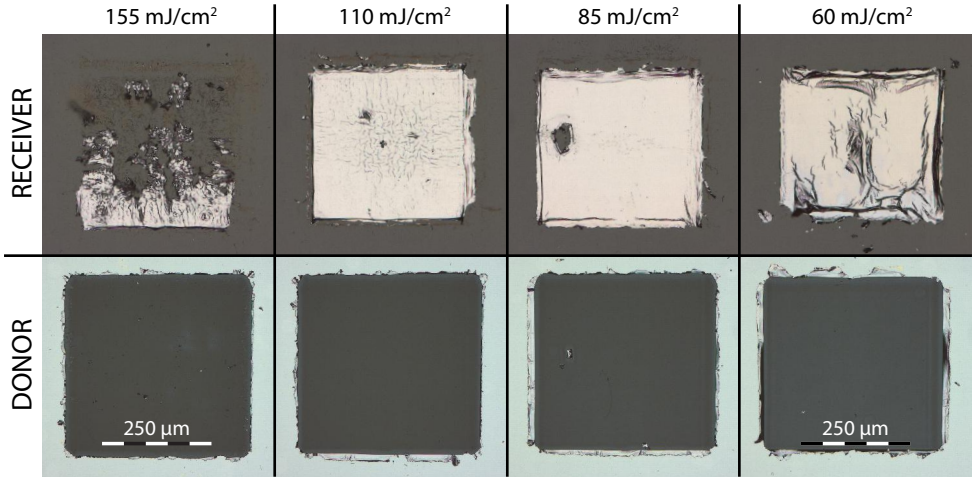

Figure 4.17 Alq_3 / Al pixels deposited on a glass / PEDOT:PSS / PVK receiver substrate. The top images are the receiver substrate pixels, and the bottom images are the ablation crater on the donor substrate corresponding to the pixel above. Pixels deposited at four different laser fluences are shown.

90 nm Al / 80 nm Alq_3 stacks have been successfully transferred in the same way as the PFO stacks in the previous section 4.3, and the fluence dependence of the pixels deposited by the LIFT process are shown in figure 4.17. As can be seen, Alq_3 pixels can be deposited at a range of fluences nearly as wide as PFO in the previous section. This is remarkable for two reasons: firstly, Alq_3 is a small molecule, meaning that the films are likely to have less internal cohesion than polymers, making them more brittle and susceptible to fragmentation; and secondly, Alq_3 typically sublimes at fairly low temperatures around 300 °C [166]. The fact that both of these effects are mitigated suggests that the organic layer is protected from both large thermal and mechanical loads.

The best pixel morphology in figure 4.17 came from transfer at a fluence of 85 mJ/cm^2. This fluence was used to fabricate functional pixels, shown from both above (a) and through the substrate (b) in figure 4.18. The quality of these Alq_3 pixels, when compared to the Alq_3 pixels in section 4.2 and appendix C, demonstrates the significant improvement in transfer that the following factors have: 1) the removal of air resistance by reducing the pressure, and (to a lesser extent) 2) the introduction of a gap. The pixel in figure 4.18 and others have been tested in section 5.4.

A direct comparison between Alq_3 and PFN pixels, transferred at the same fluences with the same Al thickness is shown in figure 4.19. This shows that, despite the fact that the morphology is good, and the pixels work, the Alq_3 pixels are more prone to morphological defects such as cracks and folds than the polymeric PFN pixels.

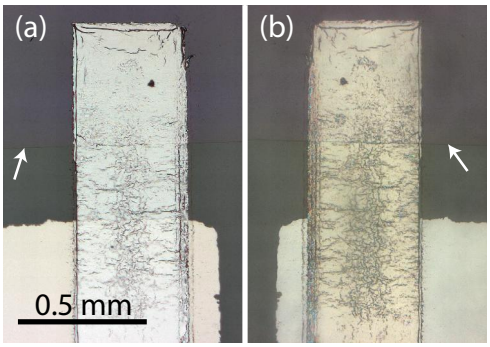

Figure 4.18 A transferred Alq_3 / TBA / Al pixel looking from above the deposition onto the aluminium (a), and through the glass substrate to the Alq_3 / PVK interface (b). The ITO is only coated on the glass substrate in the the top half of the images only, above the line highlighted by the arrows. The pixel was transferred at a laser fluence of 85 mJ/cm^2.

4.4.3 Conclusions from Alq_3 pixel fabrication

The observation that the Alq_3 does not decompose at fluences below 150 mJ/cm^2 is intriguing as it indicates that at the laser fluences less than 100 mJ/cm^2, used for the optimised transfers such as the pixel in figure 4.18, the temperature in the organic layer over the aluminium is certainly below 300 °C [166]. Despite the fact that this is probably higher than the decomposition temperature of the polymeric materials investigated (MEH-PPV, PFO, and PFN), any onset of this reaction is likely to have a greater physical effect than polymeric decomposition, and this is not observed. However, there are fine cracks or folds which are particularly obvious when compared with PFN in figure 4.19.

The fine cracks and folds in the Alq_3 in figures 4.17 4.18, and 4.19 are similar to those obtained in atmospheric pressure in appendix C.1, in figure C.2 in particular. Like the polymeric cracks obtained, for MEH-PPV in section 4.1 and PFO in appendix C.1, the cracks are probably the result of the brittleness in the film. Given that the polymers are considerably more ductile than the small-molecule Alq_3 this is not surprising. In fact, it is a little surprising that the cracks are not more prevalent.

Overall, the results of LIFT of Alq_3 pixels set down a good marker for the LIFT process by demonstrating the flexibility of the LIFT process for use with both polymeric and small-molecule organic materials.

4.5 Fabrication of PFN pixels at reduced pressures[5]

PFN pixels have been fabricated in two different ways with LIFT. They have been made by the the same process as the PFO pixels in section 4.3, and the Alq_3 pixels in the previous section 4.4, using single-step LIFT with a donor substrate containing an aluminium layer

[5]The results from this section will be published in [167].

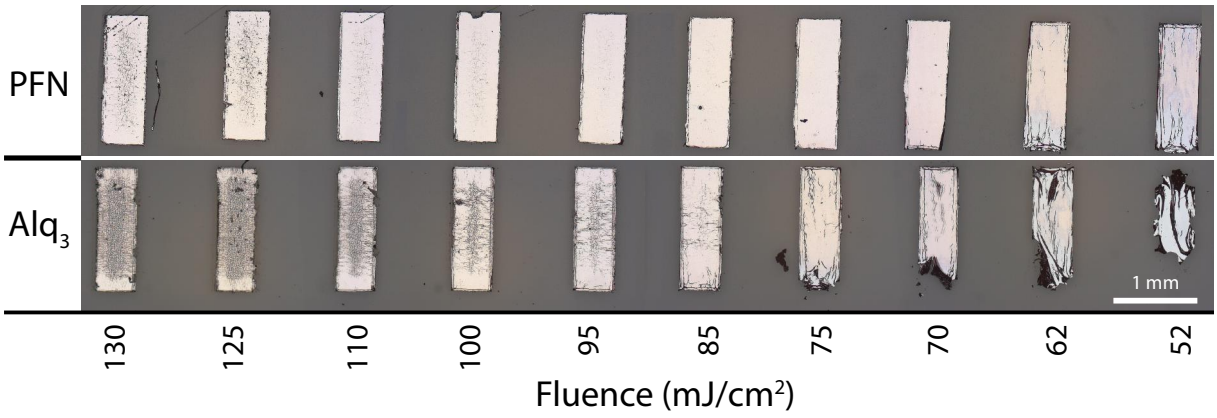

Figure 4.19 A comparison between PFN (top) and Alq_3 (bottom) pixels transferred in identical conditions, with the only difference the organic layer.

between the PFN and the TP. The pixels resulting from the transfer of these Al / PFN bilayer stacks have been termed *normal* LIFTed pixels to differentiate them from the *sequential* LIFTed PFN pixels. Sequential LIFT is the second way used to fabricate PFN pixels, and involves the transfer of two single layers in separate steps; a PFN film first, then an Al film. An overview of the process is shown in figure 4.20.

4.5.1 Specific experimentals

Because PFN was dissolved in a methanol:DMF (99:1) solution, it could be spin-coated directly on top of the TP which is insoluble in that solution. This led to the idea of trying to fabricate pixels by using LIFT twice to deposit single layers on top of each other, in a process coined 'sequential LIFT'. The process is shown in the scheme in figure 4.20, with all the layers shown in different colours according to the key. The thicknesses are exaggerated and not to scale.

For all the receiver substrates, ITO / 60 nm PEDOT:PSS / 40 nm PVK have been used. Normal LIFTed pixels use a standard 190 nm TP / 90 nm Al / 50 nm PFN donor substrate, but sequentially LIFTed pixels use two donor substrates: 190 nm TP / 50 nm PFN, and 190 nm TP / 80 nm Al. A light micrograph of a *normal* donor substrate is shown in figure 4.21, highlighting a periodic undulation in the PFN film which is probably linked to the spin-coating process.

All these LIFTed pixels were fabricated using the same basic LIFT process as the optimised PFO pixels in section 5.3.1, with a donor-receiver substrate gap of ~ 15 μm and an environmental pressure of 1 mbar. The only difference for the sequentially LIFTed pixels is that they had two stages of LIFT rather than a single transfer stage.

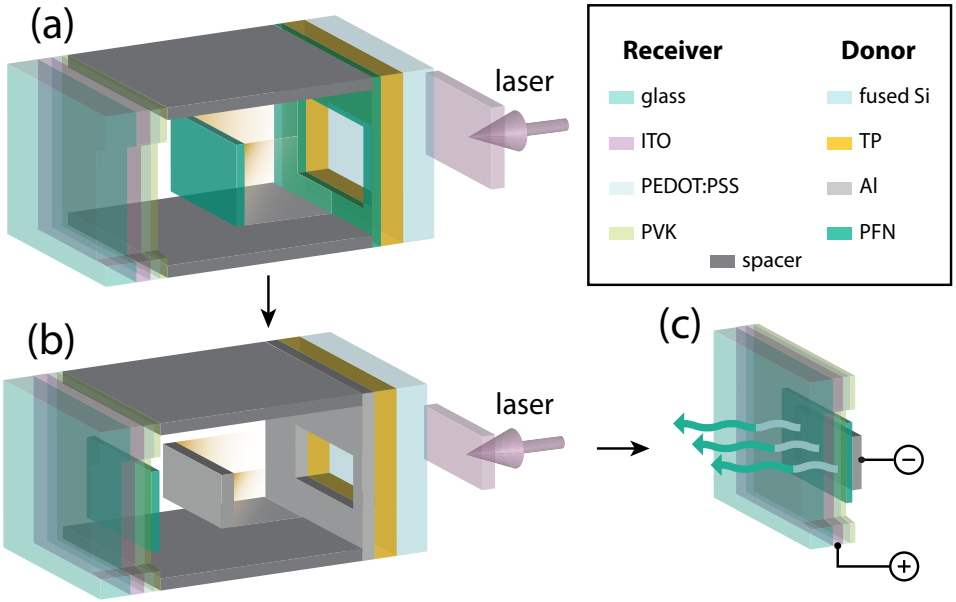

Figure 4.20 A scheme showing the sequential LIFT process used in this study of PFN. (a) shows the deposition of the PFN on the glass / ITO / PEDOT:PSS / PVK receiver substrate; (b) shows the deposition of the Al on top of the PFN; and (c) shows the final PLED with a bias applied

4.5.2 Normal LIFTed pixels

The PFN pixels transferred as well as PFO, despite coming from a different solvent and appearing to fabricate slightly different films (see the periodic undulation on the PFN film on the donor substrate in figure 4.21). Transferred pixels are shown in comparison with the Alq_3 pixels in figure 4.19. Pixels with device functionalities very similar to conventional devices were fabricated by LIFT in this normal way. The PFN could have been doped with iridium dyes like the PFO [60], but the sequential transfer became of more interest than replicating the three colours with a different polymer host.

As mentioned in discussion of the previous section 4.4 on Alq_3, the PFN layer in the metal / organic bilayer creates pixels with much smoother morphologies than for the small molecule Alq_3. This is shown in figure 4.19 for different LIFT laser fluences from 52 mJ/cm^2 to 130 mJ/cm^2. Over this large range of fluences, the pixels are remarkably homogeneous in terms of larger-scale features visible in figure 4.19. This shows that the LIFT process is very accommodating for small deviations in laser fluence.

4.5.3 Sequential LIFTed pixels

The optimal fluence for the transfer of 80 nm Al / 50 nm polyfluorene bilayers has previously been determined to be around 75mJ/cm^2, from section 4.2 and this was the fluence ($\pm$10mJ/cm^2) used for the transfers of both layers of the functional OLED pixels in this study. The PFN could be transferred fairly successfully at quite a wide range of fluences,

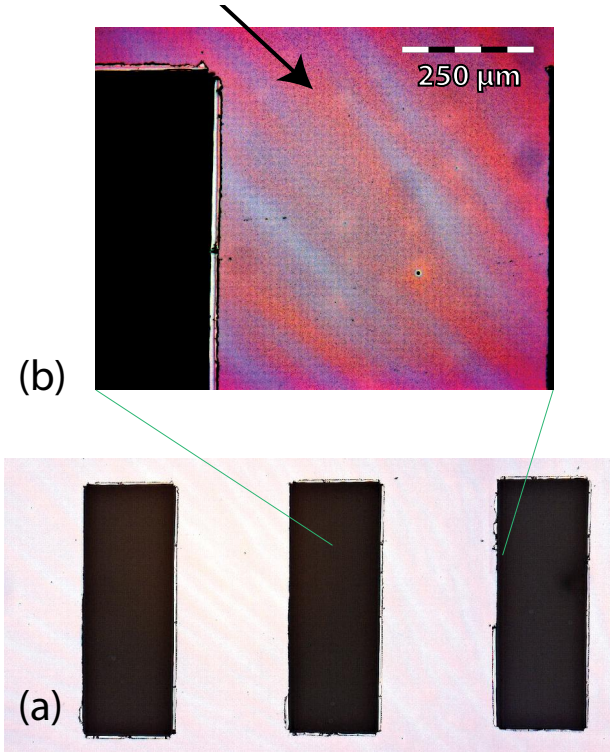

Figure 4.21 The PFN donor substrate for the pixels on the receiver substrate in figure 4.19a, transferred at laser fluences of 85 (left), 75, and 62 mJ/cm^2 (a), and a close-up on the gap between the 75 and 62 mJ/cm^2 ablation craters, with the contrast increased to show the periodic pattern more clearly (b).

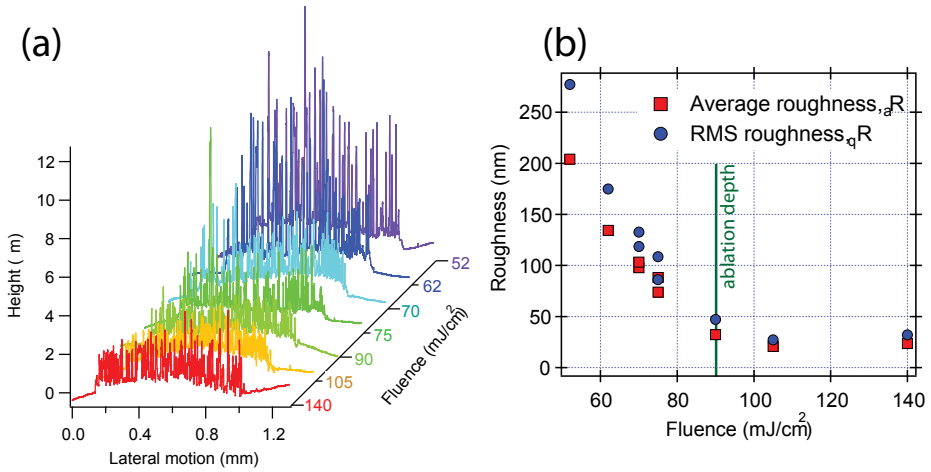

Figure 4.22 The surface roughness of PFN pixels transferred at different fluences. The roughness values (b) were calculated from the surface profiles in (a). The green line indicates the fluence ($\sim$ 90 mJ/cm^2) required for frontside ablation of the TP thickness [79].

but figure 4.22 shows how the PFN surface roughness increases as the fluence decreases. The pre-transfer PFN film on the donor substrate is very smooth, with a roughness of less

than 4 nm compared with the transferred values in figure 4.22e.

The microscopy images in figures 4.23a-c show the nature of the roughness, with a mosaic pattern that increases as the fluence decreases. Below 50 mJ/cm^2, and above 140 mJ/cm^2, effectively no transfer was observed. The pixel from transfer at 52 mJ/cm^2, figure 4.23a, shows has dark yellow and purple colouration which decreases in intensity at the higher fluence transfers, figures 4.23b and c. In combination, there is a mosaic pattern, the outline of which probably provides the ridges which contribute to the large surface roughness in figures 4.22d and e. The mosaic pattern becomes finer as the fluence increases. The combination of the colour differences and the coarse mosaic structure points towards distortion of the film in the transfer process.

In order to understand these observations, possible differences in the transfers at different fluences need to be considered. Firstly, more TP will be ablated at higher fluences. In fact, about 80mJ/cm^2 is required to fully ablate 190 nm TP in the 'frontside' ablation configuration [147], meaning that some TP should remain un-ablated on the pixel for the transfers at 52 and 70mJ/cm^2, figures 4.23a and b. In addition to the greater ablation depth of the TP, the thermal build-up in the PFN layer will be higher at higher fluences, and the flyer (flyer = pixel when being transferred) will also travel faster across the gap at higher fluences [159].

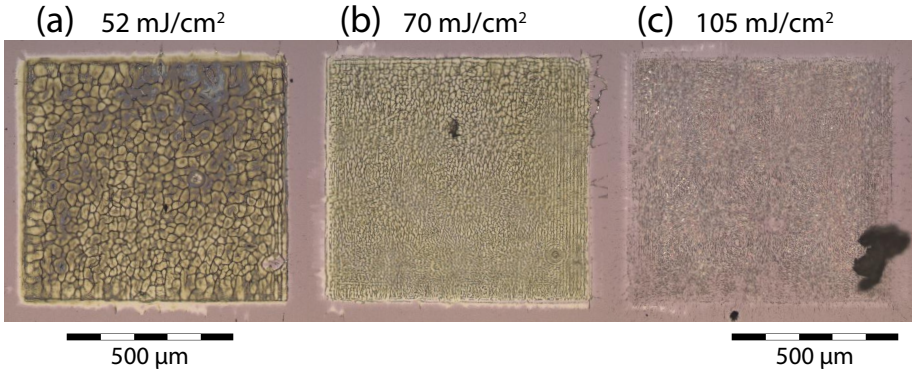

Figure 4.23 Light micrographs of single-layer PFN pixels transferred at 52 mJ/cm^2 (a), 70 mJ/cm^2 (b), and 105 mJ/cm^2 (c).

The difference between TP ablation depths is probably the best explanation for the different interference colours of the PFN pixels in the micrographs in figures 4.23a-c, but the mosaic pattern is not easily explained by more or less triazene polymer ablation. Nevertheless, similar observations have been made from triazene ablation firstly in shadowgraphy of single-layer TP films, where the flyers showed clear morphological distortion [159], and secondly in the microscopy of transferred polymeric pixels 'in contact', where similar pixel surface roughness was observed for both single-layer TP films [147] and gelatine films with a TP DRL [168]. The mechanism behind these morphological distortions is not yet understood, but is probably derived from a thermal and/or a mechanical origin [163].

Early research into triazene surface modification by UV laser modification shows a remarkably similar pattern to the mosaic pattern in figure 4.23a [144]. In the previous research, the boundaries were troughs rather than peaks, therefore termed 'volcanos' structures, and the consequence of 250 pulses of 36 mJ/cm^2 248 nm irradiation. This is obviously a very different mechanism of formation, but the similarity between the patterns points towards a common laser-based origin.

4.5.4 Conclusions from PFN pixel fabrication

Comparing the normal LIFT technique to the sequential LIFT technique is fascinating. It has been thought that the polymeric layer stabilises the metal layer before [152], but the idea that the metal layer stabilises the polymer is less obvious. Nevertheless, the difference between the normal LIFTed pixels in figure 4.19 and the single-layer PFN pixels in figure 4.23 is amazing. The roughness of the single-layer PFN pixels is also remarkable, with peak heights reaching over 10 μm. In addition, it is interesting that the PFN pixel roughness appears to level off at approximately the fluence where all the TP should have been ablated by frontside ablation $\sim$ 90 mJ/cm^2.

Chapter 5

Organic light-emitting diode functionality and characterisation

This chapter concerns OLED functionality. The terminology can be confusing, and for this reason it is clarified here. *LIFTed pixels* or *LIFT pixels* are the OLEDs fabricated using LIFT. *Conventionally fabricated devices* or *conventional devices* are those OLEDs made using the 'conventional' approach, i.e. standard ITO anode-up architecture with standard thin film deposition methods before patterned thermal evaporation of the cathode, but using exactly the same materials as the LIFTed OLEDs. This means that *conventional devices* usually refer to devices fabricated in this study, rather than the best literature equivalents. Where literature devices have been looked at, this is made clear. Finally, although 'devices' could refer to both types of OLEDs, it is used to refer only to conventional devices, apart from when talking about 'device characteristics' which has been used to refer to the electrical characteristics of an OLED, LIFTed or conventional. In general, when referring to both LIFTed and conventional devices, the words 'OLED' or 'PLED' are generally used without any clarifying adjective (LIFTed or conventional).

5.1 MEH-PPV PLEDs[1]

5.1.1 Specific experimentals

The devices in this section consist of: anode / LEP / Al, where the anode was always 140 nm ITO / 50 nm PEDOT for conventionally fabricated devices, and was just ITO or ITO / 50 nm PEDOT:PSS for the LIFTed pixels. For the LIFT donor substrates, 150 nm TP was used with 80 nm evaporated Al before the LEP layer. Donor substrates were either just ITO (140 nm) on glass, or 50 nm PEDOT:PSS / ITO. The LIFT process has been outlined in section 4.1, and is summarised in figure 5.1. The donor and receiver substrate are 'in contact', and the LIFT process is done at atmospheric pressure.

[1]The data from this section was published as part of [153].

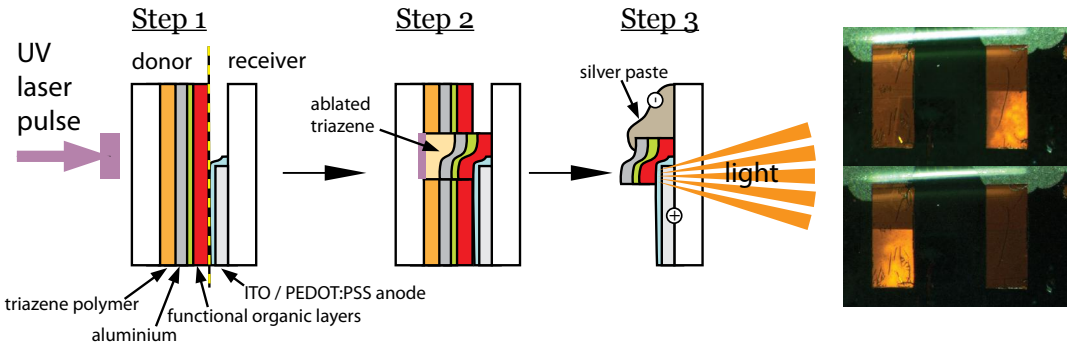

Figure 5.1 The scheme outlining the LIFT process to fabricate MEH-PPV PLEDs, taken from figure 4.1 in section 4.1, with the resulting pixels.

The pixels in this section build directly upon the first transfer of an MEH-PPV OLED using LIFT [118]. The transfer conditions are essentially the same – 'in contact' at atmospheric pressure – but there is an attempt to improve the device performance by adding layers to aid charge injection. In particular, a PEDOT:PSS layer has been added to the anode [135, 136], and PEO has been added to the cathode; both as an interlayer between the MEH-PPV, and as a blend with the MEH-PPV [128, 130, 131].

MEH-PPV and 9:1 MEH-PPV:PEO chlorobenzene solutions with a concentration of 0.8 wt% were made. These solutions were filtered through 1 μm PTFE filter and spin-coated at 1500 rpm. These gave films of $\sim$ 70 nm, but because of the poor film-forming capabilities of MEH-PPV, the error was around 10 nm, which has a significant effect on the operating voltage. For this reason, the electric field strength (Voltage / LEP thickness) has been used instead of the voltage. The PEO film was made from 0.2 wt% PEO solution in acetonitrile, spin-coated at 6000 rpm, giving a film thickness of 7 nm $\pm$ 4 nm. Three different PLED LIFT donor stacks were made: 150 nm TP / 80 nm Al / MEH-PPV (single-layer); TP / Al / PEO / MEH-PPV (bilayer); TP / Al / MEH-PPV:PEO (blend).

5.1.2 Conventional MEH-PPV devices

Devices were conventionally fabricated to characterise the MEH-PPV polymer's electroluminescence (EL) and to act as control devices for the pixels fabricated using LIFT. PEDOT:PSS was added onto the ITO anode to act as an hole-transporting layer (HTL). Whilst this will not particularly improve hole-injection because injection from ITO is already good – the ITO work function ($\sim$ 5.1 eV) is well matched to the HOMO of the MEH-PPV ($\sim$ 5.2 eV) – there are good reasons to use an intermediate PEDOT:PSS layer to improve device reliability and lifetime [135, 136].

The addition of a PEO layer shows mixed results for device performance. Figure 5.2 a shows how the operating electric field strength increases, but figure 5.2 b shows the im-

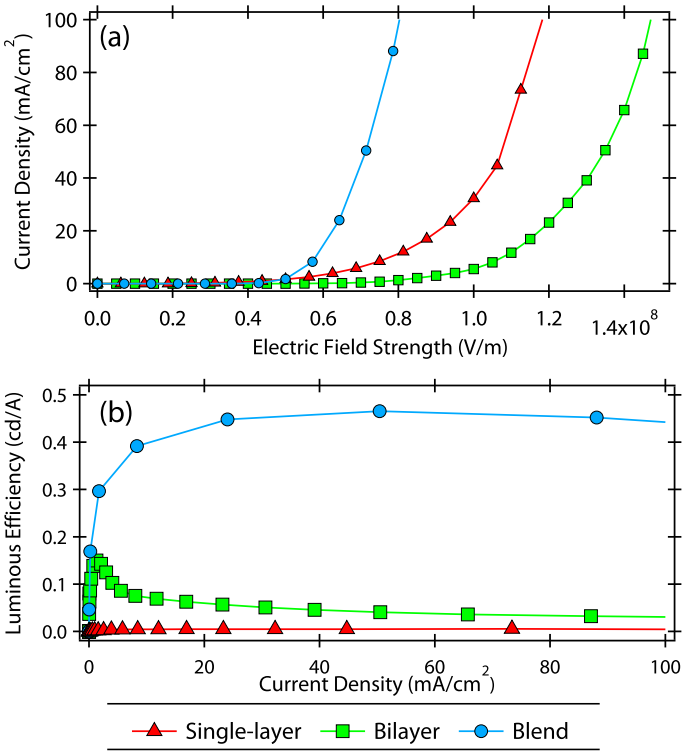

Figure 5.2 (a) Current density as a function of electric field strength, and (b) luminous efficiency as a function of current density for the three types of conventionally fabricated devices. The crosses represent bilayer devices; the solid squares represent blend devices; the hollow circles represent single-layer devices.

proved luminous efficiency of more than an order of magnitude greater than that obtained with single-layer MEH-PPV devices. The positive effect of a thin PEO film on electron injection has been observed before [131, 169], but the mechanism is debatable. The third type of device that we fabricate was a MEH-PPV:PEO blend, which showed even better device performance than the bilayer devices with a luminous efficiency (LE) over two orders of magnitude larger, and an operating electric field strength of about a half. Blend devices show a maximum luminous efficiency of 0.45 cd/A and a brightness of 400 cd/m^2 at $0.7 \cdot 10^8$ V/m. This is in comparison to single-layer devices which have a maximum LE of 0.004 cd/A and a brightness of 3.6 cd/m^2 at $1.1 \cdot 10^8$ V/m. The single-layer devices present similar efficiencies to the best MEH-PPV devices reported in the literature [130].

A mechanism whereby oxygen atoms from poly(ethylene glycol) (PEG) coordinate with aluminium atoms to form an ultra-thin layer of interfacial n-type MEH-PPV (which would move the recombination zone further away from the quenching aluminium cathode) has been proposed to explain the electron-barrier lowering phenomenon that was observed in a MEH-PPV:PEG blend [128]. This mechanism can also be applied to a MEH-PPV:PEO blend as PEO incorporates the same monomeric chemical structure as PEG, but with a much greater molecular weight. A similar effect has been observed with other polar polymers

and surfactants [170] after earlier research on metal cation-containing surfactants with the surfactant both blended and single-layered [171]. In the last study an explanation was taken from the hypothesis that a self-assembled monolayer of orientated dipoles chemically attached to the electrode will have an electric field across the dipole layer which will increase the open circuit voltage [172]. Interfacial dipole layers are indeed well known to induce considerable surface potential shifts and may well reduce the energy barrier for electron injection [173]. A stable interfacial layer may also act as a barrier to aluminium diffusion into the organic layers [174, 175]. Another mechanism which should be kept in mind is phase separation of the blend [176] because this would probably have an effect on the depth distribution of PEO in the final films, as well as making lateral structures which would influence device characteristics.

The self-assembling dipole layer is a reasonable explanation for the effect of simply adding PEO, but there is another interesting observation from the bilayer device characteristics. At low current densities there is a big peak in the luminous efficiency below 5 mA/cm^2, observable in figure 5.2b. Figure 5.3 shows the current density and luminance plotted against electric field strength. In figure 5.3b the shape of the luminance curve can be seen to differ with respect to the current density. This is in contrast to both the single-layer and blend devices (figures 5.3a & c) where the luminance and current density curves match each other almost identically. In conjunction with the increased operating electric field strength, one possible explanation for this heightened LE in the bilayer devices is that the PEO is forming an insulating layer. It has been observed that PEO is a good hole blocker and promotes electron injection when present as 10 nm films, with a calcium cathode [169]. The PEO layer in this work is less than 10 nm thick, but thick enough (7 nm $\pm$ 4 nm) to act like the insulating layer of a capacitor. The layer is thin enough that current may possibly pass through the PEO by electron field emission which would benefit the luminance in particular by moving the recombination zone away from the quenching aluminium cathode to the other side of the PEO film. However, there will also be migration of aluminium into the PEO; aggregate formation and diffusion from the initial evaporation [174, 175], which will then be annealed by applying a bias [177]; secondly by possible oxide barrier-layer formation, if there is any contamination [178, 179]; and finally by electric field induced diffusion, if the bias applied is large enough [180]. As the electric field across the PEO film increases, electron tunnelling across the PEO will also increase, but eventually there will be a breakdown of the dielectric barrier by the formation of aluminium channels through the PEO from the mechanisms mentioned above. In this case it would be expected that the original electron tunnelling, and corresponding luminous efficiency (LE) peak observed, will disappear if a second L-J-V run is made. For subsequent runs, there is indeed no initial LE peak, the operating voltage (or electric field strength) decreases, and the open-circuit voltage also increases. The latter observation suggests that a dipolar layer, similar to that proposed for the MEH-PPV:PEO blend, then acts as the main component of the MEH-PPV / Al electron-injecting interface, rather than a tunnelling-inducing dielectric

PEO layer.

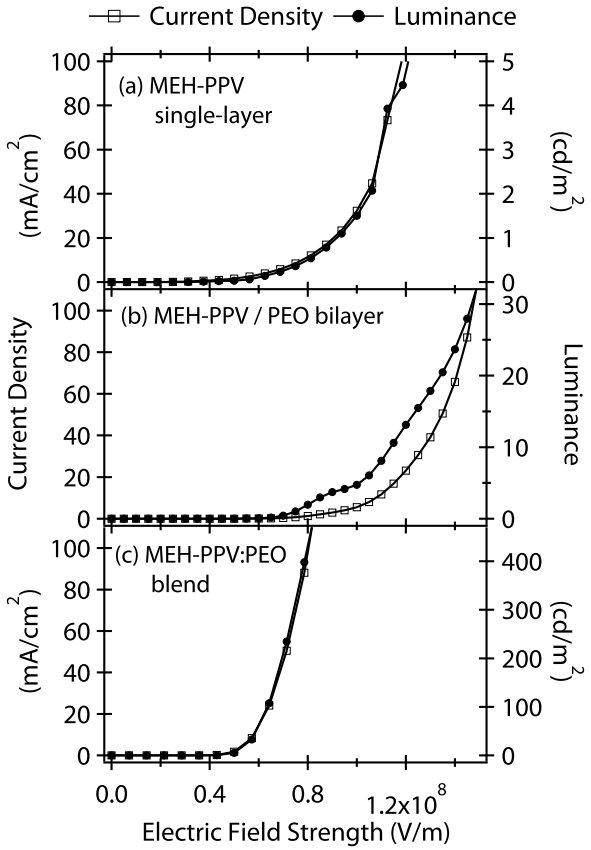

Figure 5.3 Current density and luminance as a function of electric field strength for the three types of conventionally fabricated devices: (a) single-layer, (b) bilayer, and (c) blend. The solid circles are the luminance, and the hollow squares are the current density.

5.1.3 LIFTed MEH-PPV pixels

Figure 5.4 shows J-V curves (a) and luminous efficiency vs current density (b) for six different device architectures, fabricated by LIFT (LIFTed pixels). Before analysing the device performances, it must be taken into account that the pixels without PEDOT:PSS were transferred at $\sim$ 250 mJ/cm^2, whilst those with PEDOT:PSS were transferred at $\sim$ 90 mJ/cm^2. The transfer of these pixels is investigated in section 4.1. Figure 5.4a shows that the pixels transferred onto plain ITO have a higher leakage current than those transferred onto PEDOT:PSS. The plain ITO anode pixels also have very low efficiencies when compared to the pixels made with PEDOT:PSS, seen in figure 5.4b. These observations are easy to explain, because the samples were transferred at much higher fluences which increases the thermal and mechanical load on the pixel, increasing the chance of the aluminium short-circuiting the LEP, although the lack of a PEDOT:PSS 'buffer' layer may also increase the chance of short-circuits. It is harder to compare the J-V curves of the different LEP compositions,

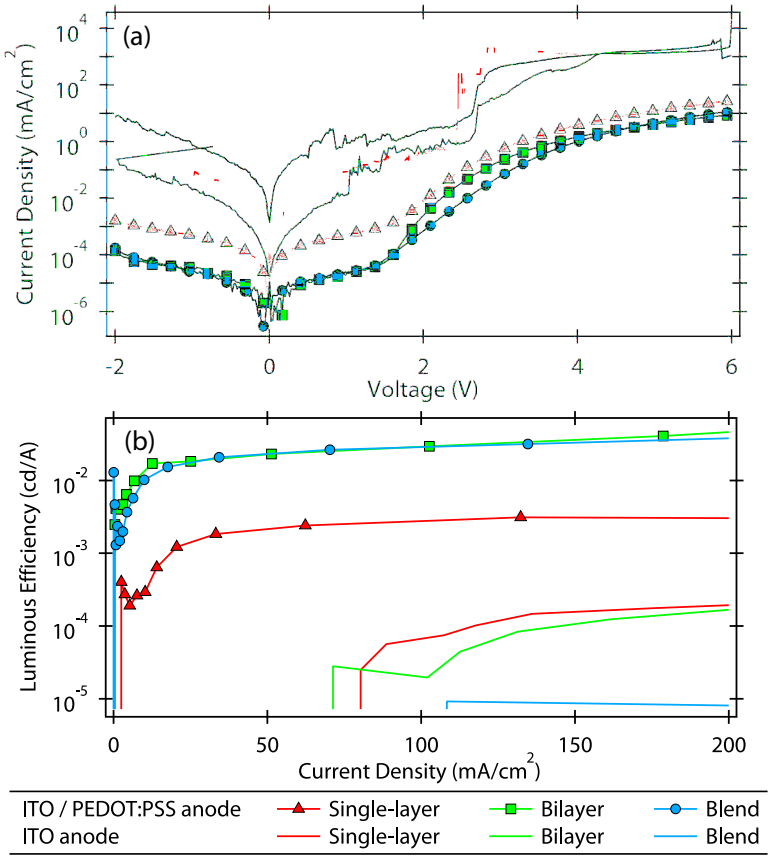

Figure 5.4 Transferred device characterisation, showing all six different types of pixels. (a) shows how the current density varies as a function of voltage. (b) shows the luminous efficiency of these pixels as a function of current density, on the first I-V run (see figure 6 for a graph of how these values changed with subsequent runs).

but the one thing that is distinguishable is a slightly higher current for single-layer MEH-PPV on PEDOT:PSS at lower voltages which is perhaps because the single-layer MEH-PPV film was 60 nm thick whereas the bilayer and blend films were 70 nm thick. The efficiencies of the pixels transferred onto PEDOT:PSS shown in figure 5.4b demonstrate that the single-layer MEH-PPV pixel has a considerably lower luminous efficiency compared to both PEO-containing pixels. However, this difference is only so large for the first operation run; figure 5.5 demonstrates that this first run acts as a sort of electrical annealing step, and improved pixel device performance is subsequently observed.

Being exposed to ambient conditions, the LIFTed pixels are possibly limited by oxygen and water damage of the organic layers and the electrodes [178, 181]. Water uptake by the hygroscopic PEDOT:PSS and ITO on the receiver substrates is most likely to be the main source of contamination [135, 136]. This aside, the pixels still show good device characteristics. On the first run, it appears that the pixels show the differences expected from those observed with conventionally made devices, but subsequent runs show a distinct change, shown in figure 5.5. The single-layer pixel initially shows an efficiency of around 0.003

cd/A at a fairly high electric field strength of $1.8 \cdot 10^8$ V/m. However, after this initial I-V run the efficiency jumps up to above 0.01 cd/A and reaches nearly 0.03 cd/A at a much lower electric field strength of $1.3 \cdot 10^8$ V/m. In figure 5.5b, both the PEO bilayer and blend pixels have efficiencies that start off above 0.01 cd/A and increase considerably on subsequent runs, although not above 0.1 cd/A. The tunnelling peak observed for the conventionally fabricated MEH-PPV / PEO bilayer devices (in figure 5.2b) is not observed for the LIFTed devices. In fact, the bilayer pixel exhibits marginally better device performance than the MEH-PPV:PEO blend pixel. The reason for the lack of a dielectric layer could be that the PEO film is redissolved by the MEH-PPV solution subsequently spin-coated on top of the PEO layer on the LIFT donor substrates; PEO powder is soluble in chlorobenzene, as seen in the MEH-PPV:PEO blend solutions. If the PEO layer is redissolved, we would expect the blend and bilayer pixels to have the same performance. Indeed, the operating electric field strengths, both on the first runs and on subsequent runs, appear to be the same, and the luminous efficiencies are also very similar. The single-layer pixel seems to have a slightly higher initial operating electric field strength, but on the subsequent run the operating electric field strength comes down to that of the PEO-containing devices, figure 5.5a. The luminous efficiency, however, only reaches that of the PEO-containing devices on their first run, figure 5.5b.

The differences between the conventional devices and LIFTed pixels are not just constrained to the PEO-containing devices. The single-layer MEH-PPV LIFTed pixel, on the subsequent run, exhibits a LE an order of magnitude greater than the single-layer conventionally fabricated device (figure 5.2). One reason for this difference may be the different fabrication methods, particularly at the Al cathode interface. The aluminium evaporation directly onto the MEH-PPV in the conventional orientation is likely to have a detrimental effect on device performance. Evaporated aluminium will diffuse into the light emitting polymer (LEP), creating aggregates and a porous structure, and react with the top layer of the LEP [175]. This aluminium diffusion in the conventional device architecture effectively increases the surface area of the LEP / Al interface and therefore also increases the chances of exciton quenching relative to the chances of quenching at the smoother LEP / Al interface of LIFTed pixels. If there is PEO at the top of the LEP this will, in effect, make the polymer surface more reactive (similar to activating the surface with plasma treatment) and reduce metal diffusion into the polymer [182], which helps to explain why the PEO-containing conventionally fabricated devices exhibit such high efficiencies. For the LIFT donor substrates, the LEP is spin-coated on top of the stable Al film. Aluminium diffusion from evaporation, and the consequent porous interface [175], will not occur, and reactions with the LEP layer are much less likely with the spin-coating deposition process at room temperature. Two other methods of diffusion which may still occur for LIFTed pixels upon operation are the electric field induced ionic drift [180] and electric field driven metal diffusion and subsequent oxidation [178, 179]. However, by spin-coating on top of a uniform Al film to fabricate the LIFT donor substrates, a much more homogeneous and stable Al_2O_3

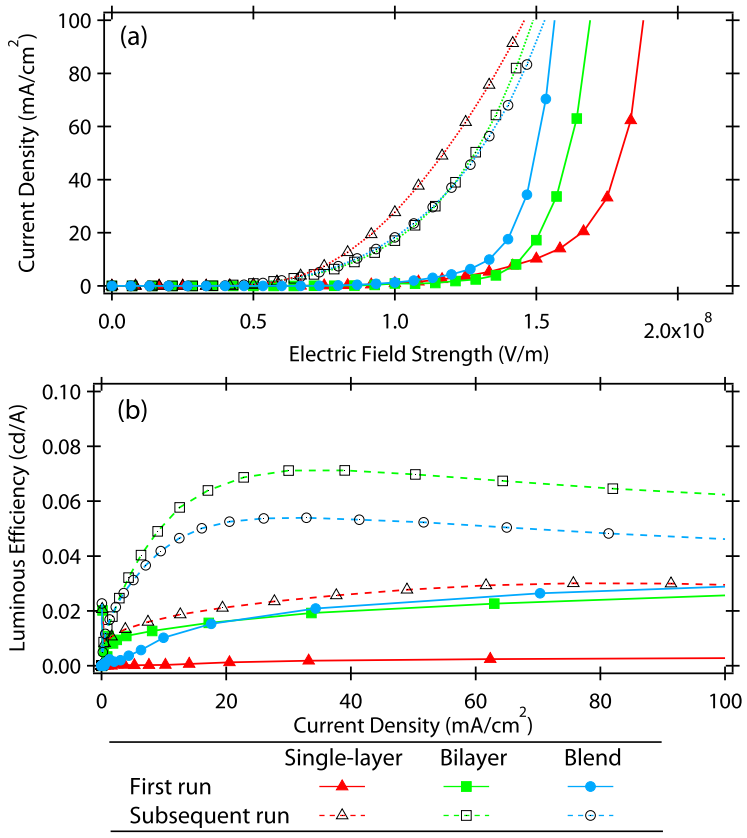

Figure 5.5 (a) Current density as a function of electric field strength, and (b) luminous efficiency as a function of current density for the three types of LIFTed pixels on a first I-V run (solid lines), then showing the change upon a subsequent run (dotted lines). The crosses represent bilayer pixels; the solid squares represent blend pixels; the hollow circles represent single-layer pixels.

barrier layer is likely to be formed as the Al / LEP interface, according to Mott's *Theory of the Formation of Protective Oxide Films on Metals* [179]. This oxide film may degrade the LIFTed pixels in terms of making them less conductive, but will also keep the cathode / LEP interface more uniform, reducing non-radiative quenching of the electron-hole pairs by polarons [183, 184]. It has been observed that local spikes during operation, which may be enhanced by a non-uniform cathode / LEP interface, will cause rapid device degradation [185].

The observation from figure 5.5 that the pixels improve on subsequent I-V runs after the initial run is very interesting. It appears to be linked to electrical thermal annealing, possibly simply removing oxygen and water contamination [186], but further work is needed to fully understand this phenomenon. None of the other types of pixels fabricated in this chapter exhibited the same improvement, but the conventional PFN device in section figure 5.5.2 also show improvement on the second run. Nevertheless, the mechanism for the LIFTed MEH-PPV pixels is almost certainly different from the that for the conventional PFN

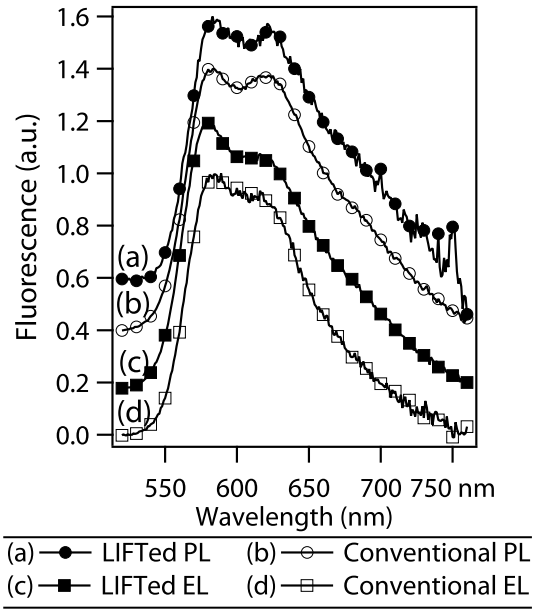

Figure 5.6 Fluorescence spectra of MEH-PPV:PEO films showing photoluminescence of (a) LIFTed pixels (on PEDOT:PSS / ITO), and (b) pristine LIFT donor; and electroluminescence of (c) a LIFTed pixel, and (d) conventionally fabricated device (both on PEDOT:PSS / ITO)

devices.

In figure 5.6 the photoluminescence spectra of LIFTed MEH-PPV:PEO pixels are in good agreement with the PL spectra of the pristine MEH-PPV:PEO film indicating that minimal thermal load was placed upon the MEH-PPV:PEO film during transfer. The spectra show the expected degree of aggregation of MEH-PPV films spin-coated from 1 wt% chlorobenzene solutions [187]. Also shown in figure 5.6, the electroluminescence spectra are in good agreement too, and may even hint at the recombination layer containing fewer aggregates than the average of the whole film, seen by the PL spectra. Heating above the glass temperature T_g, followed by rapid quenching may also reduce the aggregates in the LIFted pixel.

Two working pixels showing the distinctive orange-red electroluminescence are shown in figure 5.7. The area where the transferred pixel overlaps with the ITO on the receiver substrate, i.e. where electroluminescence is observed, is the *LIFTed pixel*. Some cracks in the aluminium can be seen clearly through the MEH-PPV, indicated by green arrows, and the heterogeneity of light intensity across the device is visible too, but the EL functionality is clearly maintained. These cracks are fairly remarkable, and appear to be brittle deformation in both the MEH-PPV and the bilayer indicating that the pixel comes under significant stress during the transfer process. This could be thermo-mechanical from either or both rapid heat quenching and the mechanics of the LIFT process: flight and impact.

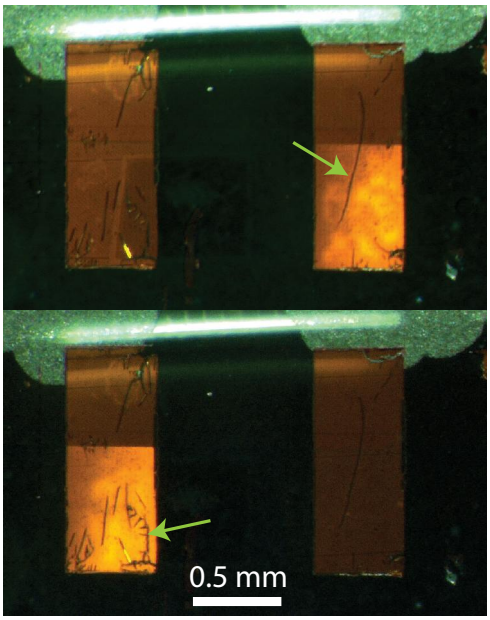

Figure 5.7 Electroluminescence from two LIFTed pixels with the architecture ITO / PEDOT:PSS / MEH-PPV:PEO / Al. They are shown side-by-side to illustrate the contrast between their on and off states. The light-emitting section of the diodes (the lower half) is where overlap between the aluminium cathode and the ITO anode occurs.

5.1.4 MEH-PPV PLEDs conclusions

These results are the first OLED pixels deposited in this work, and follow on directly from earlier work of our group [118]. They confirm that OLEDs can be fabricated by LIFT, but raised the question of where to start to optimise the devices. The addition of PEDOT:PSS onto the ITO receiver substrate is a good first step to improve not only pixel device performance, but also to improve the LIFT process (see section 4.1). By reducing the fluence required for transfer from 250 mJ/cm^2 to 80 mJ/cm^2, the pixels exhibit far superior and more reliable device characteristics than the devices LIFTed onto plain ITO. In addition, cracks seem to be prevalent in MEH-PPV pixels, as was observed in the earlier work [118]. The cracks could well be brittle deformation from the flight and impact of the flyer during the LIFT process. Another logical explanation for the cracks is that the temperature raised above the MEH-PPV glass temperature (T_g) of 75 °C [188] and then cooled rapidly, cracking in either process of rapid heating or cooling (or both). An equally good, if not better, EL spectra than the conventionally fabricated device could also be due to heating the film above T_g before rapid quenching helping to remove aggregates.

PEO definitely helps MEH-PPV, but not only, or even primarily, through the simple dielectric layer originally posited. The improved efficiency of PEO-containing devices can be well explained by a self-assembling dipolar monolayer theory [172], although there is evidence for a little electron field emission with the conventional PEO layer device. The LIFTed pixels, compared with the conventionally fabricated devices, show a different pat-

tern in device performance, presumably because of the inverted deposition of the LIFT donor substrate changing the nature of both of the interfaces. The overall performance of the LIFTed PEO-containing pixels was slightly lower than for conventional devices, possibly because of oxygen and water damage by putting the substrates together in air or because of phase separation of the blend, but the plain MEH-PPV device showed elevated performance, presumably mainly due to the different LEP / Al interface.

5.2 Preliminary PFO OLEDs

5.2.1 Specific experimentals

Building on the MEH-PPV devices in section 5.1, PEDOT:PSS was always coated on the ITO anode. The use of PVK as a hole-transporting layer for PFO became an interesting possibility, particularly with the phosphorescent dopants (see section 2.1.3 and references [32, 189]). For this reason, the earliest experiments used both a single PEDOT:PSS HTL and PEDOT:PSS / PVK bilayer HTLs. Quickly it became clear that LIFTed PFO devices were much better with PVK, and so the multilayer ITO / PEDOT:PSS / PVK became the standard anode architecture, with 60 nm PEDOT:PSS and 40 nm PVK used. For the conventional architecture, high molecular weight PVK (*typical* M_w *= 1,100,000*) was needed in order to prevent redissolving of the PVK layer by the PFO solution [32].

All the devices made in this section and the next section 5.3 are based on poly(9,9-dioctylfluorenyl-2,7-diyl) capped with poss (PFO). The chemical structures of the PFO and the dyes, iridium(III) tris(2-(4-totyl)pyridinato-N,C2) (Ir(Me-ppy)$_3$) for green emission and iridium(III) bis(2-(2'-benzo-thienyl)pyridinato N,C3')(acetyl-acetonate) (btp$_2$Ir(acac)) for red emission, are shown in the experimental section 2.1.3, figure 2.2. Charge transfer to fluorescent or phosphorescent dyes was looked at in the introduction section 1.1.2.1. Iridium dyes have been used, which should at least exhibit fluorescence via Förster energy transfer from the larger HOMO-LUMO energy level gap of the PFO. For the preliminary pixel devices in this section, doping ratios of 10 wt% (green) and 2 wt% (red) were used, unlike the 5 wt% for both colours with the optimised PFO pixels. These were dissolved in the standard toluene:*p*-xylene (1:1) solution to make up 15 mg/ml solutions, and the thicknesses obtained were almost identical to the pure PFO films, 80 nm ± 10 nm.

Three different donor substrates are used with the blue, green and red LEP layers on them. Figure 5.8 summarises the LIFT process and all three depositions required to create three coloured pixels side-by-side. Of course, for individual device analyses, only one type of pixel was deposited onto a single receiver substrate. The first step (5.8c & d) is shown in detail, where the UV laser pulse is approaching the donor substrate consisting of a UV-transparent substrate coated with: firstly, a layer of the photolabile triazene polymer DRL, secondly, the metal cathode layer, and finally, the LEP layer, as shown in figure 5.8a. In this section silver, silver coated with a thin evaporated layer of Cs_2CO_3, and aluminium

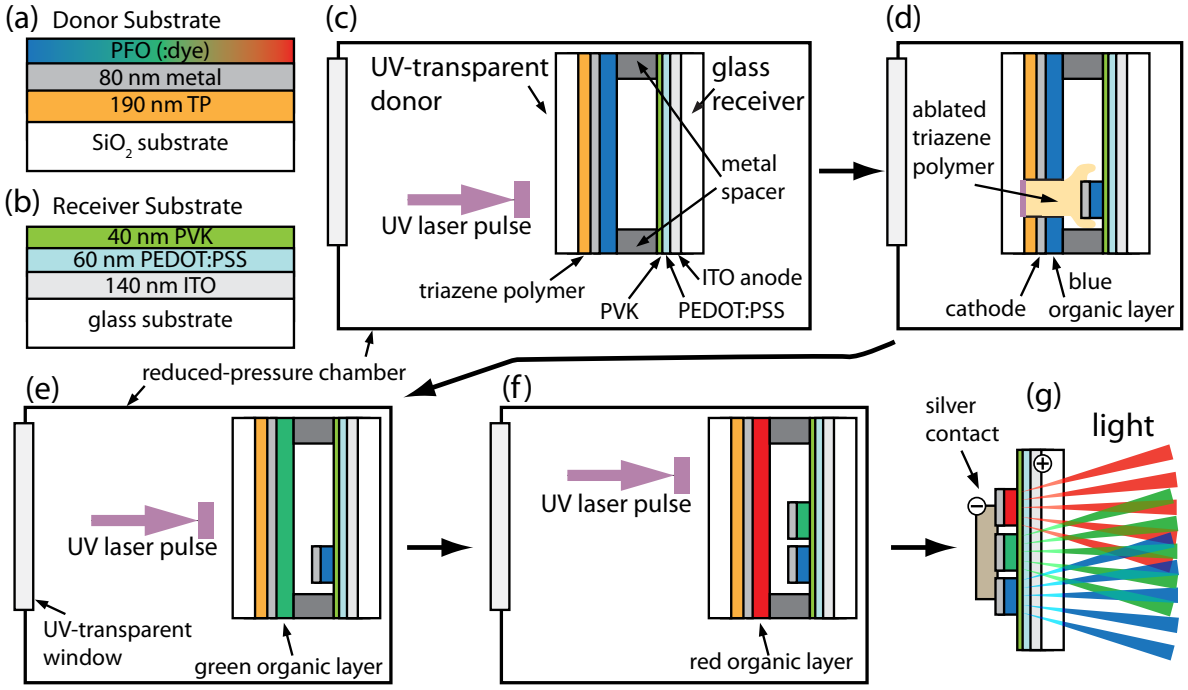

Figure 5.8 This scheme summarises the LIFT process for three colour OLED pixels based on PFO, as demonstrated in both this section 5.2 and the next section 5.3. The 1-D substrate architecture is shown for the LIFT donor substrate (a) and the receiver substrate (b). (c) shows the overall setup within the reduced-pressure chamber, with the donor substrate of the first PLED colour (blue), and the laser beam approaching; (d) shows the transfer of the blue pixel, and the triazene gas which provides the force to do the transfer; (e) shows the setup with the green PLED donor substrate and the receiver substrate with the blue pixel already transferred; (f) shows the setup with the red PLED donor substrate and the receiver substrate with the blue and green pixels already transferred; (g) shows the final receiver substrate, with all three colours side-by-side, and a bias across the devices creating light.

have been used as the cathodes, and the LEP layers are thicker than in section 5.3. The receiver substrate is made up of a glass slide coated with a patterned indium-doped tin oxide (ITO) layer and hole-transporting layers (HTLs) which aid the hole injection into the LEP, outlined in figure 5.8b. Figure 5.8d shows the laser beam being absorbed by the photolabile triazene DRL, which decomposes to gaseous products that generate a pressure force on the overlying layers and transfer them to the receiver substrate.

Building on the optimisation work in section 4.2, a gap was introduced along with a reduced environmental pressure. The Al (/ TBA) / LEP multilayer is propelled across a gap of $\sim 15\ \mu$m, defined by a spacer, and deposited onto the receiver substrate at a pressure of 1 mbar. Figures 5.8e & f show the use of different coloured donor substrates, and figures 5.11c & d illustrate the final result, tri-coloured pixels, side-by-side.

For conventionally fabricated devices, the LEP was spin-coated directly onto a LIFT receiver substrate, and the cathode evaporated directly onto the LEP (patterned using a proximal/contact mask).

Table 5.1 Device performances for various conventionally fabricated devices, at a current density of ∼ 40-50 mA/cm^2. Blue, Green and Red refer to the LEP layer, whether just plain PFO (Blue), or doped PFO (Red and Green).

Colour	Cathode	Bias [V]	Current Density [mA/cm^2]	Luminance [cd/m^2]	LE [cd/A]
Blue	*Ag*	19	42.7	29.4	0.069
	Ag/Cs_2CO_3	14	53.2	816.9	1.54
	Al	21	31.1	0.73	0.0023
Green	*Ag*	32	43.1	391.2	0.91
	Ag/Cs_2CO_3	22	36.9	885.2	2.4
	Al	37	48.3	134.6	0.28
Red	*Ag*	33	48.6	114.1	0.24
	Ag/Cs_2CO_3	21	30.8	299.1	0.97
	Al	42	41.7	49.8	0.12

5.2.2 Effect of different colours, cathodes, and laser fluence

Conventional devices

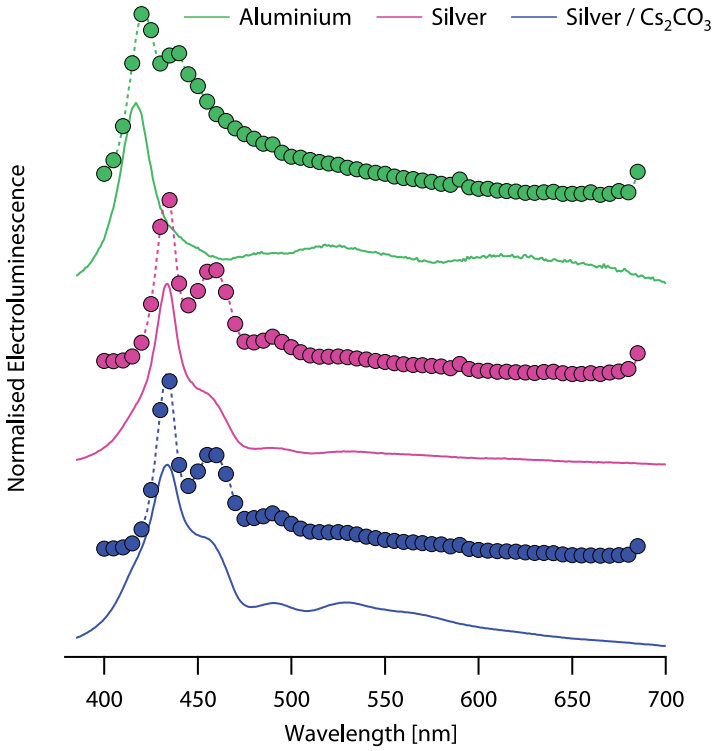

Figure 5.9 The electroluminescence (solid lines) and photoluminescence (dashed line with solid circles) spectra of conventional blue PFO devices with three different cathodes: Al, Ag, and Ag / Cs_2CO_3.

The fabrication process of the preliminary LIFTed PFO pixels is outlined in section 4.3.2, and the progress in pixel morphology can be seen in figure 4.12. Various device architec-

tures were used, with three different LEP layers based on PFO – emitting blue, green, and red light – and three different cathodes: silver, silver / Cs_2CO_3, and aluminium. Silver was used as the metal layer in the transfer optimisation studies in section 4.2, and the results of device characterisation measurements of conventionally fabricated PFO devices, in table 5.1, show that the devices with silver electrodes demonstrated better functionality than those with aluminium electrodes, for all three colours. An evaporated caesium carbonate (Cs_2CO_3) layer was also added between the LEP and the silver to aid electron injection, and this indeed helped improve the devices further, lowering the operating voltages and improving the efficiency. These relative performances are slightly unexpected, because aluminium would be expected to help electron injection better due to its smaller work function, but due to various factors it appears that silver is often better than aluminium [23]. This could be due to detrimental factors of the use of aluminium, such as those outlined in section 5.1, for how the aluminium can migrate into the PFO: firstly, via aggregate formation and diffusion from the initial evaporation [174, 175], which will then be annealed by applying a bias [177]; secondly by possible oxide barrier-layer formation, if there is any contamination [178, 179]; and finally by electric field induced diffusion, if the bias applied is large enough [180].

The EL and PL spectra of the three blue (plain PFO) conventionally fabricated devices is given in figure 5.9. These all clearly show the blue emission peak, with some small green emission in the cases of Ag / Cs_2CO_3, and Al. Interestingly, the principal blue peak for both silver cathodes is a red shifted peak relative to the principal for the aluminium cathode. This is particularly interesting when compared with the LIFTed pixel ELs in figure 5.10 where only the two Ag / Cs_2CO_3 pixels and the high fluence Al pixel have the principal peak at $\sim$ 435 nm rather than $\sim$ 420 nm for the other three pixels.

LIFTed pixels

LIFTed pixels were made with the same LEPs and cathodes as the conventional devices in table 5.1, and their device characteristics are shown in table 5.2. In addition to the different colours and cathodes, two different fluences were used for the transfer to investigate whether there was any significant variation in device performance in the fluence window for successful transfer. Successful transfer is simply where the pixel morphology appeared good on a large-ish scale, i.e. the fine surface morphology was not relevant (see section 4.2).

In table 5.2 the blue pixels show little or no difference between the high and low fluence pixels for all three types of cathode. This is not the case for red and green pixels, where, without exception, all of the pixels transferred at low fluence exhibit higher operating voltages. Efficiencies are different however, and the low fluence green pixels are all less efficient than their high fluence counterparts. The red pixels appear to have more similar efficiencies regardless of the fluence. One particular satisfying feature of the table is that all colours exhibit luminances of over 100 cd/m^2 at current densities of only 40-50 mA/cm^2.

Table 5.2 Device performances for various LIFTed pixel device architectures, at a current density of ∼ 40-50 mA/cm^2. The pixels were transferred either at HIGH FLUENCE (∼ 90 mJ/cm^2) or LOW FLUENCE (∼ 60 mJ/cm^2). The colours **Blue**, **Green** and **Red** refer to the LEP layer, whether just plain PFO (Blue), or doped PFO (Red and Green). The *Ag*, *Ag*/Cs_2CO_3, and *Al* refers to the cathode material.

		LOW FLUENCE				HIGH FLUENCE			
		Bias	**CD**	**Lum**	**LE**	**Bias**	**CD**	**Lum**	**LE**
Colour	**Cathode**	**[V]**	**[mA/cm^2]**	**[cd/m^2]**	**[cd/A]**	**[V]**	**[mA/cm^2]**	**[cd/m^2]**	**[cd/A]**
	Ag	30	47.7	19.6	0.041	30	52.7	20.1	0.038
Blue	*Ag*/Cs_2CO_3	26	48	125.9	0.26	26	50	161.4	0.32
	Al	19	56.3	283.5	0.50	19	42.3	212.1	0.50
	Ag	37	42.3	2.98	0.007	32	47	16.1	0.034
Green	*Ag*/Cs_2CO_3	31	52.3	65	0.12	24	48.7	132.3	0.27
	Al	29	44.3	92.8	0.21	27	49	134.1	0.27
	Ag	40	50.3	16.2	0.032	26	51	11	0.022
Red	*Ag*/Cs_2CO_3	29	43.3	47.4	0.11	25	43.7	43.3	0.099
	Al	25	48.3	103.3	0.21	24	51.3	127.9	0.25

This is particularly good when compared with the conventional aluminium devices in table 5.1, where, of the aluminium devices, only green devices give a luminance of over 100 cd/m^2. The conventional green Al device is only equally as efficient as the green Al LIFTed pixel (0.28 cd/A vs 0.21 & 0.27 cd/A), with a much higher operating voltage (37 V vs 29 & 27 V). and the red and blue Al conventional devices are markedly less efficient than the red and blue Al LIFTed pixels (red: 0.12 cd/A vs 0.21 & 0.25 cd/A; blue: 0.0023 cd/A vs 0.5 & 0.5 cd/A), with higher operating voltages (red: 42 V vs 25 & 24 V; blue: 21 V vs 19 & 19 V).

There is a distinct trend in the blue (plain PFO) EL spectra, in figure 5.10a. A peak at ∼ 500 nm is always larger for the pixels LIFTed at higher fluence, irrespective of the cathode. This is not present in the PL spectra in figures 5.10b & c, suggesting that the green emission effect is happening at narrow depth range corresponding to the recombination zone. This is probably next to the cathode interface given the electron mobility in PFO. In terms of the effect of the cathode, there is a trend of an increase in the 500 nm peak from plain Ag, to Ag / Cs_2CO_3, to Al. This peak is generally associated with oxidation degradation of the PFO [190, 191]. This makes sense for explaining why the green peak may be higher for the higher fluence pixels, but it is harder to explain why the different cathodes show different green peak formation, particularly when it is barely present in the EL spectra of all three types of blue conventional devices in figure 5.9. The most logical explanation, given that higher fluences cause the green emission to increase, is that the Al conducts heat faster than the silver, and heats up the PFO film more than the pixels with Ag cathodes, creating more oxidation defects. However, silver conducts heat much more than aluminium [165] suggesting that there must be another aspect to the process. There is another explanation to do with aggregate/excimer formation [192], which could be linked

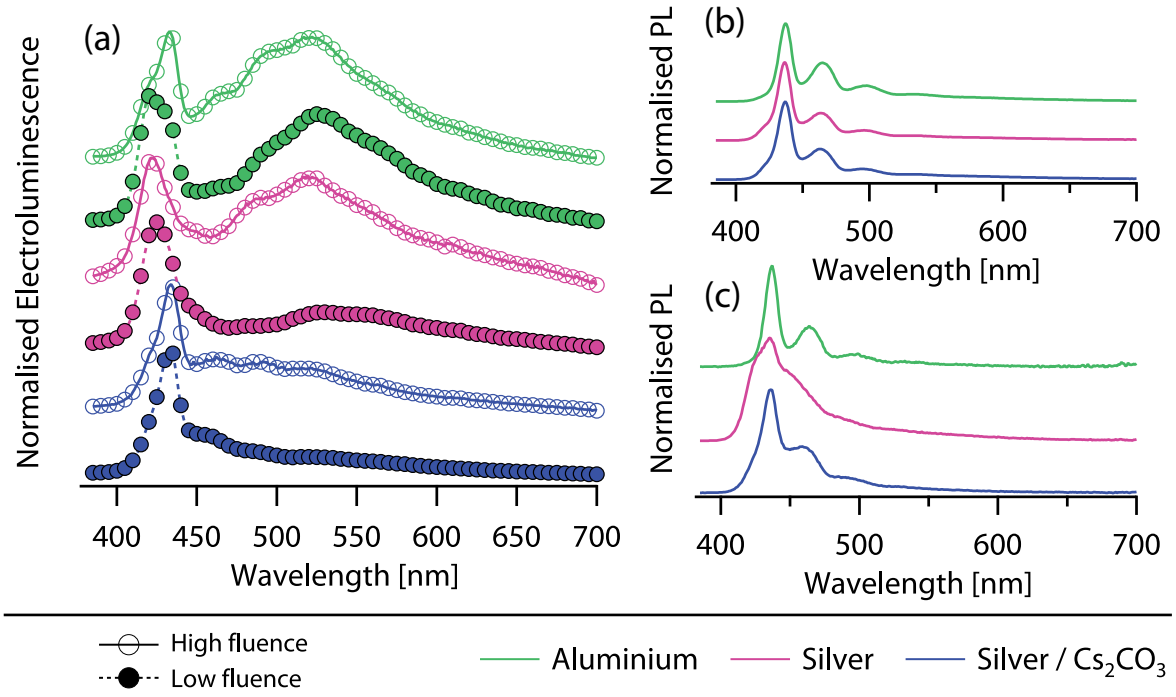

Figure 5.10 Three collections of different fluorescent spectra are shown: electroluminescence spectra of various LIFTed pixels with the architecture PEDOT:PSS / PVK / blue PFO / cathode, deposited at two different fluences (low = 60 mJ/cm^2 and high = 90 mJ/cm^2) (a); photoluminescence spectra of the pristine donor substrates (b); and photoluminescence spectra of the low fluence pixels (c). The spectra correspond to the blue Al, Ag, and Ag / Cs_2CO_3 pixels with the characteristics in table 5.2

to the reactivity of aluminium, even though it should have been passified partly before the PFO was spin-coated.

5.3 Optimised three-colour PFO OLED pixels[2]

5.3.1 Specific experimentals

In this section, all the PLEDs are again based on PFO. The devices in this section were all based on the architecture glass / 140 nm ITO / 60 nm PEDOT:PSS / 40 nm PVK / ∼ 50 nm light-emitting polymer (LEP) / Cathode, as optimised in the previous section 5.2.

The LEP was either plain for blue emission, or PFO doped with 5 wt% iridium(III) tris(2-(4-totyl)pyridinato-N,C2) (Ir(Me-ppy)$_3$) for green emission, or PFO doped with 5 wt% iridium(III) bis(2-(2'-benzo-thienyl)pyridinato N,C3')(acetyl-acetonate) (btp$_2$Ir(acac)) for red emission. For the LIFT donor substrates, the LEP was spin-coated at 1500 rpm onto the cathode, from a 10 mg/ml toluene:p-xylene (1:1) solution. From profilometry this was observed to give film thicknesses of 40 nm (± 10 nm). The conventionally-fabricated devices

[2]Results from this section have been published in reference [193].

were fabricated in the same way as the LIFT receiver substrates, but the LEP layer was then spin-coated on top of the PVK. 50 nm of calcium and100 nm silver were evaporated on top through a mask to make devices with a circular area of either 3.5 or 7 mm2. From the deposition of the LEP, all of the samples were kept in an inert nitrogen environment, and only exposed to air briefly when transferred into the reduced-pressure chamber for the LIFT experiments.

For the LEP, a single conjugated polymer system of a blue-emitting polyfluorene (PFO) is used; red and green emission are achieved by doping the PFO with iridium complexes. The device architecture is based on previous work by Cao and co-workers [32]. The LIFT deposited devices are referred to as a LIFTed pixel to differentiate them from conventionally fabricated devices.

The LIFT process used to fabricate these three-colour pixels is outlined in detail in section 4.3.1 with figure 5.8. The main differences between the preliminary LIFTed PFO pixels and the optimised ones in this section are that only aluminium was used for the cathode, coated with TBA for further electron-injection improvement, and the laser fluence was controlled more precisely to be around the optimal fluence, $\sim$ 75 mJ/cm^2. The pixels have a width of 500 μm, but smaller sizes as low as 20 μm should be possible (see section 4.3.4), providing the high resolution required for 300 ppi high-definition (HD) displays for handheld electronic devices.

5.3.2 Effect of different cathodes and colours

Figures 5.11c & d show light microscopy images of three coloured pixels, transferred side-by-side and illuminated by applying biases across the devices. An important feature of these devices is the colour contrast induced by the different doping of the LEP layer, which is also backed-up by the electroluminescent (EL) spectra in figures 5.11a and b. Figures 5.11a & b show the EL spectra of the LIFTed pixels with and without TBA, respectively, with the EL spectra of the conventionally fabricated devices in the background. The EL spectra of the LIFTed red and green pixels are not hugely different to the conventionally fabricated devices, but the blue devices show a significant shift towards green emission. Even if the two blue LIFTed pixels look slightly different, the EL spectra reveal that the spectral emission is actually the same. Any differences between the appearance of the pixel colours in figures 5.11c and 5.11d can be explained by differences in relative brightness. High wavelength emission of PFO has been investigated in detail by others, and the accepted explanation is triplet emission from oxidised keto-defects, but the mechanisms for the ketone formation are not well understood [191]. However, thermal annealing of the conventional devices caused no change in the blue EL spectrum, suggesting that the process may be linked to the fast dynamics of the LIFT process.

The blue LIFTed PFO EL spectra in figures 5.11a & b are particularly interesting when compared with the LIFted pixels with aluminium cathodes in figure 5.10. A particularly noticeable feature is that whilst there is significant green emission of the preliminary LIFTed

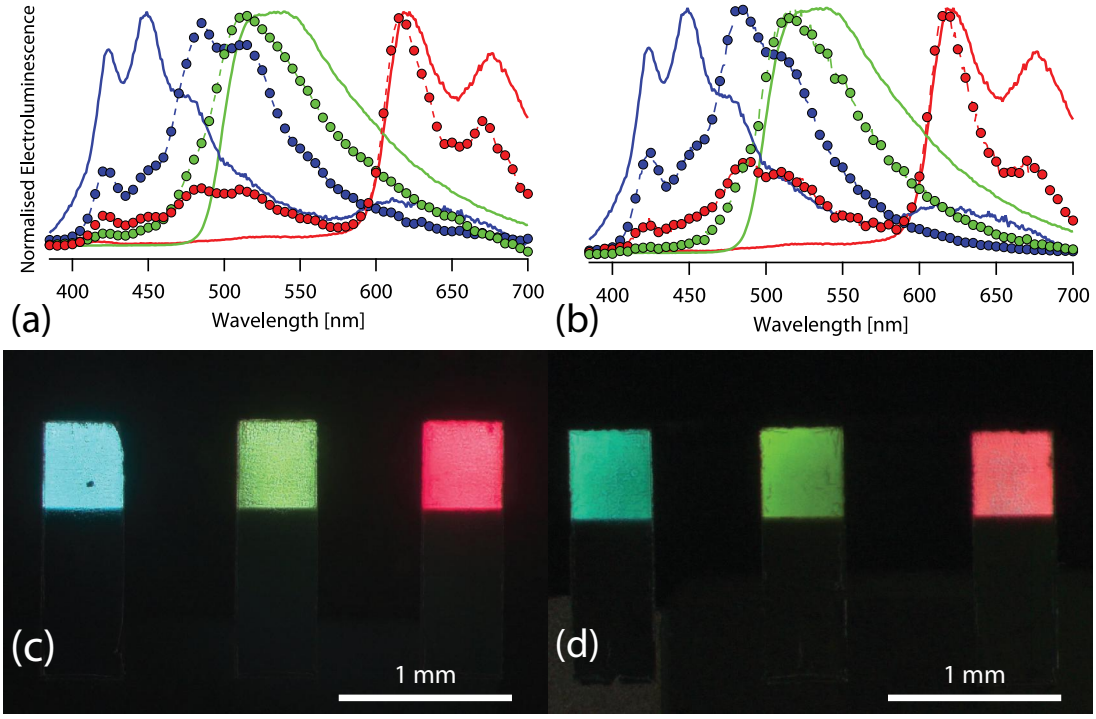

Figure 5.11 Electroluminescence spectra of tri-colour LIFT pixels with an Al / TBA cathode (a), and with an Al cathode (b). On both graphs the conventionally fabricated conventionally fabricated devices' EL spectra are shown with a solid line and a colour corresponding to the relevant device. The blue pixels are represented by the blue squares, the green pixels are green triangles, and the red pixels are red circles. Tri-colour pixels imaged using a light microscope are shown in (c) and (d). The pixels in (c) are made using an Al / TBA cathode, and have a bias of 20 V applied across them. The pixels in (d) are made with a plain Al cathode, and have a bias of 24 V.

Al devices, there is also a large peak at ∼ 420 nm. Neither of the blue pixel spectra in this section have large peaks at wavelengths shorter than the green peak at ∼ 490 nm. The main difference between the optimised blue PFO Al pixels and the preliminary blue Al pixels is that the PFO films were thicker for the preliminary PFO devices. However, the operating voltages of the optimised blue Al pixels in this section are actually higher than the preliminary PFO pixel (see table 5.3 vs table 5.2). The EL spectra of the blue conventional Al devices are also in disagreement. The EL spectrum of the preliminary conventional Al device in figure 5.9 has only one large peak, whereas the EL spectrum of the conventional Al device in figure 5.11 has two or three peaks at longer wavelengths. This suggests that the 50 nm film may have different structural arrangements of the molecules giving lower-energy photon emission, and may suggest that the PFO thickness is important.

In addition to the main advantages of patterned direct-write deposition of functional PLEDs across a gap, a peculiar advantage of the LIFT process stems from the inverse order of the donor substrate layer deposition in contrast with conventionally fabricated devices. The LEP is deposited on top of the cathode, allowing for direct cathode surface modification. From table 5.3, the addition of tetrabutylammonium hydroxide (TBA) onto the aluminium

does not change the operating voltages much, but it does significantly increase the efficiencies (both LE and EQE) by about 50 % for all three colours. The interest in TBA stems from the possibility to create an adsorbed layer with a large dipole which will reduce the energy barrier to electron injection [126]. In previous literature, TBA has only been applied to ITO as a hole-blocking layer [127], but in this study, TBA was used to promote electron injection, giving more efficient devices. Figures 5.11a and 5.11b show a comparison of the EL spectra of plain Al cathode devices and Al / TBA cathodes, which are remarkably similar for all three colours. Figures 5.11c and 5.11d show the same cathode comparison of operating devices. Due to the higher efficiency, the Al / TBA devices have lower operating voltages for the same brightness, which is why the blue pixels appear slightly different in colour.

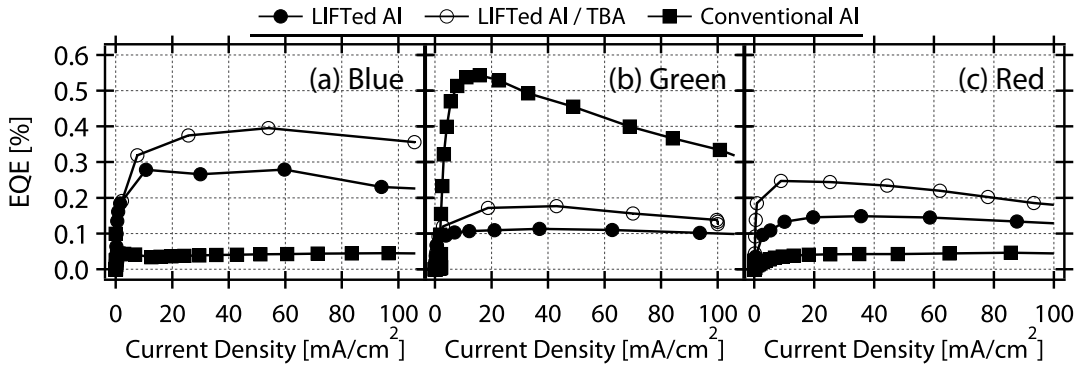

Figure 5.12 The external quantum efficiencies plotted against current density for the all the optimised R-G-B PFO devices with an aluminium cathode.

The device performances are shown in table 5.3 for a current density of 36-51 mA/cm^2. The operating voltages of the LIFTed pixels are around 20 V. When compared to the conventionally-fabricated devices using aluminium electrodes (Convent Ca in table 5.3), the voltage of the pixel is slightly higher. As mentioned before, the EL spectra of LIFTed pixels are different from the conventionally-fabricated devices, particularly the blue ones. The blue conventionally-fabricated device also has a much lower operating voltage but the main figure-of-merit differences between the conventional devices and the LIFTed pixels are the efficiencies, both the luminous efficiency (LE) and the external quantum efficiency (EQE). The green and red LIFTed pixels are noticeably less efficient than their conventional counterpart, but the blue LIFTed pixels are slightly more efficient. These differences are possibly due to the different cathodes, and the better electron-injection of calcium vs aluminium [10, 23], but the short air exposure of the LIFTed pixels during the fabrication process may provoke some deterioration of the interfaces. The green shift of the EL spectra of the blue LIFTed pixels relative to the conventional blue devices may partly explain some of the LE improvement, but EQE is the fraction of photons emitted for every electron of current, and the blue LIFTed pixels have considerably higher EQEs than the conventional devices (0.27 and 0.40 % vs 0.042 % and 0.17 %).

Table 5.3 Device performances for various device architectures, at a current density of ∼ 40-50 mA/cm^2. Blue, Green and Red refer to the LEP layer, whether just plain PFO (Blue), or doped PFO (Red and Green). The *LIFT Al* are the LIFTed pixels with plain Al electrodes, *LIFT Al / TBA* are the LIFTed pixels with Al / tetrabutylammonium electrodes, the *Convent Al* are the conventionally fabricated devices with Al electrodes, and *Convent Ca* are the conventionally fabricated devices with Ca electrodes.

		Bias [V]	**Current Density** [mA/cm^2]	**Luminance** [cd/m^2]	**LE** [cd/A]	**EQE** [%]
Blue	*LIFT Al*	22	51	306.2	0.60	0.27
	LIFT Al / TBA	21	48.32	540	0.89	0.40
	Convent Al	18	51.16	25.4	0.05	0.042
	Convent Ca	13	49.23	102.3	0.21	0.17
Green	*LIFT Al*	26	37	134.5	0.36	0.11
	LIFT Al / TBA	24	43	232.4	0.54	0.46
	Convent Al	39	48.9	715.6	1.46	0.46
	Convent Ca	22	44.5	3311	7.44	2.31
Red	*LIFT Al*	19	35.67	84.7	0.24	0.15
	LIFT Al / TBA	22	44.33	145.2	0.33	0.23
	Convent Al	40	47.9	14.5	0.03	0.043
	Convent Ca	18	45.14	726.5	1.64	2.32

A variation of the laser-induced forward transfer (LIFT) process has been used to print basic tri-colour pixels based on polyfluorene for the first time. In addition, the inverse donor substrate architecture allows for direct cathode modification, and tetrabutylammonium hydroxide (TBA) has been used to demonstrate this by improving electron injection from aluminium. The LIFT process uses a ns pulsed laser to ablate a sacrificial DRL of triazene polymer with a multilayer Al (/ TBA) / LEP stack on top. The speed of the ablation process means that LIFT has the potential to be an extremely rapid pixel deposition technique. Multilayer stacks have been transferred across a gap of ∼ 15 μm at a pressure of 1 mbar to a receiver substrate consisting of glass coated with ITO / PEDOT:PSS / PVK. The multilayer stacks are transferred intact, with no fragmentation of the layers, allowing for the fabrication of functional organic semiconductor light-emitting devices. The deposited pixels have a width of 500 μm and layer thicknesses of less than 100 nm. These results represent the first 'dry' deposition of R-G-B PLED pixels across a gap to create devices of comparable functionality to those fabricated conventionally.

5.3.3 All PFO OLEDs conclusions

The PFO devices presented in both this section and section 5.2 all utilise a PEDOT:PSS / PVK anode, and this architecture with PFO has precedence in the literature [32, 139, 189]. In fact, PFO and PVK have both been used as host materials for phosphorescent dyes, and an inverse architecture of PEDOT:PSS / PFO / PVK has even been used before [194]. Nevertheless, literature device architectures usually have better electron-injecting materials

such as an oxadiazole known as PBD as well as lower function metal like calcium or barium [32, 139, 189]. However, because of the need to expose the LIFT substrates to air, even if only for a few minutes, it was decided to focus on air-stable electrodes, starting with plain silver and aluminium.

Cs_2CO_3 was used as an electron-injecting interlayer in section 5.2, and it certainly helped the conventional devices characteristics, in table 5.1, but did not have such a big affect upon LIFTed pixel device characteristics, in table 5.2. Because of this, and the unknown nature of the actual chemical structure deposited by Cs_2CO_3 evaporation [26, 30, 133, 134], it was decided to not to continue using Cs_2CO_3 after the preliminary LIFTed pixels were fabricated. Interestingly, the plain silver and aluminium electrodes had a performance role reversal from conventional devices to LIFTed pixels in section 5.2; the Al LIFTed pixels were better than their conventional counterparts, in general, and the Ag LIFTed pixels were noticably poorer. This points towards the nature of the cathode / LEP interface differing significantly between the two modes of device fabrication.

Another interesting feature from the preliminary devices in section 5.2 was the changing nature of the plain blue LIFTed pixel EL spectra in figure 5.10, especially compared to the conventional device EL spectra, figure 5.9. The green emission from these plain PFO pixels, well studied before [190, 191], shows two fascinating trends in terms of higher fluence giving a bigger green peak, and in terms of the different cathodes giving more green emission going from Ag / Cs_2CO_3 (least) to Ag to Al (most green emission). The reason for this has been discussed, and a thermal hypothesis proposed, where the aluminium conducts more heat. This is backed up by the fact that the higher laser fluences increases the green emission for all cathode types. However, there are a couple of critical factors that count against this hypothesis. Firstly, silver is much more conductive than aluminium [165], in fact it is the most conductive pure metal. This suggests that the mechanism for this green emission is unlikely to be purely thermal, and may (at least in part) be physical, via pressure from the impact, or chemical, such as a chemical reaction at the interface between the cathode and the LEP. All of these ideas are just speculation, but the trend is worth remembering.

Despite the green emission of the plain PFO Al pixels, it was decided to use Al over Ag for the optimised pixels because of two reasons: firstly, the LIFTed Al pixels demonstrated far better device performances than the LIFTed Ag pixels in table 5.2; and secondly, the Al pixel morphologies were significantly better than the Ag pixels in section 4.3.2, particularly in terms of surface smoothness.

The optimised PFO pixels show good efficiency compared with the conventional Al device in figure 5.12. When combined with the improved pixel morphologies in figures 5.11, the results here show how optimisation of the LIFT process really can improve the pixels. However, the differences between the electroluminescence data of the preliminary and the optimised devices highlight the need for greater analysis of the OLED materials.

5.4 Alq_3 SMOLEDs

Alq_3 was the first material used for low voltage, efficient OLED devices by Tang and Van Slyke in 1987 [7]. It is a small-molecule material, in contrast to the other polymeric materials used as the light-emitting layer in this thesis: MEH-PPV, PFO, and PFN. Because of the lower mechanical and thermal stability of small-molecule organic films relative to polymers, the functionality of these devices is of particular interest.

5.4.1 Specific experimentals

The main device architecture used for the Alq_3 devices again contained the multi-layer anode of ITO / PEDOT:PSS / PVK. Like sections 5.3.1 and 5.5.1, 60 nm PEDOT:PSS was spin-coated before 40 nm of PVK. The cathode material used is aluminium, and tetrabutylammonium hydroxide (TBA) has been used as an electron-injection layer (EIL) for some LIFTed pixels. For all the devices in this section, an 80 nm film of Alq_3 has been used as the active layer, whether evaporated directly on the PVK, for the conventional device, or whether evaporated onto the donor substrate.

For the LIFT donor substrates, 90 nm Al has been evaporated onto 190 nm TP. On one donor substrate tetrabutyl ammonium hydroxide (TBA) has been spin-coated in the same way as the PFO LIFT donor substrates in section 5.3, from a methanol solution. The conditions for the LIFT were the same as for all the other optimised devices, at 1 mbar with a donor-receiver gap of 15 μm.

5.4.2 Conventional Alq_3 devices

Due to the ubiquity of Alq_3 in OLED literature it is easy to compare the devices to previous devices, and figure 5.13a shows the EQE plotted against current density of the conventionally-fabricated PVK / 80 nm Alq_3 /Al device with the some EQEs reported from the literature for comparison. The device is better than older PVK / Alq_3 devices from the 1990s [31,195]. It is easy to speculate on differences, but one difference noted in the articles is that all the measurements in the references [31, 195] were undertaken in ambient conditions (unlike references [7,138] which were kept in inert oxygen-free atmospheres). It is particularly interesting that the EQE value from reference [31] is so close to the value obtained here (0.25 % vs 0.4 %). The original OLED by Tang and Van Slyke has a good efficiency, partly because it was made under a very well controlled oxygen-free atmosphere, but also because the charge-injection was optimised using a hole-transporting diamine and a low work-function Mg:Ag alloyed cathode. Whilst a different hole-transporting layer may have helped a bit, the main limitation is probably the lower work function cathode helping electron-injection.

Figure 5.13b shows the current density and luminance as a function of voltage. As can be seen, the luminance reaches very high brightness levels above 1000 cd/m^2 at relatively low current densities. The operating voltage is fairly high which is partly due to the high

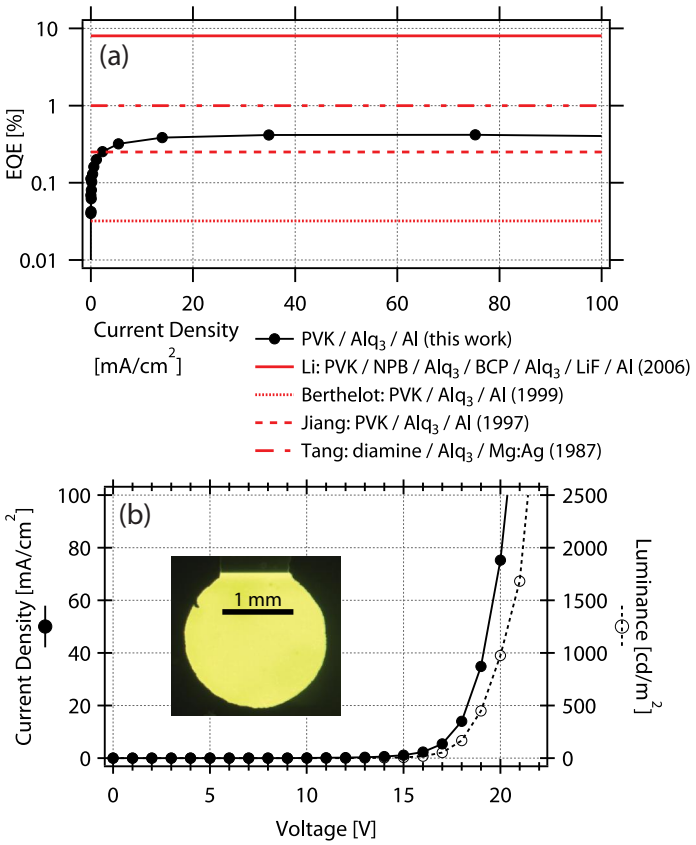

Figure 5.13 (a) The external quantum efficiency (EQE) is plotted as a function of current density for the conventionally-fabricated PVK /Alq_3 / Al device from this study compared with the best Alq_3 devices with PVK and Al [138], earlier PVK / Alq_3 / Al devices [31, 195], and the original OLED with a diamine / Alq_3 / Mg:Ag structure [7]. (b) The current density and luminance as a function of voltage for the PVK / Alq_3 device fabricated in this study.

thickness of the Alq_3 (80 nm), and partly due to the charge injection at the electrodes which is probably not quite ideal. The J-V and L-V curves in figure 5.13b are in very good agreement to those in reference [31].

5.4.3 LIFTed Alq_3 pixels

A large aim of this study was to demonstrate the versatility of the LIFT process. After the fabrication of normal MEH-PPV devices (section 5.1 and [118, 153]), the research has focussed on polymeric materials; PFO (section 5.3) and PFN (section 5.5). The fabrication of small-molecule OLEDs (SMOLEDs) by LIFT demonstrates that this variant of LIFT with a TP DRL is potentially applicable to all solid thin-film OLED materials.

In addition to just demonstrating a proof of principle, TBA was added onto the aluminium cathode to improve electron injection (as was done with the PFO in section 5.3). Figure 5.14 shows a comparison of the conventional and LIFTed pixel device performances.

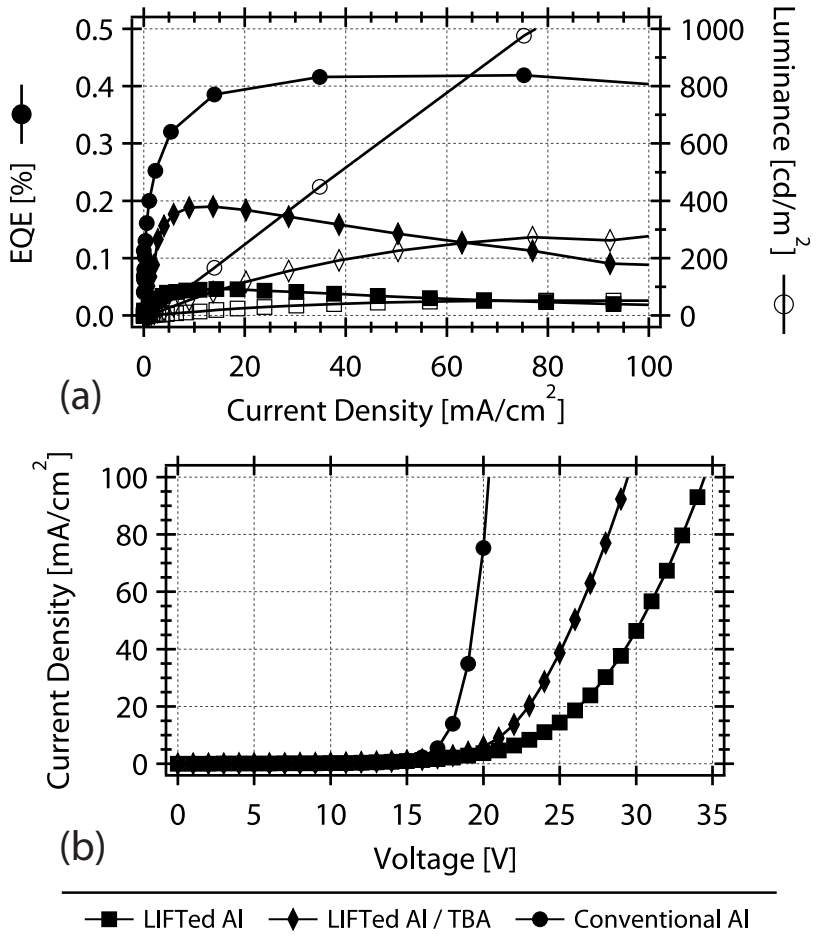

Figure 5.14 A comparison of LIFTed pixel (square, just Alq_3, and diamond, with TBA interlayer) and conventionally-fabricated (circle) device characteristics. The graphs show the external quantum efficiency (EQE) and luminance as a function of current density (a), and current density as a function of voltage (b). The LIFTed pixel characteristics used here are from pixels transferred at 85 mJ/cm^2.

Whilst the LIFTed pixels are clearly not quite as good as the conventional device, they appear to have a similar turn-on voltage in figure 5.14b, and not too high operating voltages (they are comparable to the PFO and PFN devices). In terms of efficiency, in figure 5.14a, the LIFTed pixels exhibit good external quantum efficiencies above 0.05 %.

When comparing the LIFTed pixels with and without TBA, the Alq_3 devices show a significant difference. The pixel device characteristics in figure 5.14 show that the peak EQE increases from about 0.06 % without TBA to 0.19 % with TBA. This improvement with Alq_3 is even more marked than for PFO (section 5.3). The operating voltage is also improved significantly in figure 5.14 with a reduction (at $\sim$ 50 mA/cm^2) from 31 V without TBA to 26 V with TBA. LIFTed pixels are shown in figure 5.15, a-c show a pixel without TBA, and d-f show a pixel with TBA. The illumination of the pixels in figures 5.15b & e demonstrate that there is no distinct difference in the pixels with and without TBA.

The pixel before and after operation is shown in figure 5.15, and demonstrates that

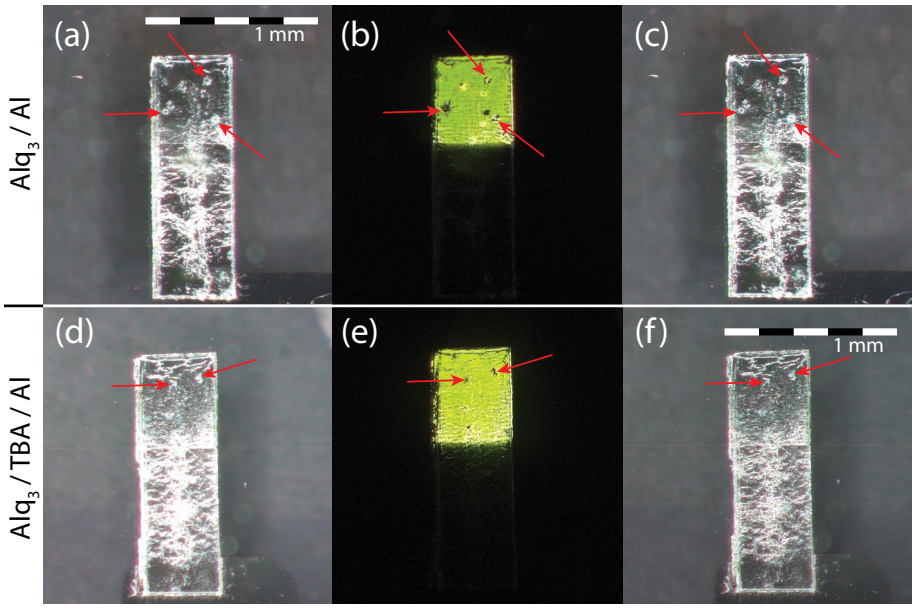

Figure 5.15 Micrographs of an Alq_3 pixel with an Al cathode before (a), during (b), and after (c) operation, and micrographs of Alq_3 / TBA / Al pixel before (d), during (e), and after (f) operation. Both the pixels were transferred at a fluence of 85 mJ/cm^2.

the morphological defects mainly come from the transfer rather than operation. Whilst this may appear to be a disadvantage with the LIFT process, the pixels do not exhibit significantly more defects than the polymers in previous sections, and show the potential to be optimised. In fact, the lack of black-spot defects in the OLEDs from operation due to oxygen or water contamination reflects positively upon LIFT [181]. Alq_3 appears to transfer as well as any of the other materials with the optimised LIFT conditions of 1 mbar and a 15 μm gap. The electroluminescence spectra all match very well, and the LIFTed pixel efficiencies are only just below the conventional device efficiencies, which perhaps perform better than polymers because the detrimental effects of aluminium evaporation on polymers is not so marked with Alq_3.

Figure 5.16 shows a final interesting feature of the data on LIFTed Alq_3 pixels, where a slight trend in device performance was observed as a function of laser fluence. The lower the laser fluence of deposition, the higher luminance for a given current density/voltage (i.e. the higher the efficiency). Figure 5.16 serves to show both this increase in efficiency at lower laser fluences, and to show the absolute values for luminance: over 300 cd/m^2. The insets also give some idea of the pixel morphologies. All three pixels show some defects, like those in figure 5.15, but the lowest fluence, 75 mJ/cm^2, is clearly the pixel with the most defects. This does follow the pattern set by the polymers, particularly observed in the optimisation study in section 4.2.

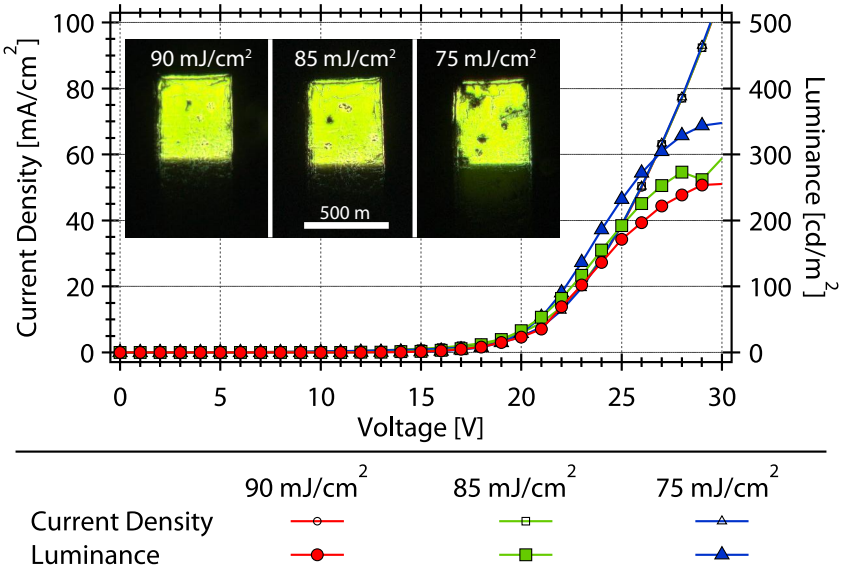

Figure 5.16 A device performance comparison of Alq_3 / TBA / Al pixels transferred at different fluences: 90, 85, and 75 mJ/cm^2. Micrographs of the relevant pixel devices are shown as insets.

5.4.4 Alq_3 SMOLEDs conclusions

The operation of LIFTed Alq_3 pixels demonstrates that LIFT may be applied to all types of OLED materials successfully. Despite the good quality of the LIFTed pixels, they are not as good as the conventional devices. One reason for this may be that Alq_3, unlike the polymeric materials, is not damaged by aluminium evaporation. For this reason, the evaporation of Al directly onto the Alq_3 may actually be favourable over the inverse orientation used when making the LIFT donor substrate (Al first and then Alq_3). Even if this is not the case, there are other explanations for the poorer device characteristics of the LIFTed pixels, particularly the film morphology when compared to the polymeric PFN pixels in figure 4.19 in chapter 4.

The fact that LIFTed Alq_3 pixels were fabricated with efficiencies only $1/10^{th}$ of the conventionally fabricated devices is actually a success given that the process was not optimised for Alq_3, and that the addition of an un-optimised TBA layer increase electron injection significantly enough to make the efficiency as high as $1/3^{rd}$ of the conventionally fabricated devices.

One aspect of the Alq_3 pixels which is worth looking at in detail is the morphology of the pixels. The comparison with the PLED pixels in figure 4.19 is particularly revealing as it highlights how many fewer defects the polymeric pixels have. Rather than different mechanical properties (there is no thin-film data on the OLED materials in this thesis), a good explanation for the differences between Alq_3 and the PLED materials comes from the sublimation temperature of Alq_3. A detailed analysis of the Alq_3 bought from Aldrich has shown an onset of sublimation at 300 °C [166]. Even though this is roughly the same as

the thermal decomposition temperatures of MEH-PPV and PFO [196], as a phase change rather than a thermal reaction (governed by Arrhenius kinetics) it is more likely to happen on the short time-scales of the laser pulse. An indication of the nature of pulse laser thermal degradation is indirectly shown via a recent study on the deposition of MEH-PPV, PFO and Alq_3 by RIR-PLD (resonant infrared pulsed laser deposition) and RIR-MAPLE (resonant infrared MAPLE) [197]. Whilst Alq_3 could be deposited via RIR-PLD without significant damage to the material, this was not the case for the polymeric materials which were all better suited to the 'softer' RIR-MAPLE technique where the polymer is dissolved in a host matrix at a concentration of ~ 1 %. This shows how the Alq_3 sublimes without any chemical structure damage, but the polymers will not sublime, or even melt without some chemical structure damage. This suggests that any effect of Alq_3 sublimation on the LIFTed pixels is likely to be due to morphological problems from small areas subliming.

This hypothesis is partly backed up by the data in figure 5.16, particularly by the low 90 mJ/cm^2 vs 75 mJ/cm^2 device performance data, where the lower fluence pixel is considerably more efficient than the higher fluence pixel. However, the images tell a different story – the lower the fluence the more heterogeneity and defects in the pixel. This may actually be a LIFT effect of exaggerated heterogeneity at lower fluences as they are closer to the threshold.

5.5 PFN PLEDs[3]

5.5.1 Specific experimentals

The poly((9,9-di(3,3'-N,N'-trimethyl ammonium) propyl fluorenyl-2,7-diyl)-alt-(9,9-dioctyl fluorenyl-2,7-diyl)) (PFN) layer was spin-coated from a 10 mg/ml solution in methanol:DMF (99:1) at 1500 rpm to create a film $\sim$ 50 nm. In the same way as all the optimised pixels (see sections 5.3.1 & 5.4.1), 60 nm PEDOT:PSS / 40 nm PVK have been used as the HTLs on top of the ITO anode. For conventionally fabricated devices the PFN was spin-coated directly onto the PVK and Al cathodes were then evaporated onto the PFN film.

The normal LIFTed pixels were fabricated using the same basic LIFT process as the optimised PFO devices in section 5.3.1, with a donor-receiver substrate gap of $\sim$ 15 μm and an environmental pressure of 1 mbar. The donor substrates consisted of 190 nm TP / 90 nm Al / 50 nm PFN. An aluminium cathode was used, and TBA was deposited on one sample before the Al, but it had no noticeable effect on the device performance, presumably because the TBA was in a methanol solution, and was redissolved when the PFN was spin-coated on top.

The sequentially LIFTed pixels used two *sequential* transfers of separate donor substrates: 190 nm TP / 50 nm PFN, then 190 nm TP / 80 nm Al. The process is outlined in figure 5.17 where the transfer of a single-layer PFN pixel is shown in step 1, followed

[3]The results from this section will be published in [167].

by the transfer of a (deliberately smaller) aluminium pixel in step 2, and device operation of the whole pixel in step 3. The LIFT conditions are identical to the other optimised LIFT devices, namely a donor-receiver substrate gap of ~ 15 μm at a reduced pressure of 1 mbar.

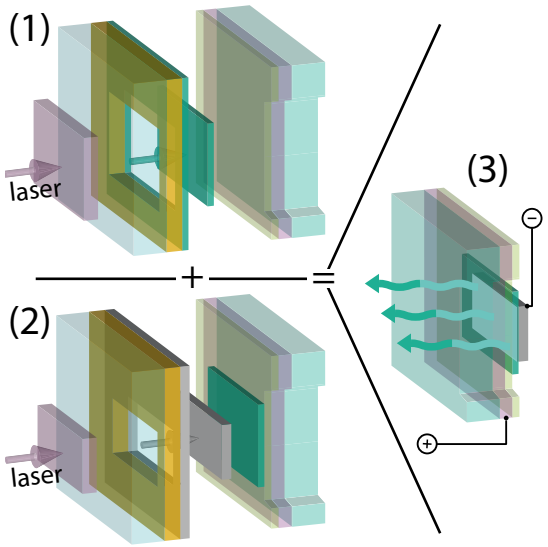

Figure 5.17 A summary of the sequential LIFT process to fabrciate PFN devices. In step 1 the PFN film is deposited, in step 2 the aluminium cathode is deposited on top of the PFN, and in step 3 the device is operated.

5.5.2 Conventional PFN devices

PFN is a standard material, well studied in the literature, but normally used as an electron-injecting layer or a host for phosphorescent dopants [53,60,189]. PFN is particularly useful because it is soluble in methanol, which does not dissolve most of the other polymeric films soluble in other organic solvents. This means that it can be spin-coated directly on top of TP, and the first fabrication of a functional device following LIFT of a single solid-film layer intact is shown in section 5.5.4.

Conventionally fabricated devices with the architecture PEDOT:PSS / PVK / PFN / Al are shown in figure 5.18. There are two plots, a first run up to 100 mA/cm^2, and then a second run of the same device. The difference is most stark in figure 5.18b where the luminance of the conventional device on the first run is shown to stay below 5 cd/m^2 all the way up to 100 mA/cm^2, while it starts to rise dramatically above 20 mA/cm^2 on the second run, and this difference in luminance is reflected in the efficiency rise on the second run. The external quantum efficiency is over an order of magnitude higher on the second run than the first run.

A second key observation is shown in the micrograph inset, figure 5.18c, where the electroluminescence can be seen directly. There are distinct striations running diagonally through the device, highlighted by white arrows pointing them out. They look like ripples

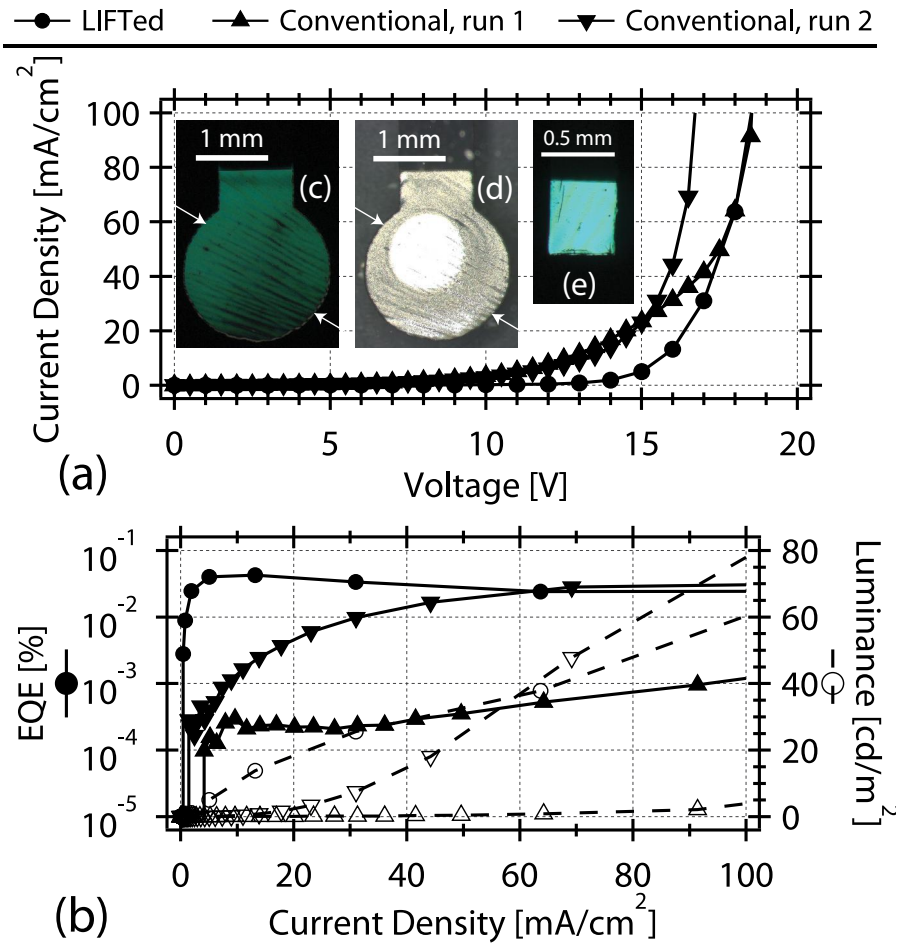

Figure 5.18 The device characteristics for both the conventionally fabricated device and the normal LIFTed PFN pixel are shown. The current density plotted against voltage is in (a), and the external quantum efficiency and luminance are both plotted against current density in (b). Micrographs of a conventional device during operation (c) and after burn-out (d), and a LIFTed pixel during operation (e) are shown as insets.

with peaks and troughs of light-outcoupling. They appear to be permanent features in the PFN films, but are hard to identify when the device is not in operation, except when the device is burnt through, figure 5.18d. This indicates that the brightness peaks probably do correspond to where the majority of the current is passing through the device, as that would then burn-in the pattern after overloading the device. The conventional PFN device exhibits decent performance as long as the voltage stays well below 20 V. At current densities only just above 100 mA/cm^2, the burnout begins, therefore luminances above 80 cd/m^2 are hard to reach. At that point the device burns out, leaving the white product shown in figure 5.18d.

Compared to literature values, these devices exhibit comparable performance (on the second run) [53]. The EQE for PVK / PFN / Al reported in that paper was 0.09 %, which is not far above the 0.03 % in this study. However, that article was the first report on this class

of ionic, alcohol-soluble polyfluorenes and they: a) used a different anion (Br^- instead of I^- used in this study), b) they synthesised the compounds themselves, guaranteeing their purity, and c) the PL (and to a more minor extent, the EL) thin-film spectra werere different from that presented in figure 5.19, but the PL spectrum in solution in reference [53] is similar to that in figure 5.19.

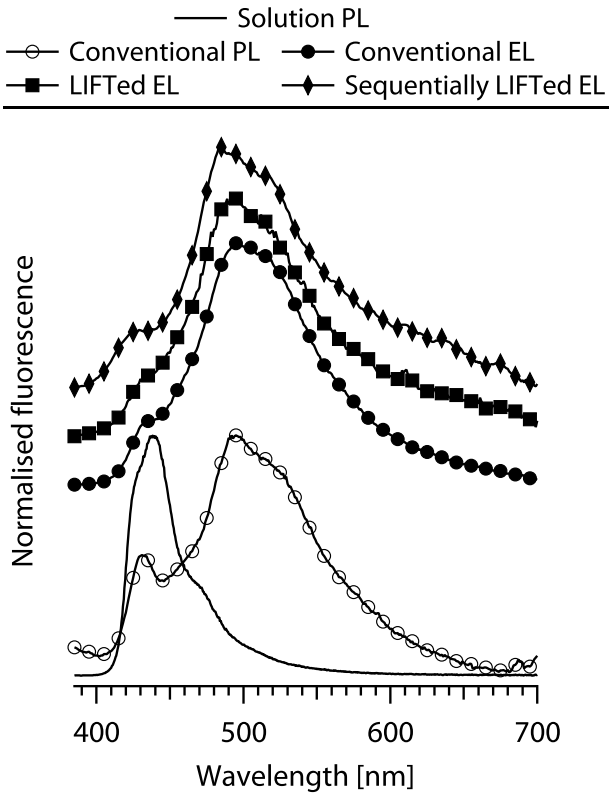

Figure 5.19 A comparison between LIFTed pixels and conventionally fabricated PFN devices' electroluminescence (EL) spectra (top). The photoluminescence (PL) spectra of the PFN methanol solution, and the conventionally fabricated PFN device are also shown (bottom).

5.5.3 Normal LIFTed PFN pixels

The device characteristics in figure 5.18 show that the LIFTed pixels demonstrate very similar performance to the conventionally fabricated device, and actually performs more efficiently on the first run. The burnout voltage and current density is also the same, and the ripples observed in the conventional devices can also be seen in the LIFTed pixels. However, as the ripples are only a fairly large scale ($\sim$ 100 μm), they are not as obvious, but in figures 5.20b & c they can be seen running along the pink arrow at the top of the pixel.

Some minor LIFT effects have been highlighted in figure 5.20 to compare with the other LIFTed pixels. The green arrows highlights a spot defect which grows upon operation, and

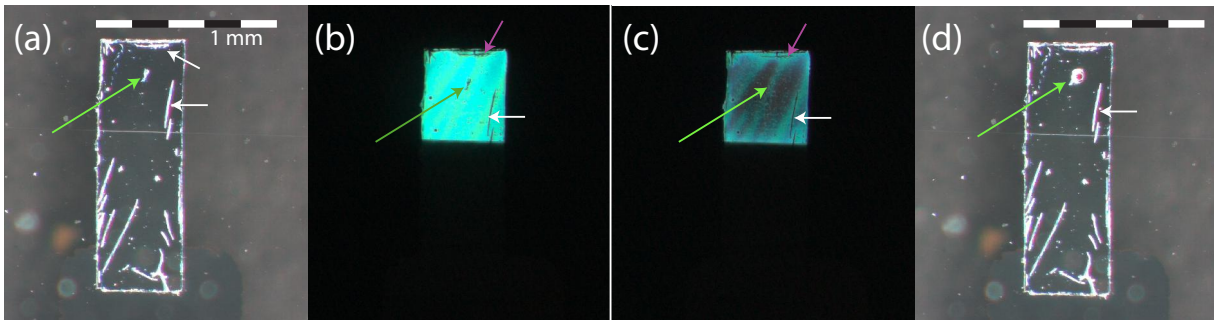

Figure 5.20 Images of a LIFTed PFN pixel, from an Al / PFN stacked donor substrate before (a), during (b) & (c), and after (d) operation. The green arrow points out an existing defect which grows upon operation, and the white arrows point out folds which do not grow.

the white arrows show folds which appear to be completely benign upon operation.

5.5.4 Sequential LIFTed PFN pixels

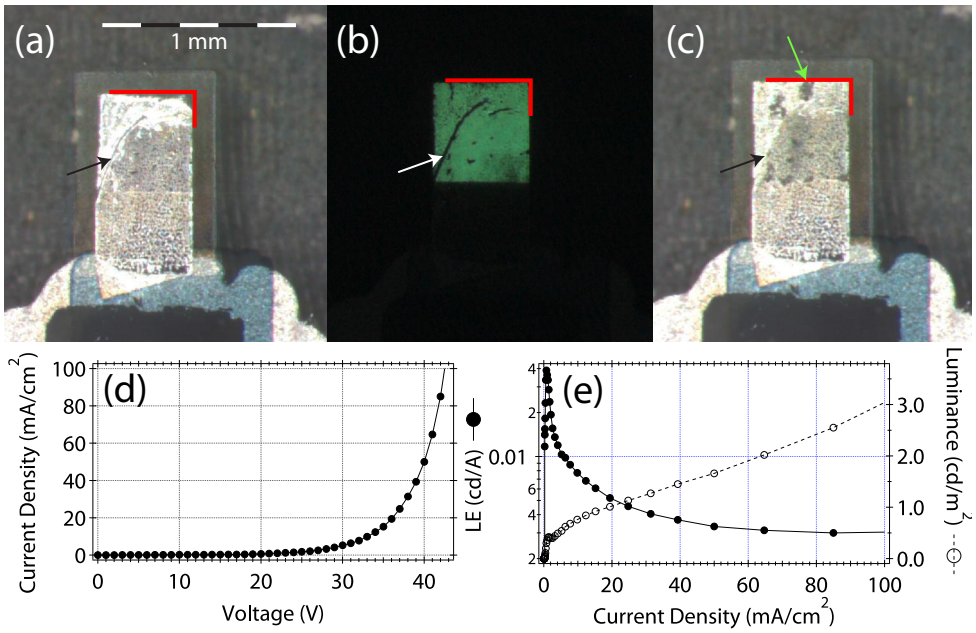

Figure 5.21 Images of a sequentially transferred PFN PLED before (a), during (b), and after (c) operation. The red lines are their to highlight a corner 'smoothed out' by the operation, the black/white arrow is pointing out a permanent fold, and the green arrow shows an example of where the device has burnt through by overloading during operation. In addition, the device characteristics for sequentially transferred PFN PLED pixels are shown: current density vs voltage (d), and luminous efficiency and luminance vs current density (e).

Devices were fabricated by sequential LIFT of the PFN film then the Al cathode, as

outlined in section 4.5.3. Figure 5.21 shows the performance of a device fabricated in this way. The morphology of a pixel before and after operation is shown in figure 5.21a and c. The morphology clearly changes significantly upon operation, figure 5.21b. The first observation is that the smaller ripples and folds (e.g. the top right-hand corner of the pixel, highlighted with a red corner in figures 5.21a-c) are smoothed out, but the big ones (e.g the arc down the left of the pixel, shown by an arrow in figures 5.21a-c) are retained and give off no light. When a high bias is applied, burn-out of the aluminium cathode begins, and the holes are formed such as that highlighted with a black arrow in figure 5.21c.

Figure 5.21d shows the diode behaviour of the device, albeit at large voltages. The device shows good current density - voltage diode characteristics, with a distinct turn-on voltage around 30 V. The luminance and luminous efficiency (LE) are presented in figure 5.21e as a function of current density. The device efficiency shows a large fall from a low current-density value of above 0.02 cd/A to a stable value of around 0.003 cd/A. This is not spectacular, but comparable to previous multi-layer transfers of MEH-PPV. [118, 153] The electroluminescence in figure 5.21b shows the blue-green nature of the emission, matching the EL spectra in figure 5.19, and the original EL spectra from the literature [53].

The high operating voltage of these devices could easily be attributed to porosity in the PFN film, which is indicated by the thickness and roughness of the films in section 4.5.3. This porosity would act as a barrier to charge transport, and may also create further gaps between the PFN and the Al which would act as significant barriers to electron-injection (often the limiting factor in PLEDs [23]). However, despite this rough morphology, functional PLED devices were made using this 2-stage LIFT process.

5.5.5 PFN PLEDs conclusions

A wide range of data has been presented here on PFN PLEDs, all based on the device architecture ITO / PEDOT:PSS / PVK / PFN / Al. Just looking at the normal LIFTed pixel, it showed impressive device performance, far better than the conventional device on its first run. Strangely, the conventional PFN device improved upon its second run, suggesting that electrical annealing was necessary to initiate good device performance. On top of these properties, both the normal LIFTed pixel and the conventionally fabricated device had a low breakdown regime: at around 18 V and just above 100 mA/cm^2. In micrographs of both the normal LIFTed pixel and conventionally fabricated device, figures 5.18c-e and figure 5.20, there was evidence of a periodic undulation, confirmed in figure 4.21 in section 4.5 as a spin-coating feature.

The main feature of this section is the sequential LIFT of a PLED. This is the first time it has been achieved, and despite the high operating voltage, a good EL spectra was obtained and the efficiency was actually higher than the conventionally fabricated device on its first run. A key area for improvement is in the polymer pixel; the single-layer PFN transfer created films with roughnesses of at least 25-30 nm when the donor substrate roughness was less than 3 nm.

Chapter 6

Conclusions

This thesis has one aim, to investigate the ability of LIFT to deposit OLED materials to create functional devices. To this purpose there are two categories of conclusions: investigations into *how* the LIFT process works, and evaluation of the LIFTed OLEDs. Chapter 3 falls comfortably into the first category, and the last chapter 5 is clearly in the second category. The middle results chapter 4 fits mainly into the first category, but through the study of the pixel morphology is also evaluating the OLEDs in part.

In terms of investigating the LIFT process itself, the models presented here represent the beginning of an important direction of research needed in order to understand such a physically complex process. In addition, the experimental results in chapter 3 demonstrate the importance of considering thermal energy pathways (and loss in particular) when investigating the process. The experimental work in optimising pixel deposition in chapter 4 has indirectly given added insight to the LIFT process, from the positive results of reducing the pressure, the effect of adding a gap between the substrates, and the different transfer success or pixel morphologies depending on the materials used on both the donor and receiver substrates. In particular, the sequential LIFT in section 4.5.3 highlights that LIFTed pixels of single polymer layers have a very different morphology from the metal / polymer bilayers.

A whole optimisation process is presented here, but one aspect of the optimisation that stands out is the marked improvement in deposition on reducing the atmospheric pressure in section 4.2, and how this has enabled the deposition of polymeric, phosphorescent and small molecule OLED materials, in a bilayer with the metallic cathode. The same conditions have also led to the fabrication of an OLED by sequential LIFT of single layers in section 4.5.3. The successful deposition of multiple OLED types using LIFT demonstrates that LIFT has the potential to be a 'universal' OLED deposition technique. In addition, the LIFTed pixels were compared to conventionally fabricated devices, and demonstrated sometimes better, sometimes worse, but always comparable performances in terms of efficiency and operating voltage.

6.1 Development of LIFT process understanding

Modelling is beginning to help the understanding of the physical nature of the LIFT process. The thermal modelling in chapter 3 has been used in various ways to highlight the significance of heat diffusion as an energy loss mechanism, particularly when modelling the TP ablation with different laser pulse length. Thermal simulations have shown qualitative pictures of how the thermal energy is distributed through the TP film and fused silica substrate, and also quantitatively led to the calculation of the proportion of thermal energy lost into the substrate as a function of time. The thermal model is particularly valuable in showing how rapidly thermal energy can be lost into a fused silica substrate. Through the modelling, thermal loss into the substrate for backside ablation orientation is shown to be 40-50 % during the pulse length.

In addition to the thermal model, a flyer velocity model has been developed from a simple explosive model named after Gurney [95]. This model is a simple energy balance, and uses physically meaningful parameters. The best fit appears to use a metal model for the effective absorption coefficient based on the linear absorption coefficient. However when fitting the model, by removing a proportion of the input laser energy, a large amount of energy is unaccounted for, at least 50 %. Analysing the thermal model by integrating under the temperature profiles, 44 % of the thermal energy for 150 nm TP and 42 % of the thermal energy for 350 nm TP films is lost into the substrate by the end of the 30 ns laser pulse. As a first try, despite the lack of validation of the thermal model for backside ablation, the similarity between the heat loss calculated in the thermal model, and the energy loss uunaccounted for in the flyer velocity is very promising.

UV laser pulse length (τ = 70 ps, 5 ns, 30 ns) experiments and relectometry of thermally ablated TP flyers have helped to further investigate the thermal component in TP ablation. The pulse length experiments have been used to validate the thermal model for frontside ablation in a similar way to how it was before used [77]. Temperature profiles for different times after the laser pulse have also aided conceptual understanding of the different temperature profiles from the different lasers.

In addition to these fundamental studies, a detailed optimisation of the LIFT process was undertaken. First, the effect of altering the receiver substrate on the deposition of MEH-PPV and PFO pixel at atmospheric pressure was investigated. Next, transfer across a gap was enabled by reducing the atmospheric pressure. This followed on from a previous idea of our group that was ultimately unsuccessful [152]. The triazene polymer thickness was also optimised, with the conclusion that any thicknesses between 150 and 300 nm would work, so 190 nm was chosen. Using a gap of $\sim$ 15 μm, TP thickness of 190 nm, and an atmospheric pressure of 1 mbar, PFO PLED and phosphorescent OLED (PhOLED) pixels, Alq_3 SMOLED pixels, and both normal and sequentially LIFTed PFN PLED pixels have been successfully fabricated. Fine patterns have also been deposited showing that pixels $<$ 20 μmline width can be printed reliably.

Table 6.1 Comparison of LIFTed pixel and conventional device performances for all the main materials used in this thesis. Device performances are shown for various device architectures, at a current density of ∼ 40-50 mA/cm^2.

		Bias [V]	**Current Density** [mA/cm^2]	**Luminance** [cd/m^2]	**LE** [cd/A]	**PE** [lm/W]
MEH-PPV	*LIFT Al*[a]	11	62.3	1.5	0.0024	0.00069
	Convent Al	8.5	44.7	2.07	0.0046	0.0017
Blue PFO	*LIFT Al*	22	51	306.2	0.60	0.086
	LIFT Al / TBA	21	48.32	540	0.89	0.13
	Convent Al	18	51.16	25.4	0.05	0.0087
Green PFO	*LIFT Al*	26	37	134.5	0.36	0.11
	LIFT Al / TBA	24	43	232.4	0.54	0.46
	Convent Al	39	48.9	715.6	1.46	0.46
Red PFO	*LIFT Al*	19	35.67	84.7	0.24	0.15
	LIFT Al / TBA	22	44.33	145.2	0.33	0.23
	Convent Al	40	47.9	14.5	0.03	0.043
PFN	*LIFT Al*	17	31	25.6	0.083	0.015
	Sequential LIFT Al	45	39.3	0.96	0.0024	0.00017
	Convent Al[b]	17	41.6	0.3	0.00072	0.00013
Alq$_3$	*LIFT Al*	30	46.3	44.4	0.096	0.01
	LIFT Al / TBA	25	38.7	192.3	0.50	0.062
	Convent Al	19	34.9	448.7	1.29	0.21

[a] These results improved significantly on subsequent runs, see section 5.1
[b] This device also improved upon operation, see section 5.5

6.2 The fabrication of OLED pixels by LIFT

A wide range of OLEDs have been made and tested, and the main varieties are shown in table 6.1. The biggest achievement is to have fabricated OLEDs from every main class of OLED material: polymer (MEH-PPV, PFO, & PFN), small molecule (Alq$_3$), and phosphorescent (PFO doped with Ir(Me-ppy)$_3$ & btp$_2$Ir(acac)). The device performances of all the main classes of pixels fabricated are shown in table 6.1. Micrographs of pixels of all four of the main materials used here, fabricated by normal LIFT as bilayers with aluminium, are shown in figure 6.1.

The earliest OLED pixels, MEH-PPV, were fabricated in atmosphere and still demonstrated good performances even if the transfer reliability and reproducibility was poor. Nevertheless, LIFTed pixels with device characteristics as good and better than conventional devices were produced, and the reliability was improved by modifying the receiver substrate. This demonstrates that with fine optimisation, LIFT at atmospheric pressure is indeed possible. Precise control of the gap is necessary though.

The bulk of the PLED pixels were made at reduced pressure (1 mbar) with a substrate-substrate gap of ∼ 15 μm, with a TP thickness of ∼ 190 nm. Despite not altering these parameters for finer optimisation, good PFO, PFN, and Alq$_3$ pixels were fabricated using

the standard LIFT technique of transferring a bilayer cathode / light-emitting layer. The sequential LIFT of PFN and Al single-layers to fabricate a functioning PFN PLED was very positive, but the device characteristics were much poorer than the PFN conventional device and the normal bilayer LIFTed PFN pixel, with a much higher operating voltage and poorer efficiency. However, the EL spectrum was completely unchanged, suggesting that the chemical structure was unaltered.

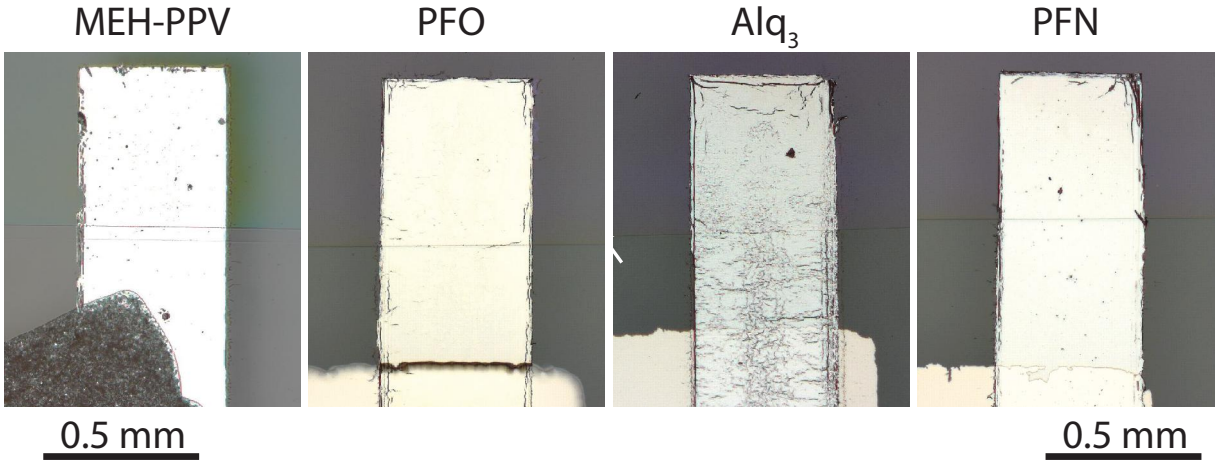

Figure 6.1 OLED pixels fabricated using the normal LIFT process for all four of the main materials used.

The adsorption of a layer of TBA onto the aluminium cathodes for PFO and Alq_3 pixels gave a significant improvement in device performances, over 50 % improvement in the efficiency of PFO pixels and more than 100 % improvement in efficiency of Alq_3 pixels. This highlighted the potential of LIFT for surface modification techniques that may not be possible using conventional OLED deposition techniques, because the TBA needs to adsorb directly on the cathode surface.

There are lots of questions that still need answering, some of which are mentioned in the outlook, but none of the obstacles look completely unsurmountable at the moment. Morphological defects (cracks, ripples, folded edges etc.) need to be addressed, particularly for pixels such as the single-layer PFN pixels, Alq_3 pixels, and the bilayer PFO pixels with silver cathodes. Atmospheric pressure LIFT needs much more precise gap measurements, controlled laser fluences, and receiver substrate compatibility in order to optimise LIFT of OLEDs composed of materials other MEH-PPV.

The results show that LIFT is a viable technique for the fabrication of OLED pixels with smooth surfaces and good EL spectra. The LIFT technique shows the potential to reach pixel resolutions below 20 μm, with a lot of flexibility in terms of material choice, and interface modification. Sequential LIFT has further added to this potential further, and optimisation of sequential LIFT to demonstrate that the TP layer can be completely decomposed would be a big advantage for the LIFT technique with a TP DRL.

Chapter 7

Outlook

Laser-induced forward transfer is the topic of this thesis, and the application is the fabrication of organic light-emitting diodes. There are two distinct ways in which this research can progress: application-driven, or fundamental understanding-driven. From this thesis, I hope it is clear that whilst the directions may be distinct, they are by no means independent. The direction in which this work must progress should be application-driven as the process is completely artificial, and without an application any research is redundant. However, in order for the LIFT process to be successful in any application, some fundamental understanding of the process needs to be gained along the way.

7.1 The use of triazene as a dynamic release layer

The ablation characteristics of triazene have been well studied and, as shown in this thesis, a polymeric TP DRL can successfully be used to LIFT sensitive materials. In many ways, the nature of the DRL, and its ablation characteristics are almost the least important part for future application of the LIFT process. The DRL needs specific properties which are well understood: good light absorption, rapid decomposition, clean ablation. Depending on the application these properties will be more or less important, and other factors may well come into the equation, such as the desire to use the DRL ablation products on the deposition.

The mechanism behind the DRL ablation would be worth investigating, and an in-depth analysis similar to that by the Garrison group on pulsed UV-ablation of PMMA would be extremely valuable [76, 198]. A temporal simulation of the ablation process would allow proper integration of the thermal model, used here in section 3.1, with the physical state of the DRL film at any given time.

7.2 Fundamental research into LIFT

As mentioned above, fundamental research should not lead the application in a field like LIFT, and this has been the case so far. Nevertheless, fundamental understanding has focussed strongly on empirically-derived models rather than physical numerical-based models. Whilst the latter type of modelling depends on some sort of understanding from experiments, it is potentially a much more powerful tool to help unpick the limiting variables in LIFT, and the scenarios in which different variables dominate. A simple flyer model has been developed in this thesis, but it is only a basis for more detailed physical descriptions to be added. Whilst there is much work into the physics of ablation, an understanding of the aerodynamics and impact physics in LIFT would be extremely valuable.

There are enormous possibilities to be explored in this direction. A significant aspect would be to develop the ablation model fully into a more comprehensive LIFT model based on that in section 3.2. Whilst there is no doubt that there are plenty of other effects in the LIFT process, the two main limitations on pixel morphology and quality appear to be thermal and mechanical, and the mechanical effects need to be investigated in particular.

7.3 LIFT as a process for the fabrication of OLED pixels

In this thesis it has been presumed that OLED pixels are a potential application for the LIFT process. This appears to be a good presumption given the growth of OLEDs in display applications and the growth potential for a successful new deposition technique. However, it was not until successful fabrication of the PFO pixels side-by-side that the LIFT process was shown to be reproducible and robust. The prediction that LIFT could be a *universal OLED deposition technique* at Plastic Electronics 2010 has been supported by the results in this thesis. In theory, the laser could be the only limiting factor to the speed of deposition in a role-to-role setup. In addition, the thesis briefly touched on one of the most promising aspects of LIFT with the first demonstration of an OLED fabricated by a multi-step LIFT process in section 4.5.3. The separate deposition of layers by LIFT introduces a much-needed new 'dry' technique for patterned deposition of materials allowing for complex device architectures.

In terms of research focussed on OLEDs, LIFT would be aided greatly by improving the experimental resources, particularly using a closed-loop stepper stage (ideally more robust than the current piezo-motors), and an apparatus to digitally control the donor-receiver substrate gap with online measurement (ideally using a diode-laser interferometer). Additionally, research into OLED materials would be invaluable whether the materials used are commercial (as presented in this thesis), or specially synthesised. It would also be extremely rewarding to analyse the pixel device characteristics in more detail, particularly lifetime effects, and this would be aided significantly by using pure, well-studied materials, and using clean fabrication processes, located near to the laser processing.

One area of great interest is the resolution of displays, which for small displays, e.g. on portable devices, means the minimum pixel size. In section 4.3.4 this has been looked at in a small way with shaped pixels, but the topic was only briefly touched upon. Line widths of 20 μm were obtained without serious optimization which suggests great promise in this area. The three experimental aspects which really need to be controlled are: 1) laser beam homogeneity; 2) laser beam mask image focus; and 3) donor-receiver substrate gap. Without further improvements to the setup at PSI, these cannot be optimised much further than demonstrated in this thesis.

7.4 Potential new applications for LIFT

Research into LIFT is redundant if a meaningful application is not kept in mind, and an application is also needed to focus research from the almost limitless spread of variables that LIFT can involve. Whilst OLEDs show great potential, the leading display research is currently dominated by heavyweight companies such as Samsung, LG, and Sony. So, without a collaborative research partnership with a large electronics company, it could prove more rewarding to explore other, novel applications for LIFT.

Current areas of research include medical implantation, sensor arrays, waveguides, injet printing, and electronic interconnects. These areas are all interesting, but during the last three years a number of other potential applications have come to my attention. Firstly, building on OLEDs, there are other organic semiconductors such as OPVs and OFETs. Another area which appears to be slightly neglected appears to be thin-film inorganic semiconductors, such as LEDs and PVs. Whilst traditional lithographic techniques may be cheaper and easier for thin-film inorganic material patterning, there is enormous potential for LIFT to embed devices into larger structures, such as fabrics and casing. In fact, in the electronics industry there is a growing desire for embedded circuit boards where components are built into circuit boards rather than being soldered in afterwards. Interconnects are potentially the first step of applying LIFT in this direction, although it may be more lucrative to start applying LIFT successfully to more valuable components, such as thin-film resistors. This could help to rapidly accelerate the miniaturisation of circuit boards.

In addition to commercial applications, a research based application has been found close to home. The shaped pixels in section 4.3.4 were fabricated using the normal LIFT process in order to create chemical maps of shapes of different metals by two different methods: X-ray fluorescence (XRF) and laser ablation ICP mass spectrometry (LA-ICPMS). This collaboration highlights the ready possibility of using LIFT for research-based, as well as commercial, applications.

Part III

Appendices and References

Appendix A

Light-meter measurement programme

The device characterisation used commonly-used commercially-available equipment in the Keithley 2400 sourcemeter and the Minolta LS-110 luminance-meter. However, there was no standard way to integrate the two different tools. The Keithley sourcemeter is well supported with various types of drivers including LabVIEW virtual instruments (VI)s. However, the handheld luminance-meter is less-commonly integrated into a computer system, despite a serial RS-232 connector.

In order to integrate the two tools, a home-built LabVIEW programme was developed to take various types of measurements, and save the results in useful formats. This chapter will outline the capabilities of the programme, but not go into the details of the LabVIEW programming.

A.1 Sourcemeter capabilities

The Keithley 2400 sourcemeter is well provided for, with a selection of drivers online, both by Keithley themselves [199], and by National Instruments [200]. The Keithley 2400 has been around for a few years, and so there are some older drivers for old versions of LabVIEW, but they seem to be updated fairly regularly to keep up with the new editions of the software being produced.

The basic function of the sourcemeter is to apply a bias and measure the current (and thus resistance too). The source can be switched so that a current can be set, and the required voltage measured. To protect devices, a compliance (maximum value) for the non-source measurement can be set in order to prevent damaging devices when approximate I-V curves are not known beforehand. For the example of an OLED device with an area $\sim$ 7 mm^2, if a sweep up to a current density of at least 100 mA/cm^2 is desired, by using a voltage source, a high maximum voltage can be given with a compliance of 0.01 A. This means that when the output current reaches 0.01 A ($\sim$ 133 mA/cm^2), the voltage will go no higher than the voltage necessary for the compliance, preventing the device from being overloaded by current.

A.2 Luminance-meter capabilities

Although the luminance meter does have RS-232 serial communications to the computer, it is not designed for static luminance measurements, and is more of a portable device. This is highlighted by the fact that there is no way of plugging in a power-cable, and the luminance meter is run by batteries alone! Nevertheless, with an additional lens, the sampling area is reduced to a circle that corresponds to a diameter of 0.4 mm when in focus. This is smaller than the LIFTed pixels, which is the main reason why this luminance meter was chosen to characterise our OLEDs.

Whilst there are no manufacturer's drivers for the Minolta LS-110 (given that it is generally used for portable applications), a LabVIEW programme designed by a U.S. government department was found online [201]. This programme was designed for using the luminance-meter to test electronic display brightnesses, not a long way from the application in this thesis. It provided a very helpful start, and a lot of the manual functions were taken directly, such as taking single measurements and controlling the exposure time (the LS-110 requires at least 2.5 seconds per measurement). These features were integrated into the manual functions, shown in figure A.1c, and the stability and I-V sweep programmes, figures A.2a-c.

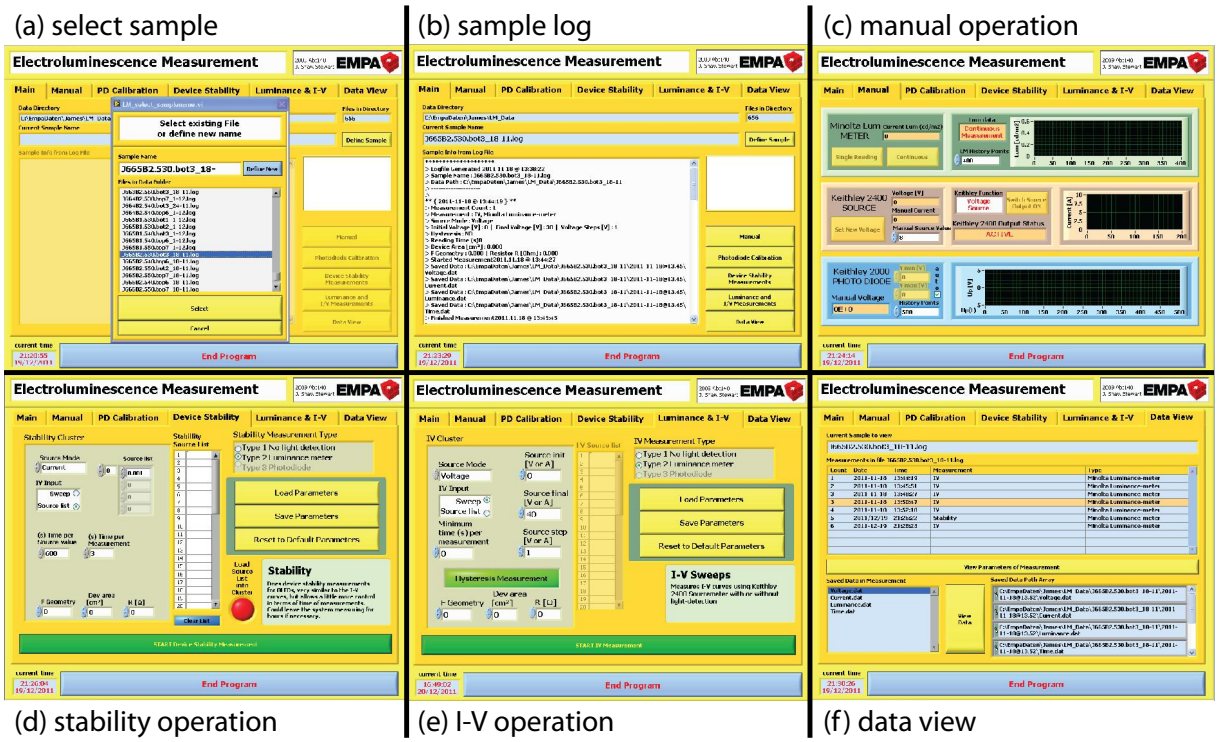

Figure A.1 The graphical user interface (GUI) for the main programme showing the home tab with the sample selection (a), the log of the current sample (b), the manual operation tab (c), the stability tab (d), the I-V sweep tab (e), and the data view tab (f).

A.3 Programme functions

The main function of the programme is to process the data adequately, and for this reason the first thing the programme asks is for a sample name, shown in figure A.1a. From then on, any measurements will be stored within this sample's folder and log file (figure A.1b) . The next screen is a manual operations screen (figure A.1c where manual control of the sourcemeter and the luminance meter can be obtained. Measurements from here cannot be saved (at the moment), although this could be added in. An additional function which may be useful for other setups is the use of a calibrated photodiode instead of a luminance meter. The programme has been set up to allow for the addition of a photodiode, through a Keithley 2000 multimeter, and even has a tab for the calibration (to a Minolta LS-110 luminance meter), but this tab has not been fully developed yet as it has not been needed.

The next tab is the stability control tab, figure A.1d. Here stability measurements can be set up and the stability programme sub VI started. A stability measurement is a long-term measurement where the interval between measurements can be controlled, and a range of input values can be done, either as a sweep at regular intervals (e.g. 0-10 V with 2 V intervals giving measurements at 0,2,4,6,8,10 V), or with values of the user's choice through a list. Different times for these values cannot be used, but multiple runs can be made, and the sweep can be made into a hysteresis measurements, meaning that a single sample could be continually measured remotely for as long as necessary. The stability measurements are actually run using a sub VI, a separate programme called by the main programme. The fourth tab is the I-V control, in figure A.1e, the main tab used for the experiments outlined in chapter 5. Here, sweep measurements can be made with or without a light-measuring tool, and hysteresis can also be added in. The final tab, figure A.1f, shows the sample selection for the data view sub VI.

Both the main operations of the programme – the stability and I-V VIs – give the same four outputs: 1) Voltage; 2) Current; 3) Time (After start of measurement); and 4) Resistance. In addition, when processing the data using the data view VI, the current density can be calculated by giving the OLED area. From this, the luminous efficiency (LE) and the power efficiency (PE) are automatically calculated. In addition, by inputing γ from equation B.7 in the following appendix B, the data view VI can also calculate the external quantum efficiency (EQE).

The stability program is shown in figure A.2a, and the two tabs of the I-V sweep programme are shown in figures A.2b & c. Both of these sub VIs simply run the operations assigned from the tabs in the main programme (figure A.1), and show some of the data as its is obtained in graphs. The data view and save programme allows for both the saving of data, figure A.2d, and the viewing of the data on both logarithmic and normal axes, figure A.2e.

The most complex part of the whole programme is probably the data-handling throughout the various sub VIs, which was developed from a programme used by our group to

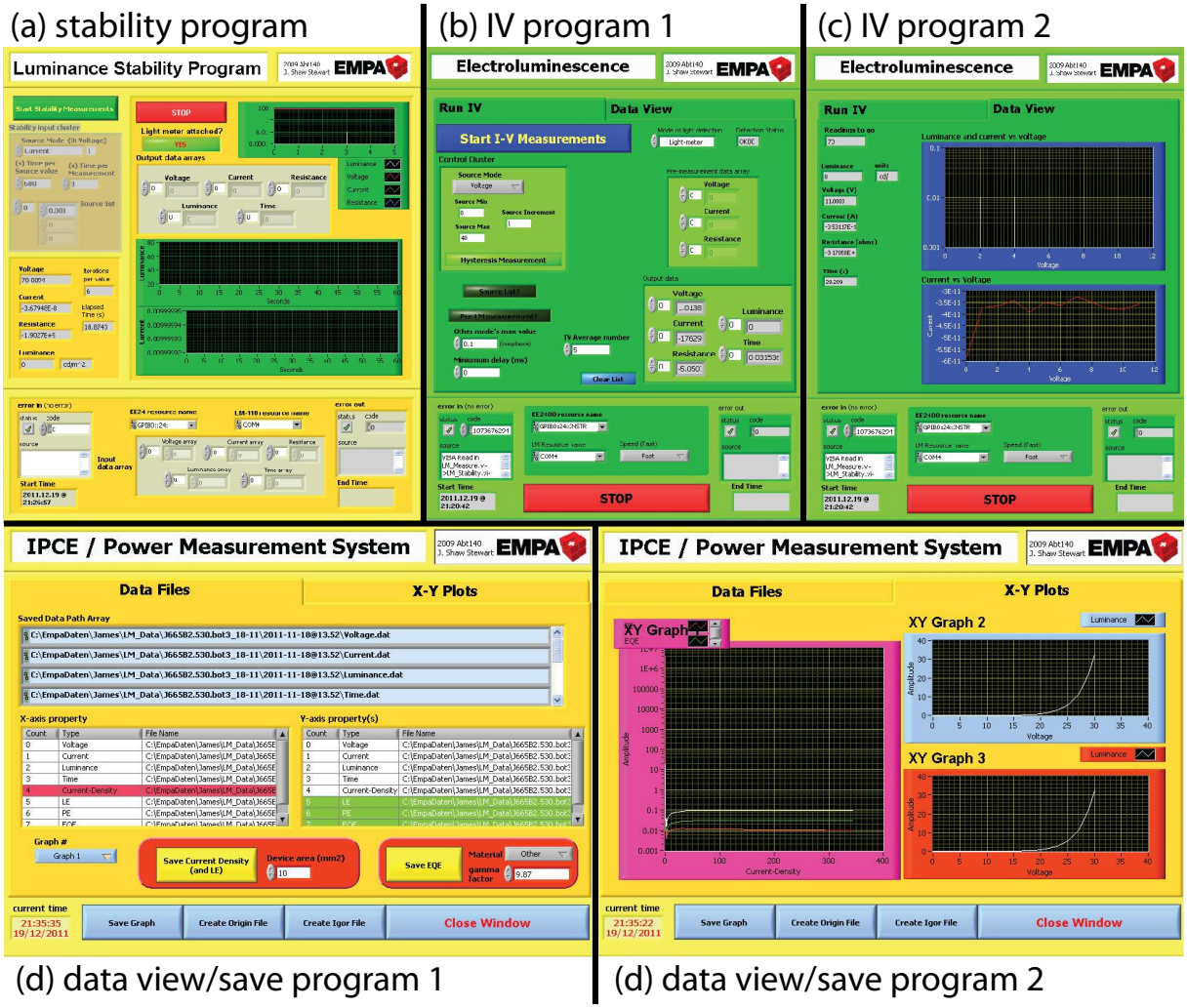

Figure A.2 The GUI of various sub VIs: the stability programme (a), the I-V sweep programme (b) & (c), and the data view and save programme (d) & (e).

characterise organic photo-voltaics (OPVs). It was developed to allow for the use of the luminance meter, and additional control in the data view and save VI.

Appendix B

Calculation of OLED power and external quantum efficiency

Efficiency of the OLED emission is an important figure-of-merit, but the actual efficiency in question can vary. The simplest efficiency to consider is the quantum efficiency (QE), the proportion of photons emitted per electron in current. Nevertheless, there are other (easier experimentally) ways of calculating the efficiency, such as the power efficiency (PE) and the luminous efficiency (LE) outlined here.

Device characterisation was undertaken using a Keithley 2400 sourcemeter coupled with a Minolta LS-110 luminance-meter using the LabVIEW programme outlined in chapter A. The Minolta LS-110 is calibrated for direct photometric measurement of the *luminance* in candela per square metre (cd/m^2). The candela is a form of energy intensity normalised to the human eye's sensitivity by the photometric spectrum in figure B.1. From basic L-I-V (light - current - voltage) measurements, a form of efficiency called luminous efficiency (LE) can easily be measured in candela per amp (cd/A). This is done by first calculating the current density (J) by dividing the current by the cross sectional area (A) of the device to get the current density:

$$J = {}^{I}/_{A} \tag{B.1}$$

Whilst the luminous efficiency is a useful parameter, it is normalised to the photometric spectrum, meaning that green devices are inherently more efficient than red and blue ones for the same number of photons emitted per electron passing through the device, i.e. the QE. For this reason it is useful to be able to calculate the QE of a device. In addition, neither of these parameters take into account the voltage required to push the current through the device, meaning that a device operating at 3 V can have the same efficiency as one at 30 V! Obviously, the higher-voltage device will use more power ($P = I \cdot V$), and so another form of efficiency is widely used, known as the power efficiency, measured in lumen per watt (lm/W). It is also photometric - the lumen is a measure of luminous flux, converted from candela (luminous intensity) by integrating over the solid angle. The electrical power (in

watts) is calculated by multiplying the voltage and current together.

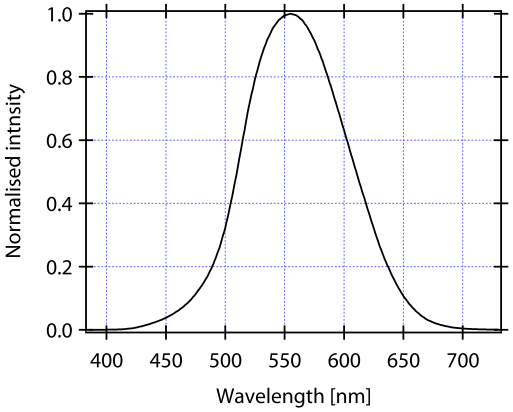

Figure B.1 The photometric spectrum, highlighting the normalised eye sensitivity, with the peak at 555 nm.

B.1 Calculating the power efficiency

The electrical power part of the efficiency measurement is easily calculated by multiplying the current density and the voltage to obtain W/m^s. Luminous emittance (M_v, measured in lux or lm/m^2) can be calculated from cd/m^2 if the angular dependence of the emission is known. It has been observed previously that the emission of an OLED follows, to a good approximation, a Lambertian light-emission profile [202, 203]. A lambertian light profile follows *Lambert's cosine law*:

$$I_\lambda(\theta) = I_\lambda(0) \cdot \cos\theta \tag{B.2}$$

Where I_λ is the luminous intensity (cd) at a given wavelength, and θ is the angle from normal (perpendicular), meaning that the intensity decreases from I_λ at $\theta = 0$ to zero at $\theta = \pi$ (where the angle is given in radians).

The conversion between luminous intensity ($I_{lambda}(0)$ in cd) and luminous flux (Φ in lm) for a Lambertian emitter is simply:

$$\Phi = I_\lambda(0) \cdot \pi \tag{B.3}$$

Meaning that the PE can be calculated from the LE as follows:

$$\mathrm{PE} = \mathrm{LE} \cdot \frac{\pi}{V} \tag{B.4}$$

Where V is the voltage.

B.2 Calculating the external quantum efficiency[1]

There are significant refractive and reflective emission losses in the substrate, depending on the relative refractive indexes. These mean that without a detailed analysis of the device and substrate architecture the actual *internal* QE is very hard to calculate [203]. For this reason, the external quantum efficiency (EQE) is commonly used as an approximation. The EQE is the proportion of photons emitted out of the device (i.e. not trapped by internal reflection in a waveguide) per electron passing through as current. This can be taken from the PE using a basic transform based on the EL spectrum, as the efficiency needs to be converted from photometric units to quanta.

$$\mathrm{EQE} = \frac{\iint \frac{\lambda}{hc}\Phi(\lambda,\theta)\,\mathrm{d}\theta\,\mathrm{d}\lambda}{I/e} = \frac{N_p}{N_e} \tag{B.5}$$

It is easy to convert the current to electrons (N_p) by dividing it by the electronic charge, e, as is shown by the denominator in equation B.5. The difficulty is to obtain the total photons (N_e) from the photometric properties obtained by the luminance-meter.

A simple way to approach this problem is to use a transform, such as that from [204] represented by a parameter γ in the following relationship:

$$\mathrm{EQE}\cdot\gamma = \mathrm{PE} \tag{B.6}$$

Where γ is essentially a transform between the photometric PE and the quantum EQE, and is given by equation B.7:

$$\gamma = \frac{683hc}{Ve}\frac{\int_{380}^{780} g(\lambda)K(\lambda)\mathrm{d}\lambda}{\int_{380}^{780} g(\lambda)\lambda\mathrm{d}\lambda} \tag{B.7}$$

Ve on the denominator of the first fraction convert N_e to power (P). The rest of the transform converts N_p into photometric luminous flux in lumen. 683 is the number of watts given off by 1 lm at λ_{max} (555 nm, see figure 1.6), and the physical constants, h and c, are used to convert N_p into energy. $g(\lambda)$ is the EL emission spectrum (it doesn't need to be normalised), $K(\lambda)$ is the normalised photometric spectrum (figure B.1), and λ is the wavelength. The second fraction in equation B.7 creates a ratio between the area under a

[1] This is based on a transform method between power efficiency and external quantum efficiency found in the literature [204]

photometrically normalised EL emission spectrum (numerator), and a normalised version of the actual EL emission spectrum (demoninator).

Essentially, for a given electrical power, $N_e = {}^{P}/_{Ve}$, and for a given wavelength, the energy of one photon $E_p(\lambda) = \frac{hc}{\lambda}$

To conclude with, once an EL spectrum is obtained it is quite simple to convert the PE to an EQE using the transform outlined in equations B.6 & B.7.

Appendix C

Extra results

C.1 Optimising LIFT in atmosphere for PFO and Alq_3

The work undertaken between sections 4.1 and 4.2 in chapter 4 was extensive, but largely unsuccessful. The poor reproducibility observed for the deposition of MEH-PPV pixels was seen to an even greater extent with Alq_3 and PFO. A large number and wide variety of experiments were attempted, but rarely gave logical results. This led to the need to optimise the LIFT process, and hence the work on the gap and the pressure was developed.

In this section, two sets of transfer results are shown. Firstly, some interesting test results when OLED pixel transfers of Alq_3 and PFO were attempted shortly after the work on MEH-PPV. The donor substrates consisted of 190 nm TP / 80 nm Al / organic layer, where the organic layer was either 60 nm Alq_3 or $\sim$ 80 nm PFO. The receiver substrates were 140 nm ITO / $\sim$ 25 nm PEDOT:PSS.

The results of the test transfers at a range of fluences, are shown in figure C.1. As can be seen with the transfers made at the right side of the samples, some pixels with a reasonably good morphology were obtained. However, rather than being for a particular fluence range, they are more noteworthy as being all to the right of the group of pixels, i.e. at the edge of the sample. As is shown by the diagram at the top of figure C.1, the fluence decreases from the top left to the bottom right. For both Alq_3 and PFO, there is some for of metal transfer at the top right, a fluence of around 220 mJ/cm^2. This compares well with the higher fluence regime for MEH-PPV transfer in atmospheric pressure in section 4.1, and with the original MEH-PPV OLED transfer [118]. Alq_3 appears to transfer more successfully than the polymeric PFO, particularly at the lower fluences (middle row) where the PFO barely seems to stick to the receiver substrate. This results adds to the hypothesis that the intra-facial forces between the flyer and the receiver substrate are important (section 4.1 and reference [123]). PEDOT:PSS probably forms a polar hydrophilic surface which is unlikely to be attractive to the hydrophobic PFO, whereas amorphic Alq_3 may have less hydrophobic surfaces. For LITI, modification of the PEDOT:PSS to make it hydrophobic was shown to improve interfacial adhesion [123].

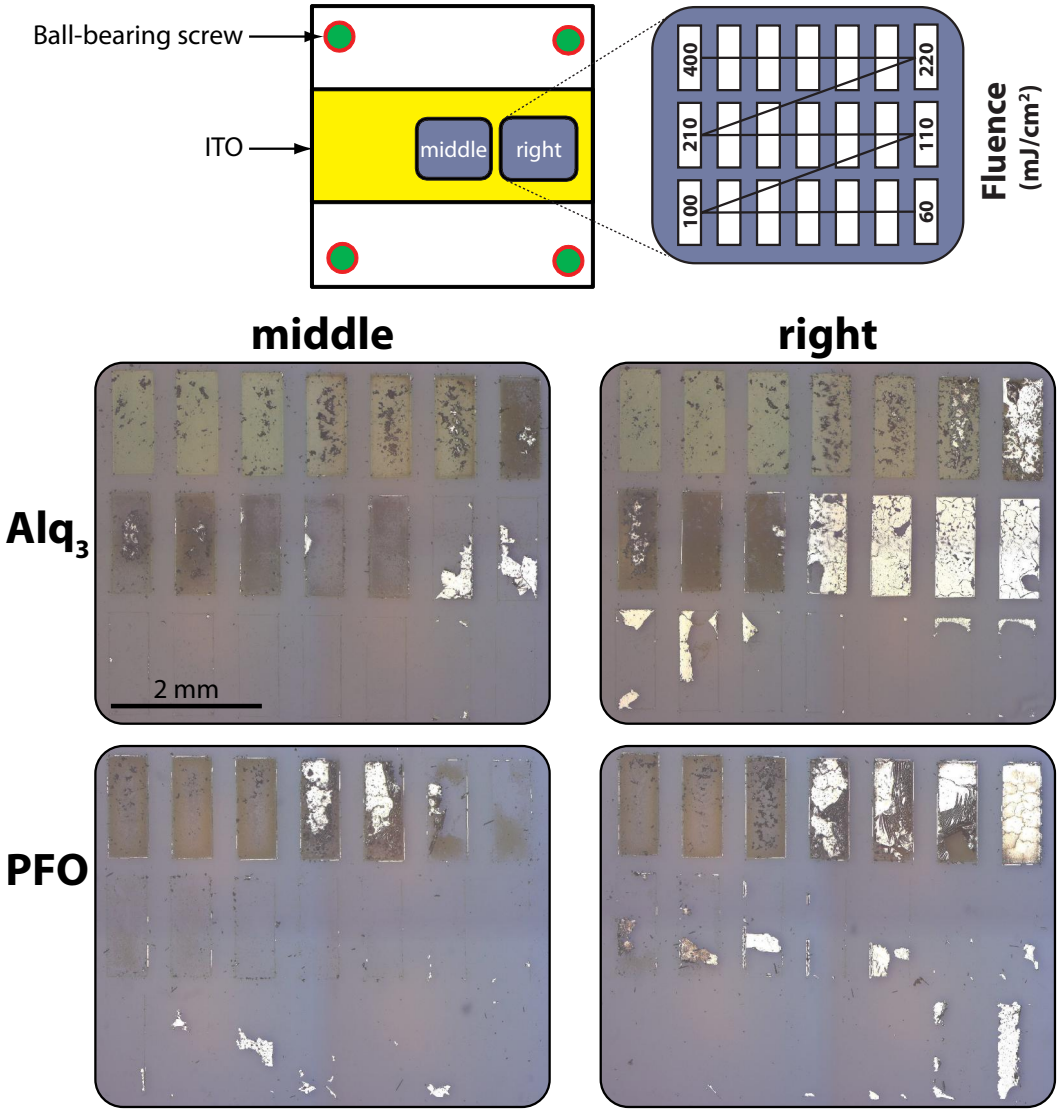

Figure C.1 Transfers of Alq_3 and PFO / Al bilayer pixels 'in contact'. The scheme at the top left shows where the sets of pixels were located on the patterned ITO glass substrate, and the scheme at the top right shows the fluence range of the pixels.

In addition, the Alq_3 appears to stick to the receiver substrate at all fluences in the top two rows, but the metal does not seem to stay adhered to the Alq_3 in the middle test at all, and is also lost to the left of the right test as well. This suggests that the poor film cohesion will play a part in the reason for a lack of Al on the receiver substrate in these different positions. The successfully deposited pixels, both Alq_3 and PFO, appear to have a large number of cracks running through them like the MEH-PPV pixels in sections 4.1 and 5.1, and in contrast to those deposited at reduced pressures in chapters 4 and 5.

The main outcome of the experiment in figure C.1 was to conclude that the success of pixel deposition had an enormous dependence on the position of the pixel on the sample, i.e. if the pixel is deposited closer to the edge of the sample, successful transfer is more

likely. Due to the position of the screws holding the substrates together, this probably means that the substrates are in closer contact at the edges, suggesting that the likelihood of a successful deposition is greater when the substrates are in closer contact, at atmospheric pressure. This led to the decision to investigate the substrate-substrate gap width in more detail, in section 4.2.

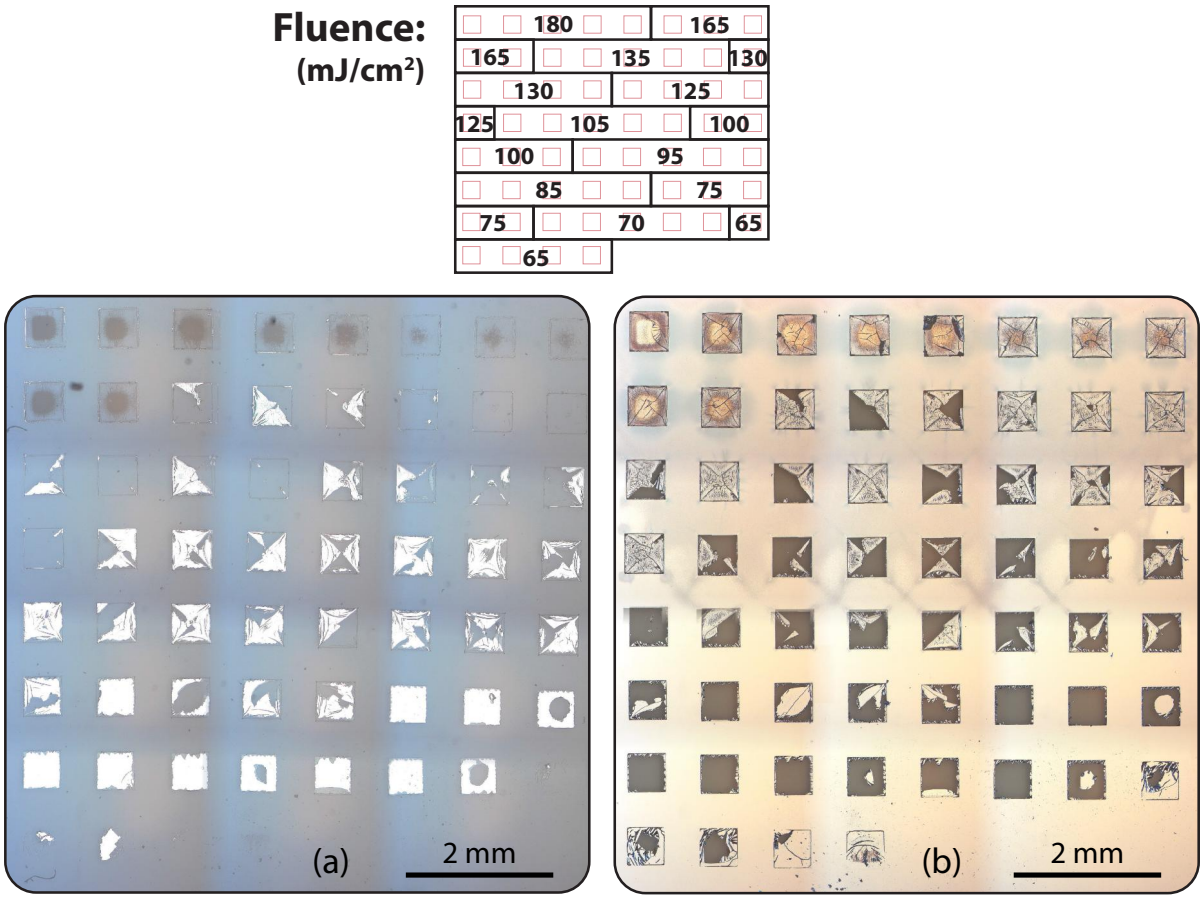

Figure C.2 LIFT of 190 nm TP / 80 nm Al / 60 nm Alq_3 pixels onto a glass / PEDOT:PSS receiver substrate. The fluences are shown at the top of the figure, the receiver substrate is on the left (a), and the donor substrate is on the right (b).

In addition to figure C.1, micrographs of the most successful transfers of Alq_3 'in contact', at atmospheric pressure, are shown in figure C.2. Sets of five pixels at different fluences are shown in a slightly irregular pattern, due to the line length not corresponding to a multiple of five, and the donor substrate is also shown in figure C.2b. Although cracks like those in figure C.1 are not as obvious (possibly because the fluences for the successful pixel deposition are lower), there are some interesting pixel patterns present, such as the diagonal crosses for the pixels transferred at 95, 100, and 105 mJ/cm^2. A similar pattern has been observed before in the partial (backside) ablation of pure TP films [147]. Because of this observation, it can be suggested that this pattern probably comes from heterogeneous stress upon the flyer from the original TP ablation. This observation may suggest

that the reason that successful transfer has been achieved is because the substrates are in close contact. Very close contact would mean that the impact of the flyer on the receiver substrate would happen shortly after the onset of ablation, meaning that any stresses directly from the ablation will not have time to be masked by other stresses, such as those from fluid dynamics during the flight from the donor to the receiver.

There are also a series of holes in the pixels at fluences below 95 mJ/cm^2 in figure C.2, although these do not look quite like the rips in section 4.2, which were thought to be because of stresses on the film during flight or impact. The holes in the pixels in C.2 look more like they originate from stresses during the separation of the two substrates. Despite the successful deposition of these pixels, very few of the pixels would create functional pixels. Even more frustratingly, this moderate success was very tricky to reproduce, probably because the good substrate-substrate contact achieved was probably not easily reproduced.

Overall, the results in this section represent a small snapshot of the series of transfers attempted between the MEH-PPV depositions in section 4.1 and the gap and pressure optimisation in section 4.2, with only moderate success at best. Nevertheless, this experience was invaluable in enabling the successes of the following depositions.

C.2 Optimising the OLED anodes and cathodes

Originally it was envisaged that the system would be kept simple with only PEDOT:PSS coated on the ITO anode. However, reports were found in the literature extolling the virtues of PVK / PFO bilayer system [32, 60, 189], particularly for fluorescent/phosphorescent iridium-complex doping of the PFO. For this reason, conventionally fabricated plain PFO devices with and without PVK were made, shown in figure C.3. Silver was used for the cathode, and Cs_2CO_3 was also added to check a slightly different architecture. As can be seen, the addition of PVK had an enormous benefit upon the device performances. The PVK used here came from Aldrich, but the molecular weight given on the bottle is *average* $M_n = 25{,}000$ unlike the PVK from reference [32] and used in the following section 5.3, which has *typical* $M_w = 1{,}100{,}000$. This means that it is likely that the toluene solution of PFO dissolved at least a part of the underlying PVK film to create a PVK:PFO blend. As shown in reference [32], a blend should indeed have a lower operating voltage, unlike a bilayer device. However in the study cited, PBD was used as an electron-injecting material (blended with the active layer), and the cathode metal was barium meaning that a direct comparison is not completely meaningful. Despite this, the results in figure C.3 are useful, particularly in showing that the addition of PVK did indeed give significantly more efficient devices in figure C.3b.

Whilst the results from figure C.3 are not conclusive, experiments were carried out with LIFTed pixels to investigate the difference between anodes with and without PVK. The Ir(Me-ppy)$_3$ dopant was used to test whether there was any noticeable difference between doped PFO and pure PFO pixels. The results are presented in figure C.4, and show an in-

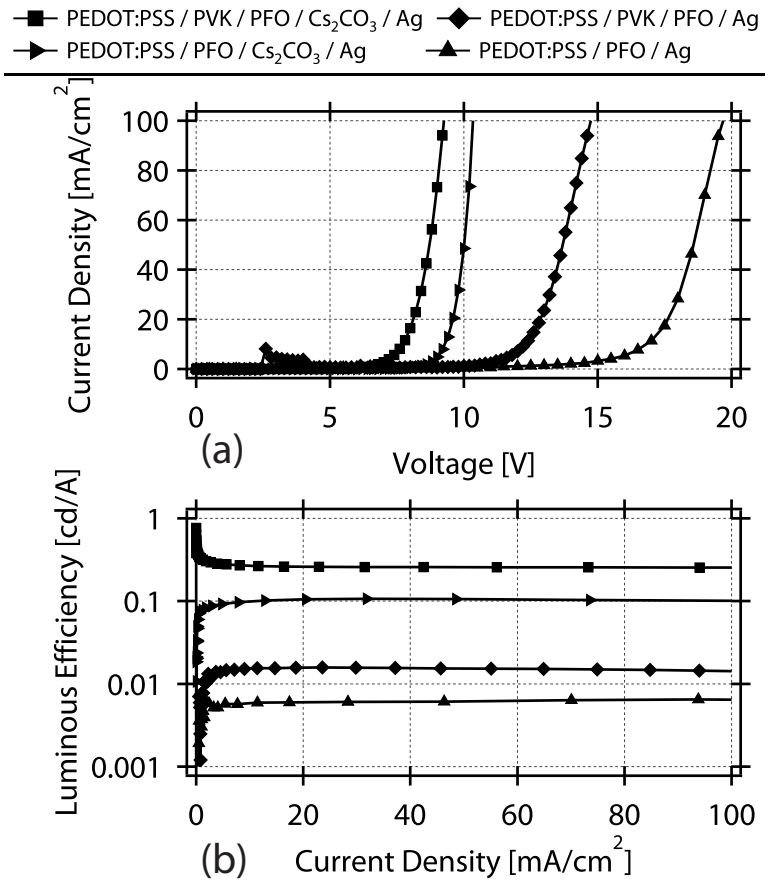

Figure C.3 The device characteristics of conventional devices fabricated with or without PVK on the anode. Silver and Cs_2CO_3 / Ag cathodes have been used. (a) gives the current density against voltage for the four different device architectures, and (b) shows the luminous efficiency as a function of current density.

teresting difference between the pure PFO and PFO:Ir(Me-ppy)$_3$ pixels, as well as between the use of an anode with or without PVK. The big conclusion from this is that the addition of PVK improved the LIFTed pixel device performance significantly: the pure PFO pixel on a PEDOT:PSS anode did not work at all. Nevertheless, the current densities of the PFO:Ir(Me-ppy)$_3$ pixels in figure C.4a show that the addition of PVK increases the operating voltage, and that similar current densities are achievable, at similar efficiencies (figure C.4b). In fact, the addition of PVK appears to increase the degradation of the device, but the devices were far more stable than those made with just PEDOT:PSS. Interestingly, all the devices exhibit approximately the same luminous efficiency, suggesting that the mechanism is dominated by factors other than recombination, probably the common denominators for all the devices which are the cathode (Cs_2CO_3 / Ag) and the PFO.

A notable difference between the plain PEDOT:PSS and PEDOT:PSS / PVK pixels is the operating voltage in figure C.4a. In fact, the lower operating voltage of plain PEDOT:PSS

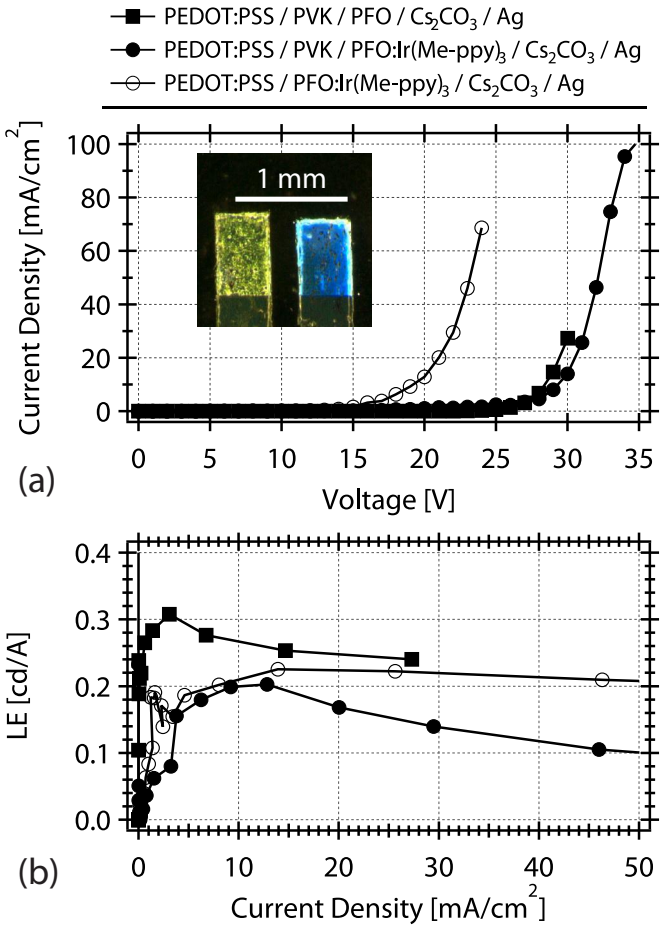

Figure C.4 The device characteristics for LIFTed PFO-based pixels using different anodes. The plain blue PFO pixel without PVK on the anode did not work at all. (a) presents the current density as a function of voltage for the plain blue PFO pixel with PVK (solid squares), the green PFO:dye pixel with PVK (solid circles) and without PVK (hollow circle). A micrograph of illuminated pixels (using PVK on the anode) is shown as an inset. (b) shows the luminous efficiency (LE) as a function of current density for the same pixels.

anode may have been helpful later on. Nevertheless, at this point in the optimisation, the stability of the PEDOT:PSS / PVK pixels was preferential, even at the detriment to the operating voltage. One area where the devices could be significantly improved in future would be in the anode, by selecting a better hole-transporting layer than PVK, as a significant reason for the poor pixel lifetimes is probably the high operating voltages of the pixels presented in this thesis, which mean there is always physical stress upon the OLEDs.

Appendix D

List of Abbreviations

Acronyms

CRT	cathode ray tube
EBL	electron-blocking layer
EL	electroluminescence
EIL	electron-injecting layer
ETL	electron-transporting layer
FWHM	full width at half maximum
HOMO	highest occupied molecular orbital
HBL	hole-blocking layer
HD	high definition
HIL	hole-injecting layer
HTL	hole transporting layer
ICCD	intensified charged-coupled device
IR	infrared
I-V	current - voltage
LCD	liquid crystal display
LDW	laser direct-write
LED	light emitting diode
LEP	light-emitting polymer
LIFT	laser-induced forward transfer
LITI	laser-induced thermal imaging
L-J-V	luminance - current density - voltage
LUMO	lowest unoccupied molecular orbital
MAPLE	matrix-assisted pulsed laser evaporation
MAPLE-DW	matrix-assisted pulsed laser evaporation direct write
Nd:YAG	neodymium-doped yttrium aluminum garnet

OLED	organic light emitting diode
OPV	organic photo-voltaic
PhOLED	phosphorescent organic light-emitting diode
PL	photoluminescence
PLD	pulsed laser deposition
PLED	polymer light emitting diode
PMMA	polymethyl methacrylate
R-G-B	red-green-blue
SEM	scanning electron microscope
SMOLED	small-molecule organic light-emitting diode
TFT	thin film transistor
UHD	ultra high definition
UV	ultraviolet
VI	LabVIEW virtual instrument

Symbols

c	speed of light in vacuum
d	ablated depth
E	energy
F	laser fluence
F_{th}	threshold laser fluence
g	temporal distribution of the laser intensity
h	film thickness (height) and Planck's constant
n	refractive index
p	Laplacian transform space variable
q	normalised spatial distribution of the absorbed laser intensity
Q	distribution of the absorbed laser intensity
r	reflection coefficient
R	reflectivity
t	time
t_l	characteristic pulse duration
T	temperature
$\tilde{T}$	Laplacian transform of the temperature
v	velocity
v_0	initial flyer velocity / velocity of flyer in vacuum
x	depth into the DRL (from substrate / DRL interface)
z	depth into the sample (from air / sample interface)

χ	thermal diffusivity
α_{lin}	linear absorption coefficient
α_{eff}	effective absorption coefficient
ΔH_{dec}	decomposition enthalpy
ε	energy per mass
κ	thermal conductivity
λ	wavelength
ρ	density
τ	laser pulse duration
χ	thermal diffusivity

Chemical names

Alq_3	green emitter, aluminium tri-8-hydroxyquinoline
$btp_2Ir(acac)$	bis(2-(2'-benzothienyl)-pyridinato-N,$C^{3'}$) iridium(acetylacetonate)
$Ir(Me\text{-}ppy)_3$	*fac*-tris(2.(4'-methyl)-phenylpyridine) iridium
ITO	transparent electrode, tin-doped indium oxide
MEH-PPV	orange-emitter, poly(2-methoxy-5-(2'-ethylhexyloxy)-1,4-phenylene vinylene)
PEDOT:PSS	conductive HTL, poly(3,4-ethylenedioxythiophene) blended with poly(sytrenesulfonate)
PEO	HBL/ETL, poly(ethylene oxide)
PFN	blue-green emitter, poly((9,9-di(3,3'-N,N'-trimethylammonium) propyl fluorenyl-2,7-diyl)-alt-(9,9-dioctylfluorenyl-2,7-diyl))
PFO	blue emitter, poly(9,9-dioctylfluorenyl-2,7-diyl)
PVK	HTL, poly(N-vinylcarbazole)
TBA	monolayer EIL, tetrabutyl-ammonium hydroxide
TP	triazene polymer, the variant with a hexalkyl linking chain, and a methyl sidegroup, shown in figure 1.11

Indices

d	DRL/ablated layer
dec	decompostion
eff	effective
f	film
g	gas

lin linear
s substrate
t transfer layer
th threshold

Bibliography

[1] D. Compton, W. Schneider, and T. Waddington, "Photoconductivity of anthracene. III," *J. Chem. Phys.*, vol. 27, no. 1, p. 160, 1957. [Online]. Available: http://dx.doi.org/10.1063/1.1743658 3, 7

[2] C. Garrett, *Semiconductors*. New York: Reinhold Publishing Corporation, 1959, ch. 15. "Organic Semiconductors", pp. 634–675. 3, 7

[3] H. Kallmann and M. Pope, "Bulk conductivity in organic crystals," *Nature*, vol. 186, no. 4718, pp. 31–33, 1960. [Online]. Available: http://dx.doi.org/10.1038/186031a0 3

[4] M. Pope and C. Swenberg, *Electronic Processes in Organic Crystals and Polymers*, 2nd ed. Oxford University Press, 1999. 3, 8, 9

[5] H. Round, "A note on carborundum," *Electrical World*, vol. 49, p. 309, 1907. 3

[6] M. Pope, H. Kallmann, and P. Magnante, "Electroluminescence in organic crystals," *The Journal of Chemical Physics*, vol. 38, no. 8, pp. 2042–2043, 1963. [Online]. Available: http://dx.doi.org/10.1063/1.1733929 3, 7

[7] C. W. Tang and S. A. VanSlyke, "Organic electroluminescent diodes," *Applied Physics Letters*, vol. 51, no. 12, pp. 913–915, 1987. [Online]. Available: http://dx.doi.org/10.1063/1.98799 3, 7, 9, 10, 31, 128, 129

[8] J. H. Burroughes, D. D. C. Bradley, A. R. Brown, R. N. Marks, K. Mackay, R. H. Friend, P. L. Burns, and A. B. Holmes, "Light-emitting diodes based on conjugated polymers," *Nature*, vol. 347, no. 6293, pp. 539–541, 1990. [Online]. Available: http://dx.doi.org/10.1038/347539a0 3, 7, 11

[9] D. Braun and A. J. Heeger, "Visible light emission from semiconducting polymer diodes," *Applied Physics Letters*, vol. 58, no. 18, pp. 1982–1984, 1991. [Online]. Available: http://dx.doi.org/10.1063/1.105039 3, 7, 11

[10] R. Friend, R. Gymer, A. Holmes, J. Burroughes, R. Marks, C. Taliani, D. Bradley, D. Dos Santos, J. Bredas, and M. Lögdlun, "Electroluminescence in conjugated polymers," *Nature*, vol. 397, no. 6715, pp. 121–128, 1999. [Online]. Available: http://dx.doi.org/10.1038/16393 3, 9, 125

[11] S. Lee, J. Lee, M. Kim, M. Suh, T. Kang, Y. Choi, J. Park, J. Kwon, H. Chung, J. Baetzold, E. Bellmann, V. Savvateev, M. Wolk, and S. Webster, "21.3: A new patterning method for full-color polymer light-emitting devices: Laser induced thermal imaging (LITI)," *SID Symposium Digest of Technical Papers*, vol. 33, no. 1, pp. 784–787, 2002. [Online]. Available: http://dx.doi.org/10.1889/1.1830899 3, 12, 17, 18, 23, 24

[12] S. Forrest, "The path to ubiquitous and low-cost organic electronic appliances on plastic," *Nature*, vol. 428, no. 6986, pp. 911–918, 2004. [Online]. Available: http://dx.doi.org/10.1038/nature02498 3

[13] W. Kylberg, F. de Castro, P. Chabrecek, U. Sonderegger, B.-T. Chu, F. Nüesch, and R. Hany, "Woven electrodes for flexible organic photovoltaic cells," *Advanced Materials*, vol. 23, no. 8, pp. 1015–1019, 2011. [Online]. Available: http://dx.doi.org/10.1002/adma.201003391 3, 11, 28

[14] H. Sirringhaus, "Materials and applications for solution-processed organic field-effect transistors," *Proceedings of the IEEE*, vol. 97, no. 9, pp. 1570–1579, 2009. [Online]. Available: http://dx.doi.org/10.1109/JPROC.2009.2021680 3

[15] C. Bettinger and Z. Bao, "Biomaterials-based organic electronic devices," *Polymer International*, vol. 59, no. 5, pp. 563–567, 2010. [Online]. Available: http://dx.doi.org/10.1002/pi.2827 3

[16] C. Chiang, J. Fincher, C.R., Y. Park, A. Heeger, H. Shirakawa, E. Louis, S. Gau, and A. MacDiarmid, "Electrical conductivity in doped polyacetylene," *Physical Review Letters*, vol. 39, no. 17, p. 1098, 1977. [Online]. Available: http://dx.doi.org/10.1103/PhysRevLett.39.1098 3, 5, 7

[17] M. Pope, "Electric currents in organic crystals," *Scientific American*, vol. 216, no. 1, pp. 86–97, 1967. [Online]. Available: http://dx.doi.org/10.1038/scientificamerican0167-86 5

[18] N. Karl, *Festkorperprobleme XIV*. Berlin / Heidelberg: Springer, 1974, ch. "Organic Semiconductors", pp. 261–290. [Online]. Available: http://dx.doi.org/10.1007/BFb0108470 5, 6, 8

[19] A. Szent-Györgyi, "Towards a new biochemistry?" *Science*, vol. 93, no. 2426, pp. 609–611, 1941. [Online]. Available: http://dx.doi.org/10.1126/science.93.2426.609 6, 8

[20] H. Witt, "Coupling of quanta, electrons, fields, ions and phosphorylation in the functional membrane of photosynthesis. results by pulse spectroscopic methods," *Quarterly Reviews of Biophysics*, vol. 4, no. 04, pp. 365–477, 1971. [Online]. Available: http://dx.doi.org/10.1017/S0033583500000834 7

[21] Q. Pei, G. Yu, C. Zhang, Y. Yang, and A. Heeger, "Polymer light-emitting electrochemical cells," *Science*, vol. 269, no. 5227, pp. 1086–1088, 1995. [Online]. Available: http://dx.doi.org/10.1126/science.269.5227.1086 7

[22] R. Fowler and L. Nordheim, "Electron emission in intense electric fields," *Proceedings of the Royal Society of London. Series A, Containing Papers of a Mathematical and Physical Character*, vol. 119, no. 781, pp. 173–181, 1928. [Online]. Available: http://dx.doi.org/10.1098/rspa.1928.0091 7, 8

[23] I. Parker, "Carrier tunneling and device characteristics in polymer light-emitting diodes," *Journal of Applied Physics*, vol. 75, no. 3, pp. 1656–1666, 1994. [Online]. Available: http://dx.doi.org/10.1063/1.356350 7, 120, 125, 138

[24] V. Coropceanu, J. Cornil, D. da Silva Filho, Y. Olivier, R. Silbey, and J.-L. Brédas, "Charge transport in organic semiconductors," *Chemical Reviews*, vol. 107, no. 4, pp. 926–952, 2007. [Online]. Available: http://dx.doi.org/10.1021/cr050140x 8, 9

[25] P.-T. Chou and Y. Chi, "Phosphorescent dyes for organic light-emitting diodes," *Chemistry – A European Journal*, vol. 13, no. 2, pp. 380–395, 2007. [Online]. Available: http://dx.doi.org/10.1002/chem.200601272 9, 10, 13

[26] H. Bolink, E. Coronado, J. Orozco, and M. Sessolo, "Efficient polymer light-emitting diode using air-stable metal oxides as electrodes," *Advanced Materials*, vol. 21, no. 1, pp. 79–82, 2009. [Online]. Available: http://dx.doi.org/10.1002/adma.200802155 9, 32, 127

[27] Y. Ohmori, M. Uchida, K. Muro, and K. Yoshino, "Blue electroluminescent diodes utilizing poly(alkylfluorene)," *Japanese Journal of Applied Physics*, vol. 30, no. Part 2, No. 11B, p. L1941, 1991. [Online]. Available: http://dx.doi.org/10.1143/JJAP.13.1023 9

[28] A. Grice, D. Bradley, M. Bernius, M. Inbasekaran, W. Wu, and E. Woo, "High brightness and efficiency blue light-emitting polymer diodes," *Applied Physics Letters*, vol. 73, no. 5, pp. 629–631, 1998. [Online]. Available: http://dx.doi.org/10.1063/1.121878 9

[29] M. Leclerc, "Polyfluorenes: Twenty years of progress," *Journal of Polymer Science Part A: Polymer Chemistry*, vol. 39, no. 17, pp. 2867–2873, 2001. [Online]. Available: http://dx.doi.org/10.1002/pola.1266 9

[30] D. Kabra, L. Lu, M. Song, H. Snaith, and R. Friend, "Efficient single-layer polymer light-emitting diodes," *Advanced Materials*, vol. 22, no. 29, pp. 3194–3198, 2010. [Online]. Available: http://dx.doi.org/10.1002/adma.201000317 9, 13, 32, 127

[31] X. Jiang, Y. Liu, X. Song, and D. Zhu, "Organic light-emitting diodes made with poly (N-vinylcarbazole) (PVK) and 8-hydroxyquinoline aluminium (Alq_3)," *Synthetic Metals*, vol. 87, no. 3, pp. 175–178, 1997. [Online]. Available: http://dx.doi.org/10.1016/s0379-6779(97)80104-x 9, 33, 128, 129

[32] Z. Chen, C. Jiang, Q. Niu, J. Peng, and Y. Cao, "Enhanced green electrophosphorescence by using polyfluorene host via interfacial energy transfer from polyvinylcarbazole," *Organic Electronics*, vol. 9, no. 6, pp. 1002–1009, 2008. [Online]. Available: http://dx.doi.org/10.1016/j.orgel.2008.07.005 9, 30, 33, 117, 123, 126, 127, 160

[33] S. Reineke, F. Lindner, G. Schwartz, N. Seidler, K. Walzer, B. Lussem, and K. Leo, "White organic light-emitting diodes with fluorescent tube efficiency," *Nature*, vol. 459, no. 7244, pp. 234–238, 2009. [Online]. Available: http://dx.doi.org/10.1038/nature08003 9, 13

[34] H. Sasabe, J.-i. Takamatsu, T. Motoyama, S. Watanabe, G. Wagenblast, N. Langer, O. Molt, E. Fuchs, C. Lennartz, and J. Kido, "High-efficiency blue and white organic light-emitting devices incorporating a blue iridium carbene complex," *Advanced Materials*, vol. 22, no. 44, pp. 5003–5007, 2010. [Online]. Available: http://dx.doi.org/10.1002/adma.201002254 9, 13

[35] Y. Fukuda, S. Miyaguchi, S. Ishizuka, T. Wakimoto, J. Funaki, H. Kubota, T. Watanabe, H. Ochi, T. Sakamoto, M. Tsuchida, I. Ohshita, H. Nakada, and T. Tohma, "Organic LED full color passive-matrix display," *SID Symposium Digest of Technical Papers*, vol. 30, no. 1, pp. 430–433, 1999. [Online]. Available: http://dx.doi.org/10.1889/1.1834049 9

[36] D. Flattery, C. Fincher, D. LeCloux, M. O'Regan, and J. Richard, "Clearing the road to mass production of OLED television," *Information Display*, vol. 27, no. 10, pp. 8–13, 2011. [Online]. Available: http://www.informationdisplay.org/article.cfm?year=2011&issue=10&file=art3 9

[37] C. Tang, S. VanSlyke, and C. Chen, "Electroluminescence of doped organic thin films," *Journal of Applied Physics*, vol. 65, no. 9, pp. 3610–3616, 1989. [Online]. Available: http://dx.doi.org/10.1063/1.343409 9

[38] D. Dexter, "A theory of sensitized luminescence in solids," *The Journal of Chemical Physics*, vol. 21, no. 5, pp. 836–850, 1953. [Online]. Available: http://dx.doi.org/10.1063/1.1699044 10

[39] D. Andrews, "A unified theory of radiative and radiationless molecular energy transfer," *Chemical Physics*, vol. 135, no. 2, pp. 195–201, 1989. [Online]. Available: http://dx.doi.org/10.1016/0301-0104(89)87019-3 10

[40] D. Andrews and D. Bradshaw, "Virtual photons, dipole fields and energy transfer: a quantum electrodynamical approach," *European Journal of Physics*, vol. 25, no. 6, p. 845, 2004. [Online]. Available: http://dx.doi.org/10.1088/0143-0807/25/6/017 10

[41] M. Baldo, D. O'Brien, Y. You, A. Shoustikov, S. Sibley, M. Thompson, and S. Forrest, "Highly efficient phosphorescent emission from organic electroluminescent devices," *Nature*, vol. 395, no. 6698, pp. 151–154, 1998. [Online]. Available: http://dx.doi.org/10.1038/25954 10

[42] S. Blumstengel, F. Meinardi, R. Tubino, M. Gurioli, M. Jandke, and P. Strohriegl, "Long-range energy transfer of singlet and triplet excitations in dye-doped tris(phenylquinoxaline)," *The Journal of Chemical Physics*, vol. 115, no. 7, pp. 3249–3255, 2001. [Online]. Available: http://dx.doi.org/10.1063/1.1388050 10

[43] M. Baldo, S. Lamansky, P. Burrows, M. Thompson, and S. Forrest, "Very high-efficiency green organic light-emitting devices based on electrophosphorescence," *Applied Physics Letters*, vol. 75, no. 1, pp. 4–6, 1999. [Online]. Available: http://dx.doi.org/10.1063/1.124258 10

[44] P. Semenza, "OLEDs in transition," *Information Display*, vol. 27, no. 10, pp. 14–16, 2011. [Online]. Available: http://www.informationdisplay.org/article.cfm?year=2011&issue=10&file=art4 10, 13, 14

[45] G. Rajeswaran, M. Itoh, M. Boroson, S. Barry, T. Hatwar, K. Kahen, K. Yoneda, R. Yokoyama, T. Yamada, N. Komiya, H. Kanno, and H. Takahashi, "40.1: Invited paper: Active matrix low temperature poly-Si TFT / OLED full color displays: Development status," *SID Symposium Digest of Technical Papers*, vol. 31, no. 1, pp. 974–977, 2000. [Online]. Available: http://dx.doi.org/10.1889/1.1833119 10

[46] M. Boroson, L. Tutt, K. Nguyen, D. Preuss, M. Culver, and G. Phelan, "16.5L: Late-news-paper: Non-contact OLED color patterning by radiation-induced sublimation transfer (RIST)," *SID Symposium Digest of Technical Papers*, vol. 36, no. 1, pp. 972–975, 2005. [Online]. Available: http://dx.doi.org/10.1889/1.2036612 10

[47] M. Kröger, M. Hüske, T. Dobbertin, J. Meyer, H. Krautwald, T. Riedl, H. Johannes, and W. Kowalsky, "A novel patterning technique for high-resolution RGB-OLED-displays: Laser induced local transfer (LILT)," *MRS Symposium Proceedings*, vol. 860E, p. H3.4.1, 2005. [Online]. Available: http://dx.doi.org/10.1117/12.608702 10

[48] T. Hirano, K. Matsuo, K. Kohinata, K. Hanawa, T. Matsumi, E. Matsuda, R. Matsuura, T. Ishibashi, A. Yoshida, and T. Sasaoka, "53.2: Distinguished paper: Novel laser transfer technology for manufacturing large-sized OLED displays," *SID Symposium*

Digest of Technical Papers, vol. 38, no. 1, pp. 1592–1595, 2007. [Online]. Available: http://dx.doi.org/10.1889/1.2785623 10

[49] J. Ju, Y. Yamagata, and T. Higuchi, "Thin-film fabrication method for organic light-emitting diodes using electrospray deposition," *Advanced Materials*, vol. 21, no. 43, pp. 4343–4347, 2009. [Online]. Available: http://dx.doi.org/10.1002/adma.200900444 11

[50] S.-C. Chang, J. Liu, J. Bharathan, Y. Yang, J. Onohara, and J. Kido, "Multicolor organic light-emitting diodes processed by hybrid inkjet printing," *Advanced Materials*, vol. 11, no. 9, pp. 734–737, 1999. [Online]. Available: http://dx.doi.org/10.1002/(SICI)1521-4095(199906)11:9<734::AID-ADMA734>3.0.CO;2-D 11, 33

[51] D. Pardo, G. Jabbour, and N. Peyghambarian, "Application of screen printing in the fabrication of organic light-emitting devices," *Advanced Materials*, vol. 12, no. 17, pp. 1249–1252, 2000. [Online]. Available: http://dx.doi.org/10.1002/1521-4095(200009)12:17<1249::aid-adma1249>3.0.co;2-y 11

[52] D. Li and L. Guo, "Organic thin film transistors and polymer light-emitting diodes patterned by polymer inking and stamping," *Journal of Physics D: Applied Physics*, vol. 41, no. 10, p. 105115, 2008. [Online]. Available: http://dx.doi.org/10.1088/0022-3727/41/10/105115 11

[53] F. Huang, H. Wu, D. Wang, W. Yang, and Y. Cao, "Novel electroluminescent conjugated polyelectrolytes based on polyfluorene," *Chemistry of Materials*, vol. 16, no. 4, pp. 708–716, 2004. [Online]. Available: http://dx.doi.org/10.1021/cm034650o 11, 30, 134, 135, 136, 138

[54] C. Zhong, C. Duan, F. Huang, H. Wu, and Y. Cao, "Materials and devices toward fully solution processable organic light-emitting diodes ," *Chemistry of Materials*, vol. 23, no. 3, pp. 326–340, 2011. [Online]. Available: http://dx.doi.org/10.1021/cm101937p 11

[55] M. Gather, A. Köhnen, A. Falcou, H. Becker, and K. Meerholz, "Solution-processed full-color polymer organic light-emitting diode displays fabricated by direct photolithography," *Advanced Functional Materials*, vol. 17, no. 2, pp. 191–200, 2007. [Online]. Available: http://dx.doi.org/10.1002/adfm.200600651 11

[56] Y. Xu, F. Zhang, and X. Feng, "Patterning of conjugated polymers for organic optoelectronic devices," *Small*, vol. 7, no. 10, pp. 1338–1360, 2011. [Online]. Available: http://dx.doi.org/10.1002/smll.201002336 11

[57] S. Forrest, "The road to high efficiency organic light emitting devices," *Organic Electronics*, vol. 4, no. 2-3, pp. 45–48, 2003. [Online]. Available: http://dx.doi.org/10.1016/j.orgel.2003.08.014 12

[58] M. Helander, Z. Wang, J. Qiu, M. Greiner, D. Puzzo, Z. Liu, and Z. Lu, "Chlorinated indium tin oxide electrodes with high work function for organic device compatibility," *Science*, vol. 332, no. 6032, pp. 944–947, 2011. [Online]. Available: http://dx.doi.org/10.1126/science.1202992 13

[59] D. Kim, N. Cho, H.-Y. Oh, J. Yang, W. Jeon, J. Park, M. Suh, and J. Kwon, "Highly efficient red phosphorescent dopants in organic light-emitting devices," *Advanced Materials*, vol. 23, no. 24, pp. 2721–2726, 2011. [Online]. Available: http://dx.doi.org/10.1002/adma.201100405 13

[60] Z. Chen, Q. Niu, Y. Zhang, L. Ying, J. Peng, and Y. Cao, "Efficient green electrophosphorescence with Al cathode using an effective electron-injecting polymer as the host," *ACS Applied Materials & Interfaces*, vol. 1, no. 12, pp. 2785–2788, 2009. [Online]. Available: http://dx.doi.org/10.1021/am9005258 13, 103, 134, 160

[61] J. Park, D. Shin, and S. Park, "Large-area OLED lightings and their applications," *Semiconductor Science and Technology*, vol. 26, no. 3, p. 034002, 2011. [Online]. Available: http://dx.doi.org/10.1088/0268-1242/26/3/034002 13

[62] H. Sasabe and J. Kido, "Multifunctional materials in high-performance OLEDs: Challenges for solid-state lighting," *Chemistry of Materials*, vol. 23, no. 3, pp. 621–630, 2011. [Online]. Available: http://dx.doi.org/10.1021/cm1024052 13

[63] H.-J. Kwon, H. Shim, S. Kim, W. Choi, Y. Chun, I. Kee, and S. Lee, "Mechanically and optically reliable folding structure with a hyperelastic material for seamless foldable displays," *Applied Physics Letters*, vol. 98, no. 15, pp. 151 904–3, 2011. [Online]. Available: http://dx.doi.org/10.1063/1.3576906 14

[64] T. Maiman, "Stimulated optical radiation in ruby," *Nature*, vol. 187, no. 4736, pp. 493–494, 1960. [Online]. Available: http://dx.doi.org/10.1038/187493a0 15

[65] M. Bertolotti, *The History of the Laser*. Bristol: Institute of Physics, 2004. [Online]. Available: http://dx.doi.org/10.1201/9781420033403.fmatt 15

[66] G. Kopitkovas, T. Lippert, C. David, R. Sulcas, J. Hobley, A. Wokaun, and J. Gobrecht, "Laser micromachining of optical devices," *Proceedings of SPIE*, vol. 5662, p. 515, 2004. [Online]. Available: http://dx.doi.org/10.1117/12.596387 15

[67] J. Wei, N. Hoogen, T. Lippert, O. Nuyken, and A. Wokaun, "Novel laser ablation resists for excimer laser ablation lithography. influence of photochemical properties on ablation," *The Journal of Physical Chemistry B*, vol. 105, no. 6, pp. 1267–1275, 2001. [Online]. Available: http://dx.doi.org/10.1021/jp003325a 15, 16, 17, 21, 50

[68] B. Seyfang, R. Fardel, T. Lippert, G. Scherer, and A. Wokaun, "Micro-patterning for polymer electrolyte fuel cells: Single pulse laser ablation of aluminum films from glassy carbon," *Applied Surface Science*, vol. 255, no. 10, pp. 5471–5475, 2009. [Online]. Available: http://dx.doi.org/10.1016/j.apsusc.2008.07.189 15

[69] B. Toftmann, M. Papantonakis, R. Auyeung, W. Kim, S. O'Malley, D. Bubb, J. Horwitz, J. Schou, P. Johansen, and R. Haglund, "UV and RIR matrix assisted pulsed laser deposition of organic MEH-PPV films," *Thin Solid Films*, vol. 453-454, pp. 177–181, 2004. [Online]. Available: http://dx.doi.org/10.1016/j.tsf.2003.11.099 15, 22

[70] M. Esposito, M. Bator, M. Dobeli, T. Lippert, C. Schneider, and A. Wokaun, "Negative ions: The overlooked species in thin film growth by pulsed laser deposition," *Applied Physics Letters*, vol. 99, no. 19, pp. 191 501–3, 2011. [Online]. Available: http://dx.doi.org/10.1063/1.3660399 15

[71] M. Wälle, J. Koch, L. Flamigni, S. Heiroth, T. Lippert, W. Hartung, and D. Günther, "Detection efficiencies in nano- and femtosecond laser ablation inductively coupled plasma mass spectrometry," *Spectrochimica Acta Part B: Atomic Spectroscopy*, vol. 64, no. 1, pp. 109–112, 2009. [Online]. Available: http://dx.doi.org/10.1016/j.sab.2008.10.021 15

[72] C. Phipps, *Laser Ablation and its Applications*. New York: Springer, 2007, vol. 129. [Online]. Available: http://dx.doi.org/10.1007/978-0-387-30453-3 15

[73] C. Arnold, P. Serra, and A. Piqué, "Laser direct-write techniques for printing of complex materials," *MRS Bulletin*, vol. 32, pp. 23–31, 2007. [Online]. Available: http://dx.doi.org/10.1557/mrs2007.11 15, 18

[74] S. Anisimov and B. Luk'yanchuk, "Selected problems of laser ablation theory," *Physics-Uspekhi*, vol. 45, no. 3, pp. 293–324, 2002. [Online]. Available: http://dx.doi.org/10.1070/PU2002v045n03ABEH000966 16

[75] N. Bityurin, B. Luk'yanchuk, M. Hong, and T. Chong, "Models for laser ablation of polymers," *Chemical Reviews*, vol. 103, pp. 519–552, 2003. [Online]. Available: http://dx.doi.org/10.1021/cr010426b 16, 17, 61, 67

[76] M. Prasad, P. Conforti, and B. Garrison, "Interplay between chemical, thermal, and mechanical processes occurring upon laser excitation of poly(methyl methacrylate) and its role in ablation," *The Journal of Physical Chemistry C*, vol. 113, no. 27, pp. 11 491–11 506, 2009. [Online]. Available: http://dx.doi.org/10.1021/jp807305r 16, 61, 66, 67, 143

[77] R. Fardel, M. Nagel, F. Nüesch, T. Lippert, A. Wokaun, and B. Luk'yanchuk, "Infuence of thermal diffusion on the laser ablation of thin polymer films," *Applied Physics*

A: Materials Science & Processing, vol. 90, no. 4, pp. 661–667, 2008. [Online]. Available: http://dx.doi.org/10.1007/s00339-007-4334-9 16, 19, 45, 46, 49, 50, 55, 56, 59, 67, 88, 140

[78] T. Lippert and J. Dickinson, "Chemical and spectroscopic aspects of polymer ablation: special features and novel directions," *Chemical Reviews*, vol. 103, no. 2, pp. 453–485, 2003. [Online]. Available: http://dx.doi.org/10.1021/cr010460q 17, 20

[79] R. Fardel, P. Feurer, T. Lippert, M. Nagel, F. Nüesch, and A. Wokaun, "Laser ablation of aryltriazene photopolymer films: effect of polymer structure on ablation properties," *Applied Surface Science*, vol. 254, no. 4, pp. 1332–1337, 2007. [Online]. Available: http://dx.doi.org/10.1016/j.apsusc.2007.08.082 17, 21, 22, 37, 57, 58, 61, 89, 92, 104

[80] J. Shaw Stewart, R. Fardel, M. Nagel, P. Delaporte, L. Rapp, C. Cibert, A.-P. Alloncle, F. Nüesch, T. Lippert, and A. Wokaun, "The effect of laser pulse length upon laser-induced forward transfer using a triazene polymer as a dynamic release layer," *Journal of Optoelectronics and Advanced Materials*, vol. 12, no. 3, pp. 605–609, 2010. [Online]. Available: http://materials.web.psi.ch/Publications/Publ_MatDev_files/2010/Jamie_JOAM_2010.pdf 17, 35, 54, 55, 57, 59

[81] N. Mansour and K. Jamshidi-Ghaleh, "Modelling of pulsed ultraviolet laser-induced ablation of polymers," *Journal of Physics D: Applied Physics*, vol. 38, no. 6, p. 852, 2005. [Online]. Available: http://dx.doi.org/10.1088/0022-3727/38/6/011 17, 50, 55

[82] Y. Ben-Eliahu, Y. Haas, and S. Welner, "Laser initiation of the decomposition of energetic polymers: Shock wave formation," *The Journal of Physical Chemistry*, vol. 99, no. 16, pp. 6010–6018, 1995. [Online]. Available: http://dx.doi.org/10.1021/j100016a042 17, 19

[83] L. S. Bennett, T. Lippert, H. Furutani, H. Fukumura, and H. Masuhara, "Laser induced microexplosions of a photosensitive polymer," *Applied Physics A: Materials Science & Processing*, vol. 63, no. 4, pp. 327–332, 1996. [Online]. Available: http://dx.doi.org/10.1007/BF01567321 17, 19, 21, 55

[84] R. Fardel, M. Nagel, F. Nüesch, T. Lippert, and A. Wokaun, "Energy balance in a laser-induced forward transfer process studied by shadowgraphy," *The Journal of Physical Chemistry C*, vol. 113, no. 27, pp. 11 628–11 633, 2009. [Online]. Available: http://dx.doi.org/10.1021/jp901340s 17, 19, 56, 64, 79, 91

[85] R. S. Braudy, "Laser writing," *Proceedings of the IEEE*, vol. 57, no. 10, pp. 1771–1772, 1969. [Online]. Available: http://dx.doi.org/10.1109/PROC.1969.7398 17

[86] M. L. Levene, R. D. Scott, and B. W. Siryj, "Material transfer recording," *Applied Optics*, vol. 9, no. 10, pp. 2260–2265, 1970. [Online]. Available: http://dx.doi.org/10.1364/AO.9.002260 17

[87] J. Bohandy, B. F. Kim, and F. J. Adrian, "Metal deposition from a supported metal film using an excimer laser," *Journal of Applied Physics*, vol. 60, no. 4, pp. 1538–1539, 1986. [Online]. Available: http://dx.doi.org/10.1063/1.337287 17

[88] W. A. Tolbert, I.-Y. Sandy Lee, M. M. Doxtader, E. W. Ellis, and D. D. Dlott, "High-speed color imaging by laser ablation transfer with a dynamic release layer: fundamental mechanisms," *Journal of Imaging Science And Technology*, vol. 37, pp. 411–421, 1993. 17, 23

[89] H. Fukumura, Y. Kohji, K.-i. Nagasawa, and H. Masuhara, "Laser implantation of pyrene molecules into poly(methyl methacrylate) films," *Journal of the American Chemical Society*, vol. 116, no. 22, pp. 10 304–10 305, 1994. [Online]. Available: http://dx.doi.org/10.1021/ja00101a062 17

[90] A. Piqué, D. B. Chrisey, R. C. Y. Auyeung, J. Fitz-Gerald, H. D. Wu, R. A. McGill, S. Lakeou, P. K. Wu, V. Nguyen, and M. Duignan, "A novel laser transfer process for direct writing of electronic and sensor materials," *Applied Physics A: Materials Science & Processing*, vol. 69, no. 7, pp. S279–S284, 1999. [Online]. Available: http://dx.doi.org/10.1007/s003390051400 18, 22

[91] D. Chrisey, A. Piqué, R. McGill, J. Horwitz, B. Ringeisen, D. Bubb, and P. Wu, "Laser deposition of polymer and biomaterial films," *Chemical Reviews*, vol. 103, pp. 553–576, 2003. [Online]. Available: http://dx.doi.org/10.1002/chin.200318292 18

[92] T. Kononenko, P. Alloncle, V. Konov, and M. Sentis, "Laser transfer of diamond nanopowder induced by metal film blistering," *Applied Physics A: Materials Science & Processing*, vol. 94, no. 3, pp. 531–536, 2009. [Online]. Available: http://dx.doi.org/10.1007/s00339-008-4972-6 18

[93] M. Brown, N. Kattamis, and C. Arnold, "Time-resolved study of polyimide absorption layers for blister-actuated laser-induced forward transfer," *Journal of Applied Physics*, vol. 107, no. 8, pp. 083 103–8, 2010. [Online]. Available: http://dx.doi.org/10.1063/1.3327432 18

[94] N. Kattamis, M. Brown, and C. Arnold, "Finite element analysis of blister formation in laser-induced forward transfer," *Journal of Materials Research*, vol. 26, no. 18, pp. 2438–2449, 2011. [Online]. Available: http://dx.doi.org/10.1557/jmr.2011.215 18, 23

[95] R. J. Lawrence and W. M. Trott, "Theoretical analysis of a pulsed-laser-driven hypervelocity flyer launcher," *International Journal of Impact Engineering*, vol. 14, no. 1-4, pp. 439–449, 1993. [Online]. Available: http://dx.doi.org/10.1016/0734-743X(93)90041-5 19, 51, 52, 53, 54, 140

[96] R. Gurney, "The initial velocities of fragments from bombs, shell, grenades," Ballistic Research Laboratories, Aberdeen Proving Ground, MD, Tech. Rep. 405, 1943. 19, 51

[97] J. Kennedy, *Explosive Effects and Applications*. New York: Springer, 2002, ch. 7. "The gurney model of explosive output for driving metal", pp. 221–257. [Online]. Available: http://dx.doi.org/10.1007/978-1-4612-0589-0_7 19, 52

[98] K. Kaur, R. Fardel, T. May-Smith, M. Nagel, D. Banks, C. Grivas, T. Lippert, and R. Eason, "Shadowgraphic studies of triazene assisted laser-induced forward transfer of ceramic thin films," *Journal of Applied Physics*, vol. 105, no. 11, p. 113119, 2009. [Online]. Available: http://dx.doi.org/10.1063/1.3132822 19

[99] T. Lippert, A. Wokaun, J. Stebani, O. Nuyken, and J. Ihlemann, "Triazene polymers designed for excimer laser ablation," *Angewandte Makromolekulare Chemie*, vol. 206, pp. 97–110, 1993. [Online]. Available: http://dx.doi.org/10.1002/apmc.1993.052060110 20, 35, 72

[100] J. Stebani, O. Nuyken, T. Lippert, and A. Wokaun, "Synthesis and characterization of a novel photosensitive triazene polymer," *Makromolekulare Chemie Rapid Communications*, vol. 14, pp. 365–365, 1993. [Online]. Available: http://dx.doi.org/10.1002/marc.1993.030140607 20

[101] M. Bolle, K. Luther, J. Troe, J. Ihlemann, and H. Gerhardt, "Photochemically assisted laser ablation of doped polymethyl-methacrylate," *Applied Surface Science*, vol. 46, no. 1-4, pp. 279–283, 1990. [Online]. Available: http://dx.doi.org/10.1016/0169-4332(90)90156-T 20

[102] T. Lippert, A. Wokaun, J. Stebani, O. Nuyken, and J. Ihlemann, "Dopant-induced laser ablation of PMMA at 308 nm: Influence of the molecular weight of PMMA and of the photochemical activity of added chromophores," *Macromolecular Materials and Engineering*, vol. 213, no. 1, pp. 127–155, 1993. [Online]. Available: http://dx.doi.org/10.1002/apmc.1993.052130113 20, 35

[103] T. Lippert, J. Stebani, J. Ihlemann, O. Nuyken, and A. Wokaun, "Excimer laser ablation of novel triazene polymers: influence of structural parameters on the ablation characteristics," *The Journal of Physical Chemistry*, vol. 97, no. 47, pp. 12 296–12 301, 1993. [Online]. Available: http://dx.doi.org/10.1021/j100149a033 20, 35

[104] O. Nuyken, J. Stebani, T. Lippert, A. Wokaun, and A. Stasko, "Photolysis, thermolysis, and protolytic decomposition of a triazene polymer in solution," *Macromolecular Chemistry and Physics*, vol. 196, no. 3, pp. 751–761, 1995. [Online]. Available: http://dx.doi.org/10.1002/macp.1995.021960306 20

[105] M. Hauer, D. Funk, T. Lippert, and A. Wokaun, "Laser ablation of polymers studied by ns-interferometry and ns-shadowgraphy measurements," *Applied Surface Science*, vol. 208-209, pp. 107–112, 2003. [Online]. Available: http://dx.doi.org/10.1016/S0169-4332(02)01345-4 20, 21

[106] T. Lippert, S. Langford, A. Wokaun, S. Georgiou, and J. Dickinson, "Analysis of neutral fragments from ultraviolet laser irradiation of a photolabile triazeno polymer," *Journal of Applied Physics*, vol. 86, no. 12, pp. 7116–7122, 1999. [Online]. Available: http://dx.doi.org/10.1063/1.371800 21, 35

[107] J. Stebani, O. Nuyken, P. Sluka, and P. Finckh, "New triazene and pentazadiene polymers, prepn. and use as photo-resist – pref. positive photoresist, esp. photolabile coating on biochemical reagent used in multistage biochemical analysis," Europe Patent EP619 337-A, 1994. 21

[108] T. Lippert, J. Wei, A. Wokaun, N. Hoogen, and O. Nuyken, "Polymers designed for laser microstructuring," *Applied Surface Science*, vol. 168, no. 1-4, pp. 270–272, 2000. [Online]. Available: http://dx.doi.org/10.1016/S0169-4332(00)00621-8 21

[109] T. Lippert, C. David, M. Hauer, T. Masubuchi, H. Masuhara, K. Nomura, O. Nuyken, C. Phipps, J. Robert, T. Tada, K. Tomita, and A. Wokaun, "Novel applications for laser ablation of photopolymers," *Applied Surface Science*, vol. 186, pp. 14–23, 2002. [Online]. Available: http://dx.doi.org/10.1016/s0169-4332(01)00656-0 21

[110] D. Karnakis, T. Lippert, N. Ichinose, S. Kawanishi, and H. Fukumura, "Laser induced molecular transfer using ablation of a triazeno-polymer," *Applied Surface Science*, vol. 127-129, pp. 781–786, 1998. [Online]. Available: http://dx.doi.org/10.1016/S0169-4332(97)00742-3 21

[111] M. Hauer, D. Funk, T. Lippert, and A. Wokaun, "Time-resolved techniques as probes for the laser ablation process," *Optics and Lasers in Engineering*, vol. 43, no. 3-5, pp. 545–556, 2005. [Online]. Available: http://dx.doi.org/10.1016/j.optlaseng.2004.03.013 21

[112] M. Nagel, R. Hany, T. Lippert, M. Molberg, F. Nüesch, and D. Rentsch, "Aryltriazene photopolymers for uv-laser applications: improved synthesis and photodecomposition study," *Macromolecular Chemistry and Physics*, vol. 208, no. 3, pp. 277–286, 2007. [Online]. Available: http://dx.doi.org/10.1002/macp.200600492 21, 29

[113] T. Mito, T. Tsujita, H. Masuhara, N. Hayashi, and K. Suzuki, "Hollowing and transfer of polymethyl methacrylate film propelled by laser ablation of triazeno polymer film," *Japanese Journal of Applied Physics*, vol. 40, no. Part 2, No. 8A, pp. L805–L806, 2001. [Online]. Available: http://dx.doi.org/10.1143/JJAP.40.L805 21

[114] A. Doraiswamy, R. Narayan, T. Lippert, L. Urech, A. Wokaun, M. Nagel, B. Hopp, M. Dinescu, R. Modi, R. Auyeung, and D. Chrisey, "Excimer laser forward transfer of mammalian cells using a novel triazene absorbing layer," *Applied Surface Science*, vol. 252, pp. 4743–4747, 2006. [Online]. Available: http://dx.doi.org/10.1016/j.apsusc.2005.07.166 22, 35

[115] J. Xu, J. Liu, D. Cui, M. Gerhold, A. Wang, M. Nagel, and T. Lippert, "Laser-assisted forward transfer of multi-spectral nanocrystal quantum dot emitters," *Nanotechnology*, vol. 18, no. 2, p. 025403, 2007. [Online]. Available: http://dx.doi.org/10.1088/0957-4484/18/2/025403 22, 35

[116] D. Banks, K. Kaur, R. Gazia, R. Fardel, M. Nagel, T. Lippert, and R. Eason, "Triazene photopolymer dynamic release layer-assisted femtosecond laser-induced forward transfer with an active carrier substrate," *EPL (Europhysics Letters)*, vol. 83, no. 3, p. 38003, 2008. [Online]. Available: http://dx.doi.org/10.1209/0295-5075/83/38003 22

[117] V. Dinca, A. Palla-Papavlu, M. Dinescu, J. Shaw-Stewart, T. Lippert, F. Di Pietrantonio, D. Cannata, M. Benetti, and E. Verona, "Polymer pixel enhancement by laser-induced forward transfer for sensor applications," *Applied Physics A: Materials Science & Processing*, vol. 101, no. 3, pp. 559–565, 2010. [Online]. Available: http://dx.doi.org/10.1007/s00339-010-5898-3 22

[118] R. Fardel, M. Nagel, F. Nüesch, T. Lippert, and A. Wokaun, "Fabrication of organic light-emitting diode pixels by laser-assisted forward transfer," *Applied Physics Letters*, vol. 91, p. 061103, 2007. [Online]. Available: http://dx.doi.org/10.1063/1.2759475 22, 24, 77, 90, 108, 116, 129, 138, 157

[119] R. McGill, R. Chung, D. Chrisey, P. Dorsey, P. Matthews, A. Pique, T. Mlsna, and J. Stepnowski, "Performance optimization of surface acoustic wave chemical sensors," *Ultrasonics, Ferroelectrics and Frequency Control, IEEE Transactions on*, vol. 45, no. 5, pp. 1370–1380, 1998. [Online]. Available: http://dx.doi.org/10.1109/FREQ.1997.638535 22

[120] N. Kattamis, N. McDaniel, S. Bernhard, and C. Arnold, "Laser direct write printing of sensitive and robust light emitting organic molecules," *Applied Physics Letters*, vol. 94, no. 10, p. 3, 2009. [Online]. Available: http://dx.doi.org/10.1063/1.3098375 23

[121] ——, "Ambient laser direct-write printing of a patterned organo-metallic electroluminescent device," *Organic Electronics*, vol. 12, no. 7, pp. 1152–1158, 2011. [Online]. Available: http://dx.doi.org/10.1016/j.orgel.2011.03.032 23

[122] M. Wolk, J. Baezold, E. Bellmann, T. Hoffend Jr., S. Lamansky, Y. Li, R. Roberts, V. Savvateev, J. Staral, and W. Tolbert, "Laser thermal patterning of OLED materials," *Proceedings of SPIE – The International Society for Optical Engineering*, vol. 5519, pp. 12–23, 2004. [Online]. Available: http://dx.doi.org/10.1117/12.563872 23

[123] J. Lee and S. Lee, "Laser-induced thermal imaging of polymer light-emitting materials on poly(3,4-ethylenedioxythiophene): Silane hole-transport layer," *Advanced Materials*, vol. 16, no. 1, pp. 51–54, 2004. [Online]. Available: http://dx.doi.org/10.1002/adma.200305699 24, 80, 157

[124] S. Lamansky, J. Hoffend, H. Le, V. Jones, M. Wolk, and W. Tolbert, "Laser induced thermal imaging of vacuum-coated OLED materials," in *Organic Light-Emitting Materials and Devices IX*, vol. 5937. SPIE, 2005, pp. 593 702–15. [Online]. Available: http://dx.doi.org/10.1117/12.627063 24

[125] V. Dinca, A. Palla Papavlu, A. Matei, C. Luculescu, M. Dinescu, T. Lippert, F. Di Pietrantonio, D. Cannata, M. Benetti, and E. Verona, "A comparative study of DRL-LIFT and LIFT on integrated polyisobutylene polymer matrices," *Applied Physics A: Materials Science & Processing*, 2010. [Online]. Available: http://dx.doi.org/10.1007/s00339-010-5826-6 28

[126] F. Nüesch, L. Rothberg, E. Forsythe, Q. Toan Le, and Y. Gao, "A photoelectron spectroscopy study on the indium tin oxide treatment by acids and bases," *Applied Physics Letters*, vol. 74, no. 6, pp. 880–882, 1999. [Online]. Available: http://dx.doi.org/10.1063/1.123397 29, 32, 125

[127] F. Nuesch, Y. Li, and L. Rothberg, "Patterned surface dipole layers for high-contrast electroluminescent displays," *Applied Physics Letters*, vol. 75, no. 12, pp. 1799–1801, 1999. [Online]. Available: http://dx.doi.org/10.1063/1.124824 29, 32, 125

[128] X. Deng, W. Lau, K. Wong, K. Low, H. Chow, and Y. Cao, "High efficiency low operating voltage polymer light-emitting diodes with aluminum cathode," *Applied Physics Letters*, vol. 84, no. 18, pp. 3522–3524, 2004. [Online]. Available: http://dx.doi.org/10.1063/1.1739510 30, 108, 109

[129] L. Flamigni, A. Barbieri, C. Sabatini, B. Ventura, and F. Barigelletti, *Photochemistry and Photophysics of Coordination Compounds: Iridium Photochemistry and Photophysics of Coordination Compounds II*. Berlin / Heidelberg: Springer, 2007, vol. 281, pp. 143–203. [Online]. Available: http://dx.doi.org/10.1007/128_2007_131 31

[130] J. Park, O. Park, J.-W. Yu, J. Kim, and Y. Kim, "Effect of polymer-insulating nanolayers on electron injection in polymer light-emitting diodes," *Applied Physics Letters*, vol. 84, no. 10, pp. 1783–1785, 2004. [Online]. Available: http://dx.doi.org/10.1063/1.1667014 32, 108, 109

[131] T.-F. Guo, F.-S. Yang, Z.-J. Tsai, T.-C. Wen, S.-N. Hsieh, and Y.-S. Fu, "High-performance polymer light-emitting diodes utilizing modified Al cathode," *Applied Physics Letters*, vol. 87, no. 1, pp. 013 504–3, 2005. [Online]. Available: http://dx.doi.org/10.1063/1.1984101 32, 108, 109

[132] T. Hasegawa, S. Miura, T. Moriyama, T. Kimura, I. Takaya, Y. Osato, and H. Mizutani, "11.3: Novel electron-injection layers for top-emission OLEDs," *SID Symposium Digest of Technical Papers*, vol. 35, no. 1, pp. 154–157, 2004. [Online]. Available: http://dx.doi.org/10.1889/1.1821373 32

[133] J. Huang, Z. Xu, and Y. Yang, "Low-work-function surface formed by solution-processed and thermally deposited nanoscale layers of cesium carbonate," *Advanced Functional Materials*, vol. 17, no. 12, pp. 1966–1973, 2007. [Online]. Available: http://dx.doi.org/10.1002/adfm.200700051 32, 127

[134] Q. Liu, L. Duan, Y. Li, J. Qiao, Z. Yu, D. Zhang, L. Wang, G. Dong, and Y. Qiu, "Study on the electron injection mechanism of thermally decomposable Cs_2CO_3," *Japanese Journal of Applied Physics*, vol. 48, no. 10, p. 102302, 2009. [Online]. Available: http://dx.doi.org/10.1143/JJAP.48.102302 32, 127

[135] Y. Cao, G. Yu, C. Zhang, R. Menon, and A. Heeger, "Polymer light-emitting diodes with polyethylene dioxythiophene-polystyrene sulfonate as the transparent anode," *Synthetic Metals*, vol. 87, no. 2, pp. 171–174, 1997. [Online]. Available: http://dx.doi.org/10.1016/S0379-6779(97)03823-X 33, 108, 112

[136] S. Carter, M. Angelopoulos, S. Karg, P. Brock, and J. Scott, "Polymeric anodes for improved polymer light-emitting diode performance," *Applied Physics Letters*, vol. 70, no. 16, pp. 2067–2069, 1997. [Online]. Available: http://dx.doi.org/10.1063/1.118953 33, 108, 112

[137] Heraeus. (2012) Clevios P VP AI 4083. [Online]. Available: http://clevios.com/en/_technik/productdetail_1034017.aspx?psMarketId=1280&psApplicationId= 33

[138] W. Li, R. Jones, S. Allen, J. Heikenfeld, and A. Steckl, "Maximizing Alq_3 OLED internal and external efficiencies: Charge balanced device structure and color conversion outcoupling lenses," *J. Display Technol.*, vol. 2, no. 2, pp. 143–152, 2006. [Online]. Available: http://dx.doi.org/10.1109/JDT.2006.874507 33, 128, 129

[139] C. Jiang, W. Yang, J. Peng, S. Xiao, and Y. Cao, "High-efficiency, saturated red-phosphorescent polymer light-emitting diodes based on conjugated and non-conjugated polymers doped with an Ir complex," *Advanced Materials*, vol. 16, no. 6, pp. 537–541, 2004. [Online]. Available: http://dx.doi.org/10.1002/adma.200306331 33, 126, 127

[140] R. Swanepoel, "Determining refractive index and thickness of thin films from wavelength measurements only," *Journal of the Optical Society of America A – Optics Image Science and Vision*, vol. 2, no. 8, pp. 1339–1343, 1985. [Online]. Available: http://dx.doi.org/10.1364/JOSAA.2.001339 34

[141] T. Lippert, J. Stebani, O. Nuyken, A. Stasko, and A. Wokaun, "Photolysis of 1-aryl-3,3-dialkytriazenes," *Journal of Photochemistry and Photobiology A: Chemistry*, vol. 78, no. 2, pp. 139–148, 1994. [Online]. Available: http://dx.doi.org/10.1016/1010-6030(93)03718-V 35

[142] T. Lippert, J. Dickinson, M. Hauer, G. Kopitkovas, S. Langford, H. Masuhara, O. Nuyken, J. Robert, H. Salmio, T. Tada, K. Tomita, and A. Wokaun, "Polymers designed for laser ablation-influence of photochemical properties," *Applied Surface Science*, vol. 197-198, no. 0, pp. 746–756, 2002. [Online]. Available: http://dx.doi.org/10.1016/s0169-4332(02)00404-x 35

[143] A. Palla-Papavlu, I. Paraico, J. Shaw-Stewart, V. Dinca, T. Savopol, E. Kovacs, T. Lippert, A. Wokaun, and M. Dinescu, "Liposome micropatterning based on laser-induced forward transfer," *Applied Physics A: Materials Science & Processing*, vol. 102, no. 3, pp. 651–659, 2011. [Online]. Available: http://dx.doi.org/10.1007/s00339-010-6114-1 35

[144] T. Lippert, T. Nakamura, H. Niino, and A. Yabe, "Irradiation wavelength selective surface modification of a triazeno polymer," *Macromolecules*, vol. 29, no. 19, pp. 6301–6309, 1996. [Online]. Available: http://dx.doi.org/10.1021/ma9517198 35, 106

[145] M. Hauer, T. Dickinson, S. Langford, T. Lippert, and A. Wokaun, "Influence of the irradiation wavelength on the ablation process of designed polymers," *Applied Surface Science*, vol. 197, pp. 791–795, 2002. [Online]. Available: http://dx.doi.org/10.1016/s0169-4332(02)00416-6 35, 72

[146] L. Rapp, A. Diallo, S. Nénon, A. Alloncle, C. Videlot-Ackermann, F. Fages, M. Nagel, T. Lippert, and P. Delaporte, "Laser printing of a semiconducting oligomer as active layer in organic thin film transistors: Impact of a protecting triazene layer," *Thin Solid Films*, vol. 520, no. 7, pp. 3043–3047, 2012. [Online]. Available: http://dx.doi.org/10.1016/j.tsf.2011.10.159 35

[147] M. Nagel, R. Fardel, P. Feurer, M. Häberli, F. Nüesch, T. Lippert, and A. Wokaun, "Aryltriazene photopolymer thin films as sacrificial release layers for laser-assisted forward transfer systems: study of photoablative decomposition and transfer behavior," *Applied Physics A: Materials Science & Processing*, vol. 92, no. 4, pp. 781–789, 2008. [Online]. Available: http://dx.doi.org/10.1007/s00339-008-4565-4 37, 52, 54, 55, 57, 88, 92, 105, 159

[148] F. Lang and P. Leiderer, "Liquid-vapour phase transitions at interfaces: sub-nanosecond investigations by monitoring the ejection of thin liquid films," *New Journal of Physics*, vol. 8, no. 1, p. 14, 2006. [Online]. Available: http://dx.doi.org/10.1088/1367-2630/8/1/014 39, 71, 73

[149] P. Frank, J. Graf, F. Lang, J. Boneberg, and P. Leiderer, "Laser-induced film ejection at interfaces: Comparison of the dynamics of liquid and solid films," *Applied Physics A: Materials Science & Processing*, vol. 101, no. 1, pp. 7–11, 2010. [Online]. Available: http://dx.doi.org/10.1007/s00339-010-5770-5 39, 71, 75

[150] J. de Mello, H. Wittmann, and R. Friend, "An improved experimental determination of external photoluminescence quantum efficiency," *Advanced Materials*, vol. 9, no. 3, pp. 230–232, 1997. [Online]. Available: http://dx.doi.org/10.1002/adma.19970090308 41

[151] J. Shaw Stewart, T. Lippert, M. Nagel, F. Nüesch, and A. Wokaun, "A simple model for flyer velocity from laser-induced forward transfer with a dynamic release layer," *Applied Surface Science*, in press. [Online]. Available: http://dx.doi.org/10.1016/j.apsusc.2011.08.111 51

[152] R. Fardel, M. Nagel, F. Nüesch, T. Lippert, and A. Wokaun, "Laser-induced forward transfer of organic LED building blocks studied by time-resolved shadowgraphy," *The Journal of Physical Chemistry C*, vol. 114, no. 12, pp. 5617–5636, 2010. [Online]. Available: http://dx.doi.org/10.1021/jp907387q 52, 55, 69, 70, 77, 79, 85, 87, 89, 90, 91, 106, 140

[153] J. Shaw-Stewart, T. Lippert, M. Nagel, F. Nüesch, and A. Wokaun, "Laser-induced forward transfer of polymer light-emitting diode pixels with increased charge injection," *ACS Applied Materials & Interfaces*, vol. 3, no. 2, pp. 309–316, 2011. [Online]. Available: http://dx.doi.org/10.1021/am100943f 52, 77, 89, 90, 92, 107, 129, 138

[154] J. Kennedy, "Gurney energy of explosives: Estimation of the velocity and impulse imparted to driven metal," Sandia Laboratories, Albuquerque, NM, Tech. Rep. SC-RR-70-790, 1970. 52

[155] T. Lippert, M. Hauer, C. Phipps, and A. Wokaun, "Fundamentals and applications of polymers designed for laser ablation," *Applied Physics A: Materials Science & Processing*, vol. 77, no. 2, pp. 259–264, 2003. [Online]. Available: http://dx.doi.org/10.1007/s00339-003-2111-y 55

[156] S. Sax, N. Rugen-Penkalla, A. Neuhold, S. Schuh, E. Zojer, E. List, and K. Müllen, "Efficient blue-light-emitting polymer heterostructure devices: The fabrication of multilayer structures from orthogonal solvents," *Advanced Materials*, vol. 22, no. 18, pp. 2087–2091, 2010. [Online]. Available: http://dx.doi.org/10.1002/adma.200903076 56

[157] J. E. Andrew, P. E. Dyer, D. Forster, and P. H. Key, "Direct etching of polymeric materials using a XeCl laser," *Applied Physics Letters*, vol. 43, no. 8, pp. 717–719, 1983. [Online]. Available: http://dx.doi.org/10.1063/1.94488 61

[158] H. Fujiwara, T. Hayashi, H. Fukumura, and H. Masuhara, "Each dopant can absorb more than ten photons: Transient absorbance measurement at excitation laser wavelength in polymer ablation," *Applied Physics Letters*, vol. 64, no. 18, pp. 2451–2453, 1994. [Online]. Available: http://dx.doi.org/10.1063/1.111596 61

[159] R. Fardel, M. Nagel, F. Nüesch, T. Lippert, and A. Wokaun, "Shadowgraphy investigation of laser-induced forward transfer: Front side and back side ablation of the triazene polymer sacrificial layer," *Applied Surface Science*, vol. 255, no. 10, pp. 5430–5434, 2009. [Online]. Available: http://dx.doi.org/10.1016/j.apsusc.2008.07.187 63, 105

[160] Heraeus. (2011) Suprasil 2 data sheet. [Online]. Available: http://optics.heraeus-quarzglas.com/media/webmedia_local/downloads/FusedsilicaandQuartzGlassforOpticsDataandProperties.pdf 67

[161] P. Frank, J. Shaw-Stewart, T. Lippert, J. Boneberg, and P. Leiderer, "Laser-induced ablation dynamics and flight of thin polymer films," *Applied Physics A: Materials Science & Processing*, vol. 104, no. 2, pp. 579–582, 2011. [Online]. Available: http://dx.doi.org/10.1007/s00339-011-6500-3 71

[162] D. H. Auston, J. A. Golovchenko, A. L. Simons, C. M. Surko, and T. N. C. Venkatesan, "Dynamics of Q-switched laser annealing," *Applied Physics Letters*, vol. 34, no. 11, pp. 777–779, 1979. [Online]. Available: http://dx.doi.org/10.1063/1.90670 71

[163] J. Shaw Stewart, B. Chu, T. Lippert, Y. Maniglio, M. Nagel, F. Nüesch, and A. Wokaun, "Improved laser-induced forward transfer of organic semiconductor thin films by reducing the environmental pressure and controlling the substrate-substrate gap width," *Applied Physics A: Materials Science & Processing*, vol. 105, no. 3, pp. 713–722, 2011. [Online]. Available: http://dx.doi.org/10.1007/s00339-011-6583-x 80, 105

[164] D. Banks, K. Kaur, and R. Eason, "Influence of optical standing waves on the femtosecond laser-induced forward transfer of transparent thin films," *Applied Optics*, vol. 48, no. 11, pp. 2058–2066, 2009. [Online]. Available: http://dx.doi.org/10.1364/AO.48.002058 81

[165] D. Lide (ed), Ed., *CRC Handbook of Chemistry and Physics*. CRC Press, 2012. [Online]. Available: http://www.hbcpnetbase.com/ 93, 121, 127

[166] T. Lee and M. Lin, "Sublimation point depression of tris(8-hydroxyquinoline)aluminum(III) (Alq_3) by crystal engineering," *Crystal Growth & Design*, vol. 7, no. 9, pp. 1803–1810, 2007. [Online]. Available: http://dx.doi.org/10.1021/cg070226e 100, 101, 132

[167] J. Shaw Stewart, T. Lippert, M. Nagel, F. Nüesch, and A. Wokaun, "Sequential printing by laser-induced forward transfer to fabricate a functional organic light-emitting diode," *ACS Applied Materials & Interfaces*, submitted for publication. 101, 133

[168] R. Fardel, M. Nagel, F. Nüesch, T. Lippert, and A. Wokaun, "Laser forward transfer using a sacrificial layer: Influence of the material properties," *Applied Surface Science*, vol. 254, pp. 1322–1326, 2007. [Online]. Available: http://dx.doi.org/10.1016/j.apsusc.2007.08.091 105

[169] C.-C. Hsiao, A.-E. Hsiao, and S.-A. Chen, "Design of hole blocking layer with electron transport channels for high performance polymer light-emitting diodes," *Advanced Materials*, vol. 20, no. 10, pp. 1982–1988, 2008. [Online]. Available: http://dx.doi.org/10.1002/adma.200702150 109, 110

[170] Y.-H. Niu, A. Jen, and C. Shu, "High-efficiency polymer light-emitting diodes using neutral surfactant modified aluminum cathode," *The Journal of Physical Chemistry B*, vol. 110, no. 12, pp. 6010–6014, 2006. [Online]. Available: http://dx.doi.org/10.1021/jp053426e 110

[171] Y. Cao, G. Yu, and A. J. Heeger, "Efficient, low operating voltage polymer light-emitting diodes with aluminum as the cathode material," *Synthetic Metals*, vol. 102, no. 1-3, pp. 881–884, 1999. [Online]. Available: http://dx.doi.org/10.1016/S0379-6779(98)00376-2 110

[172] I. H. Campbell, S. Rubin, T. A. Zawodzinski, J. D. Kress, R. L. Martin, D. L. Smith, N. N. Barashkov, and J. P. Ferraris, "Controlling schottky energy barriers in organic electronic devices using self-assembled monolayers," *Physical Review B: Condensed Matter and Materials Physics*, vol. 54, no. 20, p. R14321, 1996. [Online]. Available: http://dx.doi.org/10.1103/PhysRevB.54.R14321 110, 116

[173] F. Nüesch, F. Rotzinger, L. Si-Ahmed, and L. Zuppiroli, "Chemical potential shifts at organic device electrodes induced by grafted monolayers," *Chemical*

Physics Letters, vol. 288, no. 5-6, pp. 861–867, 1998. [Online]. Available: http://dx.doi.org/10.1016/S0009-2614(98)00350-9 110

[174] Y. Hirose, A. Kahn, V. Aristov, P. Soukiassian, V. Bulovic, and S. R. Forrest, "Chemistry and electronic properties of metal-organic semiconductor interfaces: Al, Ti, In, Sn, Ag, and Au on PTCDA," *Physical Review B*, vol. 54, no. 19, p. 13748, 1996. [Online]. Available: http://dx.doi.org/10.1103/PhysRevB.54.13748 110, 120

[175] K. Demirkan, A. Mathew, C. Weiland, M. Reid, and R. Opila, "Reactivity and morphology of vapor-deposited Al/polymer interfaces for organic semiconductor devices," *Journal of Applied Physics*, vol. 103, no. 3, pp. 034 505–7, 2008. [Online]. Available: http://dx.doi.org/10.1063/1.2837883 110, 113, 120

[176] M. Ruderer, E. Metwalli, W. Wang, G. Kaune, S. Roth, and P. Müller-Buschbaum, "Thin films of photoactive polymer blends," *ChemPhysChem*, vol. 10, no. 4, pp. 664–671, 2009. [Online]. Available: http://dx.doi.org/10.1002/cphc.200800773 110

[177] F. Castro, J. Heier, F. Nüesch, and R. Hany, "Origin of the kink in current-density versus voltage curves and efficiency enhancement of polymer-C_{60} heterojunction solar cells," *IEEE Journal of Selected Topics in Quantum Electronics*, vol. 16, no. 6, pp. 1690–1699, 2010. [Online]. Available: http://dx.doi.org/10.1109/JSTQE.2010.2040807 110, 120

[178] D. Gallardo, C. Bertoni, S. Dunn, N. Gaponik, and A. Eychmüller, "Cathodic and anodic material diffusion in polymer/semiconductor-nanocrystal composite devices," *Advanced Materials*, vol. 19, no. 20, pp. 3364–3367, 2007. [Online]. Available: http://dx.doi.org/10.1002/adma.200700394 110, 112, 113, 120

[179] N. F. Mott, "The theory of the formation of protective oxide films on metals. III," *Transactions of the Faraday Society*, vol. 43, pp. 429–434, 1947. [Online]. Available: http://dx.doi.org/10.1039/TF9474300429 110, 113, 114, 120

[180] A. Mallikarjunan, S. Murarka, and T. Lu, "Metal drift behavior in low dielectric constant organosiloxane polymer," *Applied Physics Letters*, vol. 79, no. 12, pp. 1855–1857, 2001. [Online]. Available: http://dx.doi.org/10.1063/1.1404408 110, 113, 120

[181] M. Schaer, F. Nüesch, D. Berner, W. Leo, and L. Zuppiroli, "Water vapor and oxygen degradation mechanisms in organic light emitting diodes," *Advanced Functional Materials*, vol. 11, no. 2, pp. 116–121, 2001. [Online]. Available: http://dx.doi.org/10.1002/1616-3028(200104)11:2<116::AID-ADFM116>3.0.CO;2-B 112, 131

[182] H. Kupfer and G. Wolf, "Plasma and ion beam assisted metallization of polymers and their application," *Nuclear Instruments and Methods in Physics Research Section B: Beam Interactions with Materials and Atoms*, vol. 166-167, pp. 722–731, 2000. [Online]. Available: http://dx.doi.org/10.1016/S0168-583X(99)01192-1 113

[183] M. Ariu, D. Lidzey, M. Sims, A. Cadby, P. Lane, and D. Bradley, "The effect of morphology on the temperature-dependent photoluminescence quantum efficiency of the conjugated polymer poly(9, 9-dioctylfluorene)," *Journal of Physics: Condensed Matter*, vol. 14, no. 42, pp. 9975–9986, 2002. [Online]. Available: http://dx.doi.org/10.1088/0953-8984/14/42/310 114

[184] J. Bolinger, M. Traub, T. Adachi, and P. Barbara, "Ultralong-range polaron-induced quenching of excitons in isolated conjugated polymers," *Science*, vol. 331, no. 6017, pp. 565–567, 2011. [Online]. Available: http://dx.doi.org/10.1126/science.1199140 114

[185] S. Gardonio, L. Gregoratti, P. Melpignano, L. Aballe, V. Biondo, R. Zamboni, M. Murgia, S. Caria, and M. Kiskinova, "Degradation of organic light-emitting diodes under different environment at high drive conditions," *Organic Electronics*, vol. 8, no. 1, pp. 37–43, 2007. [Online]. Available: http://dx.doi.org/10.1016/j.orgel.2006.10.005 114

[186] A. Sevim and S. Mutlu, "Post-fabrication electric field and thermal treatment of polymer light emitting diodes and their photovoltaic properties," *Organic Electronics*, vol. 10, no. 1, pp. 18–26, 2009. [Online]. Available: http://dx.doi.org/10.1016/j.orgel.2008.09.003 114

[187] T.-Q. Nguyen, I. Martini, J. Liu, and B. Schwartz, "Controlling interchain interactions in conjugated polymers: The effects of chain morphology on exciton-exciton annihilation and aggregation in MEH-PPV films," *The Journal of Physical Chemistry B*, vol. 104, no. 2, pp. 237–255, 2000. [Online]. Available: http://dx.doi.org/10.1021/jp993190c 115

[188] J. Liu, T.-F. Guo, and Y. Yang, "Effects of thermal annealing on the performance of polymer light emitting diodes," *Journal of Applied Physics*, vol. 91, no. 3, pp. 1595–1600, 2002. [Online]. Available: http://dx.doi.org/10.1063/1.1427435 116

[189] H. Wu, F. Huang, J. Peng, and Y. Cao, "Efficient electron injection from bilayer cathode with aluminum as cathode," *Synthetic Metals*, vol. 153, no. 1-3, pp. 197–200, 2005. [Online]. Available: http://dx.doi.org/DOI:10.1016/j.synthmet.2005.07.285 117, 126, 127, 134, 160

[190] W. Zhao, T. Cao, and J. White, "On the origin of green emission in polyfluorene polymers: The roles of thermal oxidation degradation and crosslinking," *Advanced*

Functional Materials, vol. 14, no. 8, pp. 783–790, 2004. [Online]. Available: http://dx.doi.org/10.1002/adfm.200305173 121, 127

[191] T. Ferenczi, M. Sims, and D. Bradley, "On the nature of the fluorenone-based emission in oxidized poly(dialkyl-fluorene)s," *Journal of Physics: Condensed Matter*, vol. 20, no. 4, p. 045220, 2008. [Online]. Available: http://dx.doi.org/10.1088/0953-8984/20/04/045220 121, 123, 127

[192] J. Kang, J. Jo, Y. Jo, S. Lee, P. Keivanidis, G. Wegner, and D. Yoon, "Time-resolved photoluminescence study of low-energy emission mechanisms in oligofluorene and polyfluorene films," *Polymer*, vol. 49, no. 26, pp. 5700–5704, 2008. [Online]. Available: http://dx.doi.org/10.1016/j.polymer.2008.10.006 121

[193] J. Shaw Stewart, T. Lippert, M. Nagel, F. Nüesch, and A. Wokaun, "Red-green-blue polymer light-emitting diode pixels printed by optimized laser-induced forward transfer," *Applied Physics Letters*, vol. 100, no. 20, pp. 203 303–4, 2012. [Online]. Available: http://dx.doi.org/10.1063/1.4717463 122

[194] S. Choulis, V.-E. Choong, M. Mathai, and F. So, "The effect of interfacial layer on the performance of organic light-emitting diodes," *Applied Physics Letters*, vol. 87, no. 11, pp. 113 503–3, 2005. [Online]. Available: http://dx.doi.org/10.1063/1.2042635 126

[195] L. Berthelot, J. Tardy, M. Garrigues, P. Cremillieu, J. Joseph, and B. Masenelli, "ITO/PVK/Alq/metal LEDs: influence of PVK doping with DCM and of passivation with sputtered Si_3N_4," *Optical Materials*, vol. 12, no. 2-3, pp. 261–266, 1999. [Online]. Available: http://dx.doi.org/10.1016/s0925-3467(99)00052-x 128, 129

[196] S. Xiao, M. Nguyen, X. Gong, Y. Cao, H. Wu, D. Moses, and A. Heeger, "Stabilization of semiconducting polymers with silsesquioxane," *Advanced Functional Materials*, vol. 13, no. 1, pp. 25–29, 2003. [Online]. Available: http://dx.doi.org/10.1002/adfm.200390000 133

[197] H. Park, K. Schriver, and R. Haglund, "Resonant infrared laser deposition of polymer-nanocomposite materials for optoelectronic applications," *Applied Physics A: Materials Science & Processing*, vol. 105, no. 3, pp. 583–592, 2011. [Online]. Available: http://dx.doi.org/10.1007/s00339-011-6604-9 133

[198] L. Zhigilei, E. Leveugle, B. Garrison, Y. Yingling, and M. Zeifman, "Computer simulations of laser ablation of molecular substrates," *Chemical Reviews*, vol. 103, no. 2, pp. 321–348, 2003. [Online]. Available: http://dx.doi.org/10.1021/cr010459r 143

[199] Keithley. (2012) Keithley 2400 Sourcemeter Downloads. [Online]. Available: http://www.keithley.com/products/dcac/dmm/broadpurpose/?path=2400/Downloads#4 149

[200] National Instruments. (2012) Keithley 2400 Available Drivers. [Online]. Available: http://sine.ni.com/apps/utf8/niid_web_display.model_page?p_model_id=1583 149

[201] J. Treinen, "Automated luminance-meter control software for electronic-display measurements," National Institute of Standards and Technology, Tech. Rep. NISTIR 6638, 2005. [Online]. Available: http://www.nist.gov/manuscript-publication-search.cfm?pub_id=32060 150

[202] N. Greenham, R. Friend, and D. Bradley, "Angular dependence of the emission from a conjugated polymer light-emitting diode: Implications for efficiency calculations," *Advanced Materials*, vol. 6, no. 6, pp. 491–494, 1994. [Online]. Available: http://dx.doi.org/10.1002/adma.19940060612 154

[203] J.-S. Kim, P. Ho, N. Greenham, and R. Friend, "Electroluminescence emission pattern of organic light-emitting diodes: Implications for device efficiency calculations," *Journal of Applied Physics*, vol. 88, no. 2, pp. 1073–1081, 2000. [Online]. Available: http://dx.doi.org/10.1063/1.373779 154, 155

[204] H. Li, C. Zhang, D. Li, and Y. Duan, "Simulation of transform for external quantum efficiency and power efficiency of electroluminescent devices," *Journal of Luminescence*, vol. 122-123, pp. 626–628, 2007. [Online]. Available: http://dx.doi.org/10.1016/j.jlumin.2006.01.243 155

Curriculum Vitae

James Shaw Stewart

British Citizen, Born 4th April 1986, Stirling

Education

2008 – 2012 PhD thesis at ETH Zürich, Empa and Paul Scherrer Institut
▷ *Optimising the fabrication of organic light-emitting diodes by laser-induced forward transfer*
Experimental work carried out at Empa, Laboratory for Functional Polymers and PSI, Materials Group in the General Energy Research Department

2007 – 2008 Master of Science in Natural Science (Geological Sciences)
Pembroke College, Cambridge, UK
▷ *Investigating the interaction between ferromagnetic and ferroelastic domain walls below the Verwey transition in magnetite*

2004 – 2007 Bachelor of Arts in Natural Science (Geological Sciences)
Pembroke College, Cambridge, UK
▷ *A geological map of the area around Lac de Bious-Artigues, Val d'Ossau, Pyrénées-Atlantiques, France*

1997 – 2004 5 A-levels (all As) and 11 GCSEs (all As and A*s)
Merchiston Castle School, Edinburgh, UK

Publications

Publications as first author

- J. Shaw Stewart, R. Fardel, M. Nagel, P. Delaporte, L. Rapp, C. Cibert, A.-P. Alloncle, F. Nüesch, T. Lippert, A. Wokaun (2010), *The effect of laser pulse length upon laser-*

induced forward transfer using a triazene polymer as a dynamic release layer, J. Optoelectro. Adv. Mater., **12**, 605.

- J. Shaw Stewart, T. Lippert, M. Nagel, F. Nüesch, A. Wokaun (2010), *Laser-Induced Forward Transfer Using Triazene Polymer Dynamic Releaser Layer*, AIP Conf. Proc., **1278**, 789.

- J. Shaw-Stewart, T. Lippert, M. Nagel, F. Nüesch, A. Wokaun (2011), *Laser-Induced Forward Transfer of Polymer Light-Emitting Diode Pixels with Increased Charge Injection*, ACS Appl. Mater. Interfaces, **3**, 309.

- J. Shaw Stewart, B. Chu, T. Lippert, Y. Maniglio, M. Nagel, F. Nüesch, A. Wokaun (2011), *Improved laser-induced forward transfer of organic semiconductor thin films by reducing the environmental pressure and controlling the substrate-substrate gap width*, Appl. Phys. A: Mater. Sci. Process., **105**, 713

- J. Shaw Stewart, T. Lippert, M. Nagel, F. Nüesch, A. Wokaun (2012), *A simple model for flyer velocity from laser-induced forward transfer with a dynamic release layer*, Appl. Surf. Sci., **in press**, doi: 10.1016/j.apsusc.2011.08.111.

- J. Shaw-Stewart, T. Lippert, M. Nagel, F. Nüesch, A. Wokaun (2012), *Red-green-blue polymer light-emitting diode pixels printed by optimized laser-induced forward transfer*, Appl. Phys. Lett., **100**, 203303.

- J. Shaw-Stewart, T. Lippert, M. Nagel, F. Nüesch, A. Wokaun (2012), *Sequential Printing by Laser-Induced Forward Transfer to Fabricate a Polymer Light-Emitting Diode*, ACS Appl. Mater. Interfaces, **submitted**.

Publications as co-author

- V. Dinca, A. Palla-Papavlu, M. Dinescu, J. Shaw-Stewart, T. Lippert, F. Di Pietrantonio, D. Cannata, M. Benetti, E. Verona (2010), *Polymer pixel enhancement by laser-induced forward transfer for sensor applications*, Appl. Phys. A: Mater. Sci. Process., **101**, 559. 605.

- V. Dinca, R. Fardel, J. Shaw Stewart, F. Di Pietrantonio, D. Cannata, M. Benetti, E. Verona, A. Palla Papavlu, M. Dinescu, T. Lippert (2010), *Laser-Induced Forward Transfer: An Approach to Single-Step Polymer Microsensor Fabrication*, Sens. Lett., **8**, 436.

- A. Palla-Papavlu, V. Dinca, C. Luculescu, J. Shaw-Stewart, M. Nagel, T. Lippert, M. Dinescu (2010), *Laser induced forward transfer of soft materials*, J. Opt., **12**, 124014.

- A. Palla-Papavlu, V. Dinca, I. Paraico, A. Moldovan, J. Shaw-Stewart, C.W. Schneider, E. Kovacs, T. Lippert, M. Dinescu (2010), *Microfabrication of polystyrene microbead arrays by laser induced forward transfer*, J. Appl. Phys., **108**, 033111-6.
- A. Palla-Papavlu, I. Paraico, J. Shaw-Stewart, V. Dinca, T. Savopol, E. Kovacs, T. Lippert, A. Wokaun, M. Dinescu (2011), *Liposome micropatterning based on laser-induced forward transfer*, Appl. Phys. A: Mater. Sci. Process., **102**, 651.
- P. Frank, J. Shaw-Stewart, T. Lippert, J. Boneberg, P. Leiderer (2011), *Laser-induced ablation dynamics and flight of thin polymer films*, Appl. Phys. A: Mater. Sci. Process., **104**, 579.
- T. Mattle, J. Shaw-Stewart, C.W. Schneider, T. Lippert, A. Wokaun (2012), *Laser induced forward transfer aluminum layers: Process investigation by time resolved imaging*, Appl. Surf. Sci., **in press**, doi: 10.1016/j.apsusc.2011.08.113.

Conferences

- Empa PhD Students Symposium 2010, Empa Dübendorf, 7 October 2010, Organising Committee

Oral presentations

- J. Shaw Stewart, M. Zäch, T. Lippert, M. Nagel, F. Nüesch, A. Wokaun, *Transfer of a single light-emitting polymer layer using laser induced forward transfer*, COLA 2009, Singapore, 22-27 November 2009
- J. Shaw Stewart, T. Lippert, M. Nagel, F. Nüesch, A. Wokaun, *Laser-induced forward transfer (LIFT): a universal OLED pixel deposition technique?*, Plastic Electronics 2010, Dresden, October 19-21 2010
- J. Shaw Stewart, B. Chu, T. Lippert, Y. Maniglio, M. Nagel, F. Nüesch, A. Wokaun, *A tri-colour OLED pixel by laser-induced forward transfer*, EMRS 2011, Nice, May 9-13 2011
- J. Shaw Stewart, T. Lippert, M. Nagel, F. Nüesch, A. Wokaun, *A tri-colour PLED pixel by laser-induced forward transfer*, COLA 2011, Cancún, 13-19 November 2011

Poster presentations

- J. Shaw Stewart, R. Fardel, M. Nagel, P. Delaporte, L. Rapp, C. Cibert, A.-P. Alloncle, F. Nüesch, T. Lippert, A. Wokaun (2010), *The effect of different laser pulse lengths upon laser-induced forward transfer using a triazene polymer as a dynamic release layer*, EMRS 2009, Strasbourg, 8-12 June 2009

- J. Shaw Stewart, T. Lippert, M. Nagel, F. Nüesch, A. Wokaun, *The fabrication of polymer light-emitting diodes using laser-induced forward transfer*, Swiss-ePrint, Basel, 1-2 December 2011
- J. Shaw Stewart, T. Mattle, T. Lippert, M. Nagel, F. Nüesch, A. Wokaun, *The fabrication of organic light-emitting diodes using laser-induced forward transfer* EMRS 2012, Strasbourg, 14-18 May 2012

Acknowledgements

Many thanks to all the people who made this work possible:

Prof. Dr. Alexander Wokaun for being my Doktorvater, and supervising the thesis;

PD Dr. Thomas Lippert, Prof. Dr. Frank Nüesch, and Dr. Matthias Nagel, for their supervision, help, and advice;

Prof. Dr. Christophe Copéret for being my co-referee, and Prof. Dr. Detlef Günther, the head of D-CHAB;

Dr. Romain Fardel for his introduction to all aspects of the project, and Thomas Mattle for all his practical help and useful discussions, at PSI;

Dr. Bryan Chu for all his help and support in general at Empa, Martin Zäch and Ylenia Maniglio for the synthesis and characterisation of the triazene polymer, Dr. Thomas Geiger for the GPC measurements, Heinz Altorfer for all his help in designing sample holders and the like;

Dr. Pascal Frank, Dr. Julien Boneberg, and Prof. Dr. Leiderer for the reflectometry studies at Konstanz;

Dr. Valentina Dinca, Dr. Alexandra Palla-Papavlu, and Prof. Dr. Marie Dinescu for the collaboration with National Institute of Lasers in Bucharest, Romania;

Dr. Willam Kylberg, Dr. Fernando de Castro, Manuel Egger, Jean-Nicholas Tisserant, Dr. Gaëtan Wicht, Dr. Jakob Heier, and Dr. Roland Hany, for their practical help with organic semiconductors, and all the people of the Laboratory for Functional Polymers in general,

Dr. Martin Esposito, Dr. Bernhard Seyfang, Dr. Sebastian Heiroth, Dr. Ivan Marozau, Dr. Franziska Simmen, Matthias Bator, Dieter Stender, Yi Hu, Dr. Giedrius Kopitkovas, Jikun Chen, and PD Dr. Christof Schneider for all their help in the laser lab and elsewhere at PSI,

Hao Wang, at the Günther Group in ETH, for collaborating on the fabrication of shaped pixels;

Dr. Quang Thai, Dieter Stender, and Aimee McCreedy, for reading through the thesis, and PD Dr. Christof Schneider for help with printing and submission of the thesis;

And finally, thank you to the Swiss National Science Foundation, the EU e-LIFT project, Empa, and PSI for the financial support.

In addition to those who were directly involved in the PhD, I would like to extend my particular gratitude to all those who have welcomed Aimee and I to Switzerland, and helped us through the last three and a half years:

Quang Thai, Manuel Egger, Bryan Chu, Dimas Alfaruq, Andy Norris, William Kylberg, all in the Functional Polymers Group, the Wednesday Uni-Hoc players, and all those at Empa who welcomed me so kindly; Martin Espositio, all in the Materials Group, and all those at PSI who welcomed me so kindly; Nathalie Wieland, Katy Woolcock, Joe Warrington, Alex Mansfield, Michelle Witen, the indoor football (and outdoors during the summer) crowd, the Zürich and St Gallen Gaelic footballers and hurlers, Fritz Senn and the James Joyce Foundation, and all those around Zürich for giving me some laughs between the work; Ian McDonald, all at the Scots Kirk, and all those in and around Lausanne who made Aimee and me feel so at home in Westschweiz; Hendrik Schroeder, for helping me to settle into Zürich in his inimitable way, and for being my best man at my wedding; and the friendship of mine and Aimee's friends and family around the world.

Finally, I would like to thank Aimee for her unwavering support during my studies.

Should auld acquaintance be forgot,
and never brought to mind?
Should auld acquaintance be forgot,
and auld lang syne?

Robert Burns